

**The XENON1T water Cherenkov
muon veto system and
commissioning of the XENON1T
Dark Matter experiment**



Dissertation

zur Erlangung des Grades
“Doktor der Naturwissenschaften”

am Fachbereich 08 - Physik, Mathematik und Informatik
der Johannes Gutenberg-Universität in Mainz

vorgelegt von

Christopher Werner Geis

geboren am 08. Januar 1985 in Groß-Umstadt

Mainz, Januar 2018

1. Gutachter:

2. Gutachter:

Datum der mündlichen Prüfung: 15.06.2018

Eidesstattliche Versicherung

Hiermit versichere ich an Eides statt, dass gemäß §12, Absatz e) der Promotionsordnung des Fachbereichs 08 - Physik, Mathematik und Informatik der Johannes Gutenberg-Universität Mainz vom 2. Dezember 2013,

- die vorliegende Arbeit von mir selbstständig verfasst wurde, ausschließlich die angegebenen Quellen und Hilfsmittel verwendet wurden und von der Ordnung zur Sicherung guter wissenschaftlicher Praxis in Forschung und Lehre und zum Verfahren zum Umgang mit wissenschaftlichem Fehlverhalten Kenntnis genommen wurde.
- ich die Dissertation nicht als Prüfungsarbeit für eine andere Prüfung eingereicht habe.
- ich die gleiche Abhandlung oder Teile davon noch nicht als Dissertation bei einer anderen Fakultät oder einem anderen Fachbereich eingereicht habe.

Mainz, Januar 2018

Christopher Werner Geis

Abstract

There is strong evidence that roughly a quarter of the energy density content of the universe consists of *dark matter*. The XENON1T experiment is the most recent stage of the XENON Dark Matter Project, aiming for the direct detection of dark matter in the form of Weakly Interacting Massive Particles (WIMPs). Its sensitivity for the spin-independent WIMP-nucleon elastic scattering cross-section is $\sigma = 7.7 \cdot 10^{-47} \text{ cm}^2$ for a WIMP mass of $m_\chi = 35 \text{ GeV}/c^2$. The projected sensitivity for a full 2 t·y (ton-years) exposure is $\sigma \approx 2 \cdot 10^{-47} \text{ cm}^2$. The XENON1T detector consists of a liquid xenon time projection chamber (TPC) and is sensitive to nuclear recoils of WIMPs scattering off the xenon atoms. A water Cherenkov muon veto surrounds the XENON1T TPC to shield external backgrounds and to tag muon-induced neutrons by detection of a transiting muon or the secondary shower induced by a muon interacting in the surrounding rock. The muon veto is instrumented with 84 8" photomultiplier tubes (PMTs) with high quantum efficiency (QE) in the Cherenkov regime. The walls of the water tank are clad with the highly reflective DF2000MA foil by 3M.

This thesis presents studies on the muon veto and the TPC subsystem. First, a detailed description of the muon veto system, as well as series tests of its PMTs and development of individual and global calibration systems are presented. Further, a study of the reflective properties of the DF2000MA foil is described, together with a measurement of its wavelength shifting (WLS) properties. The impact of reflectance and WLS on the detection efficiency of the muon veto was studied using Monte Carlo simulations carried out with the GEANT4 toolkit. The data analysis of the XENON1T muon veto system was initiated with this thesis providing a software to read the processed muon veto data. The possibility to identify muon tracks in the muon veto was verified as a first use case.

Contributions to the commissioning of the XENON1T TPC are presented further. Within the framework of this thesis, capacitive liquid level meters have been developed to measure the liquid xenon level inside (four short level meters, SLM) and outside (two long level meters, LLM) of the TPC. They can provide a precision of tens of μm for SLMs and $\approx 3 \text{ mm}$ for LLMs and are read out with a self-made PCB using UTI chips. Additionally, a study of the S2 signal width is presented, compared to different level meter readings and extrapolated to statements regarding wire grid warping.

Summarized, this thesis followed the XENON1T experiment from early design phase (2012), via installation (2015-2016) to the end of commissioning phase (2016) with analyses of first commissioning data. The XENON1T experiment is taking science data since end of 2016.

Zusammenfassung

Es gibt starke Indizien, dass etwa ein Viertel der Energiedichte des Universums von *Dunkler Materie* gebildet wird. Das XENON1T Experiment ist die neueste Stufe des XENON Dark Matter Projekts mit dem Ziel des direkten Nachweises Dunkler Materie in Form von WIMPs. Die erreichte Sensitivitätsuntergrenze für den Wirkungsquerschnitt für spinunabhängige WIMP-Nukleus Streuung liegt bei $\sigma = 7.7 \cdot 10^{-47} \text{ cm}^2$ für WIMPs der Masse $m_\chi = 35 \text{ GeV}/c^2$. Die erwartete Sensitivität für 2t.y (Tonnen-Jahre) Messdauer ist $\sigma \approx 2 \cdot 10^{-47} \text{ cm}^2$. Der XENON1T Detektor ist eine Flüssig-Xenon-Zeitprojektionskammer (TPC) und ist sensitiv auf die Wechselwirkungen von WIMPs mit Xenon-Atomkernen. Ein Wasser-Tscherenkow-Myon-Veto System, welches die TPC umgibt, dient als Abschirmung gegen externe radioaktive Strahlung, als auch zur Identifikation myoninduzierter Neutronen. Es besteht aus 84 8" PMTs mit hoher Quanteneffizienz (QE) für Wellenlängen im Tscherenkow-Bereich. Auf allen Flächen der Tankinnenseite ist eine hochreflektive Folie von 3M namens DF2000MA verklebt.

Diese Dissertation präsentiert das Myon-Veto System und die TPC. Zuerst folgt eine detaillierte Beschreibung des Myon Vetos, einer Durchführung von Serientests aller PMTs, als auch der Entwicklung eines individuellen und globalen Kalibrierungssystems. Des Weiteren wird eine Studie der Reflektionseigenschaften der DF2000MA Folie und eine Messung ihrer wellenlängenschiebenden Eigenschaften vorgestellt. Der Einfluss dieser Messresultate auf die Detektionseffizienz des Myon-Vetos wurde anhand einer GEANT4 Simulation untersucht. Die Datenanalyse des Myon-Vetos wurde initiiert mit einer im Rahmen dieser Dissertation entwickelten Software, welche die prozessierten Detektordaten verarbeiten kann. Als erste Anwendung wurde die Möglichkeit zur Identifikation von Myon-Spuren im Wassertank verifiziert.

Im Weiteren wird die Inbetriebnahme der XENON1T TPC vorgestellt. Im Rahmen dieser Dissertation wurden kapazitive Füllstandsmesser für flüssiges Xenon entwickelt, um den Xenonpegel innerhalb (vier kurze Füllstandsmesser, SLM) und außerhalb (zwei lange Füllstandsmesser, LLM) der TPC zu bestimmen. Die Genauigkeit liegt bei $\approx 30 \mu\text{m}$ für die SLM und $\approx 3 \text{ mm}$ für die LLM. Die selbst entwickelte Ausleseelektronik basiert auf UTI Chips. Eine Studie der S2 Signalbreiten und ein Vergleich mit dem Messwerten der Füllstandsmesser wurde, zusammen mit einer Studie der Krümmverformungen der Elektroden, im Rahmen dieser Arbeit durchgeführt.

Zusammengefasst folgt diese Dissertation dem Lebenszyklus des XENON1T Experiments von früher Entwicklungsphase (2012), über Installation (2015-2016) bis zur Inbetriebnahme (2016) mit Analysen von ersten Detektordaten. Das XENON1T Experiment läuft seit 2016 und befindet sich momentan im zweiten Messdurchlauf.

Contents

List of Figures	xiii
List of Tables	xvii
1 Introduction	1
1.1 Introduction	1
1.2 Evidences for dark matter	3
1.2.1 Galactic scale	3
1.2.2 Cluster scale	3
1.2.3 Cosmic scale	6
1.3 Dark matter candidates	11
1.3.1 Particle candidates	11
1.3.2 Dark matter alternatives	15
1.4 Properties of WIMP dark matter	17
1.4.1 Cosmic abundance	17
1.4.2 Interaction rate in different detectors	19
2 The XENON1T Experiment	23
2.1 Detection principle	23
2.1.1 Time projection chamber (TPC)	23
2.1.2 Liquid xenon as detection medium	27
2.2 Overview over subsystems	29
2.2.1 Cryostat, TPC and PMT arrays	30
2.2.2 Water plant, water shield and muon veto	32
2.2.3 Cryogenics, purification and storage of xenon	33
2.2.4 Noble gas distillation column	34
2.2.5 Data acquisition and processing	36
2.2.6 Slow control system	37

2.2.7	Calibration	38
2.3	Physics reach	38
2.4	First results	42
3	The XENON1T Muon Veto System	45
3.1	Detection principle	45
3.2	Muon veto design overview	48
3.2.1	Mechanical design and installation	49
3.2.2	PMT array layout	50
3.2.3	Readout electronics and trigger logic	52
3.2.4	Muon veto GEANT4 simulation	54
3.2.5	Water tank and water flow simulations	56
3.3	Characterization of the DF2000MA reflective foil	58
3.3.1	Definitions: reflectance, transmittance and absorbance	59
3.3.2	Specular reflectance measurement	60
3.3.3	Measurement of wavelength shifting properties and diffuse re- flectance	62
3.4	Updated Monte Carlo simulation of the muon veto system	67
3.5	Laboratory PMT testing	71
3.5.1	PMT series tests	72
3.5.2	Water submersion tests	77
3.6	Calibration system	79
3.6.1	Design	79
3.6.2	Calibration tests and simulations	82
3.6.3	Commissioning of the calibration system	87
3.6.4	Muon veto calibration	89
3.7	Muon veto data analysis	91
3.7.1	PAX processed data and the muon veto	91
3.7.2	Muon track reconstruction	92
4	The XENON1T Time Projection Chamber	109
4.1	Detailed description of the TPC	109
4.1.1	Mechanical structure, field cage and target volume	109
4.1.2	PMT arrays and global coordinate system	111
4.1.3	“Diving bell system”, piping and liquid level control	112
4.2	Level meter system design and simulation	114
4.2.1	Short level meters (SLM)	116

4.2.2	Long level meters (LLM)	127
4.2.3	Radioactivity measurements of the level meters	132
4.3	Level meter readout electronics	133
4.3.1	The Smartec UTI chip	134
4.3.2	Printed circuit board design	140
4.3.3	Readout firmware	147
4.4	Level meter system installation, calibration and data	154
4.4.1	Installation	154
4.4.2	Detector filling and level meter calibration	155
4.4.3	Long term measurement of the LXe level	159
4.5	TPC Leveling	160
4.5.1	Compensation of residual tilt based on level meter readings	162
4.5.2	S2 signal width based leveling and mesh warping	165
4.5.3	Liquid level height versus S2 signal width	178
4.5.4	Earthquakes striking L'Aquila region	180
5	Conclusion and outlook	183
	Appendices	187
A	The MuonVetoTreeMaker	188
B	Examples of muon track reconstructions	190
C	Level meter technical drawings	196
D	Level meter readout	198
E	Zernike polynomials	201
	Bibliography	203

List of Figures

1.1	The rotation curve of a spiral galaxy	4
1.2	Examples for gravitational lensing	6
1.3	Predicted primordial abundances of light elements	8
1.4	Anisotropies in the CMB measured by the Planck satellite mission	9
1.5	Sterile neutrinos and axions as dark matter candidates	14
1.6	Theoretically predicted search regions for pMSSM neutralinos as WIMP	16
1.7	Evolution of the WIMP number density in the early universe during freeze-out.	19
1.8	WIMP velocity distribution and event rate	21
2.1	Principle of a dual-phase TPC	25
2.2	Signals and their detection of a dual-phase TPC	26
2.3	Discrimination from electronic recoils to nuclear recoils	27
2.4	Self-shielding of liquid xenon	28
2.5	The XENON1T experiment and its subsystems	30
2.6	Cryostats and TPC of XENON1T	31
2.7	Top and bottom PMT array of the experiment	32
2.8	Cryogenic system, xenon purification and storage of XENON1T	33
2.9	Cryogenic distillation column of XENON1T	35
2.10	XENON1T DAQ control page	36
2.11	Total ER and NR background of XENON1T from Monte Carlo simulations	40
2.12	Background model and projected sensitivity of the XENON1T experiment	41
2.13	First results of the XENON1T experiment	43
3.1	Vertical flux of shower particles and a water tank as radiation shield for XENON1T	46
3.2	The XENON1T Muon Veto System	49
3.3	PMT layout in the muon veto	51

3.4	The Hamamatsu R5912 ASSY PMT	51
3.5	Global scheme of the muon veto readout system and trigger logic	53
3.6	The simulated muon veto trigger rate	55
3.7	Water filling of the muon veto and passive shielding effect	56
3.8	Water flow simulation in the water tank	58
3.9	Pictures of the DF2000MA foil after installation in the water tank	59
3.10	Specular reflection measurement of the DF2000MA foil	61
3.11	Diffuse response measurement of the DF2000MA foil	63
3.12	Emission spectra for wavelength shifted light by the DF2000MA foil for different absorption wavelengths	65
3.13	Result summary for the DF2000MA reflectivity and WLS measurements	66
3.14	Implementation of specular reflection data and WLS property in the muon veto Monte Carlo code	68
3.15	Verification of wavelength shifting properties in the simulation	70
3.16	A muon veto PMT in the series test setup	72
3.17	PMT gain measurements for different high voltages	74
3.18	Dark rate measurements of the muon veto PMTs	76
3.19	Afterpulses measurements of the muon veto PMTs	77
3.20	PMT water submersion tests at LNGS	78
3.21	Designs of individual and global calibration systems	80
3.22	Diffuser ball composition	81
3.23	Diffuser ball emission versus azimuth and polar angle	83
3.24	Emission profile of a diffuser ball, normalized to the maximum	84
3.25	Geometrical implementations of the diffuser balls in GEANT4	85
3.26	Simulated PMT hits vs. PMT ID and photon lifetime for illumination with four diffuser balls	86
3.27	Calibration setup of the muon veto	87
3.28	Data obtained with both muon veto PMT calibration systems	89
3.29	Gain and counting rate calibration of the muon veto PMTs	90
3.30	Geometrical considerations to model the muon track reconstruction	94
3.31	Examples for summed waveforms of two muon veto events	97
3.32	Event display of a muon passage through the muon veto system	98
3.33	Event display of a muon passage through the muon veto system projec- tion to the origin planes	99
3.34	Fit residuals of a muon track reconstruction	102
3.35	Event display of fit function values for a reconstructed muon track	103

3.36	Event display of fit function values for a reconstructed muon track as projection to the origin planes	104
3.37	Angular distribution of all reconstructed muons in 410 live-hours of data	105
3.38	Fit residuals of a muon track reconstruction on a simulated Monte Carlo event	107
4.1	Detailed overview of the TPC components	110
4.2	Cathode and anode electrode grids	111
4.3	Top and bottom PMT array layout and TPC coordinate system	112
4.4	Liquid level control mechanism with diving bell and “bleeding tube”	113
4.5	Piping on top of the TPC	114
4.6	Cylindric designs for the short level meters	117
4.7	Finite element simulations of a simple cylindric capacitor	118
4.8	Simulated capacitance versus liquid level height for different cylindric level meters	119
4.9	Simulated capacitance versus liquid level height for different plate level meters	121
4.10	Technical drawings of the mechanical short level meter design	122
4.11	Implementation of the SLM position in CAD and FEM simulations	123
4.12	In situ electric simulation of the SLMs in the TPC	124
4.13	The fabricated five SLMs	125
4.14	Short level meter laboratory tests with liquid nitrogen	126
4.15	Design and simulation of a printed circuit comb-shaped long level meter with vertical teeth	128
4.16	Simulated capacitance versus liquid level height for cylindric long level meters	129
4.17	CAD model for mechanical incorporation of the LLMs in the TPC	131
4.18	Pin layout and block diagram of the UTI Chip	134
4.19	Schematic of failing capacitance measurement for $C_p > C_x$	135
4.20	The UTI four wire measurement technique	136
4.21	Schematic connection overview of the UTI three signal technique	137
4.22	Output signal composition of the UTI	139
4.23	Example of oscilloscope measurement of the three measurement phases	140
4.24	Schematic of the printed circuit board	141
4.25	Power supply port of the level meter readout PCB	142
4.26	UTI/level meter port	143
4.27	Processing unit and RS-485 communication port of the PCB	145

4.28	Picture of the level meter readout printed circuit board	147
4.29	Firmware flow chart for the PIC16F877A microcontroller	149
4.30	Installed SLM on the TPC top ring	155
4.31	Post-installation tests of all level meters	156
4.32	Liquid xenon filling to the TPC	156
4.33	Examples for calibrations of SLMs and LLMs	158
4.34	Long term display of short and long level meters	161
4.35	The XENON1T leveling system	162
4.36	Coarse TPC leveling with the SLMs	164
4.37	Fine TPC leveling with the SLMs	165
4.38	Liquid level and pressure stability during the data taking period of the S2 width study	168
4.39	Peak rate and S2 event selection for the S2 width study (liquid + gas circulation)	169
4.40	xy distribution of S2 peak rates across the TPC (liquid + gas circulation)	170
4.41	Distributions of S2 width mean and standard deviation	171
4.42	Zernike Polynomials up to the 4th order	174
4.43	Selected fit function values for the S2 width xy distribution (liquid + gas circulation)	176
4.44	S2 width versus short level meter readings	178
4.45	Comparing the calculated S2 width at the level meter (x, y) positions with the level meter readings	181
4.46	Sensor readings of an earthquake at 2016/08/24	182
5.1	Projected sensitivity of XENONnT as successor of XENON1T	185
B.2	Muon track reconstruction example with a muon intersecting only the lateral surface	190
B.3	Muon barely intersecting the tank volume but crossing top surface . . .	191
B.4	Muon transiting the tank at very high radii	192
B.5	No intersection of reconstructed track with tank volume	193
B.6	Reconstruction algorithm fits the data poorly	194
B.7	No muon event but random noise coincidence of enough PMTs	195
D.1	Level meter readout PCB - Schematic diagram of the electric circuit . .	199
D.2	Level meter readout PCB - Board layout	200

List of Tables

1.1	Energy densities Ω of baryonic matter, dark matter and dark energy in the universe	11
3.1	Optical filters used to inspect wavelength shifting properties of the DF2000MA foil	63
3.2	Impact on modified reflectivity and WLS on the muon veto tagging efficiency	71
3.3	Diffuser ball composition	82
3.4	Start values for parameters of a muon track reconstruction fit	100
3.5	Calculated fit values for a muon track reconstruction using f_0 and methods 1 and 2	100
3.6	Fractional cut rejection and survival during track reconstruction of 410 live-hours of data	105
3.7	Comparison of the reconstruction algorithm with MC truth	106
4.1	Overview of the final SLM design	125
4.2	Overview of the final LLM design	132
4.3	Measured activities of short and long level meters	133
4.4	Activated interrupts in the readout firmware	151
4.5	Level meter positions in the XENON1T coordinate system	154
4.6	Calibration values for the SLMs	159
4.7	Calibration values for the LLMs	160
4.8	SLM values and corresponding tilt parameters for the TPC leveling . .	166
4.9	Data live times used for the S2 width study	167
4.10	Goodness of Fit for all tested models for fitting the S2 width xy distribution	175
4.11	Tilt parameters obtained from the S2 width analysis for the TPC at different circulation methods	177
4.12	Probing the assumption of one SLM being out-of-plane	179

Chapter 1

Introduction

“Would you like to know more?”

Newsreel announcer, *Starship Troopers*, 1997

1.1 Introduction

The actual state of knowledge in cosmology indicates the existence of a non visible, “dark” matter, a factor ≈ 5 more numerous in the universe than baryonic matter. Stunning evidences imply that we, Earth, stars and galaxies are actually consisting of the “exotic form” of matter in the universe, embedded in a collision-less type of matter, interacting neither electromagnetically nor by strong interaction. As a large part of the energy density content of the universe it is also playing a major role for its evolution after the Big Bang. As going to be presented in the following parts of chapter 1, more than 80 years after Fritz Zwicky¹ observed an astronomical discrepancy and introduced the term “Dunkle Materie” (engl. Dark Matter), it has become an essential, but not yet understood phenomenon of the universe.

What is dark matter made of? And, equally important, can it be probed experimentally? Numerous laboratory experiments try to find dark matter in various ways, however probing only a fraction of the even more numerous theoretical models. Section 1.3 glances at some of the more recognized options and provides pointers to experimental and observational constraints. However, the nature of the dark matter

¹Fritz Zwicky, swiss astronomer, 1898 – 1974

particle is yet unknown. Theories provide a particle class called WIMPs (**W**eakly **I**nteracting **M**assive **P**article) being considered a suitable candidate for dark matter. Their mass is expected to be in a range of about $10 \text{ GeV}/c^2$ to several TeV/c^2 . The XENON collaboration uses liquid xenon time projection chambers (TPC) to search for dark matter particles scattering off xenon nuclei. The subsequent emission of scintillation photons and free electrons enable a photometric and an electrometric measurement channel to those interactions. The newest experiment of the XENON dark matter project is XENON1T, being introduced in chapter 2 and being based on $\approx 1 \text{ t}$ of liquid xenon as detection medium, with a projected sensitivity for the spin-independent WIMP-nucleon elastic cross-section of $\sigma \approx 2 \times 10^{-47} \text{ cm}^2$ for 2 t·y (ton-years) of exposure. It was constructed from 2012-2015 and is running currently in its second science run, after a first run verified its functionality and science impact. As a typical example of *rare-event searches* and considering the very low recoil energies $\mathcal{O}(\text{keV})$ from WIMP interactions, controlling background sources of XENON1T is very important.

This thesis is based on three major work items, contributing differently to the success of XENON1T. First, in case of XENON1T, one type of background originates from neutrons induced by cosmic muons. One major pillar of this PhD thesis was therefore the contribution to the design [29], installation, commissioning and data analysis of a water Cherenkov muon veto system surrounding the TPC. Its inner surfaces are clad with a highly reflective foil, increasing the Cherenkov light detection efficiency. A dedicated measurement of the reflective and wavelength shifting properties of the foil, as well as its impact on the muon veto efficiency was performed within the scope of this thesis and has been published [84]. A detailed description of these two items is presented in chapter 3. The third part of my PhD thesis consists of the development of liquid xenon level meters inside the TPC, acting as important sensors during filling and operation of the TPC. As the responsible developer of the full level meter system including electronic readout, I accompanied it from the design phase, to implementation, installation, commissioning and routine operation. A detailed description of the XENON1T TPC, including the full level meter project, as well as readout electronics and TPC data analysis having been performed within the framework of this thesis and is presented in chapter 4. I am closing this thesis with a conclusion and an outlook in chapter 5, summarizing my results and giving an overview about the projected future of the XENON Dark Matter project.

1.2 Evidences for dark matter

1.2.1 Galactic scale

One major evidence for Dark Matter comes from the rotation of spiral galaxies. Spiral galaxies are aggregations of stars in form of a rotation disk with a central bulge. On the scale of their size (the typical diameter of most galaxies has a value between 1 kpc and 100 kpc) one can examine the mass profile $M(r)$ of that galaxy by inspecting the motion of single stars or gas clouds surrounding it. Applying Newtons law leads to

$$v(r) = \sqrt{\frac{G \cdot M(r)}{r}} \quad (1.1)$$

for the velocity distribution $v(r)$, where G is the gravitational constant² and r the distance with respect to the center of the galaxy. For $r < r_{Bulge}$ where $M(r)$ scales with r^3 for an spherical assumed bulk with constant density, this leads to $v(r) \propto r$. Outside of the outer rim of the galaxy the relation $v(r) \propto r^{-1/2}$ of equation (1.1) is valid since now $M(r)$ matches the mass of the whole galaxy. However, measurements using the observation of 21 cm emission lines of hydrogen clouds surrounding the galaxy NGC6503 [48] discovered that their velocity

$$v(r) = \text{constant} \quad (1.2)$$

for very large r (compare figure 1.1).

This effect can be observed over distances also larger than multiple diameters of the galaxy, which means that $M(r) \propto r$. This relation indicates the existence of a huge mass which (in the easiest way) can be assumed spherical such that its density drops $\rho \propto r^{-2}$ to explain the observed constant velocity.

1.2.2 Cluster scale

Redshift observations of single galaxies in clusters

As mentioned in the introduction of this chapter the first evidence of extra matter in the universe was based on the results of observations by Fritz Zwicky [149] of the motion of galaxies in the Coma cluster. He considered the coma cluster as a closed system in a stationary state and thus applied the virial theorem

²Gravitational constant: $G = 6.67 \cdot 10^{-11} \frac{\text{m}^3}{\text{kg} \cdot \text{s}^2}$.

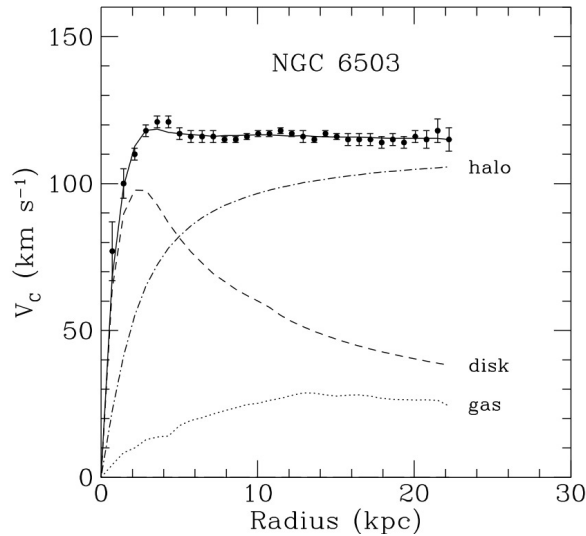


Figure 1.1: Rotation curve of the spiral galaxy NGC6503. The constant behavior until distances far outside the optical end of the galaxy can neither be explained by the stellar density in that region, nor if one adds the mass of the hydrogen gas (which was used to measure the rotation curve). A halo of invisible matter has to be present to explain the observed effect.

$$2\langle E_{kin} \rangle + \langle E_{pot} \rangle, \quad (1.3)$$

which provides a relation for the kinetic energy E_{kin} of such a system to its potential energy E_{pot} . For a cluster of N galaxies this leads to

$$\langle E_{kin} \rangle = \frac{1}{2}N\langle mv^2 \rangle \quad \text{and} \quad \langle E_{pot} \rangle = -\frac{1}{2}GN(N-1)\frac{\langle m^2 \rangle}{\langle r \rangle}. \quad (1.4)$$

Assuming $(N-1) \approx N$ and with $N\langle m \rangle = M$ one can estimate the dynamical mass of the system to

$$M \approx \frac{2\langle r \rangle \langle v^2 \rangle}{G}. \quad (1.5)$$

One can measure $\langle v^2 \rangle$ over the redshift of the galaxies. Zwicky compared results of measurements of the mass-to-luminosity ratio $\Gamma = M/L$ of the clusters with $\Gamma_{\odot} = M_{\odot}/L_{\odot}$ of the sun and found discrepancies up to a factor 400. Small deviations from the value of Γ_{\odot} would not express a big discrepancy, since our sun is not exactly representative to conglomerations of many stars, but a value of $\Gamma \gg \Gamma_{\odot}$ indicates that there has to be an additional mass in higher density as the visible one to fulfill equation (1.5).

Mass distribution in cluster mergers

Collisions of whole galaxy clusters can also provide a evidence for Dark Matter. During a collision of galaxy clusters the single galaxies are typically too far apart to collide. The actual colliding matter is the intracluster medium (ICM, heated gas between the galaxies), accounting for the major part of the baryonic mass in the cluster. During collision, the ICM heats up by friction, is slowed down and remains in the center of the merging complex. The density and distribution of this plasma can be studied by observations of its X-ray emissions. On the other hand, the mass distribution of the cluster merger can be studied by gravitational lensing [77]. This effect describes bending of the light path of a distant source in space time, with a large gravitational potential being between source and observer, acting similar to an optical lens with negligible thickness. It can be used to reconstruct mass profiles of the lensing objects. The image of the source object appears distorted to the observer, depending on the exact alignment of the system, as multiple images or so-called *Einstein Rings*. A stunning example is shown in figure 1.2(a), with a mass of the lensing galaxy of $(5.02 \pm 0.09) \cdot 10^{12} M_{\odot}$ [75]. A configuration like this is called *strong gravitational lensing*, given its graphic strength. However, if e.g. a large extended cluster merger complex acts as the gravitational lens, the assumption as thin optical lens fails. The light path underlies effects of numerous massive objects of smaller gravitational potentials (*weak gravitational lensing*). Their mass profile is only derivable by a statistical estimate of the alignment of a larger number of objects in the background, which get enlarged and distorted. A parametrization of these distortions allows to study the mass of the lensing cluster. An example is the cluster merger 1E0657-558, commonly known as “bullet cluster” due to the characteristic shape of its right part [67].

Figure 1.2(b) shows the visible matter distribution of the bullet cluster in bright colors obtained from the X-ray emission of its hot gas compared to its reconstructed mass profile with weak lensing (displayed as contour lines). As mentioned, the interacting plasma remains in the center of the merger. The underlying mass profile, however, is clearly spatially separated. This is an evidence that invisible contributions to the cluster masses, permeate each other without being slowed down. Thus, bullet cluster observations are considered as evidence for Dark Matter on the cluster scale. Despite being a very famous example, [101] discussed that the velocities of the bullet cluster collision are incompatible with Dark Matter models. However, there are many other cluster mergers, where the evidence for Dark Matter holds, e.g MACS J0025.4-1222 [57], MACS J0717.5+3745 [108] or Abell 520 [109]. In [92], observation of 72 cluster mergers endorses the existence of dark mass as to 7.6σ significance.

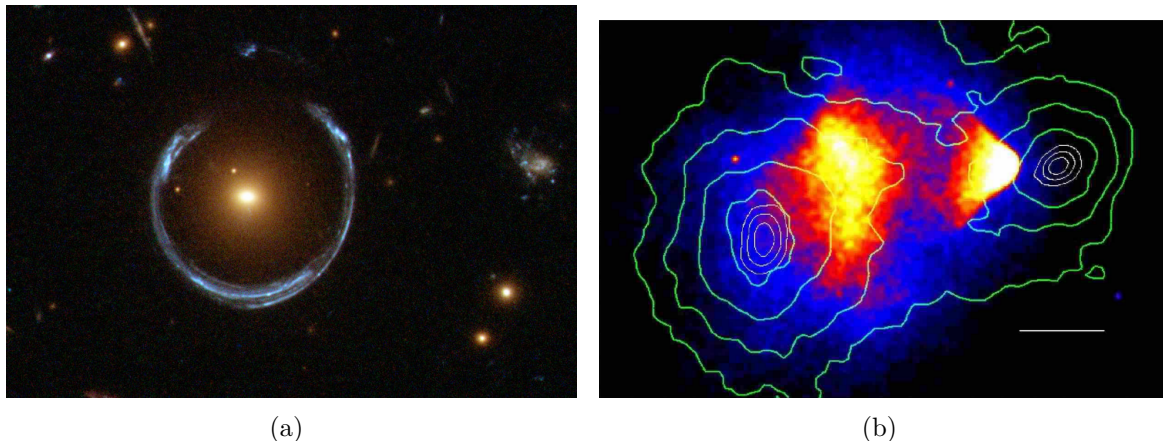
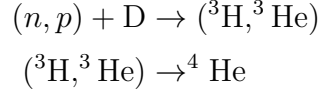


Figure 1.2: (a) Example of gravitational lensing, as the image of the more distant blue galaxy gets distorted to an Einstein ring by the mass of the closer red galaxy. This object is cataloged as LRG 3-757 and known as the “Cosmic Horseshoe”. Picture has been shot by the Hubble telescope and taken from [22]. (b) The bullet cluster. On top of a Chandra telescope image the contour lines indicate the mass profile calculated by weak lensing observations. The reconstructed regions of highest mass are not equivalent to the position of the hot gas. Picture taken from [67].

1.2.3 Cosmic scale

Big Bang nucleosynthesis

There are strong evidences for Dark Matter also in cosmology. At first, big bang nucleosynthesis (BBN) provides an evidence as the energy density of baryonic matter Ω_b is not unity. BBN is a commonly accepted theory, based on a model of the creation of the first elements of the periodic table in their correct relative abundances [16]. BBN happened at temperatures of $3 \text{ MeV} \gtrsim T \gtrsim 10 \text{ keV}$ in times $0.1 < t < 10^3 \text{ s}$ after the Big Bang. All elements heavier than lithium have been created later via fusion in stars and supernovae [63]. During expansion of the universe protons and neutrons (and their antiparticles) froze out. Equilibrium reactions of with leptons settled in and, given the small mass difference between proton and neutron, a ratio of $n/p = 1/6$ was established. As soon as the temperature of the expanding universe could not keep these reactions alive, neutrons could not get reproduced anymore and all neutrons started decaying with a mean lifetime of $\tau = 887 \text{ s}$ down to a ratio of $n/p = 1/7$. All neutrons which had been not decayed until then, had went meanwhile into fusion with protons starting the nucleosynthesis with Deuterium. Given the possible reactions of nuclei with baryons



most of the early produced baryonic matter ended up in ${}^4\text{He}$. Deuterium itself, which is according to those equations necessary to start the nucleosynthesis, is weakly bound and was easily destroyed by high energy photons. The baryon-photon ratio $\eta = n_b/n_\gamma$ is therefore a key parameter of the big bang nucleosynthesis. [120] states its actual value predicted by BBN as $5.8 \cdot 10^{10} \leq \eta_{\text{BBN}} \leq 6.6 \cdot 10^{10}$. Figure 1.3 shows the primordial abundances of several light elements over η . The y axes show the abundance of ${}^4\text{He}$ as Y_p , the fractions of D/H and ${}^3\text{H}/\text{H}$ and ${}^7\text{Li}/\text{H}$. The yellow boxes show the experimentally observed abundances. The second x axis expresses the baryonic energy content in the universe. It is obvious that the curves do intersect at $0.021 \leq \Omega_b h^2 \leq 0.024$ and not at unity (except for lithium). Hence, an additional energy density of dark matter in the universe is needed.

Cosmic microwave background

Following the big bang nucleosynthesis, a constant equilibrium between light elements and photons settled in in the early universe in terms of ionization and recombination according to, e.g.:



At that time the universe was in an opaque state known as the “radiation dominated” era. As the universe expands, temperature decreased and mean free path of the ionizing photons rose. At a temperature of $T = 3000 \text{ K}$, photon density was not high enough anymore to keep the equilibrium alive and the recombination rate overpowered the ionization rate. Hence, at $T_0 \approx 380\,000 \text{ a}$ after the Big Bang a residual photon field remained “imprinted” with the baryonic matter distribution at time of last interaction. Since decoupling, its temperature decreased by the same factor as the universe expanded. This factor is called “redshift” z . Its temperature today can be calculated with

$$T = \frac{T_0}{1+z} \quad (1.7)$$

to be $T = 2.725 \text{ K}$ which lies in the microwave regime of the electromagnetic spectrum. Therefore, this radiation is called CMB (**C**osmic **M**icrowave **B**ackground)

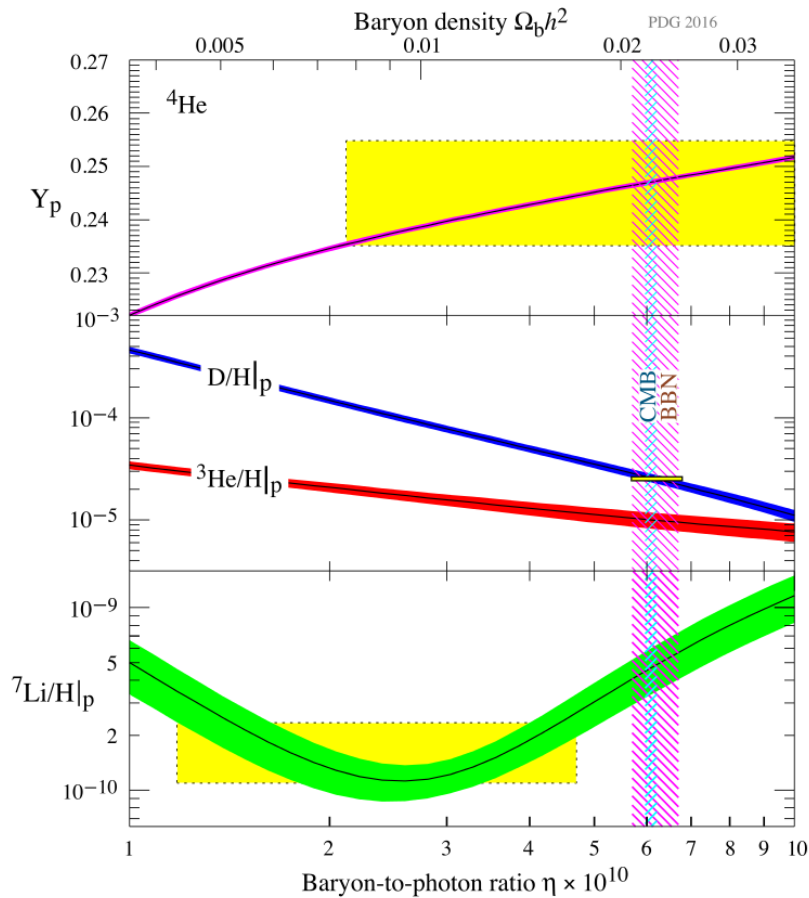


Figure 1.3: The predicted primordial abundances of ${}^4\text{He}$, ${}^2\text{H}$, ${}^3\text{He}$ and ${}^7\text{Li}$ predicted by the Big Bang nucleosynthesis theory with their 95% confidence limits. Boxes indicate the observable abundances of those light elements. The vertical hatched areas indicate the value for η and $\Omega_b h^2$ obtained from Big Bang nucleosynthesis and measurements of the cosmic background radiation (CMB). Figure taken from [120].

and can be measured with high precision as a blackbody radiation with $T = (2.7255 \pm 0.0006) \text{ K}$. [81]. Tiny anisotropies in that temperature across the sky have been measured e.g. by the WMAP satellite [95] and, more recently, the Planck satellite mission [8]. Figure 1.4(a) shows a map of the temperature fluctuations as measured by Planck. The very tiny temperature fluctuations ($\Delta T \approx \pm 500 \mu\text{K}$) originate from primordial fluctuations in the baryon-photon plasma just before decoupling of the CMB. Assuming a statistically isotropic Gaussian random field, the angular power spectrum of that map can be constructed by decomposition in spherical harmonics as shown in figure 1.4(b). It shows the squared temperature deviations versus the angular scale and the multipole moment ℓ according to

$$D_\ell = \frac{1}{2\ell + 1} \sum |a_\ell^m|^2, \quad (1.8)$$

where a_ℓ^m are the coefficients of the underlying spherical harmonics construction. The detailed peak positions and heights are sensitive to cosmological parameters, e.g. the ratio of the second to first peak enables a calculation of the baryonic energy density. Planck calculated it to be $\Omega_b h^2 = 0.0222 \pm 0.0002$, which is in excellent agreement with the estimations from the BBN (as indicated in figure 1.3, labeled as CMB).

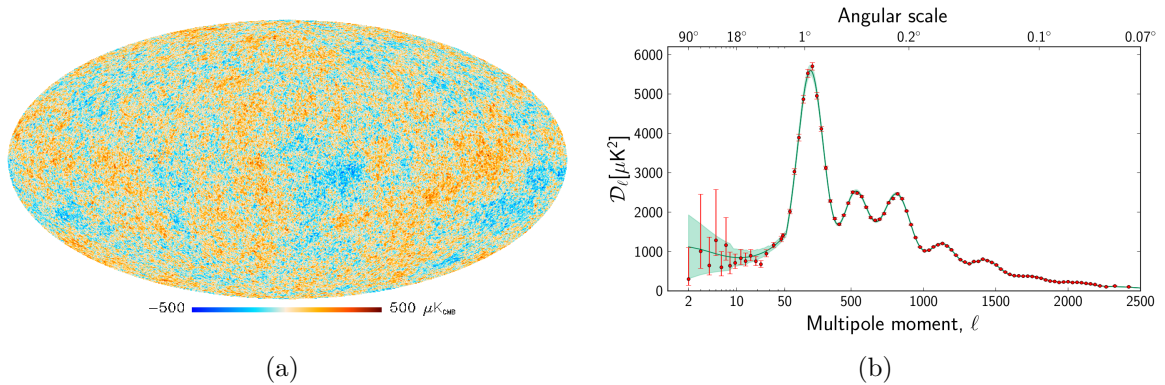


Figure 1.4: Anisotropies in the CMB measured by the Planck satellite mission. (a) Sky map of the absolute temperature anisotropies in the CMB. The deviations are very tiny (μK regime); (b) Constructing the angular power spectrum of spherical harmonics applied to the sky map, peaks at different multipole moments ℓ can be observed. They correspond to matter density anisotropies in the early universe getting imprinted into the CMB at decoupling. The peak positions and heights are sensitive to cosmic parameters as baryonic and dark matter densities. of Both plots taken from [8].

This acts as another evidence for dark matter, since, contrary to the baryon-photon plasma, where primordial fluctuations just inflicted these tiny anisotropies, collision-less dark matter could already attract itself gravitationally and built local density maxima before decoupling of the CMB. The spectrum in figure 1.4(b) is also sensitive to this. Thus, an energy density of (cold) dark matter can be derived from the relative strength of its acoustic peaks and was found to be $\Omega_c h^2 = (0.119 \pm 0.002)$ being one order of magnitude higher than for baryonic matter.

Structure formation in the universe and ΛCDM model

The local dark matter maxima described in the previous section had a influence in the structure formation of the whole universe. The MILLENNIUM simulations [137] and its successors MILLENNIUM II [56] and MILLENNIUM XXL [20] are very large

high resolution N-body simulations, where (for the latter one) 303 billion particles were simulated to represent the formation of cosmic structures in a 4.1 Gpc wide cube. This simulations contained thousands of Milky Way-like mass halos and had sufficient resolution to properly resolve many subhalos. The simulations match cosmic observations and prefer a so-called *bottom-up-scenario*, where structure formation in the universe is mainly driven by non relativistic (cold) dark matter, making it grow hierarchically with small objects attracted first by gravity and merging in a continuous hierarchy to form larger and more massive objects. An opposite scenario, the *top-down-scenario*, where the cosmic structure would have been formed by fragmentation of huge clusters, necessarily to be formed by relativistic (hot) dark matter in the early universe. The results strengthened the common acceptance of cosmology model called Λ CDM (**Λ Cold Dark Matter** model), which provides a simple cosmic sum rule

$$1 = \Omega_\Lambda + \Omega_c + \Omega_b, \quad (1.9)$$

where Ω_Λ , the energy density of dark energy, Ω_c and Ω_b as the ones for cold dark matter and baryonic matter have to sum up to unity. In this model dark energy is a force driving the expansion of the universe, expressible as its expansion rate $H = \dot{a}(t)/a(t)$, where $a(t)$ denotes the scale factor of the universe. H is known as the *Hubble parameter* and connects the expansion of the universe with dark energy by the Friedmann equation

$$H^2 = \left(\frac{\dot{a}}{a}\right)^2 = \frac{8\pi G}{3}\rho - \frac{kc^2}{a^2} + \frac{\Lambda c^2}{3}, \quad (1.10)$$

where G is the gravitational constant, k the curvature parameter of the universe, ρ the universe mass density, c vacuum light speed and Λ the cosmological constant expressing the energy density of vacuum enhanced by dark energy. The Λ CDM model is also called standard model of cosmology since it can predict structure formation and element abundances. Given, the precise measurements of the satellite missions WMAP and Planck presented above, the energy densities Ω of equation (1.9) in the universe can be calculated. Table 1.1 shows a summary of their values.

Another (also in this thesis used) common expression of the parameter Ω is a multiplication with h^2 , where $h = H_0/(100 \text{ km/s/Mpc}) \approx 0.7$ is a historically different representation of the Hubble constant H_0 , representing the Hubble parameter H at the time of today. Thus, dark energy represents the major part of energy in the universe. Only 5% of the energy budget is due to baryonic matter, $\approx 26\%$ due to dark matter.

Λ CDM model	
Parameter	Value
Ω_b	(0.049 ± 0.001)
Ω_c	(0.259 ± 0.006)
Ω_Λ	(0.691 ± 0.006)

Table 1.1: Energy densities Ω_b of baryonic matter, Ω_c of dark matter and Ω_Λ of dark energy in the universe as measured and published by [8]. Only $\approx 5\%$ of the energy density in the universe originates from baryonic matter, $\approx 26\%$ from dark matter.

A stunning cosmological result enhancing the necessity to understand the dark matter phenomenon.

1.3 Dark matter candidates

1.3.1 Particle candidates

Given the observational evidences presented in the previous sections, dark matter has to be composed of particles fulfilling the following requirements:

- Necessity to have the cosmic abundance and mass matching $\Omega_c = 0.259$.
- Necessity to be at non-relativistic speed (cold dark matter)
- Necessity to be stable or long lived.
- Necessity of having no strong and electromagnetic charge.
- Necessity of dark matter being non-baryonic.

Standard Model neutrinos

Applying these selection criteria to the standard model of particle physics (SM) rules out all quarks (strong and electromagnetically charged) as well as all force carriers, since the photon is the particle of light, all gluons have strong charge and Z , W^\pm and Higgs-bosons are not stable. Since electrons, muons and tauons also have electromagnetic charge and partly decay, the only particles of the standard model matching the requirements are the neutrinos. Neutrinos travel with light speed, which would have led to a Top-Down-Scenario for the structure formation of the universe, while galaxy surveys and deep field observations in comparison with many-particle simulations favor

a Bottom-Up-Scenario (compare section 1.2.3). They are therefore “hot dark matter” which disagrees with the Λ CDM model. Further, according to [8][120][95] the neutrino cosmic energy fraction is

$$\Omega_\nu h^2 = \frac{\sum_i m_{\nu_i}}{93.4 \text{ eV}/c^2}. \quad (1.11)$$

To account for all dark matter in the universe $\Omega_c h^2 = 0.12$, the neutrino mass would have to be $m_\nu \approx 10 \text{ eV}/c^2$ which is higher than the upper bound on neutrino masses at $2.2 \text{ eV}/c^2$ [40]. Therefore, with exclusion of the neutrinos, the standard model does not provide a particle suitable for dark matter. However, since neutrino oscillations require neutrinos to carry mass, they do form a sub-dominant form of dark matter in the form of the cosmic neutrino background (C ν B) [111].

Sterile neutrinos

The fact that neutrino mixing can be observed and thus, neutrinos are not mass-less is already a first experimental prove that there physics beyond the standard model (see a review here [55]). In a small extension of the standard model once can postulate a so-called “sterile neutrino” ν_S by adding right handed neutrinos only underlying gravitation and without electromagnetic, strong or weak charge. Sterile neutrinos do not necessarily have to have three generations, they would be able to mix with SM neutrinos and could therefore take place in weak interaction decay. Further, they would act as a natural dark matter candidate with mass in $\mathcal{O}(10 \text{ keV}/c^2)$. They are expected to decay according to

$$\nu_S \rightarrow \nu + \gamma \quad (1.12)$$

under emission of a mono-energy photon in the X-ray regime. This sharp X-ray is looked for in X-ray spectra of galaxy clusters by telescopes. Figure 1.5(a) shows the interaction strength of sterile neutrinos versus their mass. There are still areas in the parameter space which is not excluded by X-ray observatories (blue) and so called “Tremaine-Gunn argument” where Ω_{ν_S} is not large enough (purple). Examples of recent results of sterile neutrino detection experiments have been published in [5][47]. A experimental review is given in [69]

Axions and ALPs

Axions arise from the Peccei-Quinn solution of the strong CP-Problem in QCD [121]. A introduction of a U(1) symmetry compensates the violating term and spontaneous breaking of that symmetry by a new field implies a new particle a , the *Axion*. Introducing more than one symmetry leads analogously to ALPs (**A**xion **l**ike **p**articles). The axion mass m_a is

$$m_a \simeq 0.6 \text{ eV}/c^2 \frac{10^7 \text{ GeV}}{f_a}, \quad (1.13)$$

and is given in terms of the axion decay constant f_a . All axion couplings to ordinary matter are $\propto f_a^{-1}$. There are several channels of how the axion parameter space can be inspected. Figure 1.5(b) summarizes experimental and astrophysical constraints for the axion mass and decay constant. Axions could be produced in accelerators through several channels but accelerators searches have not observed it yet and ruled out masses $\gtrsim 50 \text{ keV}/c^2$. Masses $200 \text{ keV}/c^2 \gtrsim m_a \gtrsim 0.5 \text{ eV}/c^2$ can be ruled out via a disagreement of the longevity of red giants and a theoretical acceleration of star evolution by axions in that mass range. The presence of large amount of neutrinos during observation of supernova SN1987a rule out axions within the range $2 \text{ eV}/c^2 \gtrsim m_a \gtrsim 3 \cdot 10^{-3} \text{ eV}/c^2$ which should have shortened the neutrino burst. Finally if the axion mass is $< \mu\text{eV}/c^2$, it is too small to account for the cosmic energy density of dark matter. However, within the mass range of $\mu\text{eV}/c^2 \lesssim m_a \lesssim \text{meV}/c^2$ axions can still make up the observed dark matter density in the universe. Examples for axion and ALPs experiments are CAST [148], AXDM [106] as well as the CASPEr experiment [62], contributed by researchers of the university of Mainz.

Dark sector particles, dark photons

Another low energy extension of the standard model is the so-called *dark sector* or *hidden sector*. It incorporates the idea of a full sector with a rich phenomenology of additional dark matter particles as well as dark forces and mass carrying dark force mediators. Several theoretical “portals” from standard model fields to this dark sector are discussed (see [79] for a review). One example is the *dark photon* A' [7] which is motivated as being the gauge boson of a new, broken U(1) gauge field. It would couple very weakly to the standard model by kinetically mixing to the standard model photon. The corresponding coupling strength α' can be found to be

$$\alpha' = \epsilon^2 \alpha, \quad (1.14)$$

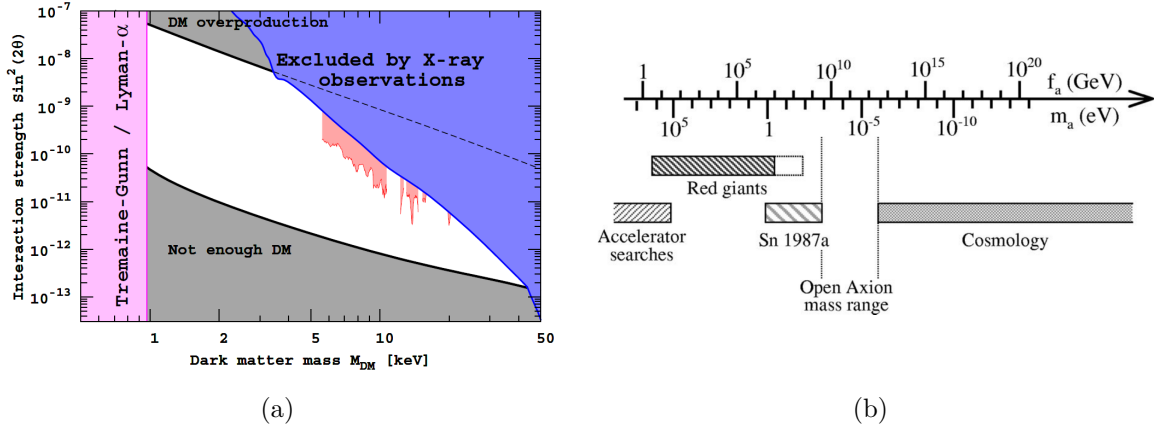


Figure 1.5: (a) The allowed region of parameters of sterile neutrino dark matter confronted with existing experimental bounds. For any combination of mass and mixing angle between two black curves the necessary amount of dark matter can be produced. The blue shaded region is excluded by the non-observation of matching X-rays. In the region below 1 keV/ c^2 (purple) sterile neutrino is “too light” and is ruled out based on “Tremaine-Gunn” like arguments. Plot taken from [55]. (b) Ranges of axion mass m_a or decay constant f_a , respectively which are ruled out by accelerator searches, the evolution of red giants, the supernova SN1987a and axion cosmological energy density. Within the mass range from $\mu\text{eV}/c^2$ to meV/c^2 axions can make up for the dark matter energy density. Plot taken from [58].

with α being the fine-structure constant³ and ϵ being a suppression factor for the mixing to the standard model photon. A dark photon within the mass range of $1 \text{ MeV}/c^2 < m_{A'} < 1 \text{ GeV}/c^2$ could explain a large number of astrophysical anomalies [18] and discrepancies between prediction and measurements of the anomalous magnetic moment of the muon [124]. Therefore, this mass range is being probed by several fixed target or collider experiments, such as KLOE [43] or APEX [6] as well as the proposed MESA experiment at the university of Mainz [93] in order to detect the dark photon.

Supersymmetric particles as WIMPs

WIMPs match, by definition, the requirements of the list mentioned above regarding mass and interaction. Besides other standard model extensions they can be postulated as lightest super symmetric particle (LSP). Supersymmetry is one of the best-motivated proposals for physics beyond the standard model. A supersymmetric transformation Q turns a bosonic state into a fermionic state and vice versa:

$${}^3\alpha = \frac{e^2}{4\pi\epsilon_0\hbar c} \approx 1/137.$$

$$Q|Boson\rangle = |Fermion\rangle \quad \text{and} \quad Q|Fermion\rangle = |Boson\rangle. \quad (1.15)$$

Each SM particle has therefore a supersymmetric *superpartner* particle. There is a wide range of supersymmetric models, but it turned out that models which introduce a new parity R as

$$R = (-1)^{3(B-L)+2S}, \quad (1.16)$$

where S is spin, B is the baryon number and L is the lepton number, and conserve this parity, provide a stable and neutral LSP, being an excellent candidate for WIMP dark matter. Candidates for LSP are e.g. sterile Sneutrinos $\tilde{\nu}_S$ (superpartner of sterile neutrinos), gravitinos \tilde{G} and axinos \tilde{a} (superpartners of the not yet discovered gravitons and axions) and the lightest of several neutralinos $\tilde{\chi}^0$. This neutralino is a linear combination of gauginos \tilde{B} , \tilde{W}^3 and higgsinos \tilde{H}_1 , \tilde{H}_2

$$\chi = \alpha\tilde{B} + \tilde{W}^3 + \gamma\tilde{H}_1 + \delta\tilde{H}_2, \quad (1.17)$$

has a relic abundance of $\Omega_\chi h^2 \approx 0.1$ and would be therefore with a mass of $m_\chi \approx 100 \text{ GeV}/c^2$ a very suitable WIMP candidate. Neutralinos can be constructed from several constrained supersymmetric models, from which the pMSSMs (**p**henomenological **m**inimal **s**upersymmetric **m**odels) [44][129] are discussed here. These models can provide search regions in a parameter space defined by mass m_χ and spin independent WIMP nucleus scattering cross-section σ of WIMPs were dark matter detection experiments can look for them. Figure 1.6 shows the theoretically predicted regions in that parameter space for neutralinos of different pMSSM models including limits of direct detection experiments.

Despite of the fact that the theoretically predicted regions are partly ruled out as well as the fact that the LHC approaches the mass regions of supersymmetry particles without an discovery so far ([1]), the neutralino as WIMP is still the best motivated dark matter candidate so far.

1.3.2 Dark matter alternatives

MOND and TeVeS

Some theories resign dark matter as a phenomenon at all. **M**odified **N**ewtonian **D**ynamics (MOND) [114] is an alternative theory, where Newtons law $-\nabla\Phi_N = \vec{a}$ is only a special case of the equation

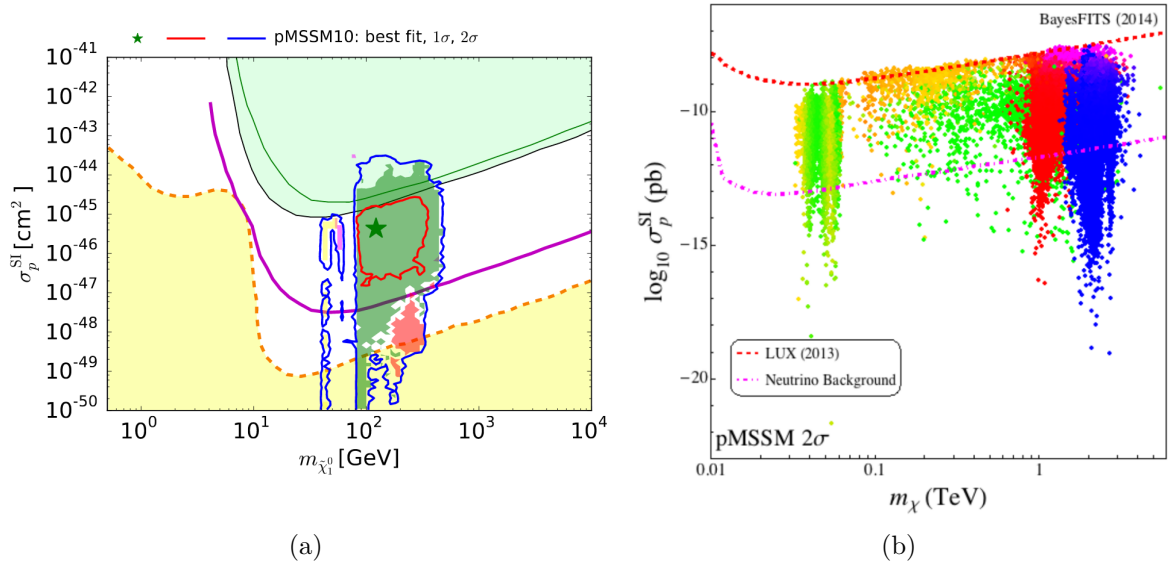


Figure 1.6: Theoretically predicted search regions in the (m_χ, σ) parameter space for pMSSM neutralinos as WIMPs. (a) The solid green and black lines are the upper limits different XENON100 [26] and LUX [14] direct detection dark matter experiments, the solid purple line the projected limit of the planned LZ experiment [110]. The dashed orange line shows the region from which coherent neutrino nucleus scattering (CNNS) will dominate the detection background (yellow region) [52]. The red and blue contour surround the 68% and 95% confidence level region, where the neutralino could be found. The best-fit point is shown as a green star. The colored shadings represent differently dominant underlying neutrino compositions. Plot taken from [44]. (b) The color coding identifies the composition of the lightest neutralino. Pure states are shown in green for \tilde{B} , blue for the \tilde{W}^3 and red for the higgsinos $\tilde{H}_{1/2}$. Mixtures are shown with intermediate colors. The dashed red line the limit of the LUX experiment, the dot-dashed magenta line shows again the CNNS limit. Plot taken from [129].

$$-\nabla\Phi_N = \mu \left(\frac{|\vec{a}|}{a_0} \right) \vec{a} \quad (1.18)$$

with μ being any function obeying the formalism $\mu(x) \rightarrow 1, \forall x \gg 1$ and $\mu(x) \rightarrow x, \forall x \ll 1$. For very small accelerations (as there is between the gravitational forces between stars), the new fundamental constant $a_0 \approx 10^{-10} \text{ m/s}^2$ marks a transition between classical Newtonian and MOND regimes, leading to different behavior. Based on that, MOND is able to explain the velocity distribution of stars at the outer rim of galaxies (as introduced in section 1.2.1) very well [130], but fails to explain the extra mass in the core of galaxy clusters. A relativistic extension of MOND called TeVeS (Tensor-vector-scalar gravity) [49] might solve this but has neither provided

yet a satisfactory explanation of the CMB anisotropies nor of the observed structure formation in the universe.

MACHOs and Primordial Black Holes (PBH)

Baryonic objects like planets, brown and white dwarfs together with primordial black holes are consolidated as MACHOs (**M**assive **C**ompact **H**alo **O**bject) and can account for invisible matter. Their detection is possible via gravitational microlensing when the MACHO transits a larger object in the foreground or possibly by a measurement of the gravitational waves emitted by a primordial black hole merger. However, extrapolation of a few discovered baryonic MACHOs in the Milky Way to the whole halo sum only up to $\lesssim 8\%$ of the dark matter [146], making them unlikely candidates for dark matter in the Milky Way. Contrary to that, primordial black holes as non-baryonic MACHOS can constitute the dark matter content in the universe if they are in a mass range of $20 M_{\odot} \lesssim M_{PBH} \lesssim 100 M_{\odot}$ [53].

1.4 Properties of WIMP dark matter

1.4.1 Cosmic abundance

As motivated in section 1.3.1, WIMPs are suitable candidates for dark matter. It is assumed that WIMPs χ were produced in collisions between standard model particles f in the plasma of the radiation dominated phase of the early universe. At temperatures⁴ $T \gg m_{\chi}$, the rate of colliding particle-antiparticle pairs with subsequent WIMP production was equal to the inverse reaction, with WIMPs converting into particle-antiparticle pairs. In many current theories WIMPs are their own antiparticles:

$$\chi + \chi \leftrightarrow f + \bar{f} \quad (1.19)$$

The time derivative number of WIMPs dN_{χ}/dt in a given region of space is

$$\frac{dN_{\chi}}{dt} = \Gamma(f\bar{f} \rightarrow \chi\chi) - \Gamma(\chi\chi \rightarrow f\bar{f}), \quad (1.20)$$

with

$$\Gamma(f\bar{f} \rightarrow \chi\chi) = N_f \cdot n_f \cdot \langle \sigma(f\bar{f} \rightarrow \chi\chi)v \rangle = n_f^2 \cdot V \cdot \langle \sigma(f\bar{f} \rightarrow \chi\chi)v \rangle \quad (1.21)$$

⁴In natural units, where $k_B = 1$, $c = 1$, $\hbar = 1$.

being the creation rate of $\chi\chi$ pairs from $f\bar{f}$ collisions at relative speed v given a corresponding cross-section σ , an absolute number of particles $N_f = n_f \cdot V$ and their volume density n_f . The angle brackets denote an average over the WIMP thermal distribution. Accordingly, for the annihilation rate $\Gamma(\chi\chi \rightarrow f\bar{f})$ of WIMPs, one can find

$$\Gamma(\chi\chi \rightarrow f\bar{f}) = N_\chi \cdot n_\chi \cdot \langle \sigma(\chi\chi \rightarrow f\bar{f})v \rangle = n_\chi^2 \cdot V \cdot \langle \sigma(\chi\chi \rightarrow f\bar{f})v \rangle. \quad (1.22)$$

The left hand side of equation (1.20), can be expressed as

$$\frac{dN_\chi}{dt} = \frac{dn_\chi V}{dt} = V \frac{dn_\chi}{dt} + n_\chi \frac{d(a(t)^3 V_0)}{dt} = V \left(\frac{dn_\chi}{dt} + 3n_\chi H \right), \quad (1.23)$$

where H is again the Hubble parameter. $\frac{dN_\chi}{dt}$ was zero at $T \gg m_\chi$ since rates $\Gamma(f\bar{f} \rightarrow \chi\chi)$ and $\Gamma(\chi\chi \rightarrow f\bar{f})$ were equal. At these early times, the WIMP density n_χ took on an equilibrium density n_{eq} , related to the fermion density n_f by

$$n_{\text{eq}}^2 = n_f^2 \cdot \frac{\langle \sigma(f\bar{f} \rightarrow \chi\chi)v \rangle}{\langle \sigma(\chi\chi \rightarrow f\bar{f})v \rangle}. \quad (1.24)$$

As the early universe expanded, the WIMP annihilation rate eventually became smaller than the expansion rate of the universe⁵. The WIMPs froze out and their number remained approximately constant from time of freeze-out until today, while the density decreased inversely with the increasing volume. Figure 1.7 shows a typical evolution of the WIMP number density (expressed as the comoving WIMP number density $Y_\chi \propto n_\chi$) in the early universe during the epoch of WIMP freeze-out.

According to the great review [85] this freeze-out happens at a temperature of $T \approx m_\chi/20$ (in natural units), which corresponds to a typical WIMP speed of $v \approx 0.27c$. Inserting equations (1.21)-(1.24) in equation (1.20), one finds for the density of WIMPs

$$\frac{dn_\chi}{dt} = -3n_\chi H - \langle \sigma(\chi\chi \rightarrow f\bar{f})v \rangle (n_\chi^2 - n_{\text{eq}}^2). \quad (1.25)$$

This equation is known as ‘‘Boltzmann equation’’. Precise calculations [138] for the cross-section, necessary to observe the current dark matter density (compare section 1.2.3) yield $\langle \sigma(\chi\chi \rightarrow f\bar{f})v \rangle = 2.2 \cdot 10^{-26} \text{ cm}^2$. Assuming a $m_\chi = 100 \text{ GeV}/c^2$ WIMP and an underlying new force of a similar coupling strength $\alpha \approx 1/137$ as the electroweak

⁵with $H \propto t^{-1}$.

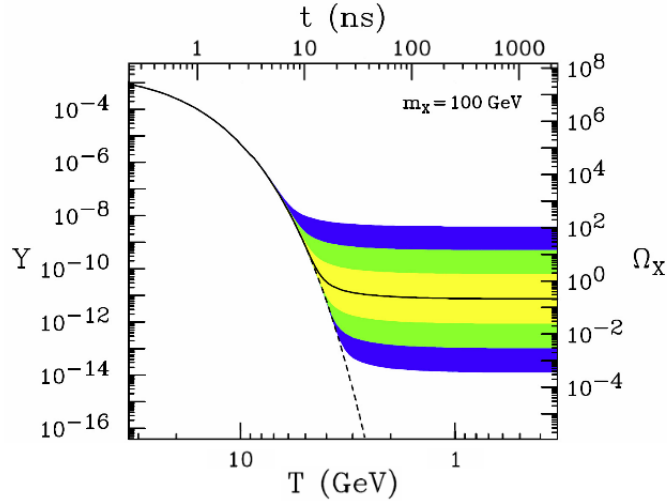


Figure 1.7: Evolution of the comoving WIMP number density $Y_\chi \propto n_\chi$ and the resulting relic density Ω_χ as a function of time t and temperature T . At high temperatures, the WIMP number density closely tracks its equilibrium value (dotted line). As temperature decreases WIMP production becomes negligible and the WIMP abundance per comoving volume reaches its final value. The solid contour is for an annihilation cross section that yields the correct relic density, and the shaded regions are for cross-sections that differ by factor 10 to 1000 from this value. Figure taken from [80].

force leads to a number of the same order of magnitude. This coincidence is commonly called *WIMP miracle* and makes the WIMP a well motivated candidate for dark matter.

However, these WIMP thermal freeze-out scenarios came under pressure by the absence of experimental evidence until now, despite of vigorous search programs of collider and indirect searches (see section 1.4.2) and direct searches (see section 2.4). Subsequently, alternative WIMP creation mechanisms are discussed with rising attention. Exemplarily, the *freeze-in* mechanism [59][89] is based on the assumption, that Dark Matter particles couple so weakly to the plasma, that they never reach thermal equilibrium and their relic abundance is not determined by the WIMP annihilation cross-section.

1.4.2 Interaction rate in different detectors

To find the dark matter particle χ three complementary approaches are possible: Production of the particle, indirect detection of the particle via decay products and direct detection of the particle via scattering off baryonic matter. *Particle production* is investigated in particle colliders, where the center of mass energy \sqrt{s} of the colliding particle needs to be higher than $2m_\chi c^2$. In that case the production of a dark matter

particle and anti-particle pair from a collision of two standard model particles f would look like

$$f + f \rightarrow \chi + \chi. \quad (1.26)$$

The dark matter particles would escape the detector and their missing mass would be the detection signal. Several model dependent results have been published with [65] being a recent one, for example. All without a hint for new physics so far. For *indirect detection*, especially neutrino search experiments look for the creation of Cherenkov light of particles resulting from a dark matter annihilation

$$\chi + \chi \rightarrow f + \bar{f}. \quad (1.27)$$

into a standard model particle and anti-particle. Publications from IceCube [4] and Super Kamiokande [66] neutrino observatories as well as γ -ray observations (Fermi) and cosmic ray spectrometer measurements (AMS-02) provide no discovery but constraints in parameter space (exemplary review [83]). Finally, *direct detection* examines scattering interactions of dark matter particle with standard model particles or baryonic matter

$$\chi + f \rightarrow \chi + f. \quad (1.28)$$

The derivation of formulas to calculate recoil interactions of WIMPs in different detector media have been published in [103] based on the common assumption that WIMPs are producing nuclear recoils [87]. The elastic scattering of WIMPs with masses of $10 \text{ GeV}/c^2 - 1000 \text{ GeV}/c^2$ would produce low energy nuclear recoils in the range of $1 \text{ keV} - 100 \text{ keV}$. They derive the differential recoil spectrum dR/dE_r from interactions of WIMPs with a detector medium as

$$\frac{dR}{dE_r}(E_r, t) = \frac{\rho_0}{m_N m_\chi} \int_{v_{min}}^{\infty} v f(\vec{v}, t) \frac{d\sigma}{dE_r}(E_r, v) d^3v. \quad (1.29)$$

m_N is the mass of the baryonic nucleus the WIMP is interacting with. $d\sigma/dE_r$ is the WIMPs differential cross-section. The values ρ_0 and $f(\vec{v}, t)$ are the dark matter density and its velocity distribution as motivated from astrophysics. The dark matter density in the Milky Way is typically assumed to be an isotropic and isothermal sphere with density profile $\rho \propto r^{-2}$, a so-called *standard halo model*. The corresponding velocity distribution is a Gaussian distribution

$$f(\vec{v}) = \frac{1}{\sqrt{2\pi}\sigma} \exp\left(-\frac{|\vec{v}|^2}{2\sigma^2}\right). \quad (1.30)$$

and is related to the local circular speed by $\sigma = \sqrt{3/2}v_c$ and $v_c = (220 \pm 20)$ km/s [143]. Figure 1.8(a) shows the velocity distributions of the Milky Way accordingly. The time dependence in equation 1.29 originates from Earth's revolution around the sun. The WIMP mass m_χ and the cross-section σ are two observables of a direct detection dark matter experiment. Further, according to [103], equation (1.29) can be rewritten as

$$\frac{dR}{dE_r} = R_0 S(E_r) F^2(E_r) I \quad (1.31)$$

where S is the modified spectral function taking into account effects from detection efficiency, material as well as earth motion around the sun, F is the nuclear form factor correction, depending on the size of the nucleus and I is an interaction function describing effects for spin-independent and spin-dependent cross-sections (see section 2.1.2 for further details). R_0 expresses a default event rate for no momentum transfer. Figure 1.8(b) shows differential energy spectra for different media used in direct detection experiments such as, e.g. germanium (green), liquid argon (blue) and liquid xenon (red). In the low energy regime, liquid xenon provides the highest interaction rates, making it an excellent detector material. Further advantages of xenon in that regard are discussed in section 2.1.2.

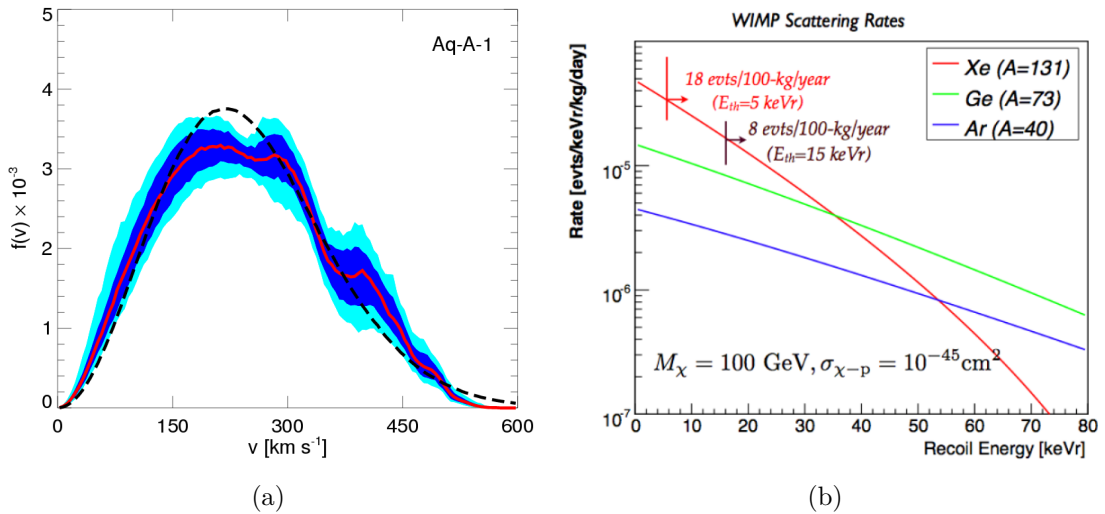


Figure 1.8: (a) Median velocity distribution (red) of WIMPs from a numerical Λ CDM many particle simulation and a Gaussian fit (black) describing the standard halo approximation for dark matter distributed in the Milky Way [143]; (b) Calculated detection rate for $m_\chi = 100$ GeV/ c^2 , $\sigma = 10^{-45}$ cm 2 WIMPs in different detector media. Liquid xenon as detector medium provides highest interaction rates in the low energy recoil regime. Figure created by the XENON collaboration.

Chapter 2

The XENON1T Experiment

“In Wahrheit heißt etwas wollen, ein Experiment machen, um zu erfahren, was wir können; darüber kann uns allein der Erfolg oder Misserfolg belehren.”

“In truth, wanting something means doing an experiment to find out what we can accomplish; only the success or failure will tell us.”

Friedrich Nietzsche, “Nachlass, KSA 9: 3(120)”, *German philosopher and poet*, * 1844; † 1900

2.1 Detection principle

2.1.1 Time projection chamber (TPC)

The XENON1T experiment [39] is the most recent stage of the XENON Dark Matter Search, aiming for the direct detection of dark matter. The detector is, like its predecessors XENON10 [25] and XENON100 [27], operated at the *Laboratori Nazionali del Gran Sasso (LNGS)* underground laboratory in Italy. The experimental halls of the laboratory are below 1400 m of rock of the Gran Sasso d’Italia mountain, protecting it from cosmic radiation. This provides a shielding equally to 3800 mwe (meters of water equivalent) [118]. The goal of the experiment is to directly detect dark matter. Its projected sensitivity for the spin-independent WIMP-nucleon elastic cross-section is about $2 \times 10^{-47} \text{ cm}^2$ [32]. Such an improvement of sensitivity requires, besides a 2 t · y

(ton-year) exposure, a background reduction of two orders of magnitude compared to XENON100. As its predecessors and its competitors LUX [13] or PandaX [64], the detection principle of the XENON1T experiment is the one of a liquid noble element dual-phase time projection chamber with xenon as detection medium. The principle is as follows: if a particle (e.g a WIMP or standard model particles) scatters off the xenon inside the TPC, small amounts of energy are transferred to the xenon. The deposit can happen by scattering off the xenon nucleus (*nuclear recoil, NR*) or scattering off the xenon electronic shell (*electronic recoil, ER*). The recoiling nucleus or electron leads partly to excitation Xe^* and partly to ionization $\text{Xe}^+ + e^-$ of surrounding xenon atoms. Xe^* combines with a neutral atom to form a xenon excimer Xe_2^* . Xenon excimers have a singlet and a triplet state, with de-excitation times of 2.2 ns and 27 ns, respectively [99]. Thus, they quickly emit a 178 nm scintillation photon and dissociate afterwards.



A measurement of these photons is called *primary scintillation signal* or S1 signal. It is measured by arrays of photomultiplier tubes (PMTs) at the bottom and at the top of the detector. Figure 2.1 schematically shows an interaction in the liquid.

A second channel of information can be obtained from the freed electrons of the scattering process. An electric field applied between cathode on the bottom and the grounded gate close to the liquid gas interface prevents them from recombining with Xe^+ ions. This *drift field* is usually in the order of 0.1 – 1 kV/cm and attracts the electrons towards the gate mesh, where they get extracted to the gaseous xenon (GXe) by a stronger *extraction field* (≈ 10 kV/cm in the gas phase and ≈ 5 kV/cm in the liquid) applied between gate and anode. During their following transit through the xenon gas, their energy is high enough to excite Xe atoms in the gas, resulting in scintillation light with an intensity proportional to the number of electrons extracted (*electroluminescence*). The measurement of this proportional scintillation light is called *ionization signal* or S2 signal. Figure 2.2 the signals of S1 and S2 in an event, exemplary of the XENON1T TPC. The first row shows the bottom and top PMT array and their observation of S1 and S2 respectively. The color scale spans from low signal intensities (blue) to high intensity (red). The middle row is a zoom of the waveform shown in the last row, containing an S1 signal at 100 μs and an S2 signal at 250 μs

Furthermore, it shows two major advantages of a dual-phase TPC: First, it provides a possibility for a full 3D reconstruction of the vertex of interaction in the xenon fiducial volume. xy resolution is yielded by reconstructing the position according to the signals of the PMT top array as visible in the “S2 top” panel in the figure. This

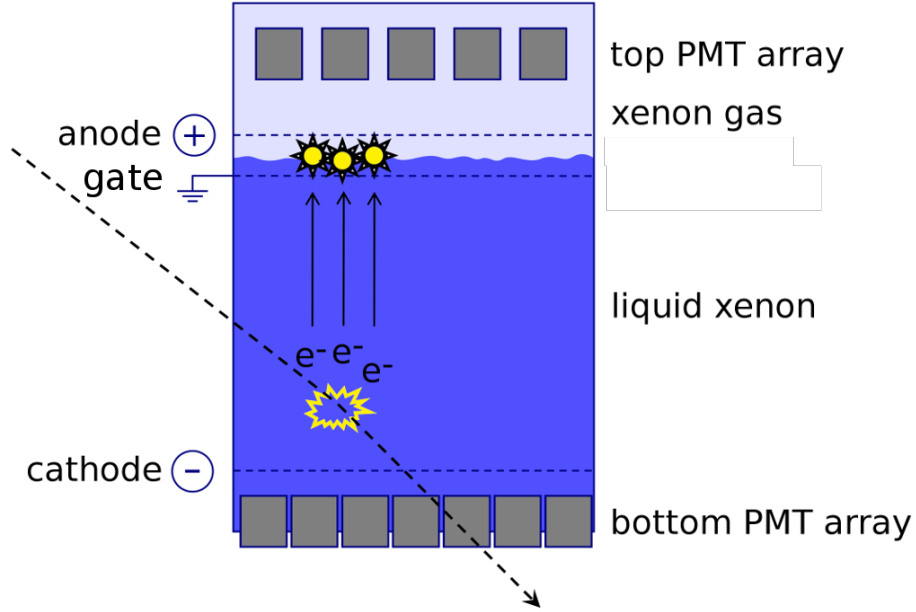


Figure 2.1: Principle of a dual-phase TPC. Particles deposit energy in the liquid xenon (LXe) resulting in a prompt scintillation light signal (S1) and free electrons. An applied drift field between cathode and gate attracts the electrons from the interaction site to the gate mesh, where they get extracted into the gaseous xenon (GXe) by a stronger electric extraction field applied between gate and anode. The subsequent passage through the GXe results in proportional scintillation called ionization signal (S2).

allows the *fiducialisation* of the detector volume by means of selecting sub-volumes in the TPC volume where the external background reached an acceptable level. The time difference between S1 and S2 allows, given the known electric drift field, for calculation of the z position below the liquid surface. Second, the TPC provides interaction type discrimination. Since the mean number of scintillation photons per unit energy, called light yield \mathcal{L}_y is different for electronic recoils [46] and nuclear recoils [24][28], the ratio between S2 and S1 signal can be used to discriminate events. Electronic recoils (produced by β or γ interactions) have a larger ratio than nuclear recoils (produced by neutron or WIMP interactions):

$$\left(\frac{S2}{S1}\right)_{ER} > \left(\frac{S2}{S1}\right)_{NR}, \quad (2.2)$$

where $(S2/S1)$ is called discrimination parameter. It is common to plot the data in terms of this parameter to have an illustration of the separation of the two interaction types versus the S1 signal as shown in figure 2.3(a) for calibration data of the XENON100 experiment. Given these results, it is possible to define a search region, where an WIMP interaction has to end up. As illustrated in figure 2.3(b) it is limited by the

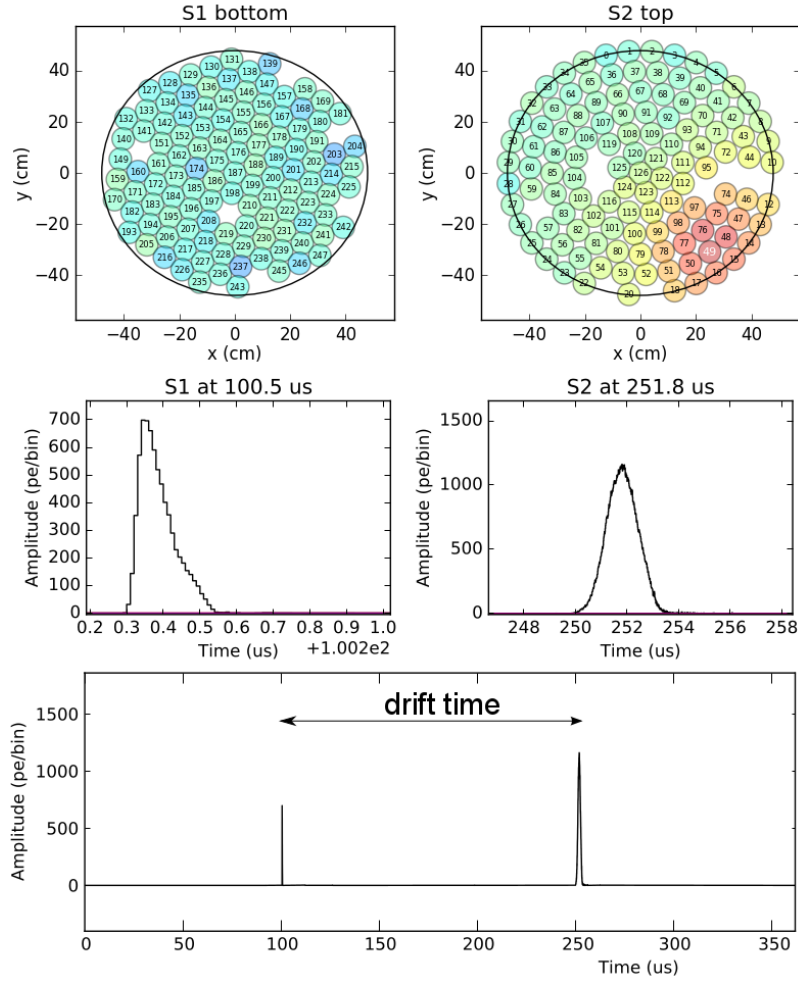


Figure 2.2: Signals and their detection of a dual-phase TPC. The prompt scintillation light S1 appears first (here at $100\ \mu\text{s}$) and is mainly detected by the top PMT array. The proportional scintillation light S2 appears later, dependent on the depth of the primary interaction. The S2 signal has higher intensity and is mainly detected by the top array, where xy position reconstruction is possible. The time difference between S1 and S2 allows position reconstruction in z . Thus, a dual-phase TPC provides full 3D vertex reconstruction.

lower and upper detection limits (vertical blue dashed lines), as well as a horizontal line representing 99.75% ER rejection in this example (green dotted line). In this example ([26]) two events have been found in the search box, agreeing with the expectation of background events leaking into the search box.

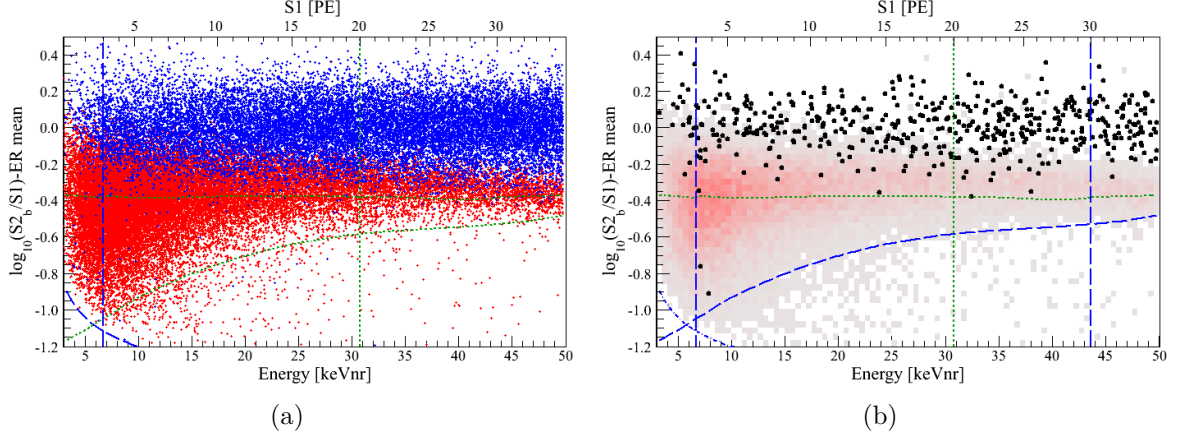


Figure 2.3: (a) Discrimination of electronic recoils (blue) and nuclear recoils (red) in the discrimination space $\log_{10}(S2/S1)_{>ER}$ mean. Figure created by the XENON collaboration; (b) XENON100 results from 225 live days of dark matter search. The benchmark WIMP search region is delimited on the y -axis by the 99.75% ER rejection cut (horizontal green dotted line) and the border running along the 97% NR quantile (inclined blue dashed curve). The delimiters on the x -axis indicate the lower analysis threshold of 6.6 keVnr and the upper limit of 30.5 keVnr (a range equivalent to 3 – 20 PE). Two events are found in the WIMP search region, agreeing with background expectations.

2.1.2 Liquid xenon as detection medium

Liquid xenon (LXe) incorporates many properties providing advantages for the field of direct detection of dark matter. Most of the stated numbers in the following are taken from the LXe detector review [23]. The reasons to choose xenon as a detector medium are:

- The high atomic weight increasing the probability of an WIMP interaction: Xenon contains a heavy nucleus with a mean atomic mass of $A_r = 131.30$: in a commonly made assumption of WIMPs coupling equally to protons and neutrons [97], the cross-section of spin independent WIMP-nucleon couplings scales with the square of the nucleus mass number A , at least for small momentum transfer:

$$\sigma_{SI} = \sigma_{p,SI} \cdot \left(\frac{\mu}{\mu_p} \right)^2 A^2, \quad (2.3)$$

where $\sigma_{p,SI}$ is the WIMP-proton cross-section. μ and μ_p are the reduced mass of the WIMP-xenon and WIMP-proton, respectively according to $\mu = M_\chi M / (M_\chi + M)$.

- The Self shielding: The high atomic number $Z = 54$ as well as its density of ρ_{LXe} of liquid xenon enhancing it with a very efficient stopping power for penetrating

external radiation. Figure 2.4 shows this effect in a set of background data of XENON1T. The amount of background events decreases by three orders of magnitude from the outer radius of the detector to its center.

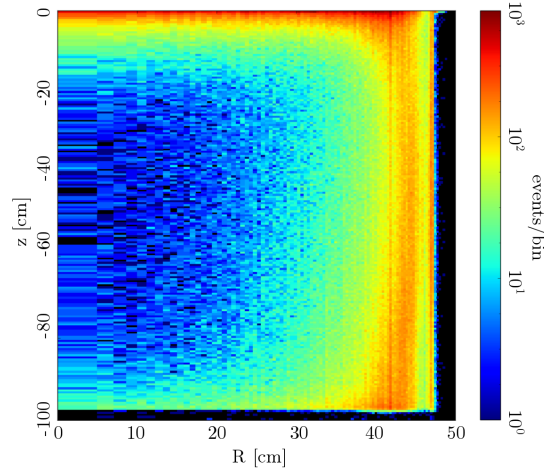


Figure 2.4: High atomic mass and density of liquid xenon generate a self-shielding effect, reducing the background rate by three orders of magnitude from the outside of the TPC to its center. Figure created by the XENON collaboration.

- **The Scalability:** Due to the liquid phase, LXe scales more favorably to large masses than, e.g., cryogenic solid-state detectors such as Ge or scintillating crystals.
- **Odd-nucleon isotopes as natural abundances:** About half of the natural abundance of xenon consists of stable ^{129}Xe and ^{131}Xe isotopes. Those odd xenon nuclei contain an unpaired neutron, which allows LXe detectors to be sensitive to the spin dependent WIMP-nucleon scattering with cross-section given by [100]:

$$\sigma_{\text{SD}} \propto \sigma_{p,\text{SD}} \cdot \left[\langle S_p \rangle + \langle S_n \rangle \frac{a_n}{a_p} \right]^2, \quad (2.4)$$

where a_p and a_n are coupling constants of a WIMP to protons and neutrons, while $\langle S_p \rangle$ and $\langle S_n \rangle$ are the average spins of protons and neutrons in the nucleus. $\sigma_{p,\text{SD}}$ is the spin dependent WIMP-proton cross-section.

- **A scintillation wavelength detectable by PMTs and affordable cryogenic effort.** As being the heaviest non-radioactive noble element, liquid xenon has the longest scintillation wavelength of 178 nm and the highest liquefaction temperature of

165.05 K at one atmosphere. Contrary to the deeper UV scintillation light of krypton (148 nm)¹, argon (128 nm) and neon (85 nm), this longer wavelength is detectable with quantum efficiencies of $\approx 30\%$ by state of the art photocathode materials of light detectors without the use of wavelength shifters. The needed cooling power is lower and it is easier to liquefy and keep xenon in liquid phase compared to the other noble elements with lower liquefaction temperatures.

- The light yield \mathcal{L}_y and charge yield \mathcal{Q}_y are the highest among liquid noble elements: The mean energy to provoke a scintillation photon in LXe is $W_{ph} = (13.8 \pm 0.9)$ eV and the mean energy to create an electron-ion pair $W = (15.6 \pm 0.3)$ eV is the lowest among all noble gases (e.g. for argon: $W_{ph} = (19.5 \pm 1.0)$ eV, $W = (23.6 \pm 0.3)$ eV) [23].
- No intrinsic background by radioactive isotopes: all abundant radioactive xenon isotopes are anthropogenic and decay within days. To be more accurate, the naturally occurring isotopes ^{124}Xe and ^{136}Xe are actually unstable and decay with half-lives of 10^{16} a and 10^{21} a, respectively. Their rates in the energy region of interest are lower than the rates from radioactive impurities of other noble element isotopes such as ^{85}Kr or ^{222}Rn .
- As shown in section 1.4.2 xenon has the largest expected rate for low mass WIMPs of all common detector materials.

2.2 Overview over subsystems

In this section all subsystems of the XENON1T experiment are introduced. The main information is taken from collaboration internal notes and presentations. Figure 2.5 shows a picture of the XENON1T experiment with the water tank, hosting the TPC and the muon veto, to the left and the support building, hosting cryogenics, data acquisition systems and operations office, to the right. The subsystems muon veto and TPC, which played a major role in this thesis, are described in detail in chapters 3 and 4.

¹Krypton as detector medium is generally no good choice, because of a intrinsic background originating from the anthropogenic ^{85}Kr , abundant in traces in the atmosphere. It decays by β^- emission with a half-life of ≈ 11 years.

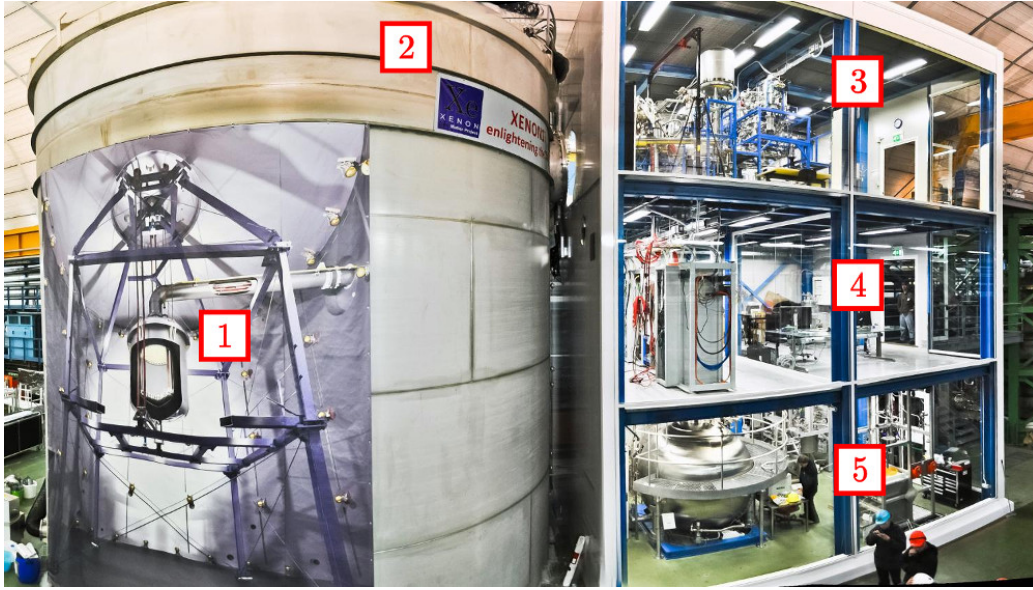


Figure 2.5: The XENON1T experiment and its subsystems. 1: Support structure, cryostats and TPC. 2: Water tank and muon veto. 3: Cryogenics floor hosting xenon cryogenics and purification subsystems. 4: DAQ floor hosting all electronics and servers. 5: Storage floor hosting ReStoX and the distillation column.

2.2.1 Cryostat, TPC and PMT arrays

The XENON1T cryostat consists of two independent cylindrical vessels made of low radioactivity stainless steel enclosing the detector and LXe. The inner vessel of 1.112 m diameter and 1.765 m height is designed to be consistent with ultra-high vacuum conditions and to host 3.5 tons of LXe at -95°C and 2 bar pressure. It is insulated with vacuum and multiple layers of mylar² for less than 50 W heat input from the environment. The outer vessel, having a diameter of 1.30 m and a height of 1.878 m height, is dimensioned to enclose a future larger inner vessel and detector for XENONnT (see chapter 5). A 6 m meter long pipe internally called “umbilical pipe” connects it to systems located in the service building. Both cryostats are held in place by a 9 m high support structure. Figure 2.6(a) shows a CAD drawing of the two cryostat shells. The innermost part of the XENON1T experiment and the sub-system which actually searches for the dark matter particle is the TPC. It contains the liquid xenon target observed by two arrays of sensitive photosensors. It also provides the electric drift field to remove the ionization signal from the interaction site, and a xenon gas phase above the liquid to convert this charge signal to light. Figure 2.6(b) shows a picture of the

²Mylar is one brand name of biaxially-oriented polyethylene terephthalate (BoPET), a polyester film used for insulations given its very good reflective properties for thermal radiation.

TPC hanging from the cryostat during installation in November 2015. The TPC as a subsystem played a major role within the scope of this thesis as it is hosting the liquid level meters. Therefore, it is explained in detail separately in section 4.1.

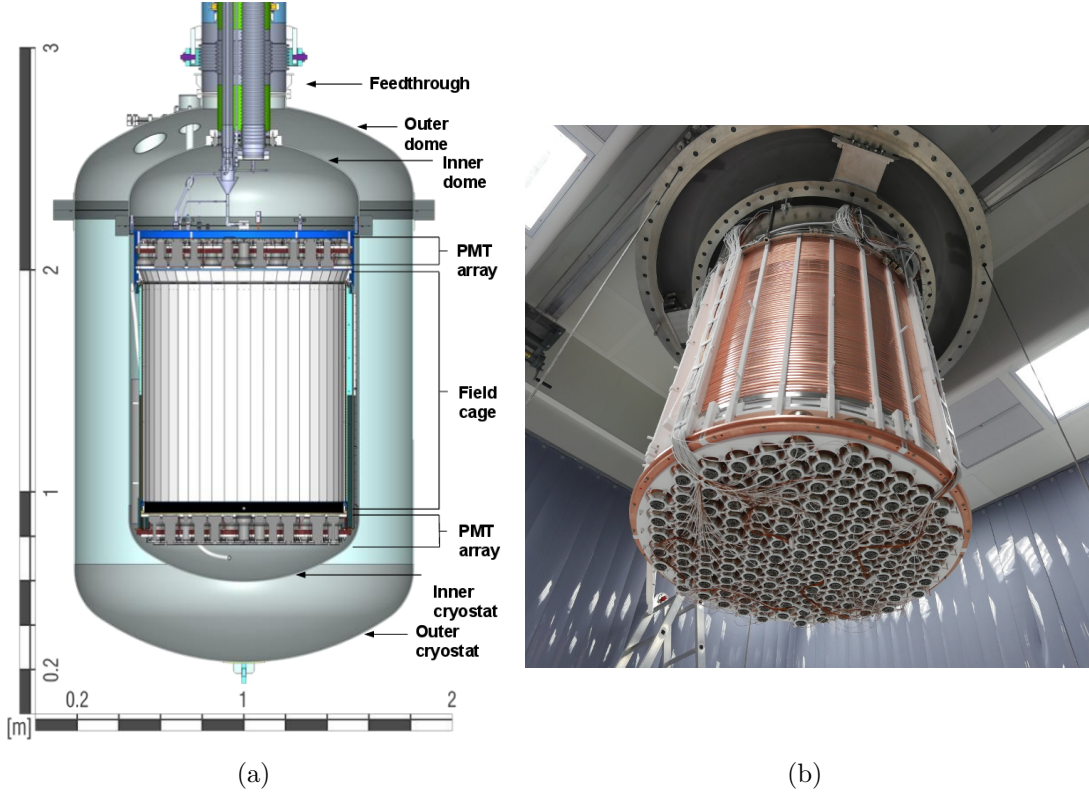


Figure 2.6: Cryostats and TPC of XENON1T. (a) Illustration of how the outer cryostat hosts the inner cryostat which hosts itself the TPC; (b) Picture of the TPC during installation in November 2015. Both cryostats are lowered. The bottom PMT array and the field cage are nicely visible.

The light produced by particle interactions in XENON1T is measured by two arrays of PMTs located at the top and bottom of the detector. The top array consists of 127 photomultipliers arranged in a radial pattern. The bottom PMT array detects most of the scintillation light and contains 121 PMTs arranged in a tight, hexagonal pattern. More details about this layout can be found in section 4.1.2. The empty regions among them are covered with a PTFE reflector to maximize the light collection. The used 3" R11410-21 PMTs have an average gain of $5 \cdot 10^6$ at -1500 V and have a high quantum efficiency of $\approx 35\%$ at 178 nm wavelength of the xenon scintillation light. They have been developed in a joint effort of the XENON collaboration and Hamamatsu to produce a highly radio-pure PMT [30]. Further, they have been tested intensively beforehand, e.g. with respect to the quantum efficiency change versus

temperature change [107] or their long term functionality in LXe [45]. Together with every other part and raw material of the TPC, they have been part of a screening campaign to estimate the full radioactive budget of the XENON1T experiment (see [36]).

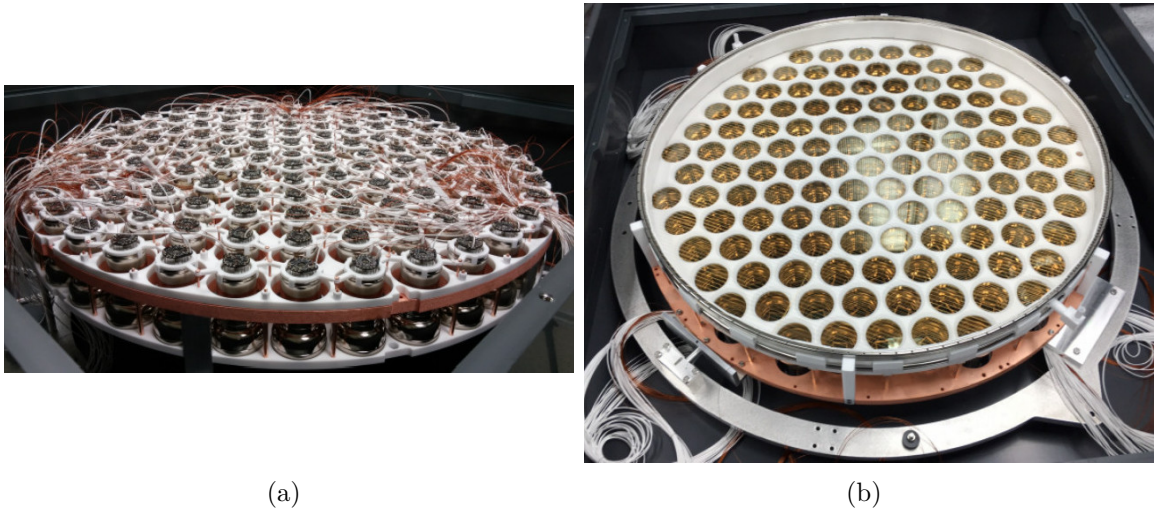


Figure 2.7: Assembled top (a) and bottom (b) PMT arrays of XENON1T prior installation.

2.2.2 Water plant, water shield and muon veto

Labeled as “2” in figure 2.5, a tank of ultra-pure water surrounding the XENON1T detector is acting as a passive shield against external radiation. Instrumented with photomultipliers, it also serves as an active muon veto. Both systems are subject of major items of this thesis and are therefore separately explained in detail in chapter 3. A purification plant is providing demineralized water to fill the tank. It is a reverse osmosis plant capable of reducing the residual conductivity of its output water to a value of $0.07 \mu\text{S}/\text{cm}$. It reduces further the number of radioactive isotopes in the water as well as the total number of organic hydrocarbon molecules to a level of $< 1 \text{ ppm}$. If not controlled, the organic molecules would promote the development of bacteria flora, which, over time, would decrease the water transparency leading to less efficient light detection with the muon veto PMTs. It can provide a maximum output rate of $2.2 \text{ m}^3/\text{h}$ water per hour. Given the tanks volume of $\approx 750 \text{ m}^3$, the filling of the full tank takes about two weeks.

2.2.3 Cryogenics, purification and storage of xenon

The cryogenics and purification plants are located on the uppermost floor of the support building (labeled “3” in figure 2.5). The cryogenic system maintains the xenon in the cryostat in liquid form, at a constant temperature and pressure for a long period on the order of years. It achieves this using pulse tube refrigerators (PTR) and liquid nitrogen cooling systems, vacuum insulation, and a host of redundancies. As mentioned before it is connected to the cryostat via the umbilical pipe. Its main system components are the two redundant PTR, responsible for the primary cooling, a backup liquid nitrogen (LN_2) cooling tower, efficient heat exchangers and redundant turbomolecular and backing pumps to maintain insulation vacuum. Remote operation and monitoring is enabled via the slow control system, including automatic safety procedures. Figure 2.8 shows the connection of the cryogenic systems to other subsystems of the experiment.

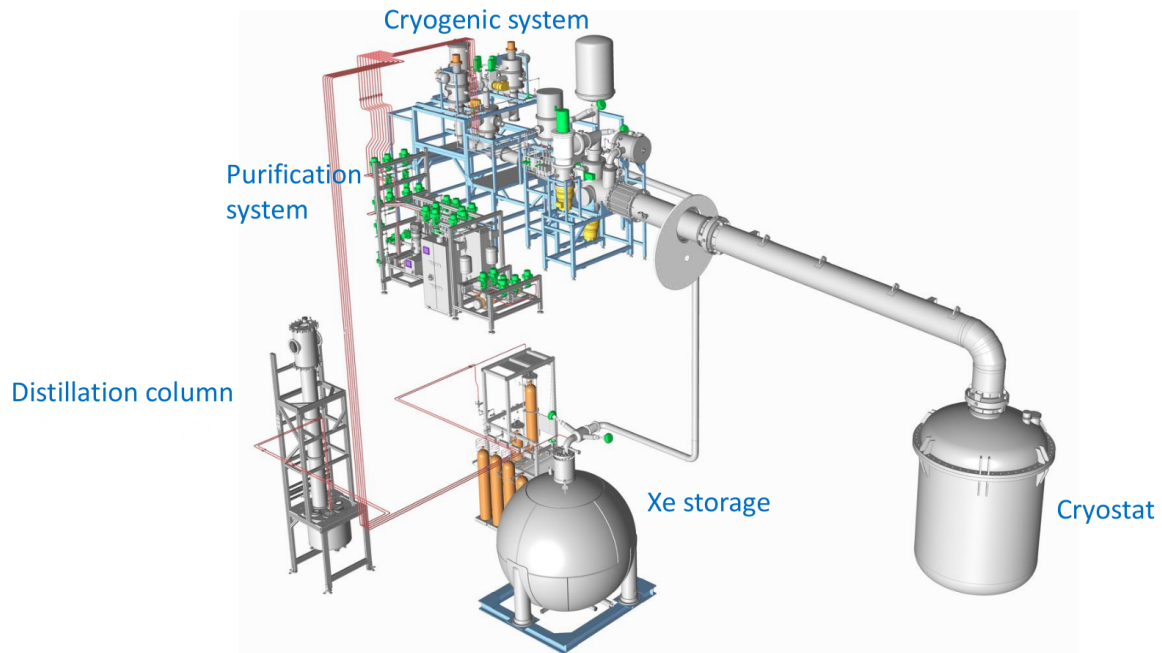


Figure 2.8: Cryogenic system, xenon purification and storage of XENON1T.

The cryogenic system is directly connected through vacuum insulated pipes to ReStoX, the xenon storage and recovery system located on the ground floor of the support building. The ReStoX system is used to fill the detector with purified liquid xenon and to provide fast recovery and safe storage of up to 7.6 t of xenon. It can operate at pressures from high vacuum up to 72 bar. Covering a temperature range from -196°C to room temperature, ReStoX is able to safely store the full xenon content of XENON1T in liquid and gaseous phases. ReStoX consists of two concentric stainless

steel spheres, with the inner one being electro-polished, 3 cm thick with 2.1 meter diameter. The primary cooling is provided by a liquid nitrogen-cooled condenser with 3 kW of cooling power. It provides efficient recovery of xenon with 8 inner fins with a total surface of 8.9 m² to increase the heat exchange of this maximum cooling power. Emergency cooling is provided by 16 liquid nitrogen lines welded on its outer surface. The inner sphere is further covered with 30 layers of mylar, and has only minimal thermal contact with the outer sphere. The space between the two spheres is evacuated to provide effective thermal insulation. The cryogenic system is further connected to the purification system, via efficient two-phase heat exchangers, to complete the TPC LXe circulation circuit. This system pumps and distributes the high purity xenon to every part of the experiment with flows up to 40 – 50 slpm (standard liter per minute³) using two parallel high capacity magnetic resonance pumps by QDrive. The purification is necessary, since the xenon gets continuously contaminated with impurities (like H₂O and O₂) outgassing from the detector materials. These impurities attenuate the light and charge signal. Therefore, continuous recirculation of the precious xenon gas through heated zirconium getters removes the impurities that impede the detector performance down to the ppb level.

2.2.4 Noble gas distillation column

Finally, the cryogenic system is connected to the cryogenic distillation column. Two sources of intrinsic contamination of the xenon itself result from traces of radioactive noble elements, namely the radio-isotopes ⁸⁵Kr and ²²²Rn. ⁸⁵Kr is a β emitter with a half-life of 10.76 a and an end point energy of 687 keV. It is intrinsically immersed⁴ in commercial xenon in concentrations of $\approx 10^{-20} - 10^{-17}$. ²²²Rn decays via α emission over ²¹⁸Po to ²¹⁴Pb, which is also a low energy β emitter. Mother nuclides of ²²²Rn trapped in the detector materials (mainly PTFE) decay and emanate the ²²²Rn continuously into the liquid xenon during the run of the experiment. Both low energy β spectra can contaminate the region of interest for dark matter search. To achieve the XENON1T background goals the concentrations of krypton and radon in the liquid xenon has to be ^{nat}Kr/Xe < 0.2 ppt⁵ and ²²²Rn/Xe < 10⁻²⁴ [32]. To achieve this, a cryogenic distillation column has been developed [128]. Its performance and functional principle

³1 slpm is the volumetric flow rate of a gas corrected to defined standard conditions of temperature ($T = 273.15$ K) and absolute pressure ($p = 1$ bar).

⁴The isotope ⁸⁵Kr is mainly produced anthropogenically in nuclear fission reactors and gets released to the atmosphere during nuclear fuel reprocessing. Xenon, extracted by distillation from air, contains therefore traces of this isotope.

⁵For an abundance of ⁸⁵Kr in natural krypton of ⁸⁵Kr/^{nat}Kr $\approx 10^{-11}$.

has been successfully shown and verified [33][126][127]. It is shown in figure 2.9(a). The column is ≈ 5.5 m high and packed with high surface package materials for the separation process. The design parameters for XENON1T are a processing xenon flow rate of 3 kg/h (8.3 slpm), a separation factor of $10^4 - 10^5$. 99% of the purified xenon can be extracted at the bottom of the column, while 1% krypton enriched xenon is purged as off gas. For the radon distillation the principle works inversely [37]. Since radon is less volatile than xenon, here the radon depleted xenon gas is extracted at the top of the column and the radon is kept at the bottom of the column. In figure 2.9(b) the reduction of krypton in xenon is visible over time during online distillation between July and November 2016. The shaded areas indicate when the distillation was conducted, the red dots are mass spectrometer measurements of xenon samples. As visible, the krypton to xenon concentration decreased to a few ppt, being the lowest krypton concentration ever achieved.

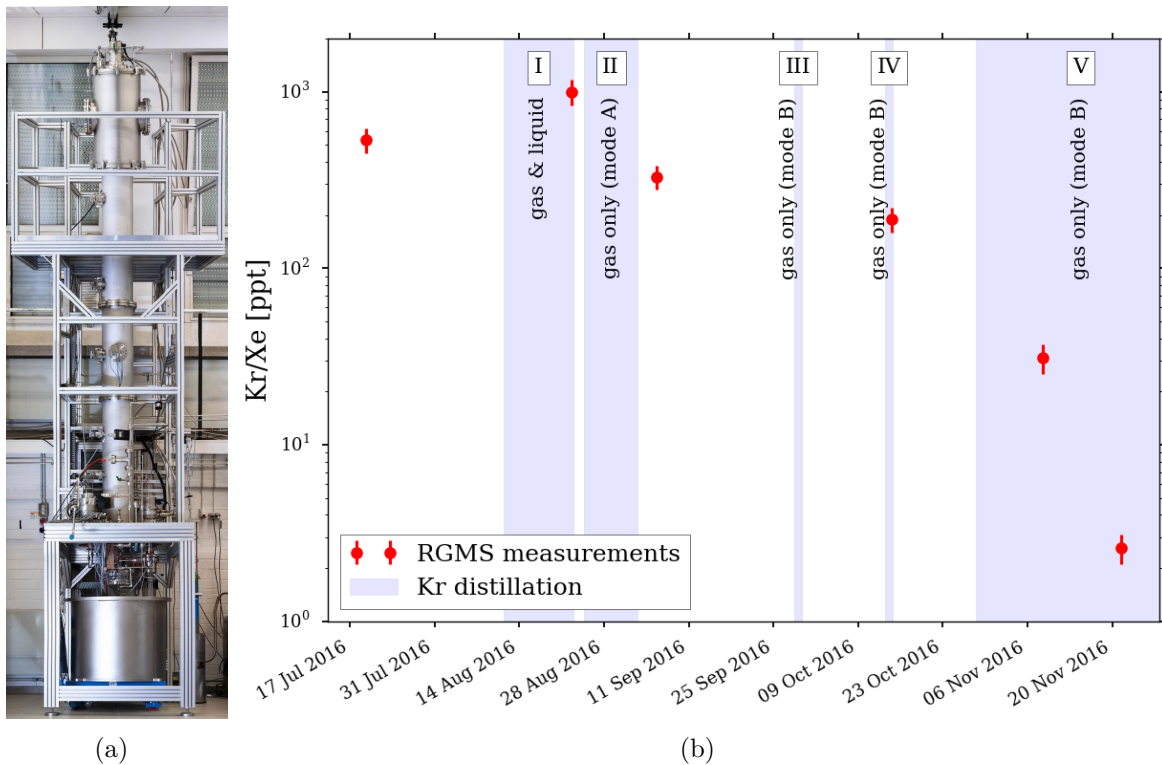


Figure 2.9: (a) A picture of the ≈ 5.5 m tall cryogenic distillation column; (b) Measurements of the Kr/Xe concentration (red dots) and its decrease over time during online krypton distillation (gray shaded areas). Figure created by Michael Murra.

2.2.5 Data acquisition and processing

The data acquisition (DAQ) is responsible for recording interactions in the detector when they occur. The design goals were to digitize and store complete waveforms with acquisition rates of ≈ 1 Hz for the dark matter search and up to 1 kHz for calibration run modes for TPC as well as muon veto. The system is based on a trigger-less readout enabled by online peak finding and triggering. Signals are recorded as digitized waveforms at 100 MSa/s using the VME acquisition boards CAEN V1724. The digitized waveforms are stored on a database buffer, followed by an event builder responsible for creating a software trigger. Triggered data are stored on the XENON1T computing centers at the universities of Chicago and Stockholm, where the processing starts. Custom software sets up the DAQ hardware, acquires and stores the data, allows viewing of the database and displays live waveforms. As an example, figure 2.10 shows exemplary a screenshot of the DAQ control page with information about TPC and MV acquisition rates as well as the database buffer status.

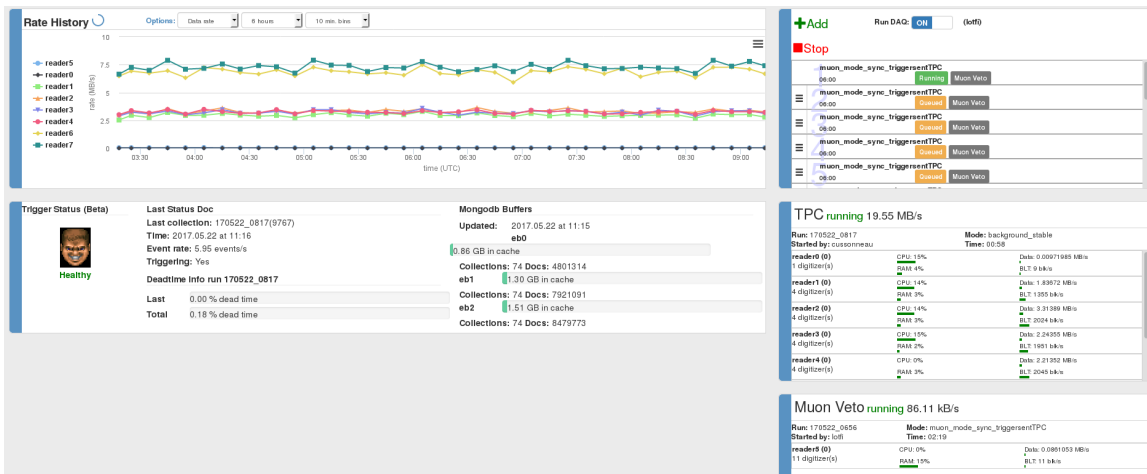


Figure 2.10: XENON1T DAQ control page.

To process the acquired data a new data processor called PAX (**P**rocessor for **A**nalyzing **X**ENON) was developed [3]. It is a free⁶, customizable processing software completely written in python and is configurable for every liquid xenon TPC. It stores events happening in the TPC in a list of PAX-Event objects, holding high-level information about an triggered event as well as a list of objects of predefined PAX subclasses. Generally, every significant upward fluctuation in an ADC channel is stored as an Hit object. Several nearby Hits across several channels are clustered as Peak objects, which get classified into lists of subclasses tailored for specific events happening

⁶PAX is licensed with a Berkeley Software Distribution license.

in a liquid xenon TPC, such as e.g. `S1` and `S2` or `Interactions`, which is a pair of `S1` and `S2` objects. All of these contain event specific informations like peak area fractions for top and bottom PMT arrays, peak heights, timestamps for peak centers and its left and right bounds as well as peak widths and are saved in an `*.root` file. To analyze the processed files, `HAX` (**H**andy **A**nalysis tools for **X**ENON, [2]) was developed by the XENON collaboration to allow users to have access to a certain, customized set of all variables of a PAX processed dataset. `HAX` is a framework of analysis tools and works in a way that it accesses the desired processed `*.root` file by creating a so called `MiniTree` from it, which is basically only a sub-selection of parameters from the overlaying PAX processed `*.root` file. To do so, it needs a `hax.minitree.TreeMaker` object which specifies which values have to be extracted from the processed data file. Various contributions have been committed to the PAX repository within the scope of this thesis in particular regarding the muon veto. For instance it was shown, that also muon veto data can be processed with PAX and analyzed afterwards (see more details on this in section 3.7.1).

2.2.6 Slow control system

The slow control system operates and monitors the experiment. By means of a unified interface it provides: secure monitoring and control by collaborators (shifters and experts at both local and remote locations). It takes care of the instrumentation and the total amount of LXe by means of alarms, guarded operations and redundant systems. Further it displays and securely stores the history of all operating parameters and sensor readings. Its design is based on a distributed architecture of networked local control units (PACs) with central **S**upervisory **C**ontrol **A**nd **D**ata **A**cquisition (SCADA) computers. Each functional sub-system or sensor in the XENON1T experiment has a dedicated controller along with a touch-panel that allows local operation through an intuitive graphical interface. The central SCADA units provide real-time visualization of all monitored sensors on short and long timescales. By default each sensor is read out at a frequency of 1 Hz. The readings are stored in a so called *historian*⁷ database. Each sensor or actuator has an unique historian identifier as e.g. `LIT1` expresses the reading of the water level meter in the water tank or `PT101` for the gas pressure inside the TPC.

⁷A industrial data management system by General Electrics (GE) [86].

2.2.7 Calibration

The large size of the detector requires novel approaches to calibration. The response of the PMTs, the purity of the xenon, and the self-shielding performance of the detector are measured. The response of the detector to electronic and nuclear recoils in both S1 and S2 signals as well as the energy scales are calibrated using both external and internal calibration sources.

- LED calibration of PMTs: the calibration system for monitoring the performance of the photomultiplier tubes and for regular gain measurements is based on external LED light sources and fiber optics to guide the light to the emission points inside the TPC.
- Internal calibration sources: Due to the large size of XENON1T, calibrating the detector response exclusively with external sources is no longer feasible given the self-shielding of LXe. Therefore, radioactive isotopes are mixed directly into the recirculating xenon stream: ^{83m}Kr to calibrate the electronic recoil energy scale and ^{212}Pb as daughter nuclide of injected ^{220}Rn for ER low energy response. Since ^{83m}Kr decays with $\tau_{1/2} = 1.86$ h to the stable ^{83}Kr it has to be distilled from the xenon, while the metallic ^{220}Rn daughters are removed with the purification getters.
- External calibration sources: Three separate belt systems allow external calibration sources to be positioned around the cryostat. Available external sources for ER calibrations are e.g. ^{137}Cs and ^{232}Th . Available neutron sources for calibration are $^{241}\text{AmBe}$ and a deuterium fusion neutron generator.

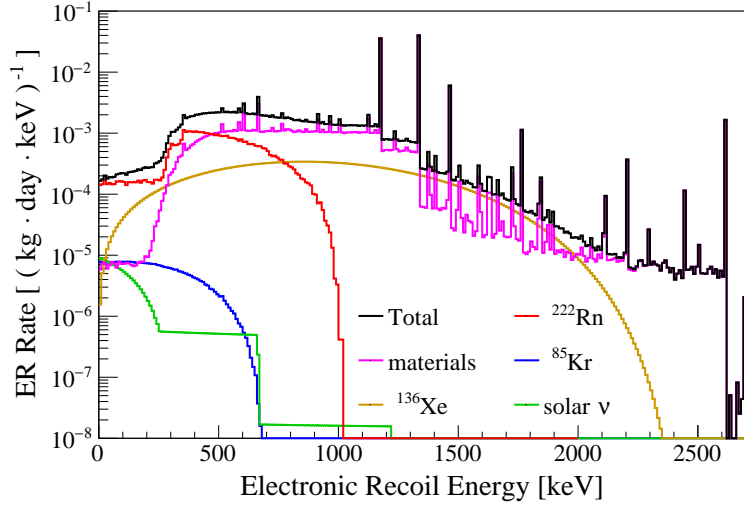
2.3 Physics reach

A dedicated Monte Carlo (MC) simulation [32] of the XENON1T experiment was performed in order to identify the background goals and the projected sensitivity of XENON1T. To do so, all possible background sources for electronic and nuclear recoils had to be identified and estimated. Figure 2.11 shows the total electronic and nuclear recoil background predictions for a fiducial volume of 1 t. The electronic recoil background in the WIMP energy range of interest is dominated by the decay of internal impurities of ^{222}Rn (compare section 2.2.4). Other background sources are ^{85}Kr , the double beta decay of ^{136}Xe , ER background from detector materials (which contribute most at larger recoil energies) as well as solar neutrinos scattering of the electronic

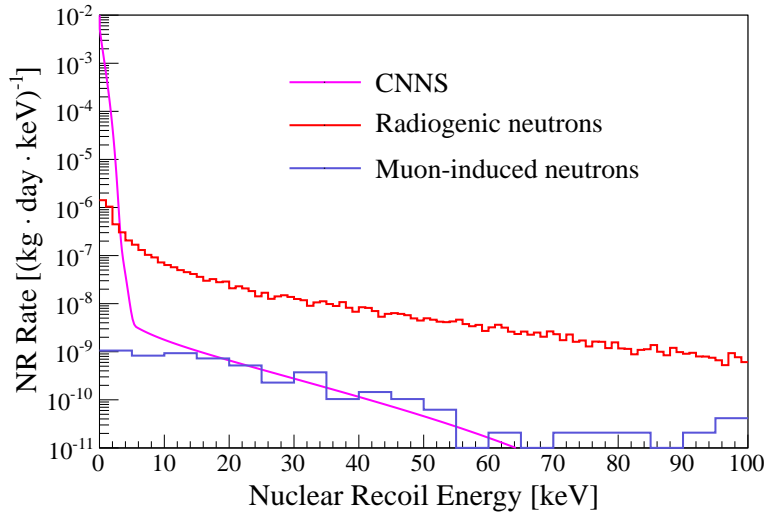
shell of the LXe. Differential background spectra are expressed in events per kg xenon per day per keV electronic recoil. As shown in section 1.4.2, WIMPs are expected to produce NRs in xenon with kinetic energies mostly below 50 keV, with a strong dependence on the WIMP mass for masses $\lesssim 100 \text{ GeV}/c^2$. Considering the differing light and charge responses of LXe to ER interactions, this NR energy corresponds to an ER energy of about 12 keV. To avoid fake events generated by accidental coincidence of PMT dark counts, a lower energy threshold of 1 keV was applied. Within this energy range the total ER background is $(1.80 \pm 0.15) \cdot 10^{-4} (\text{kg} \cdot \text{day} \cdot \text{keV})^{-1}$.

The total nuclear recoil background rate is displayed in figure 2.11(b). Here, the background is composed of radiogenic neutrons from the detector materials, cosmogenic neutrons originating from cosmic radiation (see further section 3.1) and coherent neutrino-nucleus scattering (CNNS) [52], which will be eventually, at much lower sensitivity level, an irreducible background. Within an energy range of $E = [4, 50] \text{ keV}$ and a fiducial mass of 1 t, the largest background rates for NRs result from radiogenic neutrons with (0.6 ± 0.2) events per year with the cosmogenic neutron and CNNS contributions for an operating muon veto, is only 0.02 events per year. Summarizing the shown results and adding the effects of light yield for ER and NR as well as event selections such as requiring S1 and S2 pairs and corresponding thresholds, figure 2.12(a) shows the total expected background rate versus the S1 signal size. The most prominent background sources are displayed individually in solid lines, while the green dashed lines represent the signal expectations for WIMPs of different masses and cross-sections. The total background is dominated by ERs, except below $\approx 5 \text{ PE}$, where the NRs from CNNS become more relevant.

Figure 2.12(b) shows the expected sensitivity of XENON1T for an exposure of $2t \cdot y$, expressed as a 90% confidence level upper limit assuming no WIMP signal was detected. The upper limits constrain the WIMP-nucleon cross-section as a function of WIMP mass, were calculated using the Profile Likelihood Ratio method [70]. Figure 2.12(b) shows the resulting limit amongst results other direct dark matter experiments as e.g results from XENON100 of 2012 [26] and LUX of 2013 [14]. Contours shown in red correspond to a dark matter signal discovery claim, based on annual modulation signals [51]. These discovery contours, however, are in conflict with the null results of the previously mentioned limits. Different dark matter model explanations for this discrepancy have been ruled out with several σ confidence level [31][38] and will not be discussed here. The sensitivity of CNNS (brown line) and the theoretical predicted region of a pMSSM neutralino (gray shaded contours) are shown for illustration (for



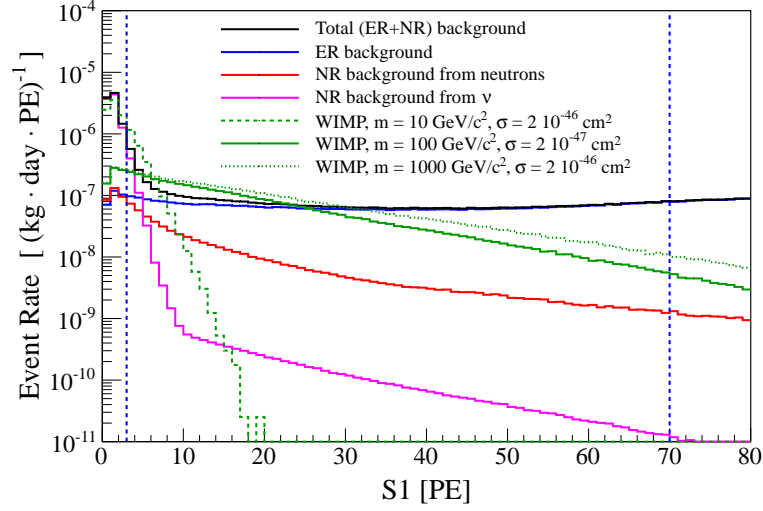
(a)



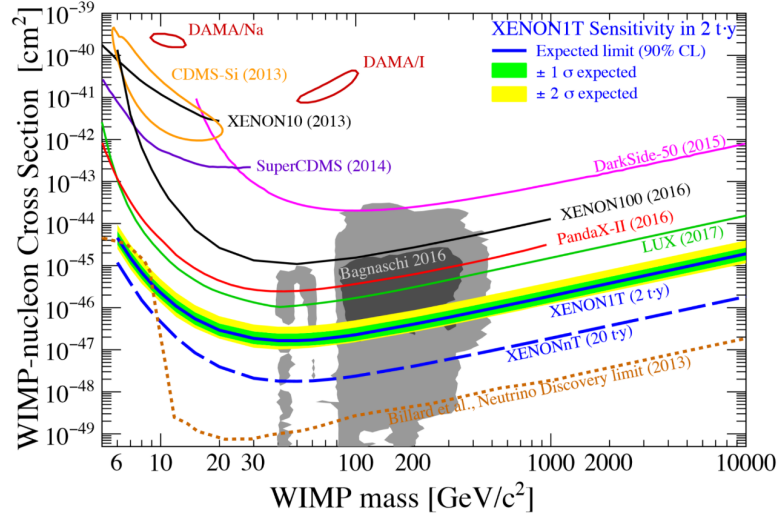
(b)

Figure 2.11: (a) Energy spectrum of the total ER background rate in the 1 t fiducial volume (black), and the separate contributions from detector components (purple), $10 \mu\text{Bq/kg}$ of ^{222}Rn (red), $0.2 \text{ ppt } ^{\text{nat}}\text{Kr}$ (blue), solar neutrinos (green) and ^{136}Xe double-beta decay (brown); (b) Energy spectrum of the NR background events in 1 t fiducial volume. The individual contributions of radiogenic neutrons from the detector components (red), coherent neutrino-nucleus scattering (purple) and muon-induced neutrons (blue) are shown. Figures taken from [32].

the latter compare figure 1.6(a)). The best sensitivity is achieved at $m_\chi = 50 \text{ GeV}/c^2$ for a spin-independent WIMP-nucleon cross-section of $1.6 \cdot 10^{-47} \text{ cm}^2$.



(a)



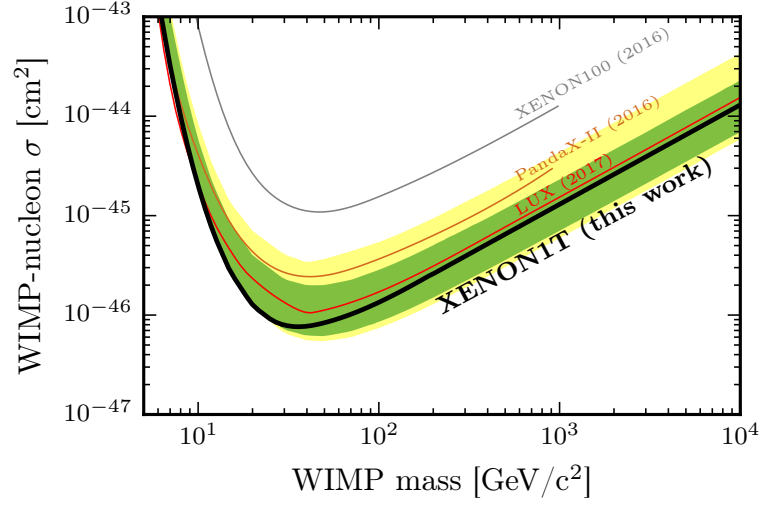
(b)

Figure 2.12: (a) Spectrum of the total background as a function of S1 (black) and of its components (colored lines) as well as NR spectra for three examples of WIMP signals (green) with masses and cross-sections as stated in the legend. The vertical dashed blue lines delimit the S1 region used in the sensitivity calculation; (b) Projected XENON1T sensitivity (90% confidence level) to spin-independent WIMP-nucleon interactions. The solid blue line and the colored bands represent the median and 1σ , 2σ bands respectively. The exclusion limits of other experiments as e.g. XENON100 and LUX are shown as well as the coherent nucleus neutrino scattering limit (brown curve). Gray shaded areas are theoretically predicted search regions as of figure 1.6(a). The red contours (labeled DAMA) are claimed dark matter signal regions from [51] in conflict to the exclusion curves of other experiments. Data taken from [32].

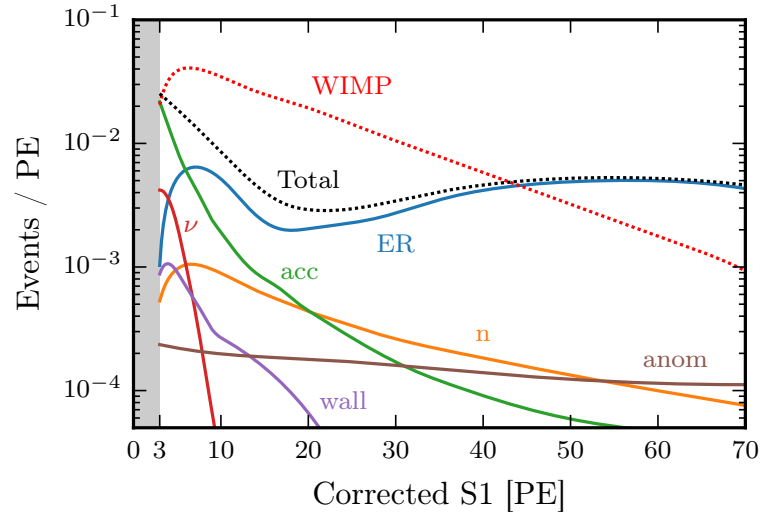
2.4 First results

After construction phase from 2013-2015 and commissioning phase from 2015-2016, XENON1T released its first scientific result on 2017/05/18 [35]. It originates from 34.2 live-days of data taken in science run 0 from November 2016 till January 2017. Within the $[5, 40]$ keV energy range of interest for WIMP searches, the electronic recoil background was $(1.93 \pm 0.25) \cdot 10^{-4}$ events/(kg·day·keV), the lowest ever achieved in a dark matter detector, very close to the expectations and about a factor of 25 lower than for XENON100. The profile likelihood analysis was compatible with the background only hypothesis. Based on that a new world leading limit for spin-independent WIMP nucleon cross-section was derived with a lowest value at WIMP masses of $m_\chi = 35$ GeV/ c^2 at $7.7 \cdot 10^{-47}$ cm² with 90% confidence level. The new limit is shown in figure 2.13(a). The underlying background model is displayed in figure 2.13(b) and is based on the backgrounds motivated above as well as detector specific background events as wrongly inwards reconstructed wall events, misidentified S1 and S2 pair events, or so-called “anomalous leakage” events, contaminating pathologically the WIMP search region and originating from incomplete light and charge collection [131].

A series of earthquakes on 2017/01/18 with many aftershocks in the following days caused high voltage trips in the detector and forced the detector to stop data taking and to evaluate the integrity of all systems. Since February 2017 a new science run 1 has been ongoing until now (2017/06/08), having already acquired more than 80 days of live-time, and XENON1T continues data taking.



(a)



(b)

Figure 2.13: (a) The spin-independent WIMP-nucleon cross-section limits as a function of WIMP mass at 90% confidence level (black) for the first science run of XENON1T. In green and yellow are the 1σ and 2σ sensitivity bands. For illustration, most recent results are shown from LUX [15] (red) and PandaX-II [139] (brown) and XENON100 [34] (gray); (b) Background model in the fiducial mass during science run 0 within a certain reference region for NR. Solid lines show the expected number of events from individual background components: ER (blue), NRs from radiogenic neutrons (orange), NR from CNNS (red), accidental coincidences of uncorrelated S1 and S2 (green), wrongly inward reconstructed wall events (violet) and anomalous leakage events (brown). The dotted black line shows the total background model, the dotted red line shows an WIMP signal with $m_\chi = 50 \text{ GeV}/c^2$ and $\sigma = 10^{-46} \text{ cm}^2$. Figures taken from [35].

Chapter 3

The XENON1T Muon Veto System

*“When you have exhausted all possibilities, remember this:
You haven’t.”*

Thomas Edison, *American inventor and business man*, * 1847; † 1931

3.1 Detection principle

For a rare event, dark matter search experiment such as XENON1T, the most dangerous kind of background are neutrons, due to the WIMP-like signature they produce when scattering off a Xe nucleus (compare section 2.1). Neutrons can be produced through spontaneous fission (for instance from ^{238}U), (α, n) reactions resulting from α -decays of isotopes of the natural decay chains (radiogenic neutrons) or by cosmogenic muons. Cosmogenic muons are generated in high-energy interactions of cosmic radiations with atoms in the upper atmosphere. High energy protons of cosmic radiation hit atoms in the earths upper atmosphere and start hadronic cascades. This happens, within the 100 mbar layer of the atmosphere and results most frequently in the production of charged pions π^\pm or, less frequent (10% probability with respect to pions [88]), in charged kaons K^\pm by strong interactions [120]. π^\pm and K^\pm may weakly decay in the following by

$$\pi^+ \rightarrow \mu^+ + \nu_\mu; \quad \pi^- \rightarrow \mu^- + \bar{\nu}_\mu \quad (3.1)$$

or

$$K^+ \rightarrow \mu^+ + \nu_\mu; \quad K^- \rightarrow \mu^- + \bar{\nu}_\mu, \quad (3.2)$$

into muons, respectively. The stopping power for high-energy muons is low, so they can reach the surface or even penetrate deep into earth and can interact via spallation in the rock, releasing eventually neutrons (cosmogenic neutrons) and showers of other secondary particles. Figure 3.1(a) shows the flux of several particles creating by cascades of cosmic rays over altitude, with muons showing the second highest flux at surface, after neutrinos.

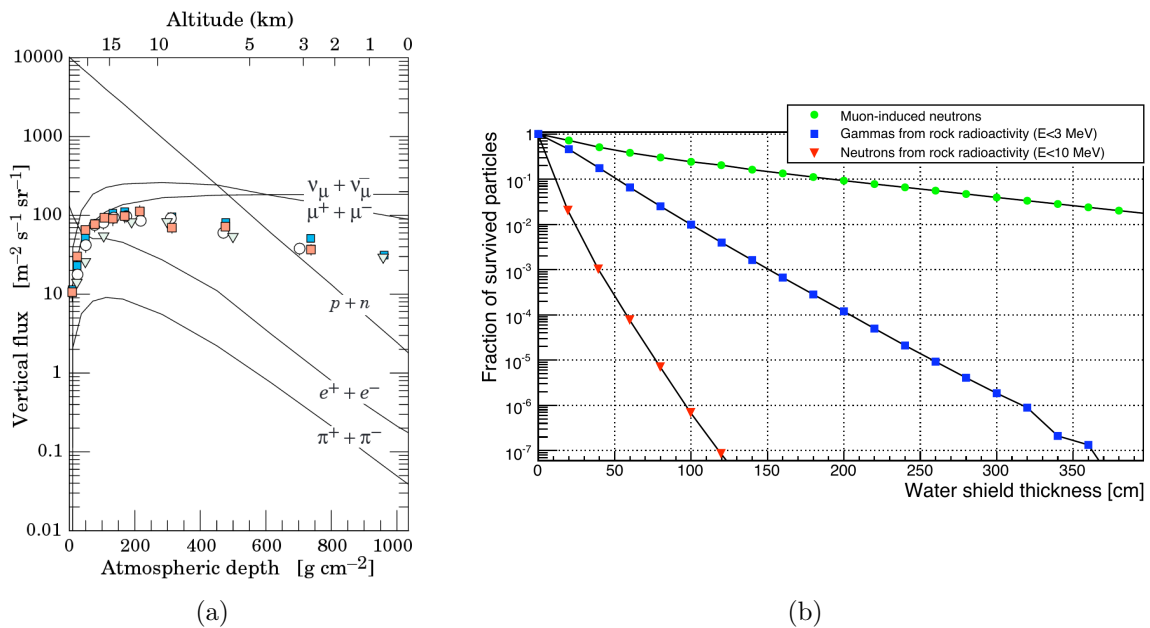


Figure 3.1: (a) Vertical fluxes of cosmic shower particles in the atmosphere. The points show measurements of negative muons with $E_\mu > 1$ GeV. Figure taken from [120]; (b) Fraction of surviving particles as a function of the thickness of a passive water shield. Circular dots for the muon-induced neutrons, squared dots for the gammas from rock radioactivity and triangular dots for neutrons from rock radioactivity. Graph taken from [29].

The succeeding cosmogenic neutron flux can first be reduced by placing the experiment at the LNGS underground laboratory, where the muon flux is lowered by six orders of magnitude compared to surface level to a value of $(3.31 \pm 0.03) \cdot 10^{-8} \mu/(\text{cm}^2\text{s})$ [132] at an average muon energy of 270 GeV [17]. The chosen type for the muon veto is a water Cherenkov¹ muon veto, consisting of a water tank filled with highly purified water acting as passive shield to minimize the rate of radiogenic neutrons. Figure 3.1(b) shows the fractional reduction particle fluxes versus the thickness of a water

¹Pavel Alekseyevich Cherenkov, soviet physicist, 1904-1990

shield for cosmic and radiogenic particles. The tank itself is equipped with PMTs to detect Cherenkov light produced during the transit of a muon or its secondary shower particles through the water. Thus, it can veto nuclear recoil events in the TPC by identifying them as neutrons originating from a cosmic muon detected in the muon veto. Cherenkov radiation occurs when a charged particle transits a dielectric medium with refractive index n faster than the phase velocity of light $c_m = c/n$ in that medium, with c being speed of light in vacuum. As the particle travels through the medium it disrupts the local electric fields of single atoms in the medium and polarizes them. This induces an electric dipole moment. The time variation of the dipole field leads to the emission of electromagnetic radiation. If the particle velocity is $v < c_m$, the dipoles are arranged symmetrically along the particle path, so the integrated dipole field is zero. The radiations of the individual dipoles interfere destructively, yielding no emission. If $v > c_m$, the dipoles are no longer arranged symmetrically and the integrated dipole moment is not zero. Nowe, the individual radiations interfere constructively, forming a coherent, conically shaped wavefront at an angle θ_c , given by

$$\cos \theta_c = \frac{1}{\beta n} \quad (3.3)$$

with respect to the trajectory of the particle. β expresses the ratio of particle speed v to speed of light in vacuum c . To reach $v > c_m$, the kinetic particle energy needs to be larger than a threshold energy E_c

$$E_c = m_0 c^2 \left(\frac{1}{\sqrt{1 - \frac{1}{n^2}}} - 1 \right) \quad (3.4)$$

where m_0 is the rest mass of the charged particle. For water ($n = 1.333$) the threshold energy for muons ($m_\mu = 105.7 \text{ MeV}/c^2$) is $E_{c,\mu} = 55 \text{ MeV}$, for electrons or positrons as typical shower particles ($m_{e^\pm} = 511 \text{ keV}/c^2$) it is $E_{c,e} = 0.26 \text{ MeV}$. Thus, all muons and secondaries arriving at LNGS have much higher energies than their Cherenkov threshold, given the muon energy mentioned above. The number of photons and therefore the intensity of the Cherenkov radiation emitted per unit wavelength λ and unit length x is given by the *Frank-Tamm formula* [102]

$$\frac{d^2 N}{d\lambda dx} = \frac{2\pi z^2 \alpha}{\lambda^2} \left(1 - \frac{1}{\beta^2 n^2} \right) = \frac{2\pi z^2 \alpha}{\lambda^2} \sin^2(\theta_c), \quad (3.5)$$

where z is expressing the number of elementary charges e of the particle², i.e. $z = 1$ for muons, and α is the fine structure constant. Note, that the intensity of Cherenkov radiation follows a continuous spectrum dropping according to $1/\lambda^2$ with wavelength and thus, most of the Cherenkov light is in the ultraviolet regime. In water, the high relativistic ($\beta \approx 1$) particles create thus ≈ 250 photons per cm within the wavelength range $300 \text{ nm} \leq \lambda \leq 500 \text{ nm}$. However, the secondary particles (e.g. electrons) are stopped in the water already within cm range for energies $\mathcal{O}(\text{MeV})$ and can thus produce less Cherenkov photons.

A conceptual design and simulation [29] for the XENON1T muon veto has been performed in GEANT4 [10] in order to find an optimal PMT array layout and estimate the detection efficiencies of muon transits (“muon events”) and transits of its secondary particles (“shower events”). These are important quantities expressing the goodness of the system as a muon veto and acting as inputs for the calculation of cosmogenic neutron background estimations in the XENON1T TPC (see [32]). A more detailed look on its results is presented in section 3.2. Figure 3.2(a) shows a CAD model of the muon veto with its PMTs surrounding the cryostat. There are two calibration systems in the muon veto: First, there is an individual calibration of every PMT with an optical fiber for each module; second, a global calibration by four custom made spherical light sources (*diffuser balls*) illuminating the muon veto in 4π solid angle. Intense tests of all PMTs and the design and production of the calibration systems have been performed within the scope of this thesis and are shown in a more detailed way in sections 3.5 and 3.6. The highly reflective foil DF2000MA [117] by 3M is clad on the tanks inner surfaces to enhance the Cherenkov photons lifetime. Its reflective and wavelength shifting properties have been measured and analyzed qualitatively and quantitatively. Results are presented in section 3.3 and have been published [84]. Finally, in section 3.7 a first approach of muon veto data analysis is presented by reconstructing muon tracks in the water tank.

3.2 Muon veto design overview

The muon veto design has been mainly performed in the scope of [29]. For the sake of completeness the design highlights are introduced here as a basis for the follow-up work done in the framework of this thesis.

² $e = 1.602 \cdot 10^{-19} \text{ As}$.

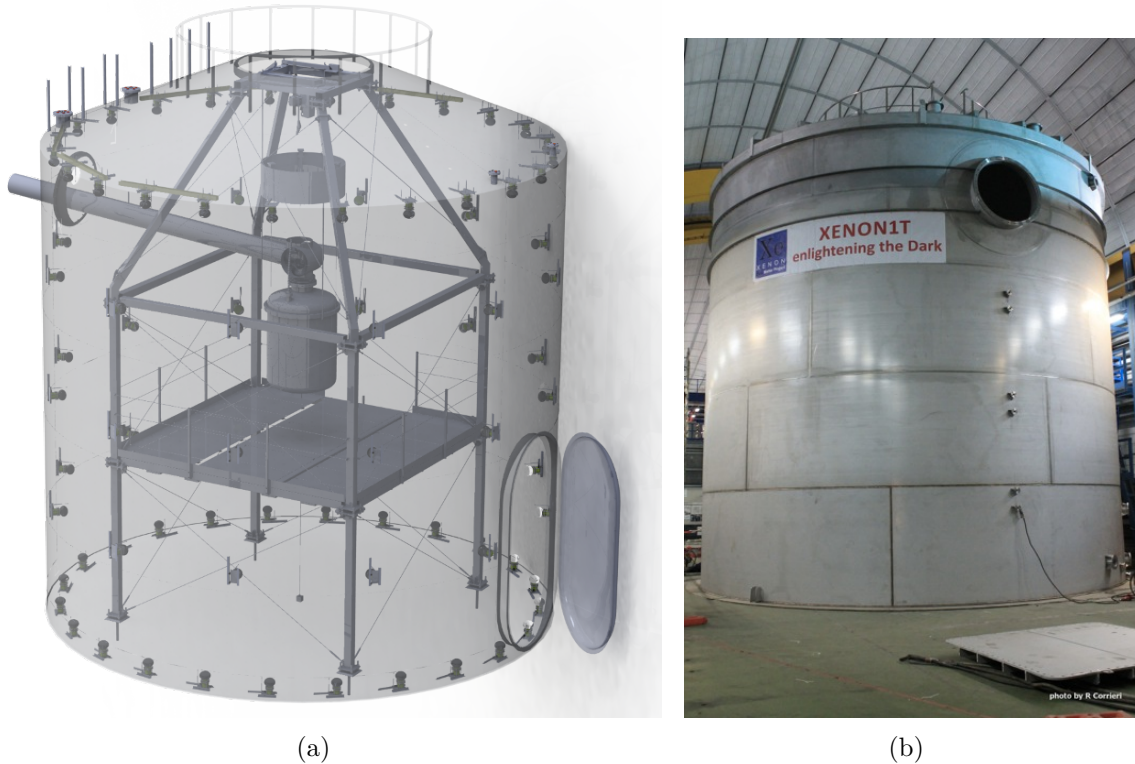


Figure 3.2: (a) CAD model of the XENON1T Muon Veto. The cryostat in the center is surrounded by a water tank exploited as muon veto by an arrangement of PMTs at the outer surfaces; (b) A picture taken of the water tank after construction in 2015.

3.2.1 Mechanical design and installation

The water tank hosting the XENON1T muon veto is a modular stainless steel tank with a diameter of $D = 9.6$ m and height $H = 10.55$ m. As shown in figure 3.2(a) it consists of a 9 m high cylinder with a 1.55 m high frustum of a cone on top, the upper end of which is a 2.4 m wide flange hosting all cable feedthroughs for the experiment. It has been constructed over a period of 2 years from 2013 – 2015. The door is of square shape with side length of 2 m. Figure 3.2(b) shows a picture of the water tank in hall B of the LNGS laboratory after construction in 2015. The big flange at the top of the cylinder acts as feedthrough for the cryogenic lines from the support building via the umbilical pipe to the cryostat. Those systems, as well as the support building were not yet constructed at that time. The DF2000MA foil has been clad on the inner cone surfaces end of 2013, on the lateral surfaces end of 2014 and on the bottom surface in early 2016. The installation of the PMTs and the calibration system took place in November 2014. Beginning from the end of this installation, the setup of readout

electronics began in early 2015. The full MV system was commissioned by the time of the XENON1T inauguration in November 2015 and has since been operational.

3.2.2 PMT array layout

The selected PMT model for the muon veto is the R5912 ASSY by Hamamatsu [90] with a 33 m long cable containing a line for high voltage supply and a coaxial cable for readout. This model provides quantum efficiencies $> 10\%$ within the wavelength range $310 \text{ nm} \leq \lambda \leq 540 \text{ nm}$, with a flat-top of quantum efficiency (QE) at $\approx 30\%$ in $340 \text{ nm} \leq \lambda \leq 430 \text{ nm}$. The PMT body, its voltage divider and the full cable is designed to be fully water tight. The photocathode is a bialkali material sputtered on the inside of the borosilicate glass bulb of 8" diameter. Ten dynodes provide a gain of $g = 10^7$ at high voltage $U = 1500 \text{ V}$ across a full resistance of the dynode separating divider chain of $12.7 \text{ M}\Omega$. The results of the MC simulations in [29] led to the use of 84 PMTs in a ring like pattern: 24 PMTs located on the bottom looking upwards (“bottom ring”, **Ring0**), 12 PMTs located on a ring at 2.25 m height (**Ring1**), 12 PMTs located on a ring at 4.5 m height (**Ring2**), 12 PMTs located on a ring at 6.75 m height (**Ring3**) and 24 PMTs located on the top of the water tanks cylindrical surface at height 9 m looking downward (“top ring”, **Ring4**). All PMTs are at a radius of 4.5 m. Figure 3.3 shows visualizations of this layout in xyz (figure 3.3(a)) and as cylindrical projection in the (φ, z) space of cylindrical coordinates, which is basically the side surface of the water tank cylinder unrolled (figure 3.3(b)). The coordinates are according to the XENON1T common coordinate system defined in section 4.1.2. Each dot corresponds to the location of one PMT. The displayed numbers are the definition of a sequential ordering of the positions within PAX playing a role in the muon veto analysis in section 3.7.1. Given the geometry of the PMT layout and the angular distances between the PMTs, seven PMTs as well as their cables have been grouped (two of the bottom ring, each one of the three lateral rings and two of the top rings) as “columns”, labeled from *A* to *L*.

Figure 3.4(a) shows a picture taken of an installed PMT on the water tanks wall, exemplarily. Every PMT was fixed in a holding structure which was screwed to studs welded on the water tank wall. The cable is fed into a vertical stainless steel cable tray. The cables were guided from the PMT inside the cable trays through water tight feedthroughs on the water tank roof along the wall of the water tank in the DAQ room of the support building, where the muon veto electronics are located. In figure 3.4(b) an example for measured quantum efficiency values versus wavelength is shown. The values have been provided by Hamamatsu.

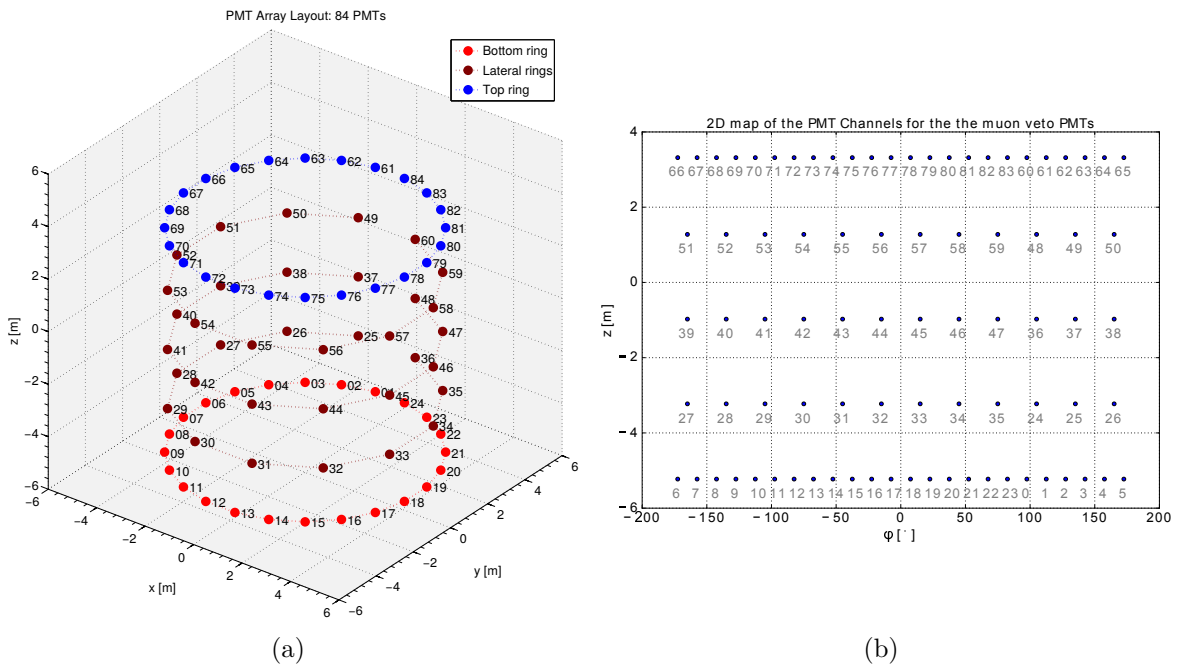
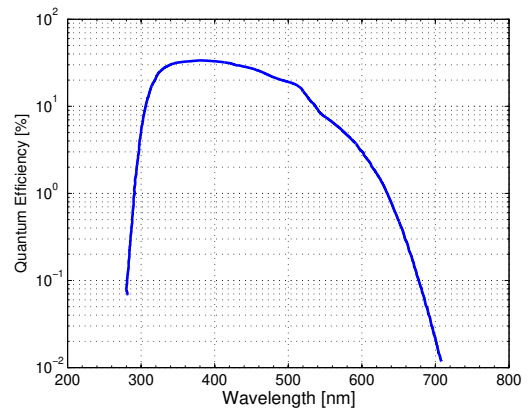


Figure 3.3: PMT layout in the muon veto in xyz (a) and in (φ, z) space (b) of cylindrical coordinates. The PMTs are arranged in five rings at the surface of the water tank. Each dot corresponds to the position of a PMT, sequentially numbered and defined in PAX. The PMTs are arranged in five rings at the surface of the water tank.



(a)



(b)

Figure 3.4: (a) A picture of a R5912 ASSY muon veto PMT at post-installation; (b) Quantum efficiency of the muon veto PMT over wavelength. It provides quantum efficiency values $> 10\%$ within the wavelength range $310 \text{ nm} \leq \lambda \leq 540 \text{ nm}$.

3.2.3 Readout electronics and trigger logic

Figure 3.5 shows a schematic flow chart of the readout electronics and the trigger logic of the muon veto. The analog signals of the 84 PMTs are distributed to 11 CAEN V1724 digitizers. When the signal of one channel overcomes a certain amplitude threshold thr in units of photoelectrons (PE) for at least tot consecutive samples (sampling rate $100\text{ MHz} \rightarrow 1\text{ Sa} = 10\text{ ns}$), the condition for the single channel trigger is fulfilled. That trigger signal is propagated to inputs of the general purpose module CAEN V1495 (blue lines in the figure). This module is in charge of generating the global trigger for the muon veto system following a predefined logic. It runs a customized firmware specifically developed in collaboration with CAEN company. The trigger unit looks for the coincidence of at least N single channel triggers inside a coincidence window Δt . Values for N and Δt are programmable via software. If the condition is fulfilled, a global trigger is generated and distributed to all eleven digitizers (red lines) starting the acquisition process of all 84 channels simultaneously. The so acquired waveform is called “event” and has a length of $5.12\ \mu\text{s}$. A timing unit is in charge of assigning an absolute time (“event time stamp”) to signals sent to one of its input channels. It is the only device shared by muon veto and TPC systems. The muon veto trigger signal is sent to the timing unit in order to be time tagged. Moreover the timing unit delivers a 50 MHz clock and a synchronize signal (**SYNC**) every 10 s . The clock is distributed to the first digitizer of the muon veto system and then propagated in daisy chain to the other ten boards (violet lines). By adjusting the clock phases on each board to take into account propagation delays, it is possible to have all the digitizers running with the same clock. The 0.1 Hz **SYNC** signal is sent to a free channel of the digitizers (green line). It generates a single channel trigger which goes to a special input of the trigger unit, which allows to generate a muon veto trigger bypassing the trigger logic. In this way the **SYNC** signal gets assigned a time stamp, will be digitized and acquired. Both the 50 MHz clock and the 0.1 Hz **SYNC** signal are distributed in parallel to the TPC system. In this way the two systems share the same clock, while the **SYNC** signal can be used by the two detectors as a common absolute time reference. The trigger logic of the muon veto is therefore based on four parameters: amplitude threshold thr in PE, number of consecutive samples tot , number of coincident single channel triggers N and the width of the coincidence window Δt . Since commissioning of the muon veto several combinations of those have been used, but typical values are e.g: $thr = 1\text{ PE}$, $tot = 1\text{ Sa}$, $N = 8$ and $\Delta t = 300\text{ ns}$.

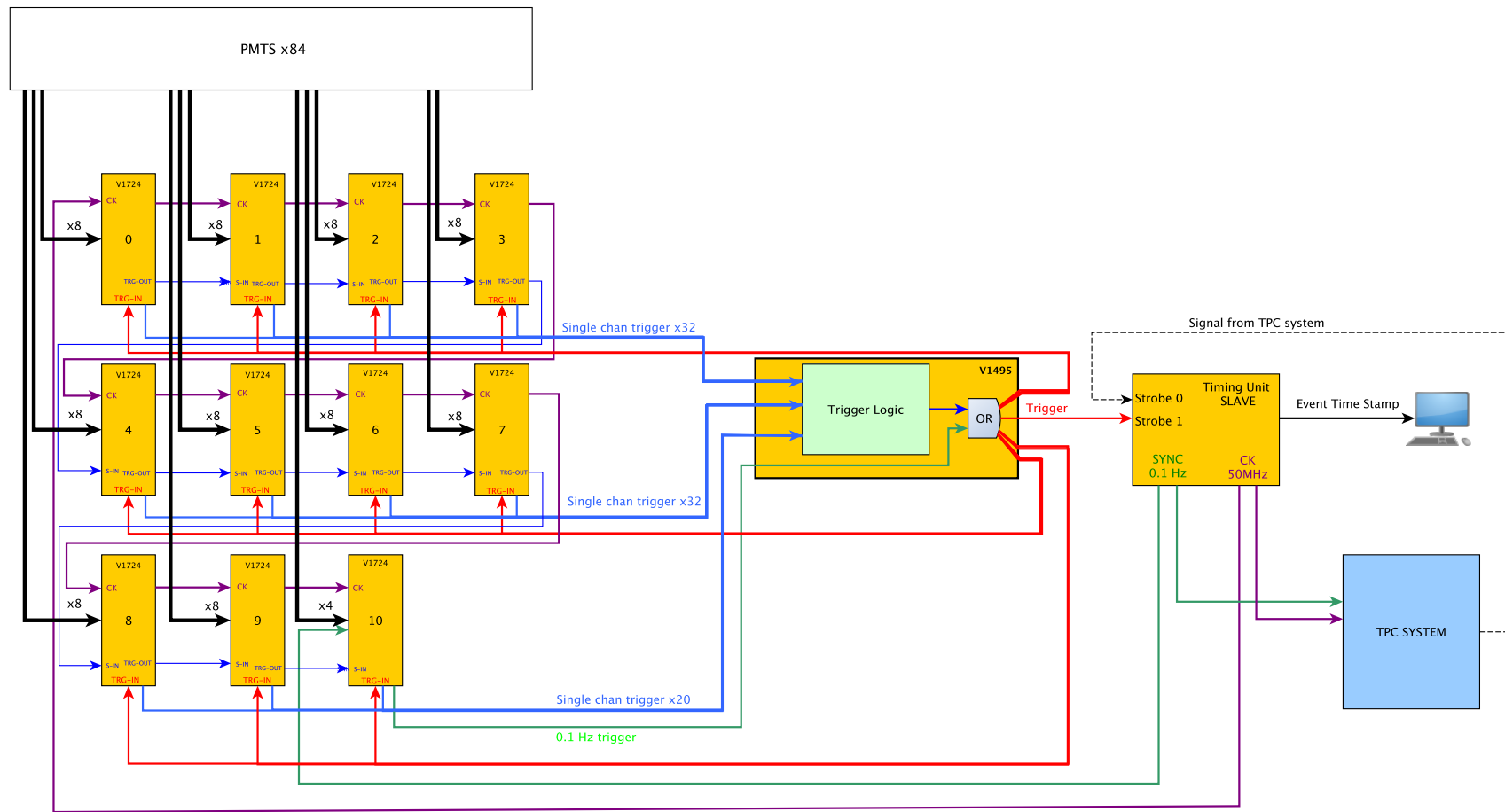


Figure 3.5: Global scheme of the muon veto readout system and trigger logic and its interface with the TPC system. Chart created by Dr. Andrea Molinaro.

3.2.4 Muon veto GEANT4 simulation

The conceptual design of the XENON1T muon veto system is based on a dedicated simulation [29], which has been carried out with a series of Monte Carlo simulations, based on the GEANT4 toolkit [10]. It was used to optimize the muon veto working configuration in order to find the highest possible tagging efficiency of the detector and was developed by Dr. Serena Fattori, a member of the XENON Mainz group. A short overview of its conclusions is given here for completeness and as motivation for the following sections. Permutations of the trigger condition parameters, presented in section 3.2.3, were evaluated in order to find the highest efficiencies for muon events and shower events, respectively. Further, the simulation contained different reflective surfaces on the inner water tanks walls, including diffuse and specular reflective foils and coatings. To do so 10^4 events of each case have been simulated and shot on the simulated geometry of the XENON1T experiment, containing the water tank, the XENON1T cryostat and its support structure. Their energy and angular distributions have been randomly drawn from histograms obtained from a Monte Carlo code called MUSIC [21], which is tuned to match, muon track measurements of the LVD supernova detector [9] in the LNGS underground laboratory. The efficiencies ϵ for each case were then calculated by

$$\epsilon = \frac{m}{N - m_0} \quad (3.6)$$

with m being the number of detected muons, N the total number of generated muons and m_0 being the number of muons not transiting the water tank. The uncertainty $\Delta\epsilon$ was calculated by the approach of a binomial error to

$$\Delta\epsilon = \sqrt{\frac{\epsilon(1 - \epsilon)}{N}}. \quad (3.7)$$

Based on the results of this simulation it is stated that $\approx 1/3$ of the events, when a cosmogenic neutron was inside the water tank, originated from “muon events”, the other $2/3$ originated from shower events. Five layout models for PMT arrangements on the top and bottom of the tank as well as two lateral array models have been simulated. The number of 84 PMTs and their array layout introduced in section 3.2.2 were found to be the optimized compromise between a sufficiently high detection efficiency for muon and shower events, and cost, scaling with the number of PMTs in the tank. The optimized value of $\Delta t = 300$ ns was obtained by an examination of the time differences of photons arriving on the PMT photocathodes in simulations of muon and shower

events. $thr = 1$ PE was found to be required to keep the detection efficiencies of shower events on a level $> 60\%$. Depending on the PE threshold thr , the simulated trigger rate of the muon veto is shown in figure 3.6. The green dashed line is the simulated muon flux hitting the water tank $R = 0.04$ Hz, given only its effective geometry. One can see that only for $tot = 1$ the trigger rate corresponds to a rate induced by the muon flux for a given number of $N = 4 - 5$ PMTs for coincidence requirement.

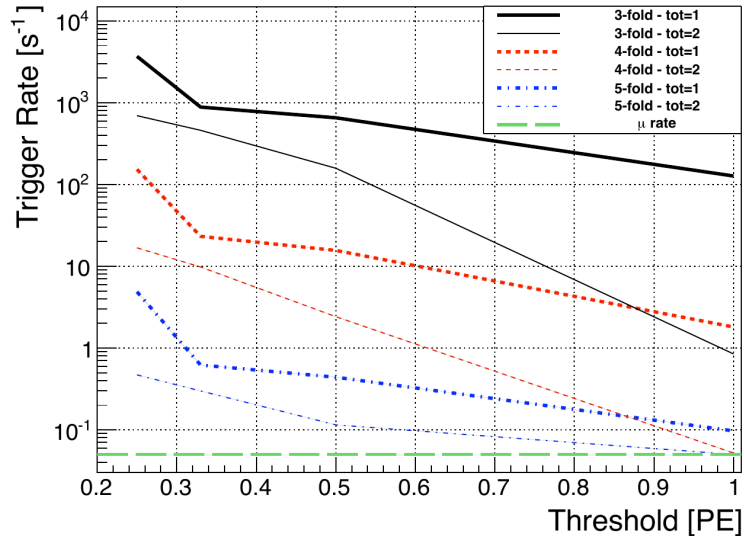


Figure 3.6: The simulated muon veto trigger rate versus for different number of samples tot above threshold thr . Only for $tot = 1$ and $thr = 1$ PE the muon veto trigger rate can match the rate induced by the muon flux in the water tank (green dashed line). Picture taken from [29].

As presented in section 3.2.3 the muon veto system verified this trigger parameters as it was successfully run in the configuration, which was found in the simulation to be optimal. After fixing the optimized trigger parameters, the tagging efficiencies were calculated with equation (3.6) to $(99.78 \pm 0.05)\%$ for muon events and $70.6 \pm 0.5\%$ for shower events. Considering these tagging efficiencies, as well as moderation and absorption of neutrons in the water shield, the residual neutron flux at the XENON1T cryostat surface is stated to be $1.2 \cdot 10^{-12}$ n/(cm² · s). After applying general selection cuts for the WIMP search, i.e. a low-energy single scatter with allowed recoil energies of 4 keV – 50 keV within 1 ton of fiducial volume a background of 0.01 events per year from muon-induced neutrons is found. It was further found, that using the reflective foil DF2000MA, leads to highest possible detection efficiencies. At that time the manufacturer did not provide a proper measurement of its reflective properties, which made the foil being subject to an intense examination within the scope of this thesis. This work is going to be presented in section 3.3.

3.2.5 Water tank and water flow simulations

The most recent filling of the water tank took place in July 2016. Given the maximum output rate of the water plant of $2.2\text{ m}^3/\text{h}$ and the tanks volume of $\approx 750\text{ m}^3$, the filling of the full tank takes about two weeks. Figure 3.7 shows the trend of water level height in the tank over time as well as the fractional rate of events measured in the TPC. Once the water level reached the cryostat, a clear decrease of the detector rate was observed, illustrating the passive shielding effect on the TPC.

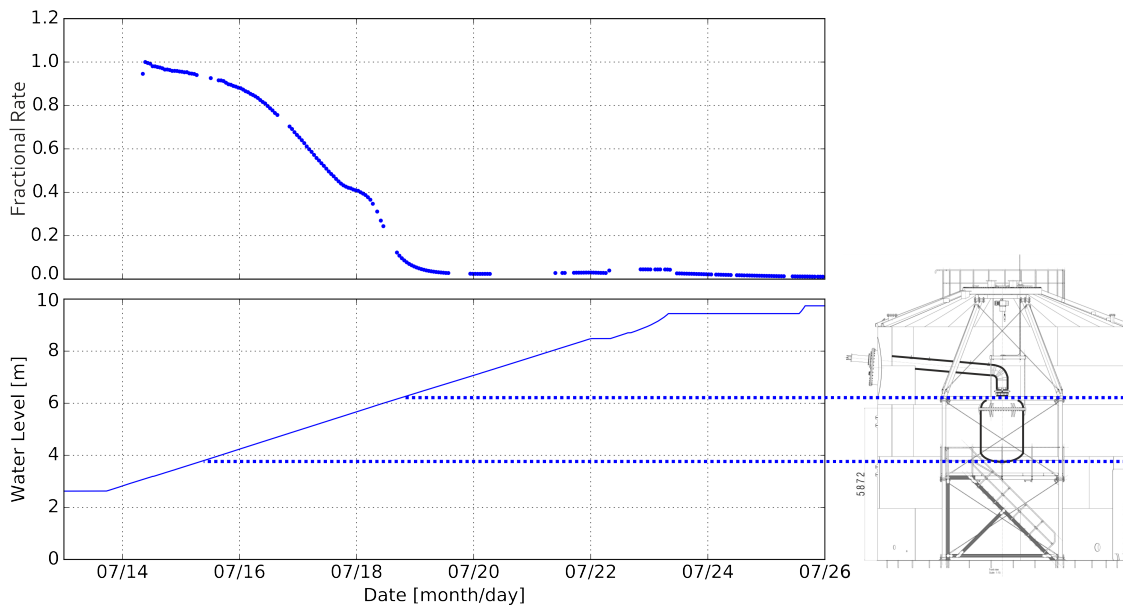


Figure 3.7: The XENON1T water tank was filled in July 2016. As the water level rises, the rate of events in the TPC drops, illustrating the passive shielding effect of the water tank. Picture created by XENON collaboration.

Once filled, the water is constantly fed out of the tank through a flange at the top of the tank into a purification loop to maintain the purity of water inside the tank. This happens with a rate of $Q_r = 4\text{ m}^3/\text{h}$, so the purification of one full tank volume is done in ≈ 10 days. The recirculation outlet pipe is of diameter $D_r = 60\text{ mm}$. For the flow velocity v of flow Q through a cross-section $A = \pi(D/2)^2$ is

$$v = \frac{Q}{A}, \quad (3.8)$$

which yields a water flow velocity of $v_r = 0.389\text{ m/s}$ at the recirculation outlet. During the design phase, we were concerned about potential shear forces on the PMTs and the water purity. Therefore a finite element method simulation of the water flow was performed within the scope of this thesis in order to verify that the projected flow

would be enough to maintain a constant purification level in the tank. The simulation was performed with COMSOL [68] to estimate the flow velocity field over the full tank volume. The simulation is solving two equations: The *Navier-Stokes equation* and the *continuity equation*. Assuming water as an incompressible, Newtonian fluid and assuming the flow to be laminar, the Navier-Stokes equation is

$$\rho(\vec{v} \cdot \nabla) \vec{v} = \nabla \left[-p\mathbf{I} + \mu \left(\nabla \vec{v} + (\nabla \vec{v})^T \right) \right] + \vec{F}, \quad (3.9)$$

with \vec{v} is the water flow velocity, ρ its density, μ is the dynamic viscosity and \mathbf{I} is the identity matrix. p is the pressure in the fluid and \vec{F} is body force of gravitation. For the same assumptions the continuity equation is

$$\rho \nabla \cdot \vec{v} = 0. \quad (3.10)$$

The Navier-Stokes equation represents the conservation of momentum, while the continuity equation represents conservation of mass. Given the flow velocity at the outlet as calculated above as boundary condition, the COMSOL simulation can predict the water flow velocity in the tank geometry. Figure 3.8 shows the result. The color scale represents the velocity magnitudes of the velocity vector field in the tank. The range goes from zero (blue) to 10^{-5} m/s (red).

The purified water is injected in the tank by a ring shaped pipe with several inlets as visible on the bottom plane of the figure, where the water has highest velocities together with regions near the outlet. The red arrows indicate the direction of the velocity vectors. As expected the lowest flow velocities can be found at the tank top on the opposing side of the outlet. There, the water moves only with a velocity of $v \approx 0.3 \cdot 10^{-5}$ m/s. This translates in the movement of a water molecule per day of $x \approx 26$ cm. To ensure, that no ‘‘pockets’’ of dirty water sustain in regions of the tank far away from the outlet, this distance has to be larger than the distance the molecule would move by diffusion only. The mean square deviation of a molecule from its initial position by self diffusion is

$$\langle x^2 \rangle = 2Dt, \quad (3.11)$$

and is therefore linearly dependent on the self diffusion coefficient D and the time t . The mean path a molecule can move is therefore:

$$\langle x \rangle = \sqrt{2Dt}. \quad (3.12)$$

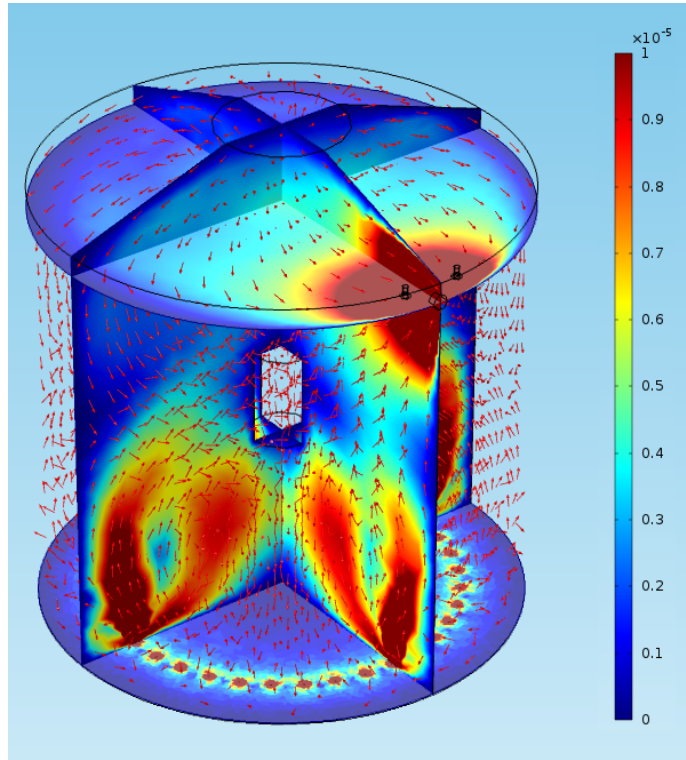


Figure 3.8: Water flow simulation in the water tank using the finite element method.

Given $D = 1.525 \cdot 10^{-9} \text{ m}^2/\text{s}$ at 10°C water temperature ([96]), the movement within one day is $\langle x \rangle = 1.62 \text{ cm}$. This is a factor of ≈ 15 lower than the movement by the applied flow, which confirmed that the projected volumetric flow rates are sufficient. It could also be shown, the shear forces were not a problem for the selected PMT positions.

3.3 Characterization of the DF2000MA reflective foil

The DF2000MA foil is a polymeric multi layer reflective foil by 3M, which was chosen to be clad to the inner surfaces of the muon veto water tank according to the results of the Monte Carlo simulations presented in section 3.2.4. According to the manufacturer, the foil provides nearly 100% reflectance for wavelengths larger than 430 nm [115]. A renewed data sheet (which had not yet been published at the time of the Monte Carlo studies) states that high reflectance is already achieved at wavelengths larger than 400 nm [117]. 3M reflective foils have widely been used in rare event searches and other experiments (see e.g. [61][78][82]). In addition, similar foils have shown wavelength

shifting (WLS) capabilities [19], absorbing lower wavelength photons and re-emitting them with their wavelength shifted to higher values. This process could shift the UV part of the Cherenkov spectrum, which drops according to equation (3.5) by $1/\lambda^2$, into the highly sensitive region of the PMTs (compare figure 3.4(b)), increasing the detection efficiency of the muon veto. The foil is clad on all inner surfaces of the water shield. Figure 3.9 shows two pictures after foil installation illustrating the high reflectance (figure 3.9(a)) and the WLS effect (figure 3.9(b)).

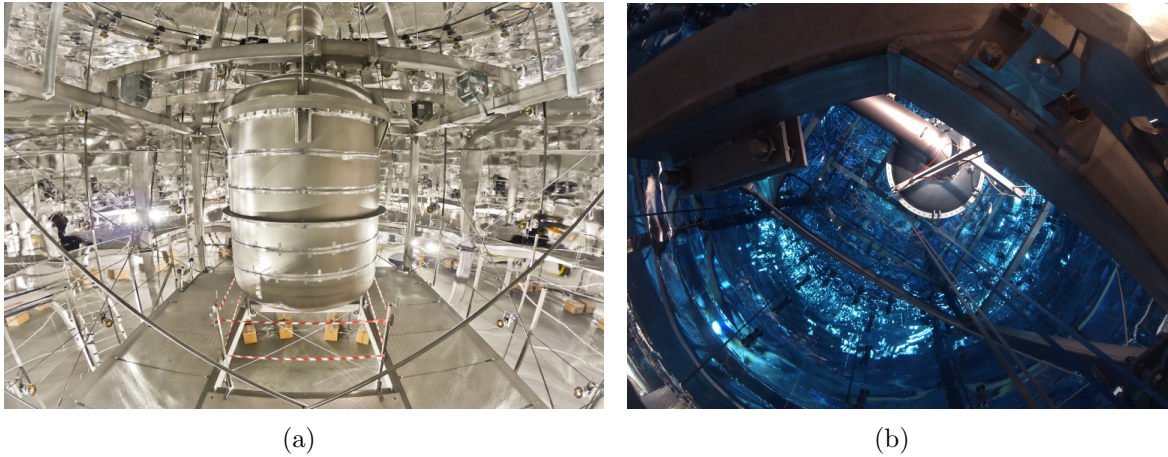


Figure 3.9: Pictures of the DF2000MA foil after installation in the water tank. (a) A picture of the inside of the water tank after installation of the foil to the lateral walls of the water tank at the end of 2015. The ground is not yet clad. The closed outer cryostat is visible in the center of the picture. All PMTs except for the bottom ring (stored in card boxes) are installed and visible. The specular reflectance of the foil is evident; (b) A picture taken during water filling through a flange on top of the water tank. Also the ground surface is now clad with the foil. The WLS effect of the foil is visible as bluish glow.

Within the scope of this thesis, the specular reflectance of the DF2000MA foil has been characterized, its high performance verified, and its WLS properties have been measured. The first Monte Carlo studies [29], based on the old reflectance values and not considering WLS, have been enhanced by the measurement results and been compared with the original values (see section 3.4). All outcomes of these measurements have been published in the JINST journal [84]. In the following, a summary of the most important results is presented.

3.3.1 Definitions: reflectance, transmittance and absorbance

Electromagnetic radiation moving at the boundary surface of two media with differing refractive indices n can be either be reflected, transmitted or absorbed. Following

[122], the reflectance ρ for a thick sample can be defined as the power ratio between the reflected light P_r and the light before reflection P_0 as

$$\rho := \frac{P_r}{P_0}. \quad (3.13)$$

ρ is usually expressed in percent and can be separated in specular reflectance and diffuse reflectance. Analogously one defines the transmittance τ as

$$\tau := \frac{P_t}{P_0}. \quad (3.14)$$

Every medium is also absorbing a relative amount α of the incident light after a distance x . Its power P_a can be found as the exponential decrease of the transmitted power P_t :

$$P_a = P_t \cdot (1 - e^{-\mu x}), \quad (3.15)$$

with μ being the absorption coefficient of the absorbing medium. The absorbance α is therefore defined as

$$\alpha = \frac{P_a}{P_0} = \frac{P_t \cdot (1 - e^{-\mu x})}{P_0} = \tau (1 - e^{-\mu x}). \quad (3.16)$$

All three mechanisms sum up to unity

$$1 = \rho + \tau + \alpha. \quad (3.17)$$

In the following, investigations of especially reflectance and absorption of the DF2000MA foil are presented.

3.3.2 Specular reflectance measurement

The specular reflectance ρ of the foil has been measured with the setup depicted in figure 3.10(a). Light from a xenon arc lamp passes a monochromator and hits the foil sample under an incidence angle θ . The monochromator LOT LSH-150 selects wavelengths in 10 nm steps within a range of 250 nm – 580 nm. The monochromator output slit was set to a width of 0.07 mm, which translates to a bandwidth of the output light of 0.38 nm [105]. The angle of incident is equal to the angle of reflection. After reflection, the light (which wavelength now denoted as λ') was measured by a silicone PIN diode, converting the intensity of the incoming light in a wavelength dependent photocurrent. Derivation of that photocurrent as well as characterization

and assessment of all systematic uncertainties of this setup are presented in detail in sections 2.2 and 5 of the publication [84]. As reflection sample, a piece of the DF2000MA foil and a Thorlabs 1" square PFSQ10 specular reflectance standard with known reflectance curve $\rho_m(\lambda)$ in the wavelength range of interest was used. The light was once measured after being reflected by the DF2000MA foil sample and once measured after being reflected by the UV mirror, without changing anything else in the setup. The resulting photocurrent $I_m(\lambda)$ for the UV mirror and $I(\lambda)$ for the foil enables to calculate the reflectance $\rho(\lambda)$ of the foil by

$$\rho(\lambda) = \frac{I(\lambda)}{I_m(\lambda)} \cdot \rho_m(\lambda). \quad (3.18)$$

The measurement was performed for two angles of incident $\theta = 12^\circ$ and $\theta = 45^\circ$. The result of this measurement is shown in figure 3.10(b). The edge of the curve, where the reflectance rises, is already observed at $\lambda = 370$ nm and not at 400 nm as specified in [115]. The rise of reflectance ends at 400 nm. There is a slight dependence of the reflectance on the angle of incidence: at 12° , the reflectance is $> 99\%$ above 400 nm, whereas at 45° , the reflectance rises from 96% at 400 nm to 99% at 450 nm. For wavelengths < 370 nm the foil reflects about 13% of the incoming light at 45° and about 10% at 12° . The error on the reflectance values is about 0.5%, increasing for $\lambda < 300$ nm to a value up to 2.5%.

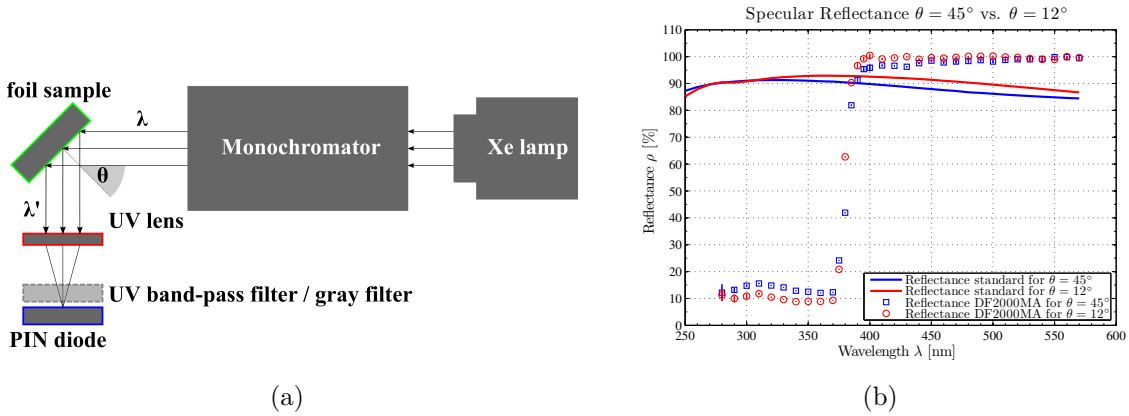


Figure 3.10: (a) Setup to measure the specular reflectance of the DF2000MA foil. λ expresses the wavelength selected at the monochromator. λ' is the wavelength of light after reflection. For specular reflection, $\lambda = \lambda'$; (b) Specular reflectance ρ of the DF2000MA foil for the two inspected angles of incidence ($\theta_1 = 45^\circ$ blue boxes, $\theta_2 = 12^\circ$ red circles) versus the wavelength λ . The thicker blue and red lines show the reflectance curve of the used specular reflectance standard at θ_1 and θ_2 , respectively.

For detailed information about results of a verification measurement performed with an OceanOptics JAZ Spectrometer as well as an inspection of the impact of slight and severe surface damages on the foil reflectance, the reader is referred to the publication. The JAZ spectrometer measurement confirmed the results of figure 3.10(b) within the error ranges. Slight scratches reduce the reflectance by $\approx 5\%$, severe damages by up to 40\$.

3.3.3 Measurement of wavelength shifting properties and diffuse reflectance

The DF2000MA foil also has wavelength shifting (WLS) properties. Photons hitting the foil with wavelength λ can get absorbed and reemitted with a higher wavelength λ'' by fluorescence. Molecules of one of the polymeric layers of the foil may get excited by the absorbed light and can deexcite while emitting a photon of a longer wavelength in diffuse directions. To characterize the wavelength shifting property of the foil, the setup described in section 3.3.2 was modified and is shown schematically in figure 3.11(a). The PIN diode was shifted out of the specular beam path to make the measurement independent of the specular reflectance of the foil. To maximize intensity, the monochromator output slit was opened to a value of 2 mm corresponding to an bandwidth of the output light of 10.81 nm [105]. A diffuse reflectance standard was used as reflection sample and can be compared with the DF2000MA foil. The used standard is a 2.5 cm diameter disk of porous PTFE with Lambertian emission characteristic (Zenith Polymer SG 3052 by SphereOptics). It has a known diffuse reflectance curve $\rho_{mf}(\lambda)$ ($> 98\%$ in the full wavelength range of interest [136]) and has no wavelength shifting properties. To quantify the diffuse reflectance and the WLS of the foil, five optical band-pass filters (Edmund Optics NT84 series) and a Thorlabs FGUV11M filter are used in front of the PIN diode. They transmit only wavelengths $\lambda_{F,i}$ within their bandwidth (see table 3.1).

Stepping through the incoming wavelength λ in 10 nm slices using the monochromator allows the measurement of the PIN diode current $I(\lambda, \lambda_{F,i})$ for all filters. Replacing the foil with the diffuse reflectance standard mentioned above allows to measure the current $I_{mf}(\lambda)$. Applying an analogous equation to (3.18), summation of all measurement values at which the monochromator wavelength λ is within the transmission window of each filter, leads to five data points. From those one can determine the diffuse reflectance $\rho_{f,0}$ of the foil with a resolution given by the bandwidth of the filters. Other light, eventually wavelength shifted to a λ'' outside of the corresponding filters

Band-pass Filters				
Filter	Bandwidth	τ [%]	$\lambda_{c,i}$ [nm]	FWHM [nm]
1	$275 \text{ nm} \leq \lambda_{F,1} \leq 375 \text{ nm}$	80 ± 5	325	100
2	$375 \text{ nm} \leq \lambda_{F,2} \leq 425 \text{ nm}$	90 ± 5	400	50
3	$425 \text{ nm} \leq \lambda_{F,3} \leq 475 \text{ nm}$	95 ± 2	450	50
4	$475 \text{ nm} \leq \lambda_{F,4} \leq 525 \text{ nm}$	95 ± 2	500	50
5	$525 \text{ nm} \leq \lambda_{F,5} \leq 575 \text{ nm}$	95 ± 2	550	50

Table 3.1: Specifications of the band-pass filters used in the setup regarding bandwidth, transmittance τ_i within the bandwidth, central wavelength $\lambda_{c,i}$, and full width at half maximum (FWHM).

transmission window, is blocked and has no influence on the PIN diode photocurrent. The five data points are shown in figure 3.11(b).

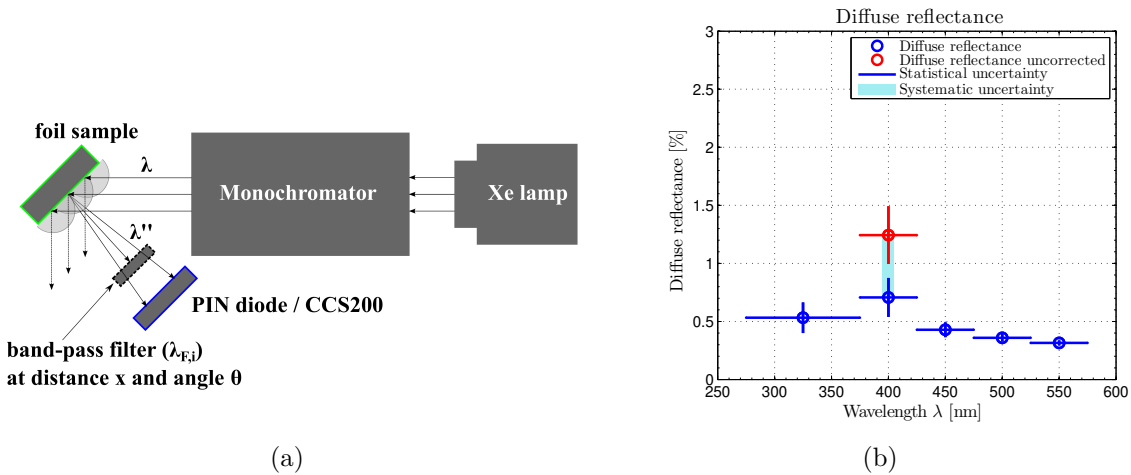


Figure 3.11: (a) Setup to measure the wavelength shifting and diffuse response properties of the DF2000MA foil. λ stands again for the wavelength selected at the monochromator. Additional band-pass filters transmitting certain wavelengths $\lambda_{F,i}$ quantify the diffusively emitted WLS light (λ'') for the PIN diode measurement. For the measurement with the CCS200 spectrometer no band-pass filters are used; (b) The diffuse reflectance $\rho_{f,0}$ of the DF2000MA foil. Values up to 0.7% can be reached when integrating individually over the full filter bandwidths (blue circles). A correction for the contribution of WLS at an absorption wavelength of 380 nm has been performed. The corresponding value includes a systematic uncertainty as indicated by the blue shaded region. If not corrected for, a higher value for the second data point is obtained (red circle).

The foil has a small component of diffuse reflectance $< 1\%$ across the filter bandwidths. The value for the filter interval $375 \text{ nm} \leq \lambda_{F,2} \leq 425 \text{ nm}$ appears increased compared to the others due to a systematic effect at an absorption wavelength of

$\lambda = 380$ nm. Only for this wavelength, diffuse reflectance and WLS emission happen in the same filter interval. Light of $\lambda = 380$ nm, for example, can get partly reflected diffusively at $\lambda'' = 380$ nm and can get partly absorbed and re-emitted wavelength-shifted at e.g. $\lambda'' = 420$ nm. Since both wavelengths are within the same filter interval, the analysis method accounts the WLS component to the diffuse reflectance, which result in the increased measurement value (red circle in figure 3.11(b)) and a clear visible peak in the WLS measurement (figure 3.12(c)). Excluding the absorption wavelength $\lambda = 380$ nm from diffuse reflectance analysis leads to the blue circle in figure 3.11(b). The resulting systematic error is indicated by the light blue band and is for the diffuse reflectance $\approx 75\%$. Absorption wavelengths of 370 nm or 390 nm do not induce this systematic error, since 370 nm is at the end of a filter interval and the higher wavelength WLS light is filtered, while for $\lambda = 390$ nm the foils specular reflectance is already high enough to almost not allow for absorption and WLS anymore (see figures 3.12(b) and 3.12(d)).

To quantify the wavelength shifting power of the foil, one defines

$$\Gamma(\lambda) := \frac{I(\lambda, \lambda_{F,i})}{I_{mf}(\lambda)} \rho_{mf}(\lambda) \quad (3.19)$$

to determine how much light gets wavelength shifted and which wavelength intervals are covered by the emission. Γ has been measured for an absorption wavelength range of $250 \text{ nm} \leq \lambda \leq 390 \text{ nm}$. Figure 3.12 shows a set of emission spectra for different absorption wavelengths. The highest ratios can be found in figure 3.12(b) ($\lambda = 370$ nm) in a range of $\approx 2\% - 3\%$. At $\lambda = 380$ nm the diffuse reflectance peak appears at $\lambda'' = 380$ nm as mentioned above. For absorption wavelengths of 390 nm (figure 3.12(d)), there is already a clearly visible reduction of the WLS, as expected from figure 3.10(b), where the specular reflectance at 390 nm is almost 100%. Besides that, the diffuse reflectance peak can be observed. No emission spectrum could be measured above 390 nm. WLS below 250 nm is probable, but was beyond the measurement range of this setup and could not be verified. As an illustration, the green areas in figure 3.12 indicate the interval where the muon veto PMTs have a quantum efficiency higher than 10%.

Because the enveloping function for the fluorescence emission spectra of the DF2000MA is unknown and the filter bandwidths provide only coarse resolution for the emission spectrum, a Thorlabs CCS200 spectrometer was used to measure the shape of the fluorescence spectrum for emission wavelengths ≥ 375 nm with a resolution of 0.25 nm. Since the CCS200 was not calibrated the spectrum measured for each wavelength had to be fit to the PIN diode measurement with a one parameter

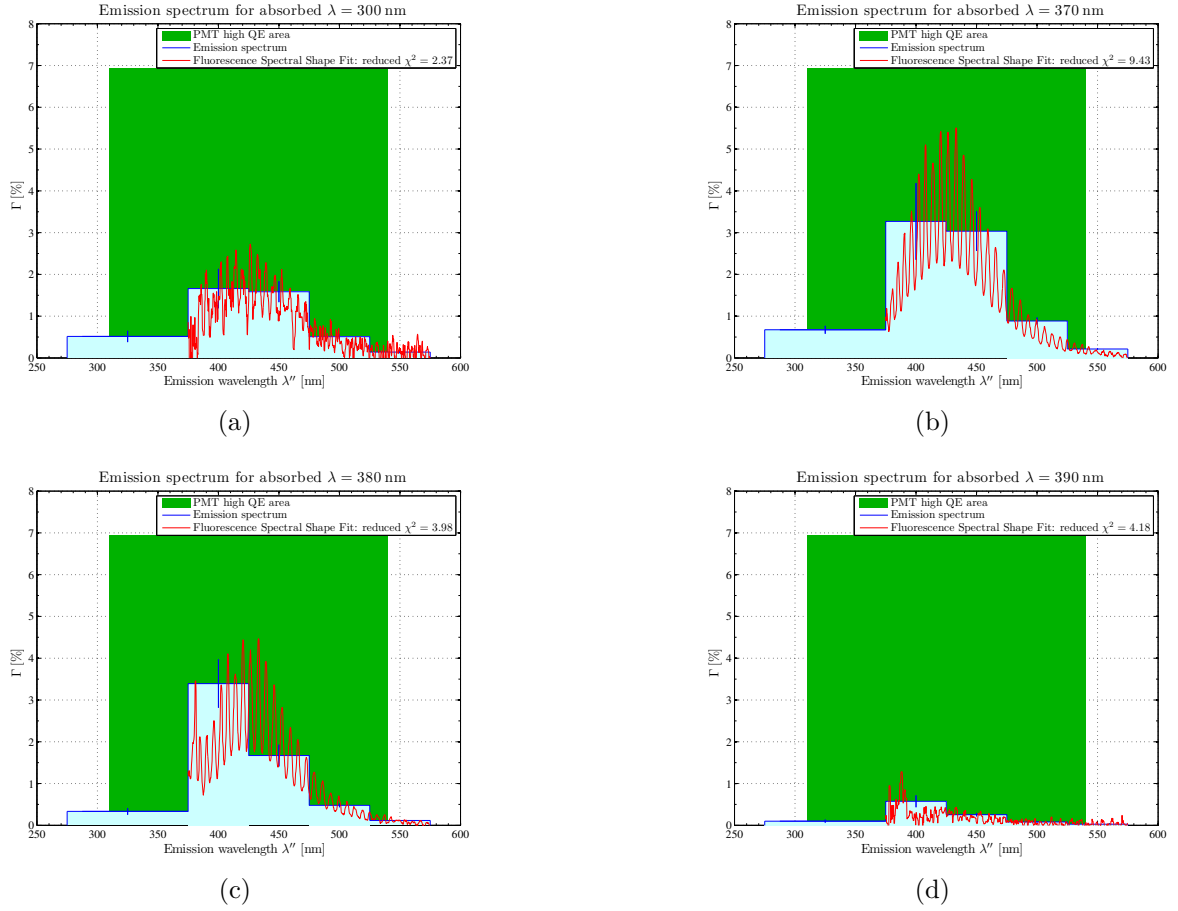


Figure 3.12: Emission spectra for wavelength shifted light by the DF2000MA foil for different absorption wavelengths (a) $\lambda = 300$ nm, (b) $\lambda = 370$ nm, (c) $\lambda = 380$ nm and (d) $\lambda = 390$ nm (blue stairs). The WLS spectrum obtained with the spectrometer for each of these wavelengths was scaled by a fit to those values in the trusted wavelength regime of the CCS200 spectrometer (red curve). In figures (c) and (d) diffuse reflectance is visible as a peak at $\lambda'' = 380$ nm and $\lambda'' = 390$ nm, respectively.

function $f(\lambda'')$, scaling the individual spectra by a factor a_0 best fitting to the PIN diode measurement data for each absorption wavelength (shown in red in figures 3.12):

$$f(\lambda'') = a_0 \cdot \varphi(\lambda''), \quad (3.20)$$

with $\varphi(\lambda'')$ being the emission spectrum obtained by the CCS200 spectrometer individually for each absorption wavelength λ . The fit was performed in the interval $375 \text{ nm} \leq \lambda \leq 575 \text{ nm}$. The shape of the spectrum suggests that the true emission curve also extends to values below 375 nm (especially in figure 3.12(b)), but only the PIN diode is sensitive to this part of the WLS emission within the 100 nm wide bandwidth of

filter 1. The obtained spectra are characteristic for the rotational-vibrational spectrum of fluorescence [41]. The vibrational sub energy levels are clearly visible as peaks and have a fixed separation of 6 nm. The highest emission values of the WLS spectrum can be observed at ≈ 430 nm. The typical width of the distribution at the half of its maximum is ≈ 80 nm.

Plotting the emission spectra for each individual absorption wavelength λ leads to a two dimensional histogram shown in figure 3.13(a). The warmer the color gets, the higher the percentage of the light ratio Γ is. The single spectra of figure 3.12 correspond to vertical slices in the histogram.

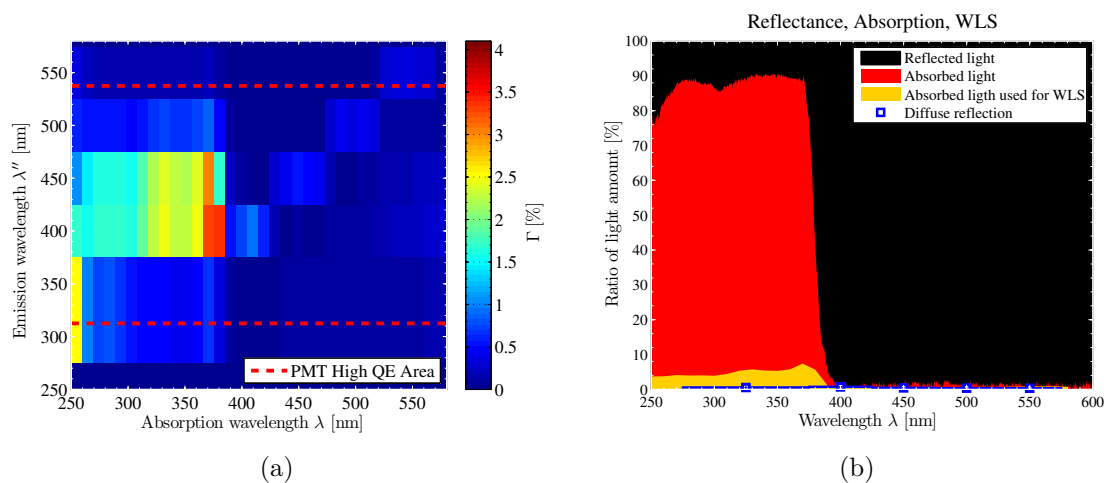


Figure 3.13: Result summary for the DF2000MA reflectivity and WLS measurements. *a)* Diffuse response of the DF2000MA foil including wavelength shift and diffuse reflection. The WLS emission maximum is between $\lambda'' = 375$ nm and 475 nm and lies in between the high QE area of the muon veto PMTs (red dashed lines). Highest values for the ratio of WLS light to entire light can be found up to 3.5%. The diffuse reflectance peaks are visible as small values along the diagonal for $\lambda = \lambda''$, overlapping with the WLS spectrum at $\lambda = 380$ nm; *b)* Pro rata visualization of how much light gets reflected, absorbed and wavelength shifted as a function of the incoming wavelength λ . About 90% of the light with a wavelength lower than 370 nm gets absorbed, while up to 7.5% gets later re-emitted as WLS light. Approximately 10% gets reflected specularly. For wavelength greater than 400 nm there is no absorption anymore. The diffuse reflection (blue squares) is less than 1%.

Almost all absorption takes place at wavelengths shorter than 390 nm. The emission spectrum reaches from 375 to 575 nm and covers all bandwidths of the used optical filters. Additional WLS to higher wavelength intervals ($\lambda > 575$ nm) was not observed during the measurements with the spectrometer, but would be anyway out of the range of interest defined by the high QE areas of the XENON1T muon veto PMTs. Once every emission spectrum is scaled with a spectral shape distribution, the spectrum values

are integrated over the emission wavelength λ'' to obtain the amount of fluorescence WLS light $\sum_i I(\lambda, \lambda_{F,i})$ relative to the entire amount of light I_{mf}/ρ_{mf} , which is just dependent on the absorption wavelength λ , but not on the emitted wavelength λ'' . This quantity is called WLS ratio and has a maximum value of $\approx 7.5\%$ for $\lambda = 370$ nm. This means that out of all photons exciting electrons to a higher energetic state by absorption in the foils molecules, just those 7.5% get reemitted in form of fluorescence light. The energy of the residual absorbed light is released via radiation-less heat transfer, not measurable by this experimental setup. As a summary figure 3.13(b) shows all measurement results combined. In case of the specular reflectance, almost 100% of the incoming light gets reflected for all wavelength larger than 400 nm. The rise of the reflectance starts already at 370 nm. These values are 30 nm below the values provided by the manufacturer in 2007 and are consistent with recent values provided by 3M. For wavelength shorter than 370 nm just $\approx 10\%$ of the light gets reflected with fluctuations of about $\pm 5\%$, depending on the wavelength. The remaining amount of light gets absorbed by the foil. Therefore, the high reflectance range covers $\approx 74\%$ of the high sensitive wavelength range of the muon veto PMTs (310 nm – 540 nm). Diffuse reflectance was observed within a 0.3% – 0.7% level and is negligible within the context of the foil use in the XENON1T experiment. The light absorbed by the foil is largely transferred into heat. Just $\approx 3 - 7.5\%$ of the incoming light is used for WLS, depending on the incoming wavelength.

3.4 Updated Monte Carlo simulation of the muon veto system

The DF2000MA reflectance and WLS measurement results have been implemented in the muon veto Monte Carlo code introduced in section 3.2.4. The foil is implemented in the Monte Carlo code not as a physical volume, but as a surface property of the inner water tank walls by defining a `G4OpticalSurface` object with type `dielectric_metal`, finish `polished` and model `unified`. Defining a `G4MaterialPropertiesTable` object with the reflectance values as reflectivity property allows to transfer that property to the defined `G4OpticalSurface` object. These properties of the DF2000MA foil in the code have now been updated according to the measurement results presented in the previous section. Figure 3.14(a) shows exemplarily the difference of the specular reflectance definition before (blue line) and after (black line) the modification according to the measurement values (green curve). For wavelengths shorter 300 nm reflectance values could be added, where in the old code version the reflectance was conservatively

set to zero. To implement the WLS in the GEANT4 simulation, the resolution of the emission spectra (compare figures 3.12) has to be improved. The resolution of the emission spectra is limited by the bandwidth of the used optical filters. Fitting the fluorescence spectral shape obtained by the CCS200 spectrometer for each absorption wavelength λ to the corresponding emission spectrum (as described in section 3.3.1) allows a finer binning of the latter, limited only by the resolution of the spectrometer (i.e. 0.25 nm). Figure 3.14(b) shows the 2D histogram shown in figure 3.13(a) with the adjusted resolution for the emission wavelength, based on the information obtained with the spectrometer measurement.

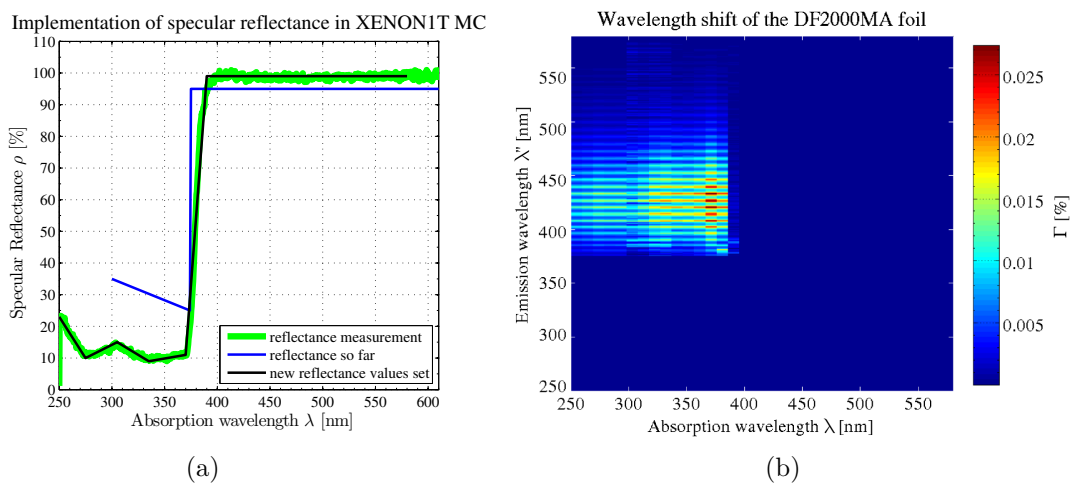


Figure 3.14: (a) Different implementations of the DF2000MA reflectance in the GEANT4 simulation. The blue curve shows the reflectance as it was defined in the MC study of [29], the black curve shows the reflectance as it was defined in this work. The green curve is the result of the reflectance measurement; (b) WLS absorption versus emission wavelength. The resolution on the emission side was improved by fitting the emission spectra for each absorption wavelength with the spectral shape of the fluorescence spectrum obtained by the CCS200 spectrometer.

Implementation of WLS in GEANT4 is not trivial. Its source code has to be changed. The physics of absorption and transmission in GEANT4³ are handled by the `G4OpBoundaryProcess` class. This class handles not reflected photons as absorbed and their `G4Track` object is killed. However, the source code of class `G4OpBoundaryProcess` provides already a commented possibility to transmit an absorbed particle and returns a new particle with a new `G4Track`, instead of killing the absorbed particle track. The corresponding lines of code in the `G4OpBoundaryProcess` are

³GEANT4 version 4.9.2.p02.

```

438 if (type == dielectric_metal) {
439     DielectricMetal();
440     // Uncomment the following lines if you wish to have
441     //         Transmission instead of Absorption
442     // if (theStatus == Absorption) {
443     //     return G4VDiscreteProcess::PostStepDoIt(aTrack, aStep);
444     // }
445 }

```

Uncommenting lines 442–443 enables the mentioned transition instead of absorption with a new particle being returned. To implement WLS instead of only transmitting this particle, it has to be wavelength shifted according to the emission probabilities determined by the ratios Γ in figure 3.14(b). The code listing below describes how the implementation was done. For the sake of clarity some lines are not displayed and replaced by “...”.

```

438 if (type == dielectric_metal) {
439     DielectricMetal();
440     // Uncomment the following lines if you wish to have
441     //         Transmission instead of Absorption
442     if (theStatus == Absorption) { // ChG: To be uncommented for WLS
443
444         ////////////////////////////////////////////////////////////////////
445         // WLS of DF2000MA ChG 14-05-12
446         // Comment everything within the "///" to disable WLS
447         ////////////////////////////////////////////////////////////////////
448
449         // Initialize new particle
450         ...
451         // Determine photon energy
452         sampledEnergy = DetermineWLSEmissionEnergy(aTrack);
453         // Generate random photon direction
454         ...
455         // Create photon momentum direction vector
456         ...
457         // Determine polarization of new photon
458         ...
459         // Generate a new photon:
460         G4DynamicParticle* aWLSPhoton =
461             new G4DynamicParticle(G4OpticalPhoton::OpticalPhoton(),
462                                   photonMomentum);
463         ...
464         aWLSPhoton->SetKineticEnergy(sampledEnergy);
465     }

```

```

466 // Generate new G4Track object:
467 ...
468 return G4VDiscreteProcess::PostStepDoIt(aTrack, aStep);
469 ///////////////////////////////////////////////////
470 }
471 }

```

The most important is line 452, where function `DetermineWLSEmissionEnergy()` is called. The 2D histogram of figure 3.14(b) is deposited in the class as a `TH2F` object and, according to the wavelength of the photon hitting the foil, random wavelengths from the emission spectra are drawn according to their chance to appear. The energy corresponding to the emission wavelength is then given to the new particle in line 464 to the new photon `aWLSPhoton` which is returned. To verify that the code is working, a large number of photons which intensity distribution following a $1/\lambda^2$ law (compare equation (3.5)) have been shot on the foil in a separate simulation. Figure 3.15(a) shows the wavelength of the resulting photons with WLS absorption enabled (blue line) and WLS absorption not enabled (red line). Below 380 nm the absorption of photons leads to lower values of the blue curve. The emission maximum of the WLS light at ≈ 410 nm is visible, whereas for longer wavelengths both curves are congruent again. A corresponding emission spectrum is shown in figure 3.15(b). The vibrational peaks are clearly visible. Shape and relative size of the spectrum match the measurements shown in red in figures 3.12.

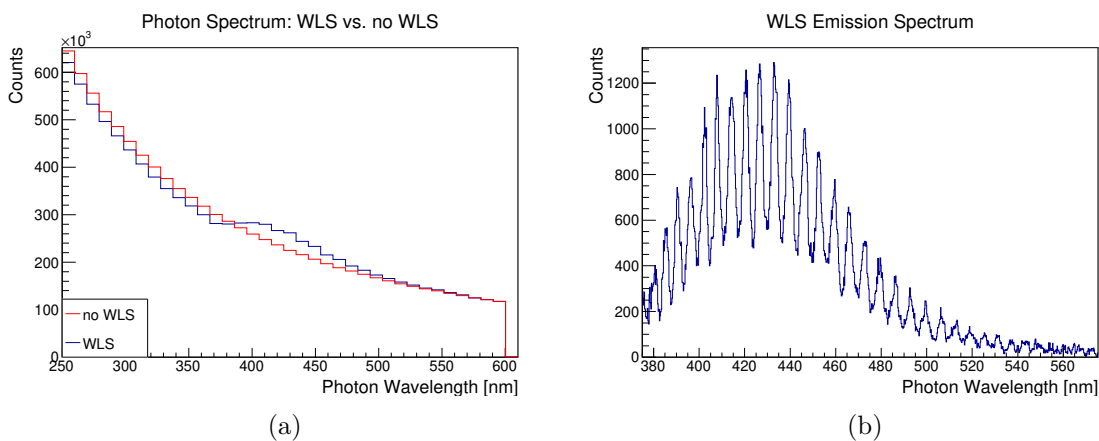


Figure 3.15: Verification of wavelength shifting properties in the simulation. (a) A $1/\lambda^2$ distributed photon intensity (red line) changes for allowed WLS to the blue line. At short wavelengths the blue distribution is lower, while at the position of the emission maximum it is above the original values. For higher wavelengths, both curves are equal; (b) Plot of a spectrum of simulated wavelength shifted photons. Shape and relative size of it match the measurements.

Running the simulations precisely as described in 3.2.4, the muon tagging efficiency ϵ_μ and shower tagging efficiency ϵ_s for the modified GEANT4 were obtained. Table 3.2 shows an overview and comparison between the results.

Band-pass Filters		
Code	ϵ_μ [%]	ϵ_s [%]
Original	99.78 ± 0.05	70.6 ± 0.5
mod. refl.	99.72 ± 0.06	70.9 ± 0.5
mod. refl. + WLS	99.69 ± 0.06	71.1 ± 0.5

Table 3.2: Impact on modified reflectivity and WLS on the muon veto tagging efficiency. The more realistic specular reflectance values lead to no significant change of the muon tagging efficiency ϵ_μ as well as the the shower tagging efficiency ϵ_s . Allowing also for WLS, ϵ_μ remains again unchanged within the statistical error, while ϵ_s increases.

The detection efficiency of the muon veto remains almost unchanged for muon events at $\epsilon_\mu = (99.72 \pm 0.06)\%$ as well as for shower events with $(70.9 \pm 0.5)\%$. The effects of the overestimated reflectance below 370 nm in the original MC simulation (shown in the blue curve in figure 3.14(a)) and the additional implemented data points below 300 nm compensate each other. If, in addition, wavelength shifting is allowed, the detection efficiency for muon events stays the same within the statistical error ($(99.69 \pm 0.06)\%$) but rises $\approx 0.5\%$ for shower events to $(71.1 \pm 0.5)\%$. Hence, there is a small increase of the muon veto efficiency due to the wavelength shifting of the DF2000MA foil. It is consistent with the physics in the muon veto. The amount of Cherenkov light created by muons is so big (≈ 3000 photons per muon), that the WLS effect has no impact, while for the shower case, due to the lower number of produced photons (≈ 400 photons per shower), one could expect a small effect on the efficiency.

3.5 Laboratory PMT testing

90 R5912 PMTs have been purchased for the muon veto. The best performing 84 to be used in the detector and 6 PMTs as spare or to use for reference measurements. The PMTs have been redundantly tested at the universities of Bologna in Italy and at the University of Mainz, where 48 of the 90 PMTs were tested. The PMTs were subject of measurements for their gain, dark rate and afterpulses. Series tests were performed for each individual PMT, as well as, after shipment to the LNGS laboratory in a small water tank in bunches. The results of these tests is presented in the following.

3.5.1 PMT series tests

In the laboratory at Mainz a test facility was constructed, consisting of four cuboid black boxes with dimensions $60\text{ cm} \times 60\text{ cm} \times 60\text{ cm}$ enabling the serial measurement of all PMTs in bunches of four. All boxes were optically tight, painted black at their inner surface and equipped with feedthroughs for high voltage, signal and PMMA⁴ optical fiber. Each PMT was fixed in the boxes by a prototype of the PMT holding structure, which later was used in the water submersion tests and in the final installation of the muon veto. In section 3.6 this is explained in more detail. For each box a PTFE piece was used to reflect light on the photocathode of the PMTs. The four fibers were the tails of a 4-to-1 fiber bundle with a blue LED ($\lambda = 470\text{ nm}$) as light source. The LED was driven by a pulse generator, which additionally provided a trigger for a CAEN V1724 fADC, acquiring the PMT signals. This was the same digitizer as used in the muon veto (compare section 3.2.3). Figure 3.16 shows a PMT in one of the boxes as well as the principle of the photocathode illumination.

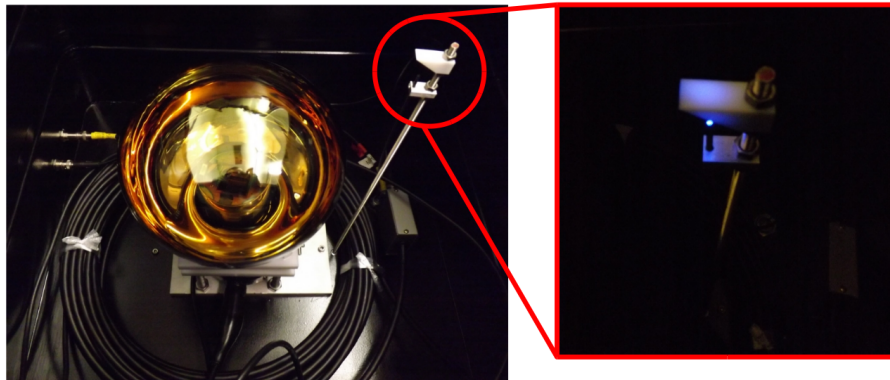


Figure 3.16: A muon veto PMT in the series test setup. A PMMA fiber guides blue light of an LED to a PTFE reflector piece to illuminate the photocathode.

For each PMT the following test protocol was performed:

- Gain measurements for nominal high voltages U , as well as nominal high voltage $\pm 50\text{ V}$, $\pm 100\text{ V}$ and $\pm 150\text{ V}$, where the nominal voltage was the one provided by Hamamatsu.
- Dark rate measurements for nominal voltages and its variations as for the gain measurement.
- Afterpulses measurements.

⁴Polymethylmethacrylate is a transparent thermoplastics widely used as material for optical fibers.

Gain measurements

The gain of a PMT is the amplification of a photoelectron current I_k into a measurable electric current at its anode I_a . It results from secondary emission of electrons throughout the dynode chain. Following [91], the secondary emission ratio δ_i for a certain dynode stage is

$$\delta_i = a\Delta U_i^k, \quad (3.21)$$

where ΔU_i^k is the interstage voltage between two dynodes. a is a constant and k expresses dynode material and structure dependent properties and has a values in the range of 0.7 – 0.8. At the first dynode, the photoelectrons current I_k hits the first dynode, where a secondary emission current I_1 is released. Therefore δ_i for the first stage is

$$\delta_1 = \frac{I_1}{I_k}. \quad (3.22)$$

For the n -th stage it is consequently given by

$$\delta_n = \frac{I_n}{I_{n-1}}. \quad (3.23)$$

The output current at the PMT anode is thus.

$$I_a = \alpha I_k \cdot \prod_{i=1}^n \delta_i. \quad (3.24)$$

As mentioned above, the gain g of a photomultiplier is the ratio of I_a and I_k , so

$$g = \frac{I_a}{I_k} = \alpha \cdot \prod_{i=1}^n \delta_i, \quad (3.25)$$

with α being the collection efficiency of the PMT. Assumptions of $\alpha = 1$, a constant ΔU across all dynode stages and insertion of equation (3.21) leads to

$$g = (a\Delta U^k)^n = a^n \cdot \left(\frac{U}{n+1}\right)^{kn} = B \cdot U^{kn} \quad (3.26)$$

with $B = a^n / (n+1)^{kn}$. Experimentally, the gain of a PMT can be obtained by the measurement of its single photoelectron (SPE) spectrum. It can be measured by illuminating the photocathode with the pulse generator driven blue LED, mentioned above. The pulse generator provides a rectangular pulse to the LED with amplitude U_{LED} , pulse width w and frequency f . U_{LED} has to be chosen such, that its light

intensity corresponds to the single photon intensity of the PMT, i.e. the intensity, where in $\approx 5\%$ of the acquired waveforms the PMT measures a photon signal. Given the voltage range of the DAQ $V_{pp} = 2.25$ V, its number of quantization levels 2^{14} , the sampling rate of $R = 100$ MSa/s, corresponding to $\Delta T = 10$ ns/Sa, and the input impedance $Z = 50$ Ω , the charge of a PMT output signal in pC can be calculated as

$$Q_{\text{pC}} = A \cdot \frac{V_{pp}}{2^{14}} \cdot \frac{\Delta T}{Z} \cdot 10^{12}, \quad (3.27)$$

with A being the integral of the signal in ADC counts \times Sa. Acquiring a certain number of waveforms and drawing Q_{pC} in a histogram is shown in blue in figure 3.17(a). This plot is from a gain measurement within the series tests of one PMT (Serial number SQ0027).

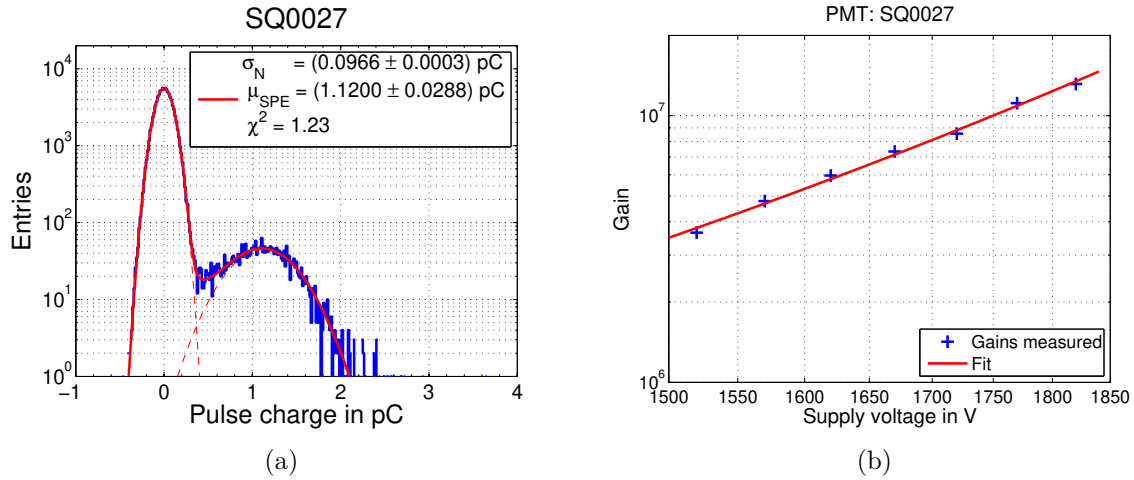


Figure 3.17: Example of a PMT gain measurement during the series tests. (a) The gain was calculated by measuring the single photoelectron peak, using the charge spectrum (blue) and fitting it with equation (3.28) (red curve). The Gaussian fit on the pedestal and on the SPE peak individually are drawn as red-dashed lines; (b) To obtain high voltage values for each PMT providing a equalized gain of all PMTs, gain measurements have been performed for the nominal high voltage ($HV = 1670$ V in this case), as well as nominal high voltage ± 50 V, ± 100 V and ± 150 V.

It contains two features: the distribution of single photons at 1.12 pC and a pedestal peak at around zero originating from electronic noise in the waveform. Assuming both to be Gaussian distributions, the spectrum can be fit with

$$f(x) = A_N \cdot e^{-0.5 \left(\frac{x - \mu_N}{\sigma_N} \right)^2} + A_{\text{SPE}} \cdot e^{-0.5 \left(\frac{x - \mu_{\text{SPE}}}{\sigma_{\text{SPE}}} \right)^2} + P_0 \cdot e^{P_1(x - P_2)}. \quad (3.28)$$

The first Gaussian term refers to the shape of the pedestal. An important parameter is σ_N which is the standard deviation of the noise pedestal and indicates how noisy the underlying waveform is. The second Gaussian is the distribution of the SPE. Its mean μ_{SPE} allows to extract the gain g as

$$g = \frac{\mu_{\text{SPE}}}{e}, \quad (3.29)$$

where e is the elementary charge. The last exponential term in equation (3.28) accounts for a contribution to the spectrum at the interface of pedestal and SPE Gaussian and accounts for primary electrons emitted at the upper dynode stages, which may have been covered with photocathode material during manufacturing of the PMT. After doing this for all voltages scheduled, one yields a plot shown in figure 3.17(b). Every blue + corresponds to a gain measurement at the corresponding high voltage. According to equation (3.26) a fit can be calculated from which that PMT supply voltage can be extracted, which leads to a certain desired gain. Using only the nominal high voltage values provided by Hamamatsu, the series tests yielded a mean gain of $g = (6.5 \pm 1.6) \cdot 10^6$. In the now running muon veto, based on these tests, the operation voltages of all PMTs have been set such, that an equalized gain of $6.0 \cdot 10^6$ is reached.

Dark rate

The dark rate of a PMT is the current one can measure at its anode, even if operated in a completely dark environment. There are several mechanisms, which contribute to the dark current from which the most important are: thermionic emission current from the photocathode and dynodes, and scintillation from activated atoms or molecules in the glass bulb of the photomultiplier after it was exposed to light. The latter mechanism is decreasing with time after operating the PMT in darkness again. Measurements showed, that dark rate reduces roughly by a factor of 3 within two days and reaches afterwards a stable level dominated by the thermionic induced dark rate. To obtain the dark rate a long waveform of 5.24 ms of the PMTs output signal was acquired without illumination of the photocathode. The number of peaks above the threshold of thr was counted. Figure 3.18(a) shows the dark rate versus threshold exemplary for PMT SQ0020. The red dashed line indicates $thr = 1$, which is the value for the single photoelectron signal, obtained from the gain measurement. If this is done for all tested PMTs, figure 3.18(b) shows the dark rate calculation for all PMTs tested in Mainz for a threshold $thr = 1$. The dark rates of all PMTs have been measured by

Hamamatsu before delivery. Our measured mean dark rate of $\approx 1.2\text{kHz}$ matches the values provided by Hamamatsu. There was no clearly noisy PMT. However, the results of these measurements were taken into account to decide which PMTs were eventually installed in the muon veto and which were kept as spares.

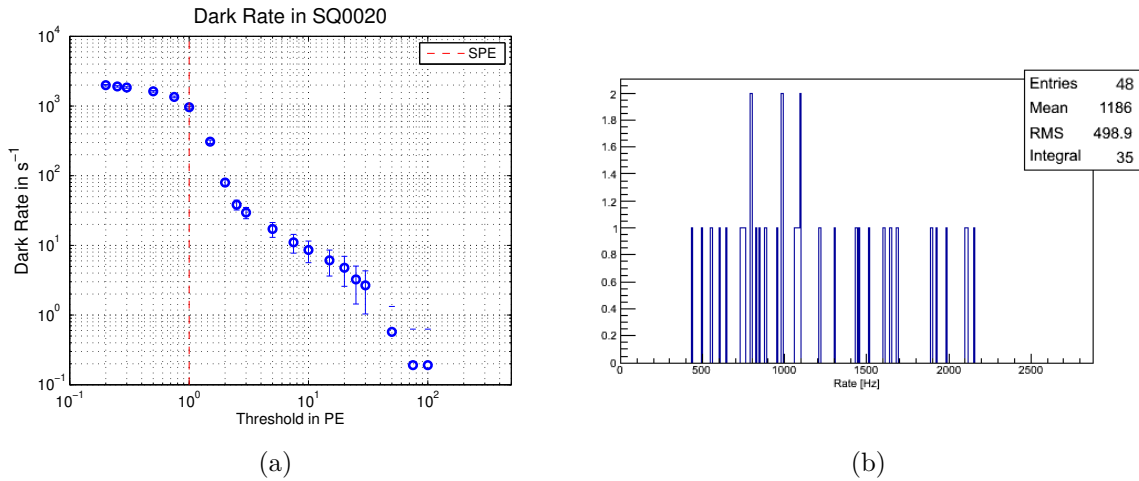


Figure 3.18: Dark rate measurements of the muon veto PMTs. (a) Dark rate versus the threshold thr (blue circles). The red dashed line indicates the threshold of $thr = 1$ PE, obtained from the gain measurements; (b) The dark rate at $thr = 1$ PE of all 48 PMTs measured in Mainz. The mean dark rate of $\approx 1.2\text{kHz}$ matches the values provided by Hamamatsu.

Afterpulses

Afterpulses occur, when photoelectrons ionize residual gas molecules inside the photomultiplier tube on their way to the dynodes. The residual gas pressure inside the tube is on the order of 10^{-5} Pa. Those positively charged ions travel along the field lines in the PMT and hit the photocathode where they release additional electrons. Their acceleration in the electric field depends on their mass, hence residual gas ions of different masses will result in additional peaks on the waveform at certain times after a primary large PMT signal. To inspect the afterpulses of a given PMT it has to be illuminated with a comparably high intensity to stimulate the production of afterpulses. In the tests presented here it was an intensity corresponding to 60 PE. Figure 3.19(a) shows a waveform of an event acquired during an afterpulses measurement performed with PMT SQ0049. The red window of $0.8\ \mu\text{s}$ length was used to obtain a baseline of the waveform. The area of the initial primary peak was integrated within $-0.1\ \mu\text{s} < \text{peak position} < 0.4\ \mu\text{s}$. Following this, the afterpulse window spans until $20\ \mu\text{s}$ after the primary peak. Afterpulses were then defined as a peak which is larger than 40 ADC

counts for at least two consecutive samples. Integrating the area of all afterpulses and comparing it to the area of the primary pulse is a measure for the quality of the vacuum inside the tube. Figure 3.19(b) shows this ratio for thresholds of 40 ADC counts (red) and 10 ADC counts (blue) for all tested PMTs. Even for the smaller threshold the majority of PMTs was observed with an afterpulse fraction < 0.2 . Two PMTs with a fraction of ≈ 0.25 were identified and used as spare PMTs.

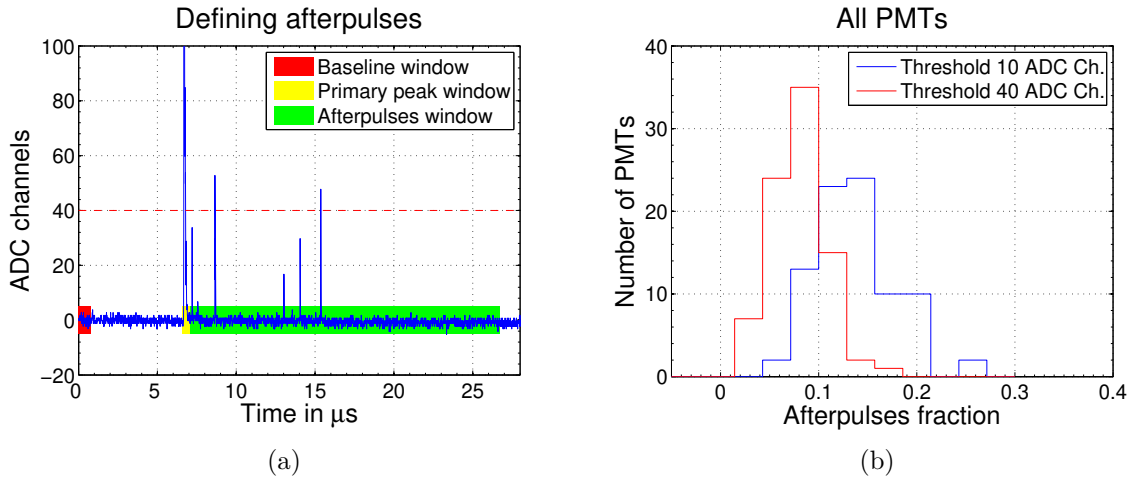
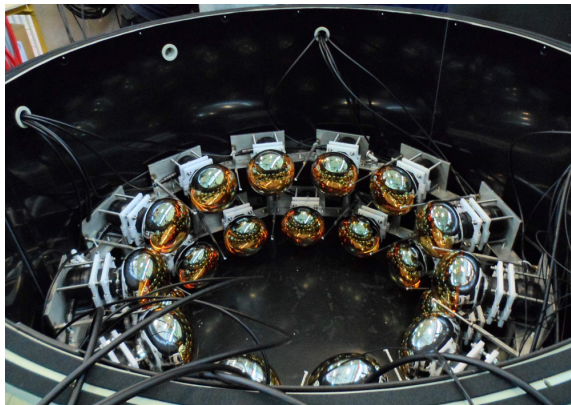


Figure 3.19: (a) A waveform of an event during an afterpulses measurement. Peaks within the green window which contain of at least two consecutive samples being higher than a threshold (red dashed line) being defined as afterpulses. (b) The area fraction of all afterpulses integrated and the primary peak integrated. The mean fractions are at ≈ 0.09 for a threshold of 40 ADC counts and 0.16 for a threshold of 10 ADC counts.

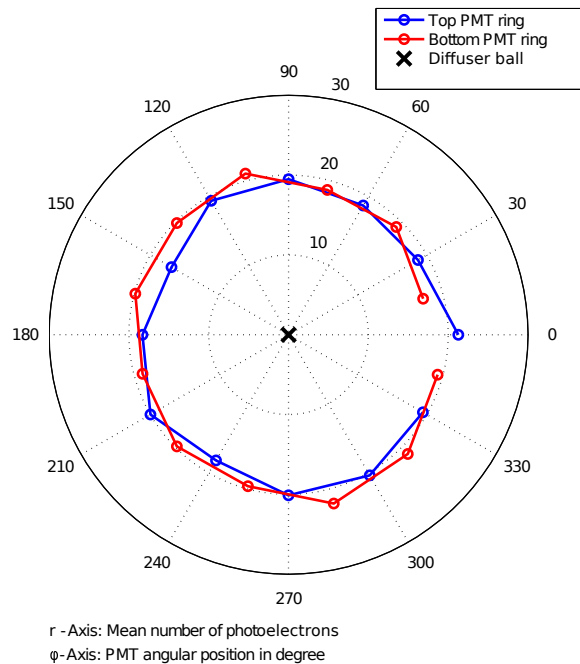
3.5.2 Water submersion tests

After the successful series tests, all PMTs have been shipped to LNGS to undergo a second test. This test was performed in a cylindrical water tank of 1.6 m diameter and 0.65 m height. A cylindrical holding structure was able to hold 24 inward looking PMTs at the same time. In the center a diffuser ball was positioned to illuminate the PMTs. The diffuser balls are the global calibration system of the muon veto, having been designed within the scope of this thesis and are explained in detail in section 3.6.1. The tank was filled with pure water and the tests aimed to verify the performance of all PMTs in water and after the transport to LNGS, as well as to test the DAQ system on multiple PMTs. Figure 3.20(a) shows a picture of the open tank fully equipped with PMTs. The PMTs were arranged in two concentric circles on top of each other with 12 PMTs each. The PMT cables have been guided into the tank via

M50 PFLITSCH feedthroughs (catalogue number 25056stpm [123]) with rubber inlets, being used also in the final installation of the muon veto. Figure 3.20(b) shows a result of the test of the first bunch of 24 PMTs. Each circle is a PMT in the water tank. The illumination intensity with the diffuser ball was chosen such that the mean number of photoelectrons in the primary peak of the PMT signals was ≈ 20 . The diffuser ball was placed in a height directly between the two PMT rings, resulting in the blue and red curve being congruent. The measured deviations in the mean number of PE of $\approx 25\%$ results from two effects: First, relative deviations in quantum efficiencies as provided by measurements of Hamamatsu amount to about 20%. Second, deviations of the emission isotropy of the diffuser ball are on the order 20% (see section 3.6.2). All PMTs have been tested successfully in the water tank. No PMT showed different behavior compared to the series tests. No damage due to water leaks could be observed.



(a)



(b)

Figure 3.20: (a) A picture of the PMT water submersion test setup after shipment to LNGS. 24 PMTs have been tested simultaneously; (b) Illumination of all PMTs with a diffuser ball in a polar plot view. Illumination intensity was chosen to result in ≈ 20 PE in the primary peak (radial axis). Blue circles represent the upper ring, red circles the lower ring. Deviations of 20% originate from deviations of quantum efficiency and emission isotropy of the light source. All PMTs showed full functionality and water tightness.

3.6 Calibration system

Two calibration systems of the muon veto PMTs have been foreseen: an individual calibration of each PMT with a single PMMA fiber and a global calibration of all PMTs with self made diffuse light sources (diffuser balls). In the following, both systems will be explained in detail concerning their design, tests and commissioning.

3.6.1 Design

Individual PMT calibration

As introduced above, the individual PMT calibration consists of a single PMMA fiber for each PMT being mounted in a holding structure. A picture of the PMT holder and of the calibration system based on a reflective PTFE piece was already shown in figures 3.4(a) and 3.16. Figure 3.21(a) shows a technical drawing of the PMT mount. It consists of a ground plate with four M12 threaded rods, hosting the PMT corpus. Four POM⁵ brackets (labeled “1” in the drawing) hold the PMT. Two L-shaped rails (labeled “26”) are mounted to the ground plate and serve as wall mount, as their holes fit the positions of welded studs on the water tank wall. This allows the full holding structure to be screwed to the wall. Each PMT mount features a bar with a PTFE reflector on top, labeled “9” and “12” in figure 3.21(a). The optical fiber is guided along this bar and is fixed by a strain relief “8”. Seven single PMMA fibers are combined to one single bundle, ending in an optical SMA connector at the feedthrough. Thus, each PMT column can be provided with one bunch of fibers, yielding 12 fiber bundles in total, each one facing a blue LED at its bundled input. The LEDs have a luminous intensity of 4700 mCd at a wavelength of 470 nm. They are stored in individual boxes and are in series with a 100 Ω resistor for current limitation.

Global PMT calibration - diffuser balls

In order to verify the functionality of the muon veto as a whole a global calibration system was designed within the scope of this thesis. The design was inspired by a similar idea of the GERDA experiment [98]. It is based on *diffuser balls*, consisting of a hollow, 50 mm diameter PTFE sphere with 2 mm wall thickness and a 10 mm diameter with a hole on top. It is filled with a mixture of optical silicone and glass bubbles. Their design is explained in detail in the following. Figure 3.21(b) shows a sketch of

⁵Polyoxymethylene (POM) is a thermoplastic providing high stiffness and dimensional stability.

the composition of the diffuser balls with labels of the most important components and their function.

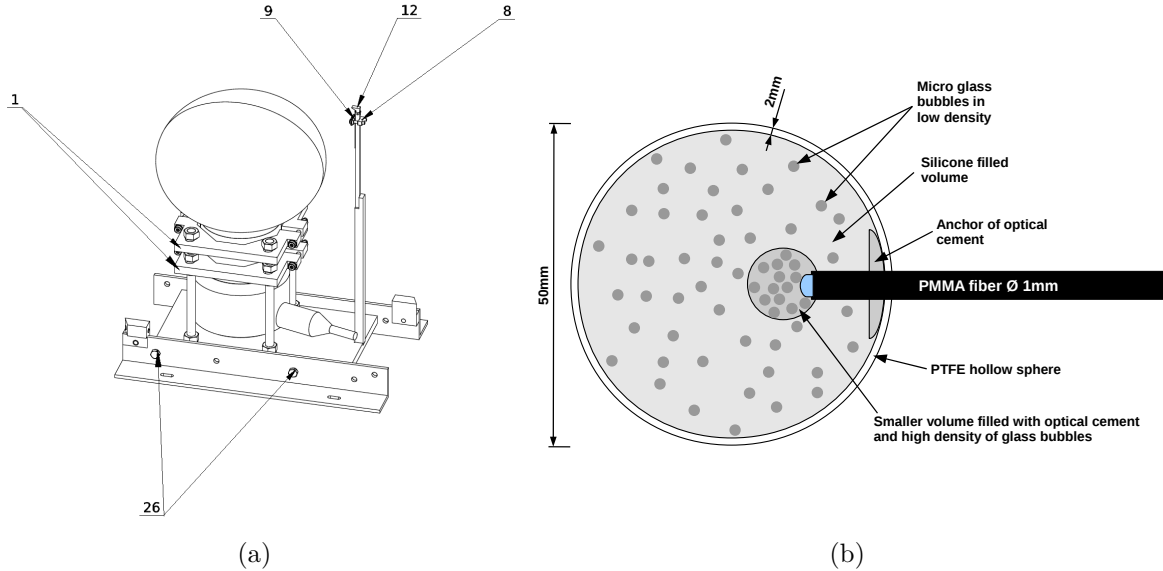


Figure 3.21: (a) Technical design of a PMT mount. Two brackets (1) hold the PMT on a ground plate which is screwed to the water tank walls with holes in its side rails (26). An optical fiber of individual calibration of each PMT is mounted at the rod (8) and (9) and illuminates a reflective PTFE piece on top of it (12) illuminating ultimately the PMT photocathode; (b) Schematic design of a diffuser ball as global calibration system of the muon veto PMTs.

The layer like composition of the diffuser balls is as follows: one end of a single fiber PMMA fiber of the same type as used for the individual calibrations of 33 m is pushed through a 10 cm long stainless steel cannula of size 3×0.2 mm. On the other side, the fiber ends in an SMA optical connector. The cannula mechanically supports the fiber and has at the lower end a disk hard soldered acting as an anchor for fixation. A 9 mm diameter quartz glass sphere is put over the end of the fiber and is filled with a mixture (mass ratio $\mu_i = 5\%$) of micro glass bubbles (S32 by 3M, mean diameter: $40 \mu\text{m}$, [116]) and optical cement (UV hardening DYMAX OP-29 [76]). A picture of this is shown in figure 3.22(a), where the steel cannula, the disk and the filled quartz glass sphere can be seen. The many small glass bubbles act as many scattering targets for the light exiting the fiber and distribute it in diffuse directions. The cannula-fiber compound enters the PTFE sphere 9 mm deep as visible in figure 3.22(b). The volume outside of the glass sphere is filled with a two component optical silicone gel (Wacker SilGel612 A&B [144]) up to 3 mm below the top. The two components have to be mixed $m(A) : m(B) = \mu_{\text{Sil}} = 1.2 : 1$ to increase hardness of the resulting vulcanizate.

S32 micro glass bubbles are mixed into the silicone in a mass ratio of $\mu_o = 1.5\%$. After letting the silicone dry the residual spherical cap volume is filled with an optical cement mixture (DYMAX OP-29 again) of $\mu_a = 1.5\%$ mass. The disk on the cannula is now embedded in the cement and acts as an anchor, providing mechanical strength to the full compound. Both, silicone and glue were selected for their high transmittance for light of 470 nm of $\tau_1 \approx 90\%$ (DYMAX OP-29) and $\tau_2 > 88\%$ (Wacker SilGel612), respectively. After hardening, the diffuser ball is finished. Coupling blue LED light into the SMA connector of the fiber leads now to a homogeneous light emission over the full spherical surface, as shown in figure 3.22(c). Each diffuser ball is illuminated by a single LED in its individual box. Type of LED and boxes are equal to the ones used for the individual fiber calibration

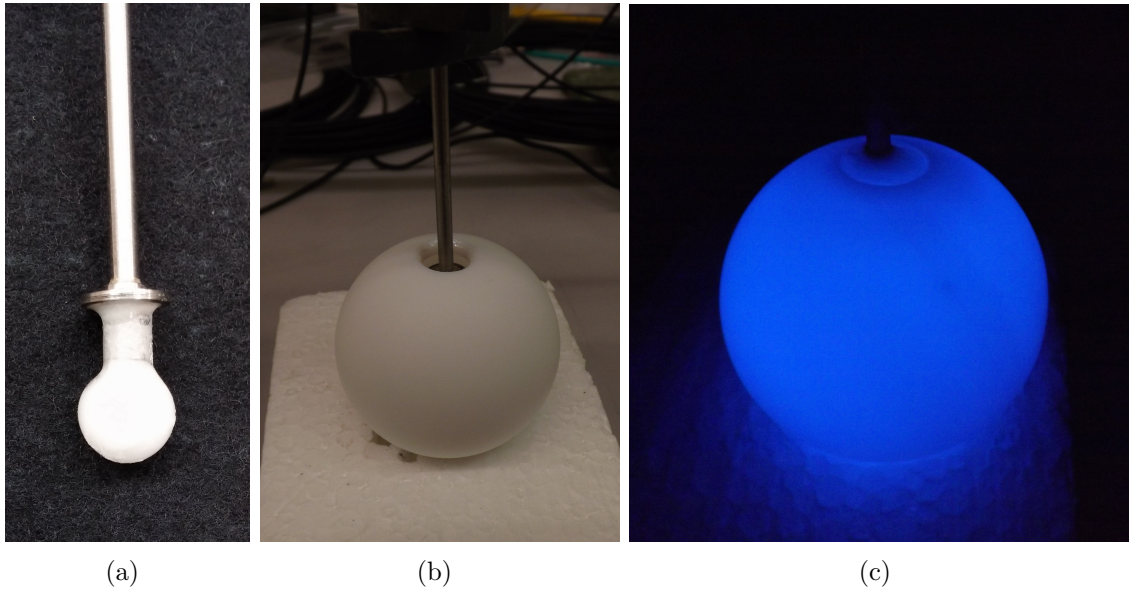


Figure 3.22: Diffuser ball composition and sub-compounds. (a) A PMMA fiber is pushed through a stainless steel cannula and glued into a quartz sphere, filled with a mixture of micro glass bubbles and optical cement; (b) The compound in (a) is lowered into the empty PTFE sphere, which is filled with a mixture of micro glass bubbles and optical silicone; (c) After hardening, the direction of light exiting the fiber straight is exiting the PTFE sphere homogeneously across its surface, due to multiple scattering inside the sphere.

In total, 8 diffuser balls have been manufactured (serial number SN #01-08), from which 5 in the final design as presented here (SN #04-08). 4 of them were installed in the muon veto with one acting as a spare. Table 3.3 shows the composition concentrations of the used chemicals. The individual substances have been weight by a scale with mg precision. The table shows that for the five produced diffuser balls the desired mass ratios have been reached with a precision of 15% and a mean deviation of $\approx 10\%$. The

total mean mass of the diffuser ball is $m = (582 \pm 2)$ g, which is ≈ 50 g heavier than a 50 mm diameter sphere of water. Therefore the diffuser balls would not float in water.

Diffuser balls overview						
	Goal	SN#04	SN#05	SN#06	SN#07	SN#08
Inner volume:						
$m(\text{OP-29})$ [mg]		472	575	533	540	530
$m(\text{S32})$ [mg]		29	30	27	34	30
μ_i [%]	5.00	5.79	4.96	4.82	5.92	5.36
Outer volume:						
$m(\text{Sil A})$ [g]		27.338	27.278	27.281	27.302	27.272
$m(\text{Sil B})$ [g]		22.519	22.886	22.804	22.841	22.730
μ_{Sil}	1.200	1.213	1.192	1.196	1.195	1.200
$m(\text{S32})$ [g]		0.745	0.763	0.754	0.754	0.765
μ_o [%]	1.50	1.49	1.52	1.51	1.50	1.53
Glue anchor:						
$m(\text{OP-29})$ [g]		1.211	1.524	1.768	1.035	1.035
$m(\text{S32})$ [g]		0.024	0.027	0.029	0.018	0.018
μ_a [%]	1.50	1.94	1.74	1.61	1.71	1.71

Table 3.3: Composition of five produced diffuser balls. The yielded mean mass ratios μ match the desired values (column “Goal”) within a maximum level of 15% and have a mean deviation of 10%.

3.6.2 Calibration tests and simulations

The individual fiber calibration was tested in the series tests as described in section 3.5.1. Since the principle was working, no further tests have been performed. Contrary to that, the diffuser balls were tested before installation in a special setup to determine the isotropy of their emission. In this setup, a single diffuser ball was facing a Hamamatsu R6041 2" PMT with a plane circular photocathode inside a black painted dark box. An LED illuminated the diffuser ball via its fiber. Diffuser ball and photocathode were 23 cm apart. In the default position, the diffuser ball was oriented such, that the cannula was pointing towards the PMT (defined as $\theta = 0^\circ$), the azimuthal position was marked as $\phi = 0^\circ$. The LED intensity was chosen corresponding to ≈ 50 pC charge in the PMT pulse for the default orientation. The diffuser ball was then sequentially rotated from 0° to 360° in steps of 45° . First in azimuthal direction ϕ and after reaching the original orientation of $\phi = 0^\circ = 360^\circ$ also in positive and negative polar directions θ ,

where for $\theta = 90^\circ$ the cannula pointed straight upwards and for $\theta = -90^\circ$ downwards, respectively. For $\theta = -180^\circ = 180^\circ$, the cannula pointed in opposite direction to the PMT. The angular precision was estimated to be $\pm 5^\circ$ for both angles. Since the PMT remained fixed, it could observe emission from differently oriented hemispheres of the diffuser ball. Each position has been measured five times to obtain an error estimation on the PMT pulse charge ($\approx \pm 0.5$ pC). Figure 3.23 shows the mean observed PMT signal charge versus azimuth and polar angles, exemplary for one diffuser ball (SN#05).

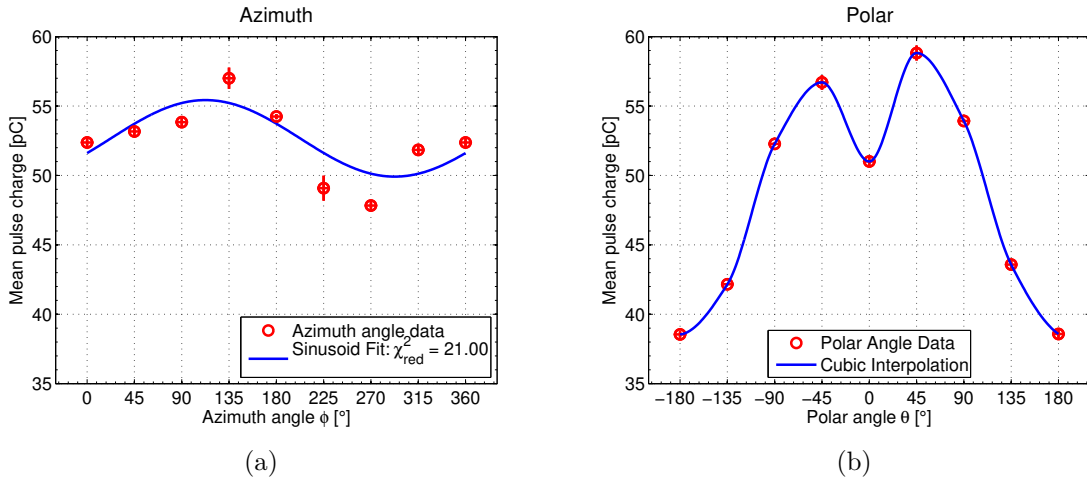


Figure 3.23: Diffuser ball emission versus azimuth and polar angle, showing the mean charge of PMT signal pulses. (a) Azimuth angle: an oscillation of $\approx 20\%$ can be observed. However, a sinusoidal fit (see equation (3.30)) does not fit the data satisfactorily; (b) Polar angle: a decline of emission intensity can be seen from top $\theta = 0^\circ$ to bottom $\theta = |180^\circ|$, where positive and negative polar angles refer to inclinations in opposing directions.

The azimuthal emission profile (red circles) shows an oscillating shape. However, fitting a sinusoidal function

$$f(x) = \hat{x} \cdot \sin(\omega x + \phi_0) + A_0, \quad (3.30)$$

can not match the data satisfactory (blue line, $\chi^2_{\text{red}} = 21.0$). Fit parameter ω was here fixed to be $2\pi/360^\circ$. The best fitting sinusoidal is drawn in the figure for an amplitude $\hat{x} = (2.8 \pm 0.2)$ pC, an offset $A_0 = (52.7 \pm 0.1)$ pC and a phase shift $\phi_0 = (-22 \pm 5)^\circ$. For the polar angle, there is a clear trend of decreasing light emission from 0° to $|180^\circ|$. Thus, the bottom hemisphere of the diffuser ball emits less light than the top. At $\theta = 0^\circ$, i.e. the cannula is pointing towards the PMT, a clear reduction of light can be seen in the plot. Given this feature, the trend is not following a sinusoidal curve, so a cubic interpolation has been drawn in the figure (blue line). The azimuthal

deviations of ≈ 10 pC can be observed smaller than the ≈ 20 pC deviations in polar angle. The results for the other tested diffuser balls showed similar trends. Combining the results of figures 3.23 allows to plot a 2D histogram mapped on a spherical surface as shown in figure 3.24. The underlying MATLAB function to do so is a modified version of [73]. Visible are two opposing hemispheres of the diffuser ball. The coordinate system in the left lower corner gives an indication of the orientation in xyz . The pC values have been normalized to one for the sake of clarity. In figure 3.24(a) one can see the decreased emission on top given the entry of the cannula. Figure 3.24(b) shows the plot upside down and rotated for 180° around the z axis. The illustration of the lower emission at the bottom of the diffuser ball compared to the top is eminent.

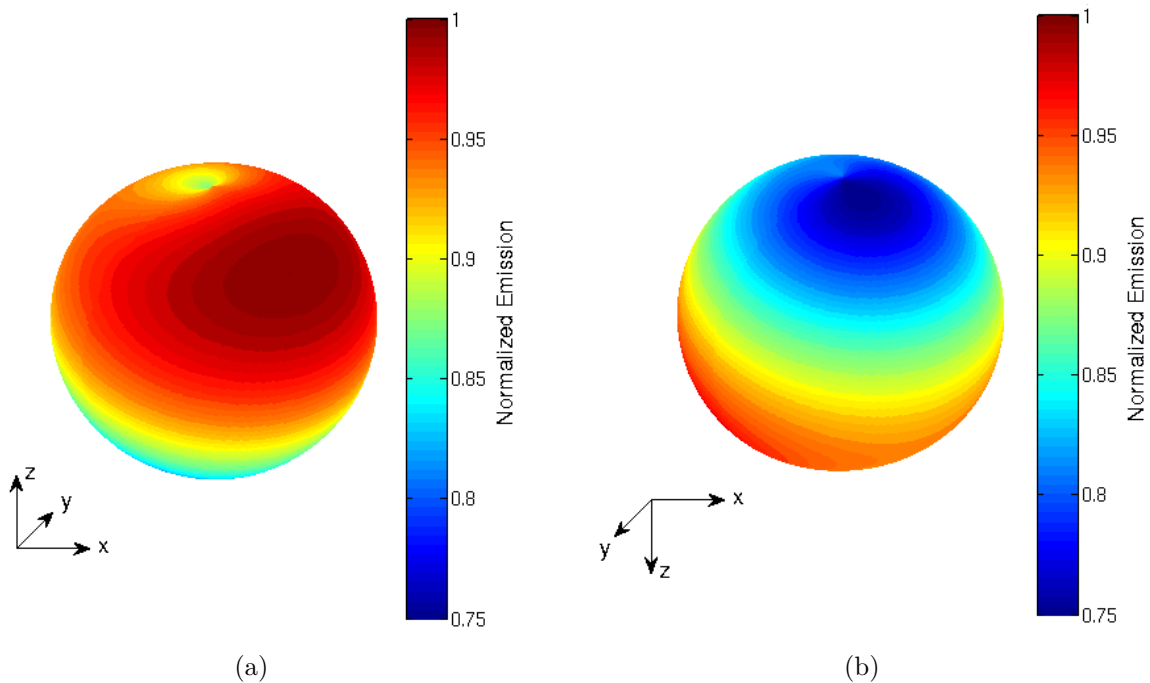


Figure 3.24: Emission profile of a diffuser ball, normalized to the maximum. (a) “Upper” hemisphere of the diffuser ball, orientation indicated by the coordinate system in the lower left corner. At the top a decrease of emission intensity is visible due to the entry of the fiber cannula; (b) An upside down view of (a), additionally rotated for 180° around the z axis. There is a 25% reduction in intensity on the lower hemisphere compared to the upper hemisphere. That clear difference determined the orientation of the diffuser balls installed in the muon veto.

Given this intensity gradient and the PMT pattern in the muon veto, the best amount and orientation of the diffuser balls in the tank are four diffuser balls in 90° angular distance oriented such, that their cannula is pointing towards the center of the tank. In order to guarantee the global calibration with this orientation, a

GEANT4 simulation was performed to see if the diffusively emitted light of four diffuser balls can reach all PMTs. The diffuser balls have therefore been implemented in the muon veto Monte Carlo code introduced in section 3.2.4 by adding them in the `...DetectorConstruction` class. Figure 3.25 shows the geometrical implementation of the diffuser balls as physics volumes in GEANT4 code. To simplify installation, the diffuser balls were placed in proximity to the second row of horizontal beams of the support structure in 6.080 m height. In an isometric view (figure 3.25(a)) they are visible as white spheres located directly below the beams. The other shown items are the cryostat, the umbilical pipe and the muon veto PMTs. A projection in top view in figure 3.25(b) shows the numbering of the four positions with position 1 pointing towards the water tank door.

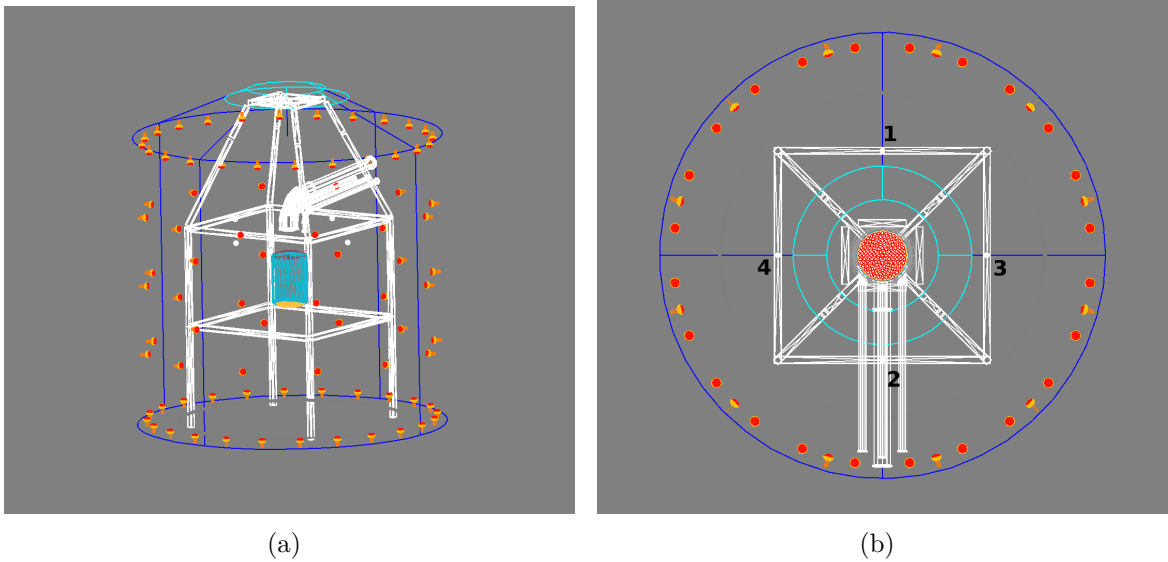


Figure 3.25: Geometrical implementations of the diffuser balls in GEANT4. (a) Isometric view of the muon veto geometry implementation. Tank, support structure, umbilical pipe, cryostat and TPCs are displayed wire-framed. The diffuser balls are located right below the upper horizontal bar of the support structure; (b) Top view. Four diffuser ball positions allow illumination of every quadrant of the water tank.

In the simulation the diffuser balls were used as particle source, shooting optical photons of 470 nm wavelength in random directions. In total per simulation, 10^6 rays were simulated containing 1000 photons each. Figure 3.26(a) shows the number of PMT Hits as blue histogram versus the muon veto PMTs as a result from this simulation. In this simulation the diffuser balls have been placed directly *below* the horizontal support structure beam. The axis PMT ID# is ordered according to the ordering system in the XENON1T Monte Carlo code. All four diffuser balls have been used as light source.

Muon veto PMTs of the top ring have ID numbers 243 – 266, PMTs of the bottom ring 267 – 290 and from bottom to top: first lateral ring 291 – 302, second lateral ring 303 – 314 and for the third ring 315 – 326. The red lines in the figure help to differentiate the PMT rings. The higher mean plateau of the top PMTs compared to the bottom PMT ring correspond to the diffuser ball position in z (which is at 6.060 m and thus higher than the center). The merlon shaped profile is a symmetric pattern resulting from different PMTs being shadowed by the beams of the support structure. The maximum factor between most and least often hit PMTs is 2.3. A similar simulation with the diffuser balls being located directly above the support structure beam resulted in a factor of 2.6. Thus the placement below the beam is preferred.

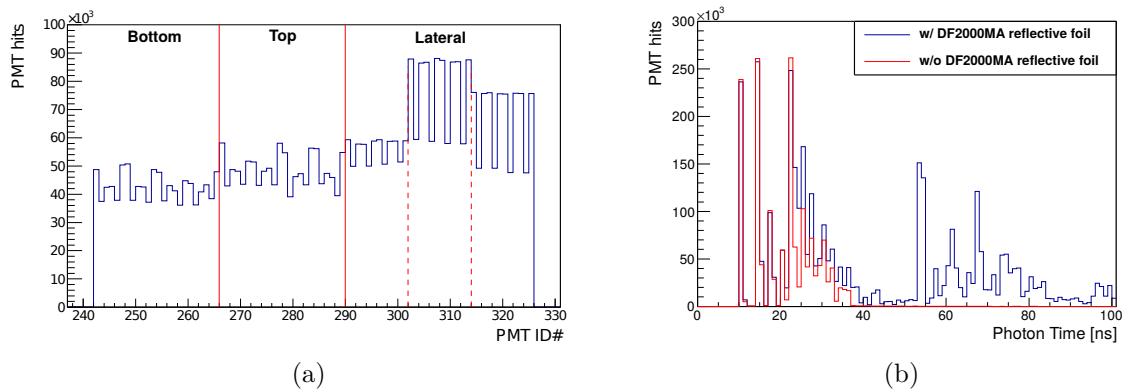


Figure 3.26: (a) Simulated PMT hits versus the PMT ID for illumination with four diffuser balls. All PMTs can be illuminated with the diffuser balls. Plateau height and the merlon shape result from the water tank geometry and shadowing of certain PMTs by support structure beams and cryostat. The factor between most and least often hit PMTs is 2.3.; (b) Simulated PMT hits versus photon lifetime from the same simulation. The observed times corresponds to path lengths considerations inside the water tank. Enabling the reflective properties of the DF2000MA foil in the water tank (blue histogram) allows for multiple reflections and leads to higher photon times.

Figure 3.26(b) shows a histogram of the times it takes for the photons to reach the PMTs. It starts at $t = 0$ when emitted from the diffuser ball. The light takes ≈ 10 ns to reach the closest lateral PMTs, visible by three sharp peaks from 10 ns to 20 ns. Later other PMTs are reached until 40 ns. Enabling (blue histogram) and disabling (red histogram) the reflectance of the DF2000MA foil in the simulation leads to the appearance or disappearance of several peaks due to reflection between the water tank walls. Those range up to 300 ns (not shown), before absorption in water eliminated the residual photons. Since the photon lifetime has direct influence on the detection

efficiency of the muon veto, this result expresses the importance of the understanding and a precise measurement of the DF2000MA foil, which is discussed in detail in section 3.3.

3.6.3 Commissioning of the calibration system

All calibration system hardware has been mounted during the major installation of the muon veto PMTs in November 2014. In the following, until inauguration of XENON1T in November 2015, the corresponding softwares and procedures have been finalized. As of now, a weekly calibration of all PMTs with the individual and the diffuser ball system is performed weekly. The global calibration scheme is shown in figure 3.27.

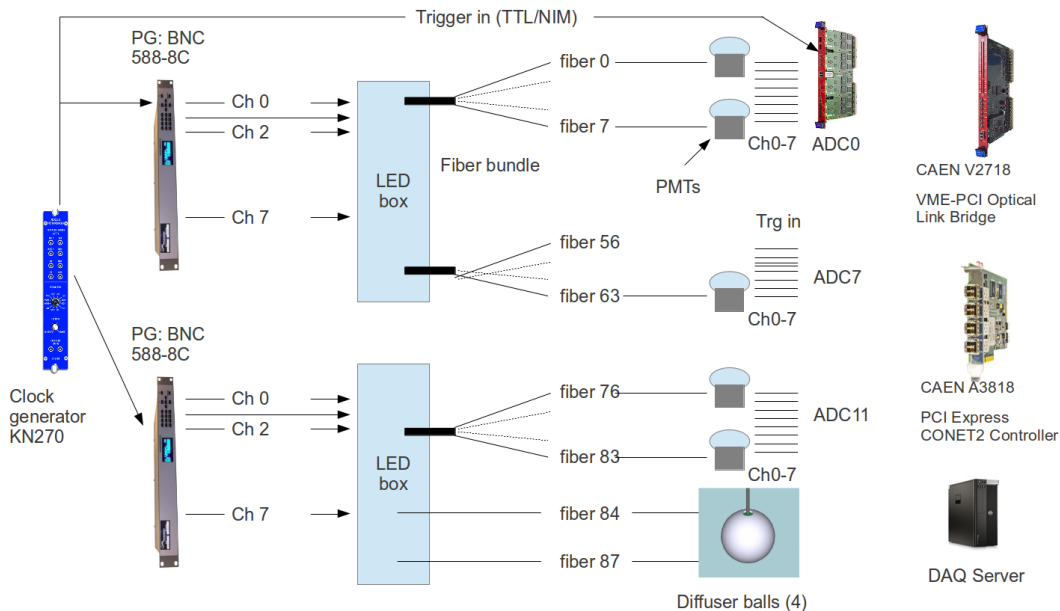


Figure 3.27: Calibration setup of the XENON1T muon veto system.

Two BNC 588-8C pulse generators, each providing eight controllable output channels, provide the voltage signal for in total 16 LED boxes. Twelve boxes for the individual calibration fiber bundles for PMT columns *A* to *L*, the other four boxes each provide light for one diffuser ball. The pulse generator settings are controlled via RS-232 using its own command set. XENON1T shifters can set the pulse generators to the desired calibration mode by executing automatized scripts containing corresponding commands via the XENON1T DAQ Control Page. As an example, a snippet from the command

script initializing one pulse generator (called pulser 0) and setting up the channel 1 for individual calibration of PMT column A is as follows:

```

1  # pulser 0
2  :display:enable           # Switch on display
3  :display:brightness 1    # and adjust brightness
4  :pulse0:period 0.01      # Set frequency to f = 100 Hz
5  :pulse0:mode norm        # Continuous output mode
6  :pulse0:trigger:mode dis # Disable external trigger
7  :pulse0:ic1:mode int     # Enable internal system clock
8  :pulse0:ocl T0          # Set clock output to defined 1/f
9  # channel 1
10 :pulse1:width 0.00000009 # Set pulse width to w = 90 ns
11 :pulse1:delay 7e-8       # Pulse position delayed for 70 ns
12 :pulse1:sync T0         # Set time reference to period 1/f
13 :pulse1:output:mode adj  # Set adjustable voltage output mode
14 :pulse1:pol norm        # Set normal polarity (active high)
15 :pulse1:output:ampl 3.70 # Set pulse amplitude U_LED = 3.70 V
16 :pulse1:cmode norm      # Select output pattern
17 :pulse1:state on        # Enables output

```

Comments are displayed in green after the individual commands. Important are the commands `:pulse0:period`, `:pulse1:width` and `:pulse1:output:ampl`, corresponding to frequency f , pulse width w and amplitude U_{LED} of the rectangular pulse. The values for individual and diffuser ball calibration are $f = 100$ Hz and $w = 90$ ns. Amplitude $U_{LED,1} = 3.70$ V differs for the individual calibration from $U_{LED,2} = 4.2$ V for the diffuser ball LED. During calibration, the digitized PMT signals are saved on the DAQ server and afterwards in the runs database.

As an example from the commissioning of the muon veto calibration system, figure 3.28(a) shows a gain measurement of all PMTs of column H for the individual PMT calibration. The seven different colors correspond to the seven PMTs of this column. The legend shows their serial numbers. The mean charge of the SPE peak in all PMTs is $\langle \mu_{SPE} \rangle = (0.93 \pm 0.09)$ pC. Applying equation (3.29) leads to a mean gain of $\langle g \rangle = (5.8 \pm 0.5) \cdot 10^6$, which is in agreement with the desired equalized gain value of $6 \cdot 10^6$ as described in section 3.5.1. The result of a diffuser ball calibration of all PMTs in parallel is shown in figure 3.28(b). The x axis represents the position of the PMTs in the water tank, ordered by columns and then by height within one column. For illustration the column identifiers $A - L$ have been added to the plot. The y axis represents the gain g in 10^6 . The color axis represents the number of hits. The pedestal was removed in this plot for clarity. A projection to the y axis for one certain PMT would lead to a SPE spectrum. A mean gain of $\langle g \rangle = (6.2 \pm 0.4) \cdot 10^6$ has been obtained

in this calibration run, again in agreement with the desired value. One outlier is PMT 41, which has a significantly higher gain than during the series tests. Therefore, its voltage was adjusted accordingly for future measurements. The low rates of column I were not a PMT issue but a DAQ issue. It turned out that the DAQ board used for this channel (serial number 853) had to be replaced by a spare one.

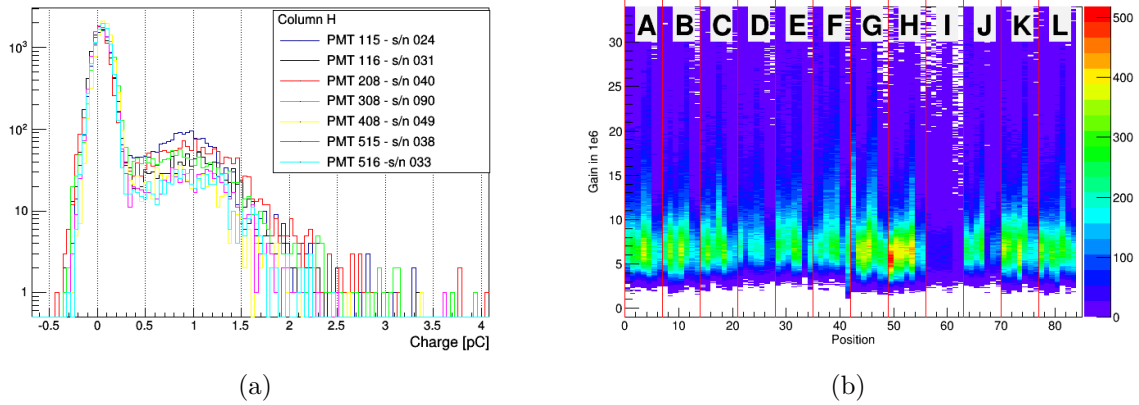


Figure 3.28: Data obtained with both muon veto PMT calibration systems. (a) Single photoelectron spectra for seven PMTs grouped in column H . The mean gain can be calculated as $\langle g \rangle = (5.8 \pm 0.5) \cdot 10^6$, being in agreement with the desired value $6 \cdot 10^6$; (b) Gain spectra of all muon veto PMTs obtained with a diffuser ball illumination, sorted for their corresponding columns $A - L$. The mean gain is $\langle g \rangle = (6.2 \pm 0.4) \cdot 10^6$ being also in agreement with desired value. PMT 41 was identified to have a higher gain than expected. An ADC problem on column I led to lower counting values for those PMTs in this run.

3.6.4 Muon veto calibration

Both calibration systems are used for regularly scheduled gain and counting rate calibration runs. Figure 3.29(a) shows exemplarily a summary of gain calibration runs from February 2017 until December 2017. The shown data points represent the average values of gain measurements of all 84 PMTs in the muon veto. Individual fiber calibrations are shown in black boxes, diffuser ball calibrations in red circles. The larger errorbars on the diffuser ball data points can be explained by the different distance between diffuser balls as light source to the individual PMTs, leading to higher deviations in the individual gain measurements. The measured average gain is between $6.6 \cdot 10^6$ and $6.9 \cdot 10^6$. A rise of the gain over the shown time period is evident and can be modeled by a linear fit with a gain rise of $(0.18 \pm 0.05) \cdot 10^6 \text{ a}^{-1}$ for the individual fibers and $(0.23 \pm 0.11) \cdot 10^6 \text{ a}^{-1}$ for the diffuser balls. Similar observations

have been made during the water submersion tests described in section 3.5.2 (mean gain rise of $(2.0 \pm 0.7) \cdot 10^6 \text{ a}^{-1}$) and a smaller submersion test in Mainz (gain rise of $(0.91 \pm 0.07) \cdot 10^6 \text{ a}^{-1}$). No gain rise was observed for measurements in air. The effect is caused by the permanent exposure of the PMTs to Cherenkov light. As stated in [91], this can affect the first dynode stages, leading to rising gain values with time.

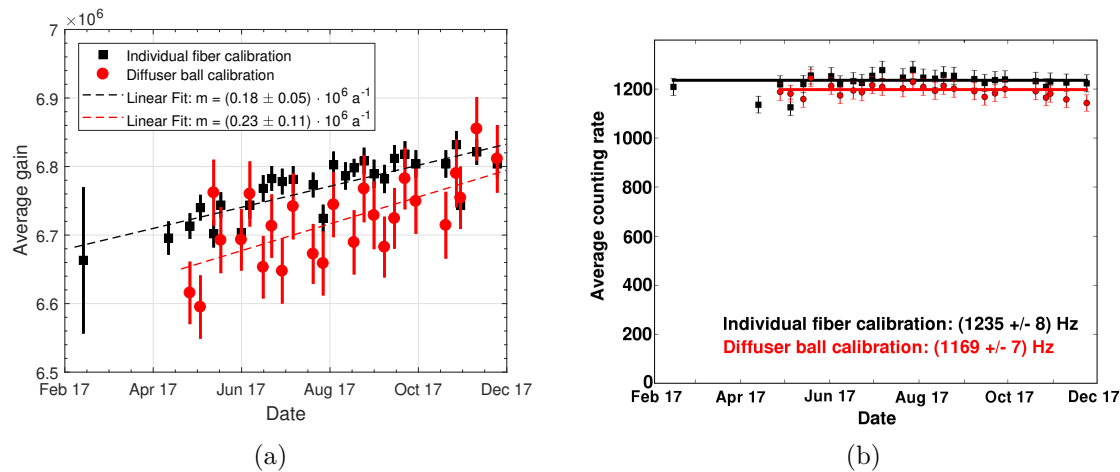


Figure 3.29: Long term calibration results of all muon veto PMTs. (a) Gain calibration done with individual fibers (black boxes) and diffuser balls (red circles). Both calibration sources show a rise of the mean gain over time, originating from effects on the first dynode stages under permanent exposure of Cherenkov light (Fits indicated by the dashed lines); (b) The average counting rate at the 1 PE level measured with individual fibers (black boxes) and diffuser balls (red circles). The counting rate remained stable for the full observation period.

Figure 3.29(b) shows a long term stability plot of the PMTs counting rate. The term counting rate is chosen, since dark rate would be inappropriate given the permanent exposure of the PMTs to Cherenkov light in the water tank. The values represent the rate at 1 PE level, once calculated with the individual fibers (black boxes) and once with the diffuser balls (red circles). In both cases, the rate remained stable for the full observation period and has, after have not been exposed to daylight since months, settled in to a value comparable to the series test dark rate measurements (compare section 3.5.1).

3.7 Muon veto data analysis

3.7.1 PAX processed data and the muon veto

Although PAX was produced to analyze TPC data, it can also be used to analyze data obtained with the muon veto system. In the following subsection it is described how to do analysis with those PAX processed muon veto datasets.

The muon veto TreeMaker

It is important to know that PAX sorts events of the muon veto (correctly) in different event classes than events in the TPC (compare section 2.2.5). There are no `S1`, `S2`, `Interaction` or `Peaks` objects in processed muon veto data, as opposed to TPC data. The muon veto events are saved as `Hit` objects in the processed root file and therefore have to be extracted in a different way than processed TPC data. A `TreeMaker` class has been written in the scope of this thesis to allow analysis of muon veto data. Since it is a contribution to the public HAX repository it is listed in appendix A.

Version 1.1.1 of the `MuonVetoTreeMaker`, extracts the following subset of parameters from PAX processed muon veto data:

- `PMTs`: PMT Channel which got hit in the event
- `Hit_area`: Area of peak in each PMT channel [PE]
- `Hit_height`: Height of peak in each PMT channel [PE/Sa] (Sa = samples)
- `Hit_left`: Left boundary of peak in each PMT channel which got hit in the event [Sa]
- `Hit_center`: Center of signal in each PMT channel [ns]
- `Hit_right`: Right boundary of peak in each PMT channel which got hit in the event [Sa]
- `Hit_noise_sigma`: Standard deviation of noise level of pulse in which the hit was found [PE/Sa]
- `tStart`: Start time of event (Unix time)
- `tStop`: Stop time of event (Unix time)

All analysis results of muon veto related data presented in this section have been performed by using those variables or values derived from it.

3.7.2 Muon track reconstruction

After its commissioning phase the XENON1T Muon Veto (MV) system is operational, provides its trigger signal to the TPC DAQ for analysis and is itself ready for dedicated analyses. One major question was if it is possible not only to detect muons crossing the tank, but also to reconstruct their path given the signals of the 84 Muon Veto PMTs arranged in ring patterns at different heights of the detector. In this section, a first method is presented of how to reconstruct these tracks using a so-called *timeline* fit given the timing informations of the PMTs.

Before starting to reconstruct muon tracks it is useful to estimate the number of muons traversing the muon veto per unit time. According to [29] the residual muon flux at LNGS results, given the geometrical acceptance of the water tank, in an expected muon trigger rate in the muon veto of $R_\mu = 0.04 \text{ Hz} = 3456 \text{ d}^{-1} = 144 \text{ h}^{-1}$ (see also section 3.2.4). For the muon track reconstruction analysis, data in the time range from October 13th to November 20th 2016 was used, with a total effective exposure of ≈ 17 live-days (≈ 410 live-hours). This corresponds to $\approx 680\,000$ events, registered by the muon veto. One can expect a total of $410 \text{ h} \cdot 144 \text{ h}^{-1} \approx 59\,000$ muons within this dataset, i.e. about 8.7% of the observed events.

Track reconstruction algorithm

A muon crossing the water tank generates Cherenkov radiation in the water along its track and leaves a signal pattern in the PMT array, which moves sequentially in the direction of the muon passage. Reconstruction of the geometrical track of this muon is therefore possible by using the time information of when single PMTs have been hit by the Cherenkov light. This approach to reconstruct muon tracks is called *timeline* fit and has been commonly used in several neutrino telescopes like AMANDA/IceCube [12] at the south pole, ANTARES [11] in the Mediterranean Sea, or neutrino detectors such as Borexino [50] at LNGS.

For the track reconstruction a fit model has to be chosen which predicts at which time a PMT detects a Cherenkov photon of a muon crossing the tank, given the Cherenkov angle in water. First, according to [17], the mean energy of muons arriving at LNGS is $\approx 270 \text{ GeV}$ which is much higher than their rest mass of $m_\mu = 105.7 \text{ MeV}/c^2$. The muons therefore can be considered to be highly relativistic and thus $\beta = 1$. Given equation (3.3) and the refractive index of water ($n = 1.333$) one can calculate a constant Cherenkov angle to be

$$\theta_c = 41.4^\circ. \quad (3.31)$$

Figure 3.30 illustrates how the fit function is modeled by geometrical considerations. A cross-section of the water tank is shown. A muon crosses the tank on the track along the direction \hat{u} . The geometrical information of the track consists of five parameters:

- The three coordinates x, y, z of an entry point E_0 or an exit point E_1 on the water tank respectively.
- Two angles of a spherical coordinate system: elevation angle ϑ and azimuth angle φ expressing the direction.

x, y, z, ϑ and φ are defined according to the XENON1T TPC coordinate system (see section 4.1.2) and their unit vector points towards the direction, where the muon is coming from. φ is going anti-clockwise, starting from the meridian ($\varphi = 0^\circ$), facing the water tank door. The direction of the muon \hat{u} , opposing the coordinate system unit vector, is then given by

$$\hat{u} = - \begin{pmatrix} \cos \vartheta \cdot \cos \varphi \\ \cos \vartheta \cdot \sin \varphi \\ \sin \vartheta \end{pmatrix}, \quad (3.32)$$

The convention of using the elevation angle ϑ , i.e., 0° on the (x, y) plane, is preferred to the polar angle θ convention, i.e., 0° on the z axis, since most muons arrive from the top of the water tank than from the side. Thus, the pole, where $\theta = 0$ and therefore φ would become arbitrary, can be avoided to ensure a better fit result.

Along the track, Cherenkov photons are emitted at the angle θ_c relative to \hat{u} . After the muon enters the tank at point E_0 at time t_0 , the time it takes a Cherenkov photon to reach a PMT at position \vec{r}_i at the speed of light in water is equal to the time the muon needs to reach point R'' at the vacuum speed of light c . The length of the line segment $[E_0R']$ is the projection of the vector $(\vec{r}_i - \vec{E}_0)$ on the direction \hat{u} :

$$\overline{E_0R'} \equiv r'_0 = \hat{u} \cdot (\vec{r}_i - \vec{E}_0). \quad (3.33)$$

With

$$\overline{R'R''} = d \cdot \tan \theta_c \quad (3.34)$$

and

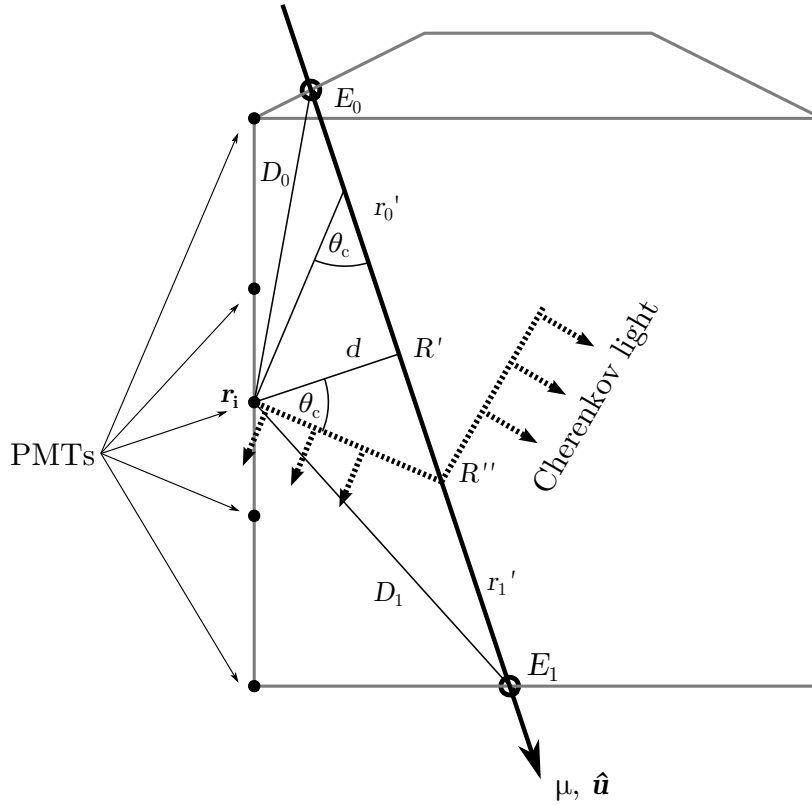


Figure 3.30: Geometrical considerations to model the muon track reconstruction fit function. Cherenkov radiation gets emitted along a track in the direction \hat{u} with an angle of θ_c . The time it takes for the Cherenkov light to reach each single PMT at position r_i can be geometrically expressed by a function of six parameters: $t_0, E_{0/1}^x, E_{0/1}^y, E_{0/1}^z, \vartheta$ and φ .

$$d = \sqrt{D_0^2 - r_0'^2} \quad (3.35)$$

one can find the time needed to reach a certain PMT at position \vec{r}_i to be

$$f_0 = t_0 + \frac{\hat{u} \cdot (\vec{r}_i - \vec{E}_0) + d \cdot \tan(\theta_c)}{c} = t_0 + \frac{\hat{u} \cdot (\vec{r}_i - \vec{E}_0) + \sqrt{D_0^2 - r_0'^2} \cdot \tan(\theta_c)}{c}, \quad (3.36)$$

with D_0 being the norm of vector $(\vec{r}_i - \vec{E}_0)$, i.e., the distance between entry point and PMT. An analogous statement can be made relative to the exit point E_1 . Here, one has to subtract $\overline{R'R''}$ from the projection $\overline{R'E_1} = r_1' = \hat{u} \cdot (\vec{E}_1 - \vec{r}_i)$, which yields

$$f_1 = t_0 + \frac{\hat{u} \cdot (\vec{E}_1 - \vec{r}_i) - d \cdot \tan(\theta_c)}{c} = t_0 + \frac{\hat{u} \cdot (\vec{E}_1 - \vec{r}_i) - \sqrt{D_1^2 - r_1'^2} \cdot \tan(\theta_c)}{c}, \quad (3.37)$$

where D_1 is now the norm of vector $(\vec{E}_1 - \vec{r}_i)$. The possible prolongation of light travel times by reflection of Cherenkov photons on the reflective foil at the water tank surface is here neglected. Given the dimensions of the water tank, the maximum time a photon would take to travel the longest possible distance in the 10 m high and 9.6 m wide cylindrical tank is $t_{\max} = \sqrt{10^2 + 9.6^2}/(0.225 \text{ ns/cm}) = 61.6 \text{ ns}$. To suppress information resulting from scattered or reflected photons, only PMT hits within a window of 7 Sa (70 ns) are considered. With equations (3.36) and (3.37) there are two possible fit functions to model the muon veto data, each depending on six fit parameters: an offset time t_0 in ns, the three coordinates of entry or exit point $E_{0/1}^x, E_{0/1}^y, E_{0/1}^z$ in m and the two direction angles ϑ and φ . Both functions are in the following used to reconstruct muon tracks in the XENON1T muon veto system.

To estimate starting values for each of the fit parameters, the following strategies have been chosen:

- \hat{t}_0 : The earliest observed `Hit_left` value within all PMTs of the event, which is closest to, but larger than the fixed position of the peak on the waveform minus one sample ($12200 \text{ ns} - 10 \text{ ns} = 12190 \text{ ns}$). This is, given the resolution of 10 ns/Sa , the earliest possible, valid point in time where an event can be observed, given a 1 Sa uncertainty.
- \hat{E}_0 : The coordinates of the centroid position of all PMTs, which see the first light, neglecting the amplitudes of the corresponding signals. It is likely the one closest to the entry point of the muon. This is a common choice as for [11],[12],[50].
- \hat{E}_1 : Two estimation strategies have been tried to estimate the starting parameter for the muon exit point:
 - Method 1: The coordinates of the centroid position of the PMTs on the bottom ring which sees the first light. Assuming (conservatively) that a major part of the muons arrive from top and might cross thus the bottom surface of the tank.
 - Method 2: The coordinates of the centroid position of the PMTs (within all PMTs) which sees the light last within a duration of t_{\max} after the first PMTs have seen light (\hat{t}_0).
- $\hat{\vartheta}$: The calculated elevation angle of the line which goes through \hat{E}_0 and \hat{E}_1 .
- $\hat{\varphi}$: The calculated azimuth angle of the line which goes through \hat{E}_0 and \hat{E}_1 .

Event selection and cuts on the data

Not every triggered event in the MV is from a muon passage through the tank or from the passage of secondaries. In fact most of the collected events are not. Figure 3.31 show waveforms of two examples which represent an event triggered by a muon and an event triggered by random noise on enough PMTs to match the coincidence requirement (in this dataset $N = 5$, see section 3.3.1).

The waveforms themselves are visible in the upper halves of each plot. In the lower half the information is shown of how many PMTs contributed to the waveform, indicated as red or blue dots with their size scaled with the area of the individual PMT signal. The color of the circles indicates their height relative to the highest amplitude from high (red) to low (blue). The plots are a modified output of the PAX waveform plotting routine. Since PAX is a tool for TPC data and the XENON1T TPC consists of 247 PMTs the “PMT channel” is scaled up to 250 and fills accordingly for muon veto events only the first 84 channels representing the muon veto PMTs. PAX does not provide a waveform plotting tool for muon veto data yet. The track reconstruction fit model has to be capable of distinguishing between muon and shower events, as well as noise events or events originating from radioactivity on the other side given its waveform information to select only those events resulting from muon passages. In a first approach every event is considered as a possible muon event and gets later, during application of the fit procedure, treated either as muon event with a successive track reconstruction or else is rejected as a non-muon event. To achieve this, events have to survive two cuts:

- **tminmask** cut: As described above, to ensure that possible reflections inside the tank are not considered, one has to select all PMT signals of in an event within a 70 ns time window.
- **tmask** cut: If the number of PMT signals surviving the **tminmask** cut is less than the number of fit parameters, the event is rejected.

Further, each event has to survive a list of data quality cuts, which result mainly from the possibility to fit the data in a reasonable way with the fit functions:

- **inf_or_nan** cut: If an event contains NaN (not a number) or inf (infinity) entries, resulting from exceptions during the processing, the event is corrupted and sorted out from analysis.
- **bad_fit** cut: If the fit routine needs more than 10000 iterations to find a solution, the event is sorted out from analysis.

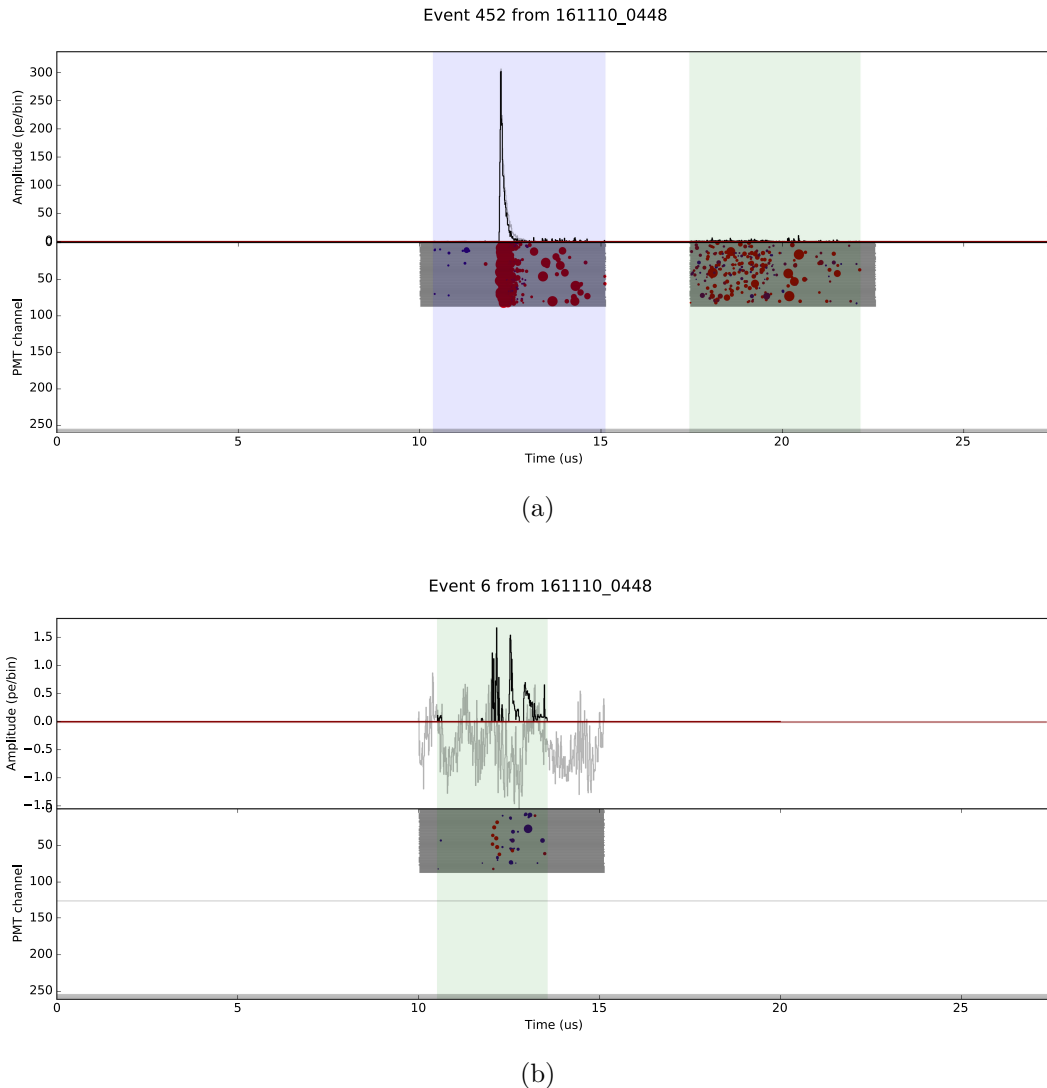


Figure 3.31: Examples for summed waveforms of two muon veto events. The waveforms visible in the upper half of each plot, the channels of which PMTs have seen light in that event indicated as red or blue circles in the lower half of each event, with their size scaled with the area of the individual signal. (a) A muon event. The waveform shows a big peak with an amplitude of several hundreds of PE per bin at a fixed position of 12200 ns. The lower half of the plot indicates that every PMT has contributed to the trigger of that event. (b) Not a muon event. For this event noise appeared at the same time in enough PMT channels to satisfy the coincidence condition. One can see no clear peak, but typical noise oscillations, a low amplitude and only a few PMTs contributed to the summed waveform as only a few circles are visible in the lower half of the plot.

- `bad_fit_chi2` cut: If the reduced χ^2 value of the fit is larger than 5, the event is neglected. The corresponding number of degrees of freedom is the number of fit parameters ($n_p = 6$) subtracted from the number of PMTs contributing to the

event. For an event, where all 84 PMTs did contribute, the number of degrees of freedom is 78.

Example of a single event track reconstruction

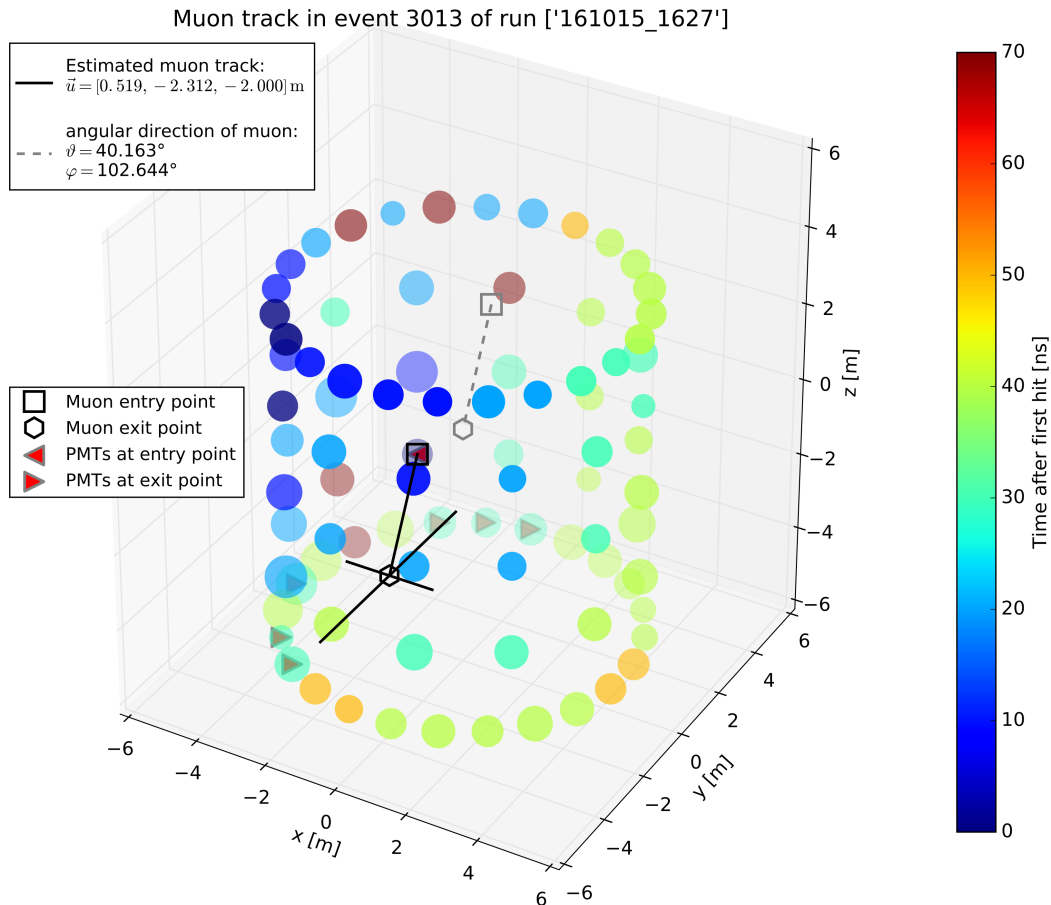


Figure 3.32: Event display of a muon passage through the muon veto system and start value estimation for the reconstruction. The dots represent in color the timing of the PMTs and in size the scaled area of their pulses. The black square and hexagon show the position of estimated entry and exit point of the muon (\hat{E}_0, \hat{E}_1) for method 1. The starting values for the angles $\hat{\vartheta}$ and $\hat{\varphi}$ can be calculated with a coordinate system transformation from Cartesian to spherical coordinates after translation of the vector $(\hat{E}_1 - \hat{E}_0)$ to the origin.

Figure 3.32 shows the event display of a muon event of the muon veto dataset 161015_1627 which is one included in the 410 live-hours of selected data for this analysis. The plot shows the 84 PMTs as they are positioned in the muon veto water tank. The color of the dots expresses the time information of the PMTs, the size of the

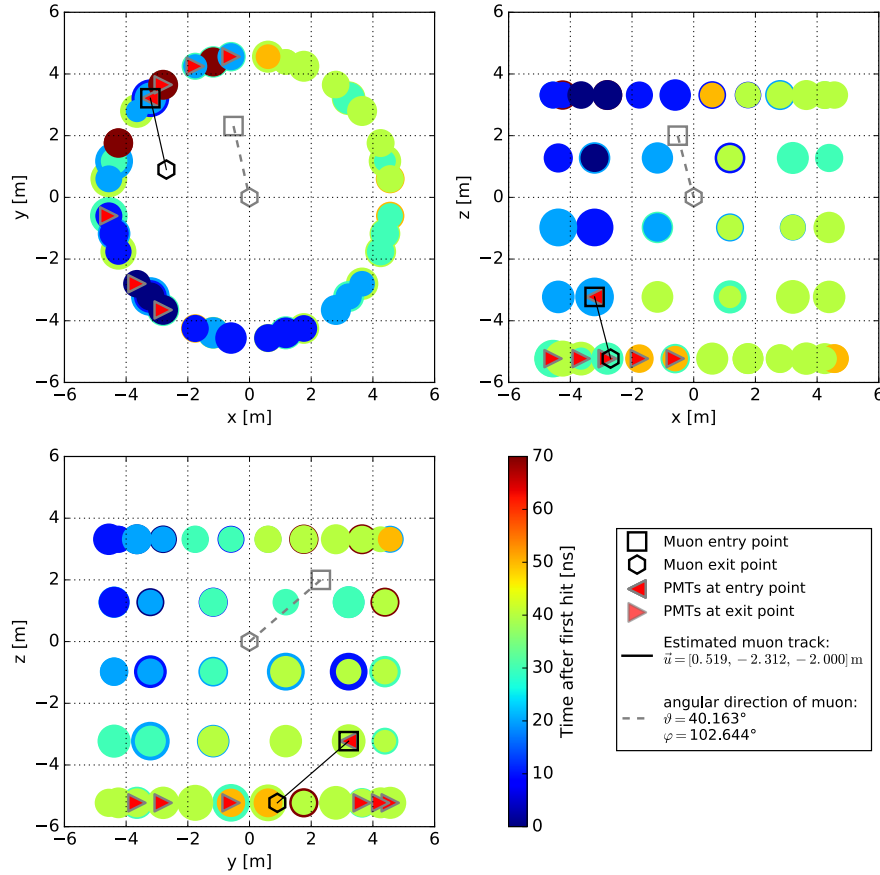


Figure 3.33: Event display of a muon passage through the muon veto system projection to the origin planes. The estimation of start values for the reconstruction fit is illustrated as in figure 3.32.

dots scales with the area of the PMT peak normalized to the lowest area. The black square shows the estimated start value for the entry point \hat{E}_0 of the muon, the hexagon shows the estimated start value for \hat{E}_1 (obtained with method 1). The direct line in between is displayed in black and represents the vector $\left(\hat{E}_1 - \hat{E}_0\right)$. The gray markers and line are copies of the black markers and line with $\left(\hat{E}_1 - \hat{E}_0\right)$ translated to the origin to calculate the start values of the angles $\hat{\vartheta}$ and $\hat{\varphi}$ by converting the Cartesian coordinates to spherical coordinates. The origin is the center of the TPC in xy plane with $z = 0$ at the height of the gate mesh (as defined in sections 3.2 and 4). To have an additional view, figure 3.33 shows the projection to the xy , xz and yz plane. Those PMTs, which positions contribute to \hat{E}_0 and \hat{E}_1 are shown as red triangles pointing left or right. In this example a few PMTs were contributing to the exit point centroid \hat{E}_1 . Table 3.4 shows an overview of the estimated starting parameters for methods 1 and 2 for this event:

Start values for fit parameters - event 3013 of dataset 161015_1627		
Parameter	Start value (method 1)	Start value (method 2)
\hat{t}_0	12200 ns	12200 ns
\hat{E}_0	[-3.21 m, 3.21 m, -3.23 m]	[-3.21 m, 3.21 m, -3.23 m]
\hat{E}_1	[-2.70 m, -0.90 m, -5.23 m]	[1.47 m, -0.85 m, -3.52 m]
$\hat{\vartheta}$	40.16°	2.69°
$\hat{\varphi}$	102.64°	139.07°
\hat{u}	[0.52 m, -2.31 m, -2.00 m]	[4.69 m, -4.06 m, -0.29 m]

Table 3.4: Estimation of the start values for the parameters of a single muon track reconstruction fit on the event shown in figure 3.32. The two different methods to estimate \hat{E}_1 can lead to big differences.

For \hat{E}_1 and consequently of $\hat{\vartheta}$, $\hat{\varphi}$ and \hat{u} there are big differences in estimating the start values. The used fit routine is the `optimize.least_squares` function of the `scipy` package of python. It has been chosen since it is accepting easily start values for the fit parameters. Fitting this specific example leads to the fit parameters shown in table 3.5. Here, the f_0 (equation (3.36)) was used, so the fit was relative to E_0 .

Calculated values for fit parameters - event 3013 of dataset 161015_1627		
Parameter	Result value (method 1)	Result value (method 2)
t_0	(12208 ± 33) ns	(12221 ± 98) ns
E_0^x	(-2.443 ± 0.238) m	(-1.513 ± 0.521) m
E_0^y	(-0.640 ± 0.630) m	(1.820 ± 1.378) m
E_0^z	(0.541 ± 0.703) m	(-2.214 ± 1.543) m
ϑ	(-46.33 ± 5.93)°	(-46.33 ± 5.95)°
φ	(69.29 ± 4.98)°	(69.29 ± 4.90)°
χ_{red}^2	1.79	2.05

Table 3.5: Calculated fit values for a muon track reconstruction using f_0 for exit point estimation methods 1 and 2. The values for E_0 is subject of further correction given geometrical definitions (it has to be on the tanks surface). The obtained values with method 2 show a less good fit.

Both fits obtain similar values with a slightly better fit for method 1 given the smaller χ_{red}^2 value. However, the coordinates of E_0 differ significantly, with method 2 leading to larger errors. In addition, the reconstructed parameters are in both cases closer to the initial estimates made with method 1. This is in fact consistent over the full event list and not only in this example. Therefore, in the following, only values obtained with method 1 are presented. Looking at E_0 , it is obvious that the point is

not on the surface of the water tank, but somewhere in its volume. One has to correct this value (also to calculate the exit point E_1) onto the tanks surface. This was done using ray tracing methods following [133]. The equation of the line \vec{s} of the muon track is given by its direction \hat{u} and the vector of the obtained entry point \vec{E}_0

$$\vec{s}(\lambda) = \vec{E}_0 + \lambda \cdot \hat{u}, \quad (3.38)$$

which has to be intersected with the equation of a cylinder with finite length

$$x^2 + y^2 = R^2, z_{\min} < z < z_{\max}, \quad (3.39)$$

simplifying the water tank to be like this by neglecting the conical top part. R represents the water tank radius. Inserting the x and y coordinates of $\vec{s}(\lambda)$ in equation (3.39) leads to a solvable quadratic equation with the solutions $\lambda_{1/2}$. If, for example, the line intersects the tank at its bottom surface the z coordinate of $\vec{s}(\lambda)$ gets smaller z_{\min} . In that case one has to calculate a $\lambda_3 = (z_{\min} - \hat{u}^z) / \vec{E}_0^z$. A similar equation holds for the z_{\max} if the line intersects the tanks top surface or even intersects both: top and bottom surface. Inserting the obtained λ values in equation (3.38) yields the real intersection points \tilde{E}_0 and \tilde{E}_1 . All from now on mentioned E_0 and E_1 will represent the corrected points on the tanks surface. The corrected values in this example are $E_0 = [-3.380 \text{ m}, -3.119 \text{ m}, 3.317 \text{ m}]$ and $E_1 = [-0.496 \text{ m}, 4.511 \text{ m}, -5.227 \text{ m}]$, which indicates that both, entry and exit points, were located on the top respectively bottom cap at radial values close to the radius of the water tank.

After comparing the result values with the estimated ones it is clear that the estimations of the start values for the fit parameters are not very good in either method, but the fit is still able to reconstruct the path for both methods in a consecutive way. A closer look to the fit is illustrated in figure 3.34.

It shows the timing of the PMTs over their sequential ordering 1 – 84, where PMTs 1 – 24 are located at the bottom ring, 25 – 36 at the first PMT ring, 37 – 48 at the second ring, 49 – 60 at the third ring and 61 – 84 at the top ring. This is nicely visible at the sinusoidal shape of the curve with higher frequency in the center given the smaller amount of PMTs on the lateral rings than on bottom and top. The modeled fit values (red squares) describe the data (blue dots) well. The total error on each data value has been estimated to be $1 \text{ Sa} = 10 \text{ ns}$. The residuals of the fit are shown as green diamonds in the lower part of the figure with a mean deviation of $\approx 6 \text{ ns}$. The fit function values are shown in figure 3.35 in the same form as for the event display together with the reconstructed muon path.

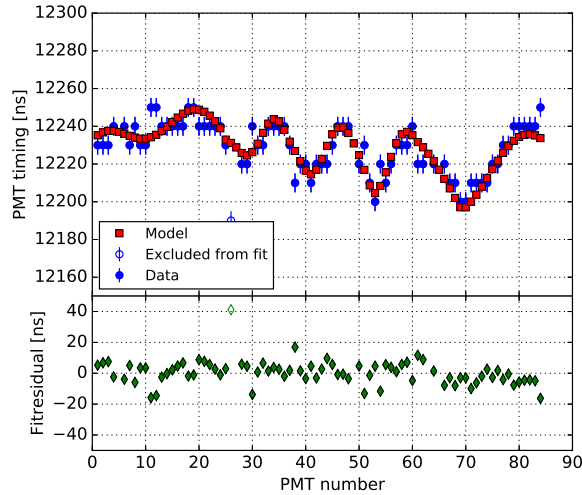


Figure 3.34: Fit residuals of a muon track reconstruction (using method 2 for estimation of muon exit point). The blue dots represent the measured timing of each PMT pulse over the consecutive number of PMTs (in the order bottom ring | 1st ring | 2nd ring | 3rd ring | top ring). Empty blue circles (in this event only for PMT number 26) represent PMTs which did not survive the `tminmask` cut and have not been considered in the fit. The values of the fit function (red squares) are describing the data well ($\chi_{\text{red}}^2 = 1.79$). The mean of residuals is about 6 ns.

As described above, elevation angles ϑ indicate the direction where the muon is coming from. To convert those directions to the opposing direction, corresponding to the muon direction, all events can be transformed according to the fact, that for spherical coordinates $(r, -\vartheta, \varphi) = (r, \vartheta, \varphi + 180^\circ)$. This is the case in the example shown in this figure and allows a comparison to measurements of the angular distribution of muons in the halls of LNGS (see the following subsection). Comparing the transformed angles obtained with the fit function (ϑ, φ) (as displayed in the legend of figure 3.32) to the estimated angles $(\hat{\vartheta}, \hat{\varphi})$ from table 3.4 it can be observed, that the estimation of the elevation angle works better than for the azimuthal angle. This holds also for all events and is understood, since the estimations of the z coordinates of entry and exit point are easier than the x and y coordinate, given the fact that a major part of the muons is expected to come from above. Figure 3.36 shows again a projection of the 3D plot in figure 3.35. The muon crossed the tank almost diagonally.

Several other examples of working and not working single track reconstructions can be found for completeness in appendix B. Those contain successfully reconstructed events at different locations in the water tank (figures B.2-B.4) as well as events, where the fit routine does not converge, gives a bad fit, or was not applied at all, since the event was not triggered by a muon passage (figures B.5-B.7).

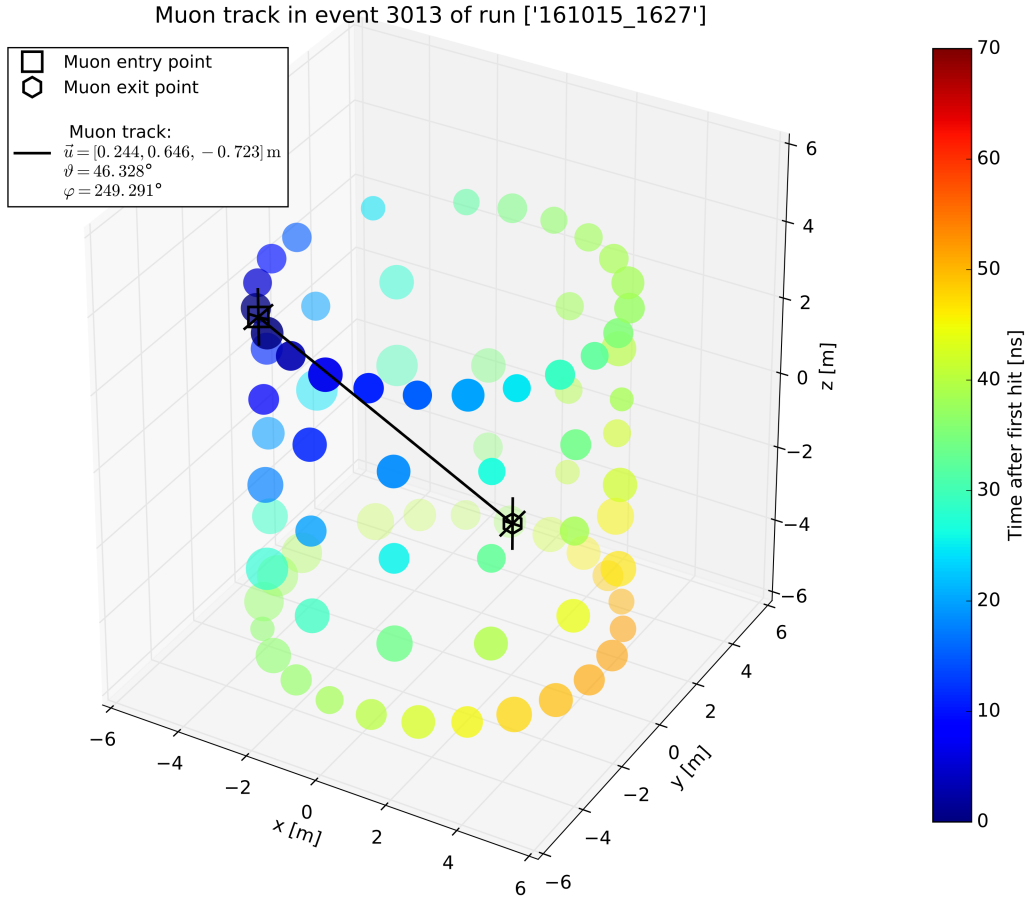


Figure 3.35: Event display of fit function values for a reconstructed muon track. One can see the smooth color change from entry point of muon to exit point. A comparison to the estimated track parameters in figure 3.32 shows that the elevation angle estimation works better than the azimuth angle estimation.

Angular distribution of muons

The reconstruction methods presented in the previous section were applied to the full event list of the above mentioned 410 live-hours of data. All events have been fit with both modeled fit functions, f_0 and f_1 , which reconstruct the track relative to the entry point E_0 or the exit point E_1 , respectively. Table 3.6 shows the number of events surviving all cuts for each fit model.

The rejection and survival ratios of the `tmask` cut, `tminmask` cut and `inf_or_nan` cut depend only on the data and not on the modeling function. Thus their values remain equal regardless applying the fit relative to entry or exit point. The `bad_fit` cut and `bad_fit_chi2` show differences. Fitting all events with f_1 yields ≈ 2000

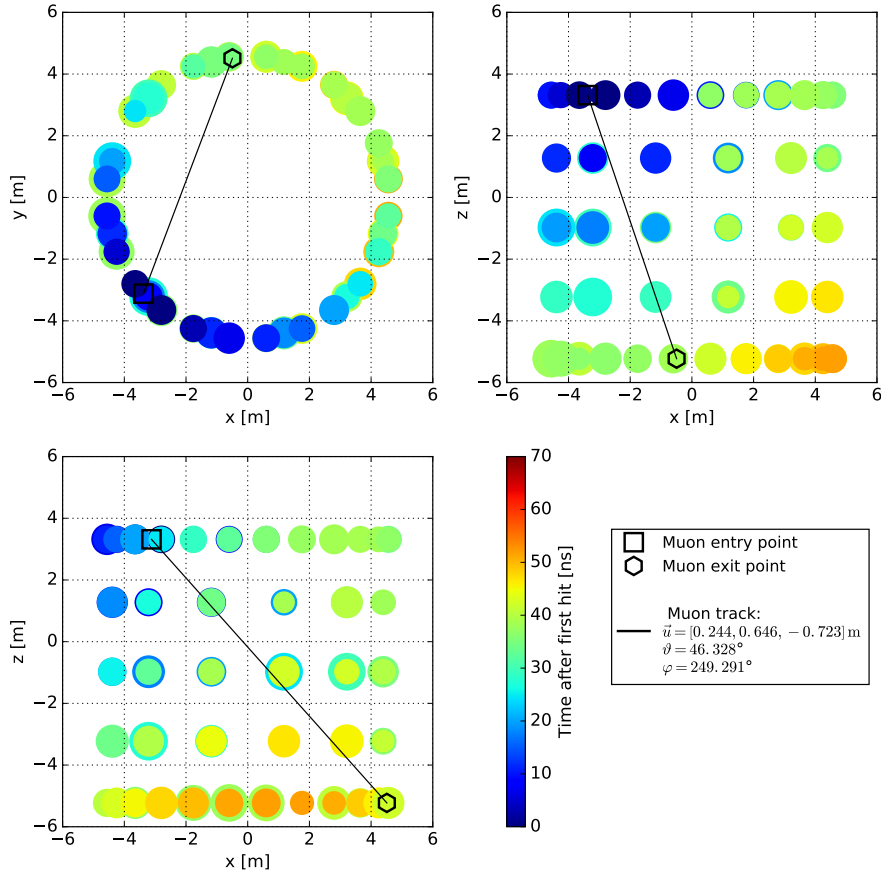


Figure 3.36: Event display of fit function values for a reconstructed muon track as projection to the origin planes. The muon crosses the tank diagonally from top to bottom.

(0.04%) additional good events compared to the f_0 fit. In total one can observe that a major part of the events ($\approx 92 - 93\%$) gets rejected or not considered as good events. Comparing those values to the ones expected and motivated above (a trigger rate of $R_\mu = 0.04$ Hz would lead to ≈ 59000 muons in the data), $\approx 11000 - 13000$ muons are not correctly reconstructed. This corresponds roughly to the cut rejection values of the cuts `inf_or_nan`, `bad_fit` and `bad_fit_chi2`, which are linked to data quality and thus can explain this discrepancy.

Figure 3.37 illustrates a comparison of results yielded with the two possible fit functions (blue and green curves). The red curves are angular distributions of muons at the LNGS underground laboratory from the Monte Carlo code MUSIC [21], as described in section 3.2.4).

To enable a quantitative comparison the ordinate values are normalized to the total number of values for each histogram. Qualitatively one can see that the shape of the distributions do not show clear features at consistent angular values, while angular

Fractional cut rejection and survival for ≈ 410 live-hours of muon veto data		
Cut Rejection	Fit with f_0	Fit with f_1
tmask	85.33 %	85.33 %
tminmask	5.22 %	5.22 %
inf_or_nan	0.39 %	0.39 %
bad_fit	0.20 %	0.27 %
bad_fit_chi2	1.29 %	0.85 %
Fractional sum	92.43 % (557247 events)	92.06 % (555012 events)
Cut Survival	7.57 % (45628 events)	7.94 % (47863 events)
Total	100 % (602875 events)	100 % (602875 events)

Table 3.6: Choosing the muon track reconstruction models to be relative to E_0 or E_1 leads to small differences in the cut rejection with a slightly higher event survival fraction observed for f_1 . The major part (92 – 93 %) of the events gets cut due to not enough PMTs contributing to the event to be fit, which indicates that there was no muon passage through the tank. About 7 – 8 % of the events could be reconstructed and can be considered as muon transit events.

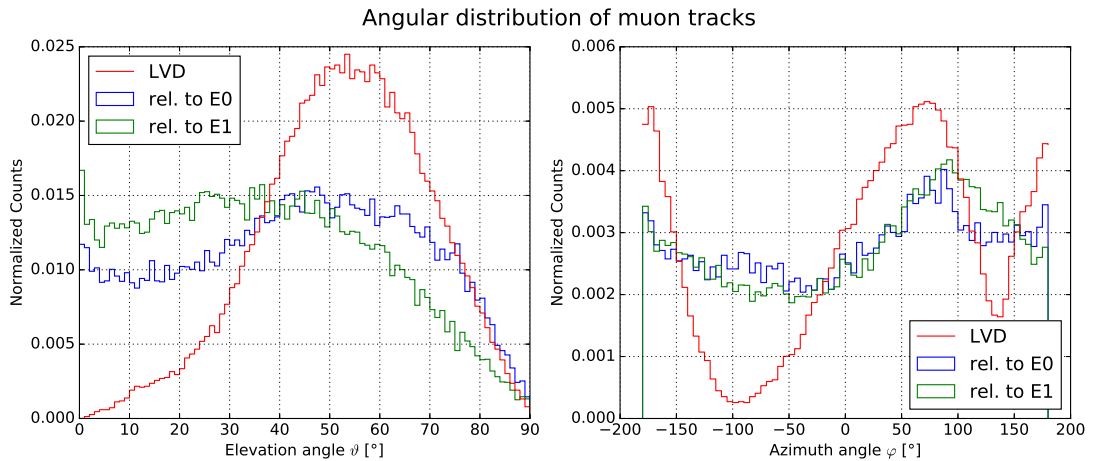


Figure 3.37: Angular distribution of all reconstructed muons in 410 live-hours of data. The blue curves show the distributions of ϑ (left) and φ (right) obtained with the fit function f_0 reconstructing the track relative to the entry point E_0 , the green curve those obtained using f_1 , relative to exit point E_1 . The red curve is the expectation from the MUSIC Monte Carlo program [21]. While both methods suffer from the limited resolution of the muon veto as a track detector, values obtained with f_0 match the expectations better.

values reconstructed with f_0 show a better agreement than the ones of f_1 , which is expected since the estimation of the exit point is less straight-forward. The azimuthal peak at $\varphi \approx 70^\circ$, matches for all curves within $10^\circ - 20^\circ$ which is about twice the size

of the angular uncertainties obtained from the fits (compare table 3.5). The other peak at $|\varphi| = 180^\circ$ corresponds to an increased number of muons, coming through a valley between the two major summits of the Gran Sasso mountain. Also for the elevation angle the curves show maxima in proximity of the expected value. The resolution of the XENON1T muon veto as a muon track detector is limited by the five discrete height values of the PMT rings. The area between blue and red curve left of $\vartheta = 36^\circ$, is about equal to the area between both curves for $\vartheta > 36^\circ$, which appears to suggest, that a increased number of PMTs at different heights would increase the resolution and would lead to a better match of both curves. In addition, effects like reflection of light by the foil, as well as by the water surface can lead to the observed discrepancies.

Comparison of the reconstruction algorithm with the XENON1T muon veto Monte Carlo

The XENON1T Muon Veto MC simulation [29] used muon energy and angular distributions from the MUSIC code, mentioned above, to simulate the muon trajectories through the water tank. Thus, the muon tracks in the simulation are created by random draws of tuples of starting points and directions based on the distributions shown in red in figure 3.37. Since the track information of the muons is stored, one can use the MC to test and verify the reconstruction algorithm by using the MC truth values as starting values for the fit parameters $E_{0/1}$, ϑ and φ . Table 3.7 shows a comparison of the MC truth values used as starting parameters and the resulting fit parameters.

Track parameters of a typical event in the XENON1T Muon Veto MC		
Parameter	Monte Carlo truth	Fit results
E_0^x	4.783 m	(4.688 ± 2.061) m
E_0^y	-0.403 m	(-1.030 ± 2.374) m
E_0^z	-1.515 m	(1.027 ± 1.079) m
ϑ	12.27°	$(18.95 \pm 4.89)^\circ$
φ	41.72°	$(49.04 \pm 4.38)^\circ$

Table 3.7: Comparison of the reconstructed track parameters of a certain MC event with the original values, which have been used as starting values for the fit parameters. The timing fit reconstructs the entry point and angles well. While for the spatial coordinates of E_0 both values agree within the error ranges (except for the z coordinate), for the angular fit values the errors do not cover the MC truth values.

Although three MC truth parameters are not matched within the uncertainties of the reconstruction fit, all values are not too far off from each other. Having a

look at the residual plot in figure 3.38 shows, that the fit can match the MC data with a $\chi^2_{\text{red}} = 4.18$ (for 67 degrees of freedom), but with higher residuals as for real data. Here, the theoretically infinite time resolution of the Monte Carlo data has been downsampled to the timing resolution of the muon veto DAQ (1 Sa = 10 ns) with the same uncertainty of 1 Sa. The MC data shows comparatively more outliers, originating from PMTs which do not survive the timing cuts, than the data. This, as well as the high reduced χ^2 value, can be presumably explained by the theoretically perfect assumptions of the detector components in the MC as e.g. perfectly flat clad reflective foil, no wires and no belts which are blocking the light, etc.

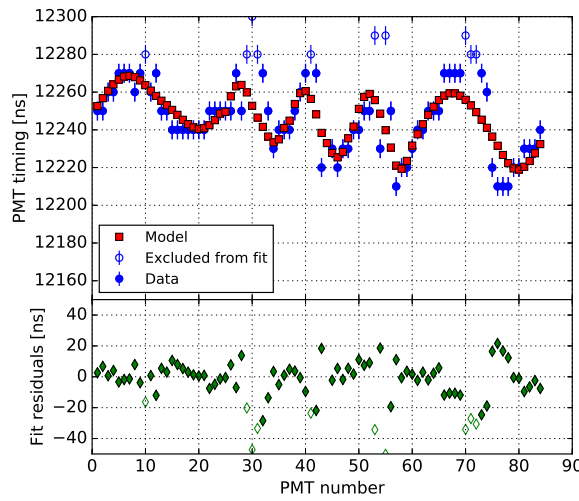


Figure 3.38: Fit residuals of a muon track reconstruction on a simulated Monte Carlo event. For MC data more outliers and a higher mean of residuals can be observed than for real data. Despite of that, the fit can describe the data with $\chi^2_{\text{red}} = 4.18$ (for 67 degrees of freedom).

Summary of the muon veto track reconstruction

In the previous subsections a method to reconstruct muon tracks in the XENON1T Muon Veto was presented. A fit based on a PMT timing model fits the data well. However, considering the muon veto as a track detector the angular reconstruction (especially the elevation angle ϑ) is limited by the low number of PMTs and their discrete distribution in height, as well as the 10 ns timing resolution of the muon veto DAQ. Given the two possible fit functions f_0 and f_1 for a track reconstruction relative to the muon entry point E_0 or exit point E_1 , respectively, it turns out that fitting relative to E_0 works better since the entry point is easier assessable in terms of a starting value for the fit. The reconstructed angular distributions of muons are in agreement with other measurements and simulations at LGNS. The reconstruction works also

on simulated MC data, but cannot perfectly reconstruct the known starting values from it. The reconstruction method could be improved by modeling also the possible reflection of Cherenkov light on the water tank wall. In addition, another improvement would be using the pulse area information of each PMT hit and weighing the timing distribution with the area value of the pulse. A second possibility for a weighing could be the results of a MC simulation of the light response (timing, amplitude) for a set of φ and ϑ values on a grid of L different entry points E_ℓ^0 (with $\ell = 1 \dots L$) distributed over the water tanks surface. Further, in hardware, one could improve the timing resolution by using a time-to-digital converter (TDC), which would be able to narrow the sample duration and therefore increase the time resolution. Neither option could be considered in the scope of this first muon veto analysis.

Chapter 4

The XENON1T Time Projection Chamber

“Do you know why the Indian rain dances always worked? Because the Indians would keep dancing until it rained.”

Sherman Alexie, *American poet, writer and filmmaker*, *1966

4.1 Detailed description of the TPC

Figure 4.1 shows two drawings of CAD model of the TPC: 4.1(a) shows the mechanical structure of the TPC with field cage and corresponding labels, while 4.1(b) shows a model of the assembled TPC, with labels identifying the individual components. In the following, different sub components will be explained in detail, especially those, which have a direct relation to design, installation or analysis of the liquid level meters which have been a major scope of this thesis and are introduced and described starting from section 4.2.

4.1.1 Mechanical structure, field cage and target volume

The TPC is fixed to the cryostat on six points. It is mechanically supported by 24 PTFE pillars, connecting the stainless steel top TPC ring with a copper bottom ring. Two of the PTFE pillars at opposing sides are widened to host the long level meters (see section 4.2.2). A PTFE tray allows to guide signal and high voltage cables of

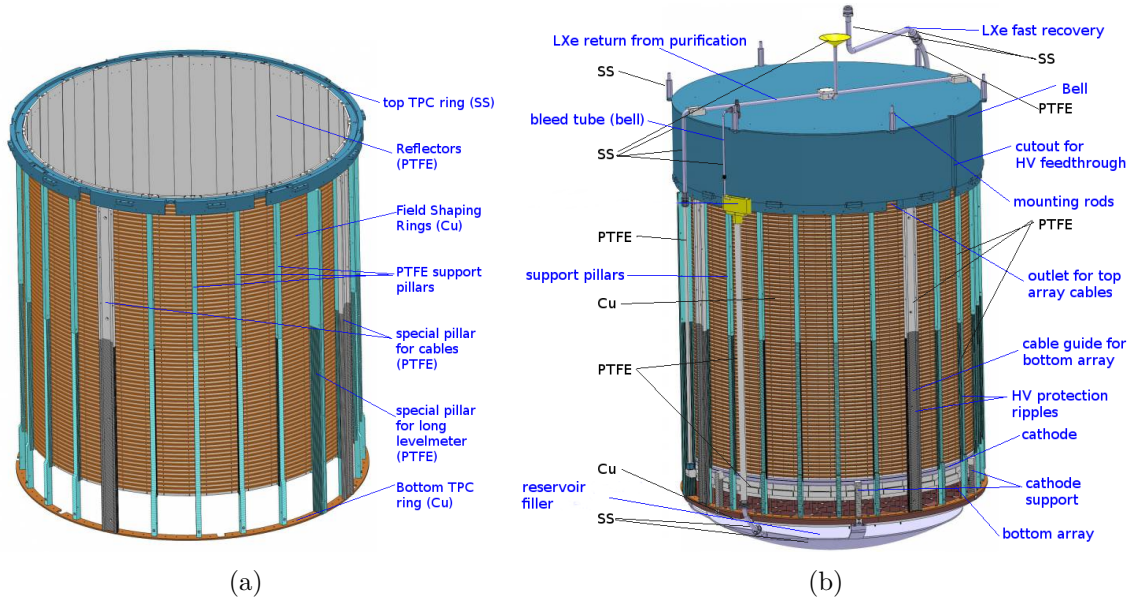


Figure 4.1: Detailed overview of the TPC components as CAD model. (a) The mechanical structure of the TPC and its field cage; (b) a fully assembled TPC. In both figures blue labels indicate sub components, while black labels indicate used materials.

the bottom PMT array to the feedthrough on top. The electric field in the TPC is generated between a cathode grid (negative HV), a gate mesh (GND) and an anode mesh (positive HV). The requirements for the grid electrodes are contradicting, since maximum electrical field uniformity requires zero optical transparency, whereas high optical transparency is required in order to detect the xenon scintillation light of even small nuclear recoils. Monte Carlo simulation studies of light collection efficiencies and electric field uniformity in the scope of [32] resulted in different designs for different electrodes. The cathode was designed to hold high voltages up to -100 kV, supplied by a custom made high voltage feedthrough. As shown in the picture of figure 4.2(a) it is a parallel wire grid with a pitch of 7.5 mm and wire diameter $216 \mu\text{m}$, resulting in an optical transparency of 97.12%. All wires are stretched and fixed between two stainless steel frames. For the gate and anode meshes, hexagonal shapes were etched with wire thicknesses of $178 \mu\text{m}$ (anode) and $127 \mu\text{m}$ (gate), stretched in four directions between two steel frames. This results in transparencies of 88.1% for the anode and 91.3% for the gate electrode. An electric field applied between these two meshes result in warping of both grids, which play a role in the S2 width analysis and the corresponding TPC leveling, to be discussed in section 4.5.2. Figure 4.2(b) shows the anode mesh during manufacturing.

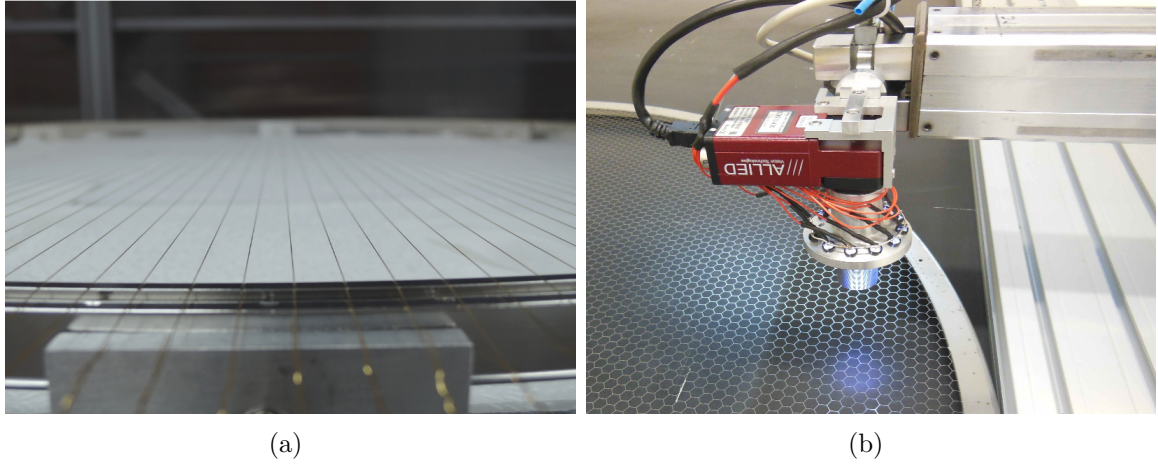


Figure 4.2: (a) The cathode mesh is a parallel wire mesh with 7.5 mm pitch and wire diameter of 216 μm ; (b) The anode mesh is etched to hexagonal shapes with a wire thickness of 178 μm . Pictures by Dr. Junji Naganoma.

Between top and bottom ring 74 field shaping electrodes made from ultra-clean copper rings ensure that the TPC field is uniform. Proper electric potentials on each ring are applied through two identical resistor chains, each consisting of 74 resistors of 5 G Ω between gate and the individual rings, and a 12.5 G Ω resistor between the lowest ring and the cathode. The total resistance of the two parallel chains is 197.5 G Ω . If one resistor would break, the total resistance would rise by 2.5 G Ω , but would still allow to run the TPC at somewhat deteriorated field uniformity. After installation, a total of (171 \pm 2) G Ω has been measured between anode and cathode. The target volume of the TPC is limited by 24 interlocking PTFE panels inside the field shaping rings. They reach from bottom to top ring and are machined with a polished surface to maximize the reflectivity for 178 nm LXe scintillation light. The interlocking design is required to compensate the PTFE shrinkage at liquid xenon temperature. For science run 0 of XENON1T, the TPC could provide an electron drift length $L = (969 \pm 2)$ mm and a target volume $V = (0.700 \pm 0.002)$ m³, already including shrinking effects at -91°C . Given the LXe density of 2.827 g/cm³, one computes a target mass is $M = (1980 \pm 4)$ kg.

4.1.2 PMT arrays and global coordinate system

The TPC is equipped with photomultiplier tubes arranged in a top and a bottom array (see 2.2.1). Figure 4.3 shows the layout of both arrays. PMTs 0 – 126 are located in the top array, PMTs 127 – 247 in the bottom array. The TPC coordinate system as

shown here is implemented in the processing tool PAX and acts therefore also for the coordinate system of the muon veto and its analysis (see section 3.7).

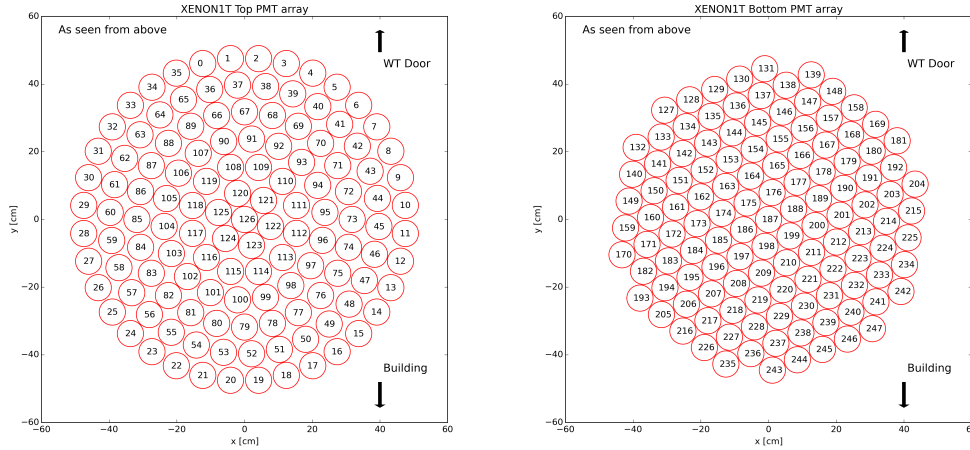


Figure 4.3: Top and bottom PMT array layout and TPC coordinate system.

Both PMT arrays are secured from the electric drift field in the TPC by a screening mesh. The top screening mesh is shaped analogously to the anode mesh hexagonal with a wire thickness of $178\ \mu\text{m}$. The bottom screening mesh is shaped as the cathode as parallel wire mesh with wire diameters of $216\ \mu\text{m}$. The PMTs are calibrated on a weekly bases via a blue LED connected to four sets of seven individual acrylic fibers placed at holes in the PFTE panels defining the TPC volume at center height.

4.1.3 “Diving bell system”, piping and liquid level control

A feedthrough connects both cryostats to the “umbilical” pipe. This is the detector life line connecting support building and cryostats and containing PMT signal and high voltage cables as well as xenon circulation and transfer lines. A continuous recirculation of the xenon in the TPC is necessary since outgassing of TPC components continuously contaminates the target material. The liquid is sucked from the cryostat via a LXe recovery line and is evaporated in a heat exchanger. A second heat exchanger warms up the gas before it reaches the purification system with a high-temperature getter and a diaphragm pump, driving the circulation. In the return path, the purified xenon gets cooled down and largely liquefied in the above mentioned heat exchangers. Liquid xenon drips into a funnel on top of the so-called bell, from where the liquid runs through the return pipes back to the liquid surface. A diving bell system, immersed in xenon, is used to maintain a gas pocket with a well-defined liquid-gas surface above

the active liquid xenon target. It is connected to the TPC top ring and has a pipe connection on its top. Its purpose is the control of the thermodynamics in its inside, using a warm GXe flow into the bell and an overflow “bleeding tube”, which can be adjusted in height via a motion feed-through, as shown in figure 4.4.

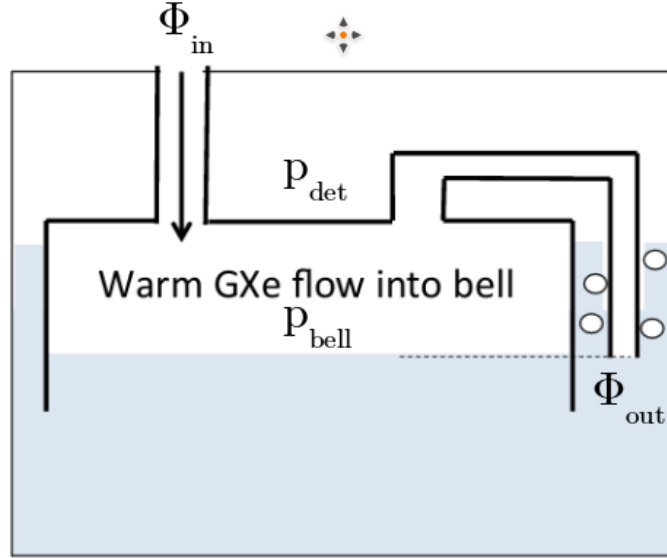


Figure 4.4: Liquid level control mechanism with diving bell and “bleeding tube”. For $\Phi_{in} \geq 0$ the power influx of warm GXe maintains the pressure difference between the pressure inside the bell p_{bell} and the detector pressure p_{det} stable. The liquid height can be controlled by the vertically movable “bleeding tube” on the right. Original schematic by Dr. Junji Naganoma.

The power of the warm GXe flow Φ_{in} is entering the bell and maintains the pressure difference $p_{bell} - p_{det}$ in its inside, where p_{bell} is the pressure inside the bell and p_{det} is the detector pressure outside of the bell. The height of the liquid level is controlled via the vertically adjustable bleeding tube. It is a tube with a hole connected to a linear motion feedthrough on top of the cryostat. This feedthrough itself is connected to a rotary feedthrough on top of the water tank, enabling to change the height of the tubes hole. The purification system is designed to maintain values for Φ up to 100slpm, while typical values in use are ≈ 50 slpm. Figure 4.5(a) shows a picture of the situation on top of the bell with the TPC lowered down during installation at 2015/12/05. The cryostat main feedthrough is visible in the center containing the fast recovery line (1/2" tube, guided to the right), the LXe recuperation line (1/4" tube, guided to the right in the background) and a GXe line for the gaseous flow inside the bell (1/4" tube, guided to the left, background). The funnel gathering the dripping

liquid can be seen in the lower center. Figure 4.5(b) shows the bell of the TPC with the U-shaped bleeding tube in the front.



Figure 4.5: Piping on top of the TPC (*a*) Main feedthrough of the TPC connecting several xenon recuperation and transfer lines from TPC with cryogenics; (*b*) The installed bell of the TPC with U-shaped bleeding tube in the front. Pictures by Dr. Junji Naganoma.

4.2 Level meter system design and simulation

Monitoring exactly the different LXe levels inside the XENON1T TPC is crucial for the operation of the detector, and very important to understand its response. In particular, a precise knowledge of the level and inclination of the interface between the liquid and the gaseous phase between gate and anode is required. Further, liquid level measurements over the full TPC provide important information during the filling and emptying of the detector with LXe. For each case, specific level meters have been designed in the scope of this thesis. They work capacitively, and change their capacitance proportional to the liquid xenon level they are immersed in. In normal operation mode, the detector is in a stationary state, so there are no changes in the liquid level. However, as described in section 4.1, the height of the liquid-gas interface can be adjusted to a higher or lower level by changing the height of the bleeding tube or changing the flow of xenon gas into the bell. The level meters had to fulfill the following requirements:

- Provide a linear dependence of total capacitance C on the LXe level.
- Possibility to be read out by the UTI (**U**niversal **T**ransducer **I**nterface) chip [134] or similar electronics.

- Low radioactivity of all components (ensured by screening of all components).
- Large capacitance per unit height dC/dh to maximize the signal-to-noise ratio.
- Communication and transmission of the measured liquid level values with the XENON1T slow control system via RS-485¹

Further, there were design specifications as follows

- 4 short level meters (SLM), located equally spaced around the stainless steel TPC top ring to measure the location of the liquid-gas interface between gate and anode.
- 2 long level meters (LLM) located on two opposite PTFE pillars of the TPC to monitor LXe filling of the TPC as well as the level outside the bell.
- 1 reservoir level meter (RLM) located in the reservoir to measure the liquid level inside. Since a previously planned LXe reservoir attached at the bottom of the TPC was not installed for the first science run of XENON1T, the planned RLM was not needed. Therefore, no aspects of its already performed simulation, design and construction are discussed in the following.

The capacitance C of any capacitor holding a charge Q at an applied voltage U and being filled with a dielectric of the relative permittivity ε_r is

$$C = \frac{Q}{U} = \frac{\oint_A \vec{D} \cdot d\vec{A}}{\int_s \vec{E} \cdot d\vec{s}} = \varepsilon_0 \varepsilon_r \cdot \frac{\oint_A \vec{E} \cdot d\vec{A}}{\int_s \vec{E} \cdot d\vec{s}}, \quad (4.1)$$

where the electric displacement field \vec{D} is the product of the electric constant ε_0 , the relative permittivity and the electric field \vec{E} in the capacitor. If the cross-section of the capacitor does not change along the z axis and if it is arranged such, that the electric field lines inside the capacitor are horizontal, integration over the surface element $d\vec{A}$ always yields a proportionality with z . Thus, a rising level z_l of a liquid of ε_l inside a capacitor of the height z , which was previously filled with a gas of ε_g can be interpreted as the parallel circuit of two capacitors with C_l and C_g . The capacitance C of the parallel circuit is:

$$C = C_l + C_g = B\varepsilon_0\varepsilon_l z_l + B\varepsilon_0\varepsilon_g z_g, \quad (4.2)$$

¹A standard defining the electrical characteristics of drivers and receivers for use in serial communications systems.

where B is a unit-less constant depending on the shape of the capacitor and results from the integration in (4.1). Since $z_g = z - z_l$,

$$C = B\varepsilon_0 \cdot (\varepsilon_l z_l + \varepsilon_g(z - z_l)) = B\varepsilon_0 \varepsilon_g z + B\varepsilon_0 (\varepsilon_l - \varepsilon_g) z_l. \quad (4.3)$$

This enables a capacitor to be employed as a liquid level meter. The first term, the offset capacitance, is the capacitance of the full capacitor filled with gas. Filling it with liquid, leads to a z_l proportionality of C with a slope depending on the permittivity difference ($\varepsilon_l - \varepsilon_g$) of the liquid and gas. LXe has a relative permittivity of $\varepsilon_{\text{LXe}} = 1.96$ [23]. For gaseous xenon it can be assumed to be $\varepsilon_{\text{GXe}} \approx 1$.

4.2.1 Short level meters (SLM)

The short level meters have to measure precisely the level of the liquid-gas interface within the gap of 5 mm between gate and anode. Their resolution is the better the higher the capacitance difference within these five millimeters. Based on two major designs, cylindric and plate capacitors, several sub designs have been developed and simulated with COMSOL [68] to find the best shape of a capacitor. The simulation is a finite element three dimensional simulation using the *Electrostatics* module based on the two following equations. First, *Gauss' Law*

$$\nabla \vec{D} = \rho_V, \quad (4.4)$$

where ρ_V is the free electric charge density. The equation is the differential form of the dividend of equation (4.1). Second,

$$\vec{E} = -\nabla \varphi, \quad (4.5)$$

which is the differential form of the denominator of equation (4.1), where φ is the electric potential. COMSOL divides the volumes to be simulated in tetrahedral finite elements, which represent small volumes of the whole physical system underlying the two equations from above. The simulated capacitors have been charged with $U_0 = +5$ V on their positive electrode and 0 V at the other electrode. The liquid level can be simulated by defining LXe as a new material with the physical properties of liquid xenon, especially the relative permittivity. The simulation computes various electrostatic quantities such as electric field, electric displacement field, potentials, as well as the energy stored in the electric field within the full simulation volume, stored in a parameter called `intWe`. The latter can be used to calculate the capacitance as

$$C = \frac{2 \cdot \text{intWe}}{U_0^2} \quad (4.6)$$

A parametric sweep over a simulated liquid level h can thus simulate the capacitors for different liquid levels and yield the progress of the capacitance with increasing liquid level.

Simulation of cylindric designs

Two different kinds of cylindric capacitors have been simulated:

- Single cylindric (sc): A simple cylindric capacitor consisting of two concentric tubes as electrodes with radii R_1 and R_2 and length L (see figure 4.6(a)).
- Double cylindric (dc): A double cylindric capacitor consisting of three concentric tubes as electrodes with radii R_1 , R_2 and R_3 and length L (see figure 4.6(b)).

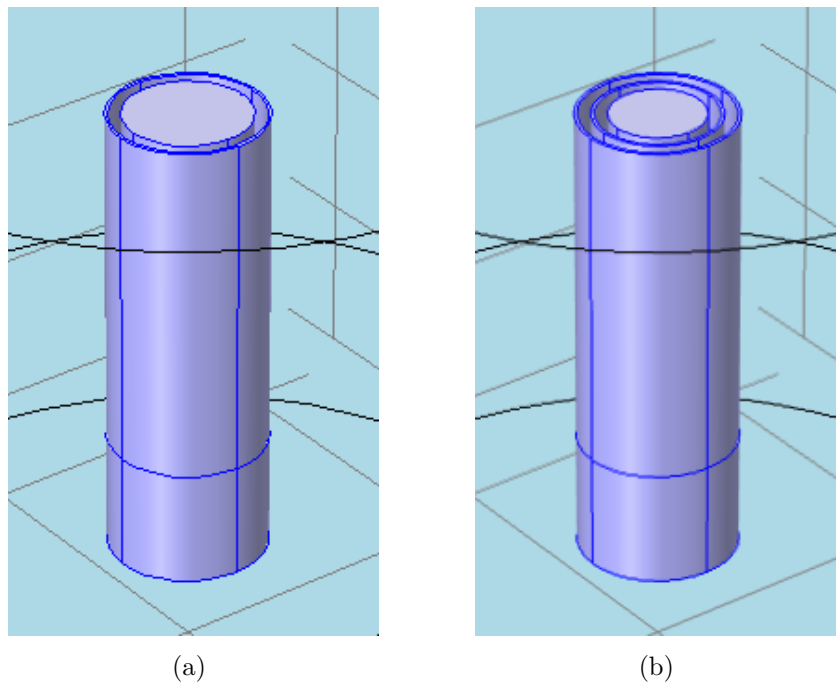


Figure 4.6: Cylindric designs for the short level meters in COMSOL with (a) two cylindric electrodes and (b) three cylindric electrodes.

Solving equation (4.1) for a cylindric capacitor yields

$$C = 2\pi\epsilon_0\epsilon_r \cdot \frac{L}{\ln\left(\frac{R_2}{R_1}\right)}. \quad (4.7)$$

To maximize C at a fixed length the ratio R_2/R_1 has to be close to one. Calculating the capacitances of a $h = 10$ mm long cylindric capacitor once filled with GXe and once completely filled with LXe and radii $R_1 = 3.0$ mm, $R_2 = 3.9$ mm leads to $C_g = 2.12$ pF and $C_l = 4.16$ pF. This corresponds to a capacitance per unit height of $\Delta C/h = 0.20$ pF/mm.

Figure 4.7 shows some results of the finite element simulations. From left to right it shows the electric potential U , the electric field \vec{E} and the electric displacement field \vec{D} for the simulation of the simple cylindric capacitor. All plots show the cross-section of the capacitor in the xz plane.

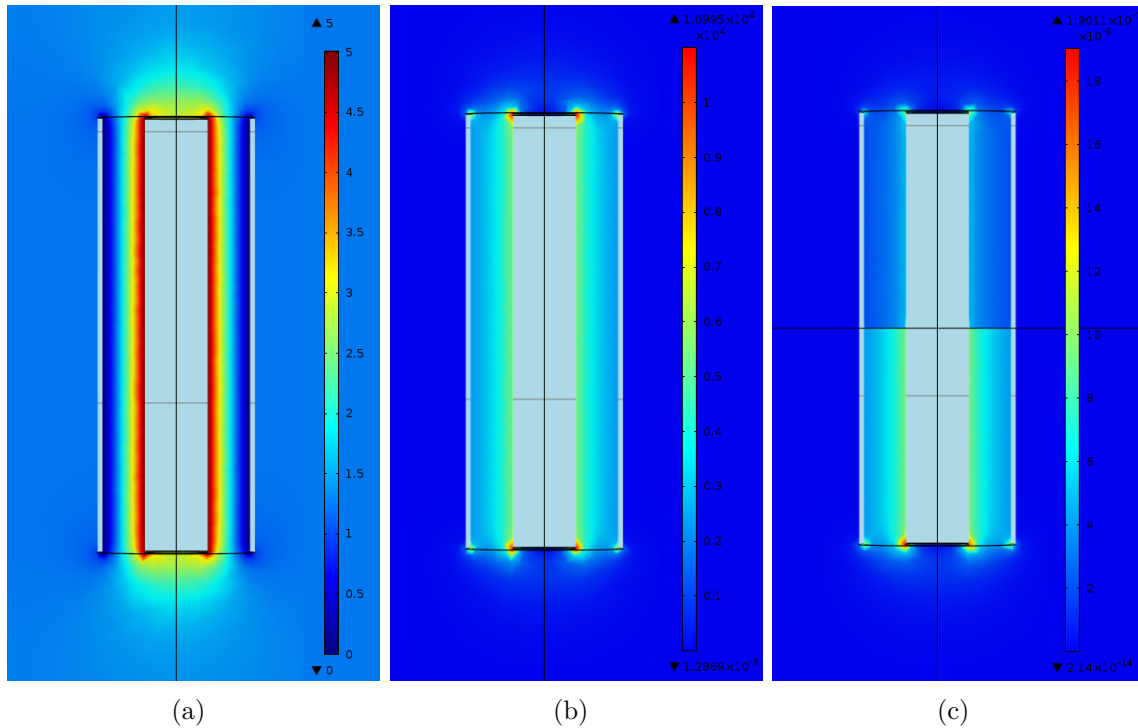


Figure 4.7: Finite element simulations of the capacitive liquid level meters exemplary for a simple cylindric capacitor. (a) The electric potential with the outer electrode being on 0 V and the inner one on +5 V; (b) Simulated values of the electric field \vec{E} with a visible $1/r$ dependence; (c) Immersion of the cylinder in the liquid results in two volumes with different electric displacement field \vec{D} .

In figure 4.7(a) the color scale shows the Potential of 0 V at the outer electrode to +5 V at the inner electrode. Figure 4.7(b) verifies the constant electric field inside the capacitor drops with $1/r$ radially, as expected for a long cylindric capacitor. The values range from ≈ 0 outside of the capacitor to values of $\mathcal{O}(10^4$ V/m). Starting to fill the liquid is visible in the change of the electric displacement field \vec{D} in figure 4.7(c).

The value for the lower half of the capacitor, which is immersed in the liquid, at values of $\approx 8 \cdot 10^{-8} \text{ As/m}^2$, which is about the factor ε_{LXe} higher than the values in the upper half ($\approx 4 \cdot 10^{-8} \text{ As/m}^2$). The maximum values for \vec{E} and \vec{D} are in the border regions of the capacitor.

The mentioned simulations were repeated in a parametric sweep for each liquid level in steps of 1 mm in the range $h \in [0.5 \text{ mm}, 19.5 \text{ mm}]$ with the 10 mm high level meters beginning at $h = 5 \text{ mm}$. The results are shown in the plot of figure 4.8. Since the double cylindric (dc, shown as yellow dots) capacitor has a bit more than twice the electrode area than the single cylindric one (sc, shown as green dots), it can store twice the charge and thus has approximately a factor 2 higher capacitance. For comparison the plot also contains results from a simulation of the XENON100 short level meters, which were single cylindric capacitors with $R_1 = 1.1 \text{ mm}$, $R_2 = 2.53 \text{ mm}$ and $L = 15 \text{ mm}$. Comparing the capacitance per unit height value, the double cylindric is with 0.42 pF/mm clearly to be preferred compared to the single cylindric (0.20 pF/mm), which is still about a factor 3 larger than the value reached by the XENON100 short level meters.

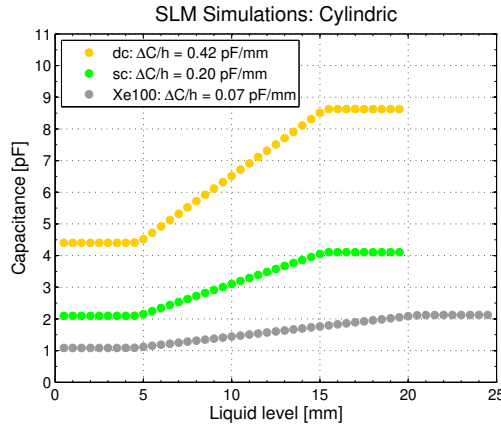


Figure 4.8: Simulated capacitance values versus liquid level height for different cylindrical level meters for XENON1T: the double cylindrical (dc, yellow dots) capacitor can reach about twice the $\Delta C/h$ value as the simple cylindrical (sc, green dots) capacitor. However, both XENON1T cylindrical designs reach higher values as the ones used by XENON100 (xe100, gray dots).

Simulation of plate designs

Solving equation (4.1) for a plate capacitor yields

$$C = \varepsilon_0 \varepsilon_r \cdot \frac{A}{d}, \quad (4.8)$$

with A being the area of the electrode plates and d their separation. The proportionality to A enables to double the capacitance by using a double plate capacitor which has been considered as a start point with two outer plates at 0 V and one inner plate at $U_0 = +5$ V. Based on this two separate designs have been simulated:

- Straight (not curved) plate: A simple plate capacitor consisting of three plates of the dimensions $l \times w \times h$ (length \times width \times height) and distance $d_1 = 1$ mm between the plates.
- The same plate capacitor with $d_2 = 2$ mm.

The electrodes of the simulated straight plate capacitor are of the dimensions of $l = 61$ mm, $w = 0.5$ mm and $h = 10$ mm which is a compromise of having the largest possible area to increase capacitance and having a point like measurement compared to the radius of the TPC. Equation (4.8) yields for the two level meters values of $\Delta C_1/h = 1.04$ pF/mm and $\Delta C_2/h = 0.52$ pF/mm. Comparing these values to the ones obtained with cylindric capacitors it is obvious that plate capacitors are the better choice, with $d_1 = 1$ mm to be preferred. Figure 4.9(a) shows a top view of the tetrahedral mesh applied to the simulation of a plate capacitor inside the cylindric shaped simulation volume around it. The mesh was customized in a way, that the region of interest (the space between the plates) is finer meshed to allow highest accuracy.

The simulation results of a parametric sweep over the liquid level is shown in figure 4.9(b). For comparison, the results for the double cylindric capacitor and the XENON100 short level meters from figure 4.8 have been added to the plot (yellow and gray dots). The red dots result from the simulation of the plate capacitor with three plates and $d_2 = 2$ mm. They agree with the values obtained from equation (4.8). The black dots are the result of a double plate level meter with $d_1 = 1$ mm. The simulated $\Delta C_1/h = 1.04$ pF/mm is again in agreement with the calculated values. The absolute capacitance values are however higher than the theoretical value, due to additional holdings and shielding structures described below.

Mechanical design and in situ simulation in realistic electric environment

Since the double plate capacitor was selected as the electric design for the XENON1T short level meters, a mechanical holding structure had to be designed and a realistic simulation of the level meters in the electrostatic environment of the TPC electrodes had to be performed. Figure 4.10 shows the mechanical design of the full short

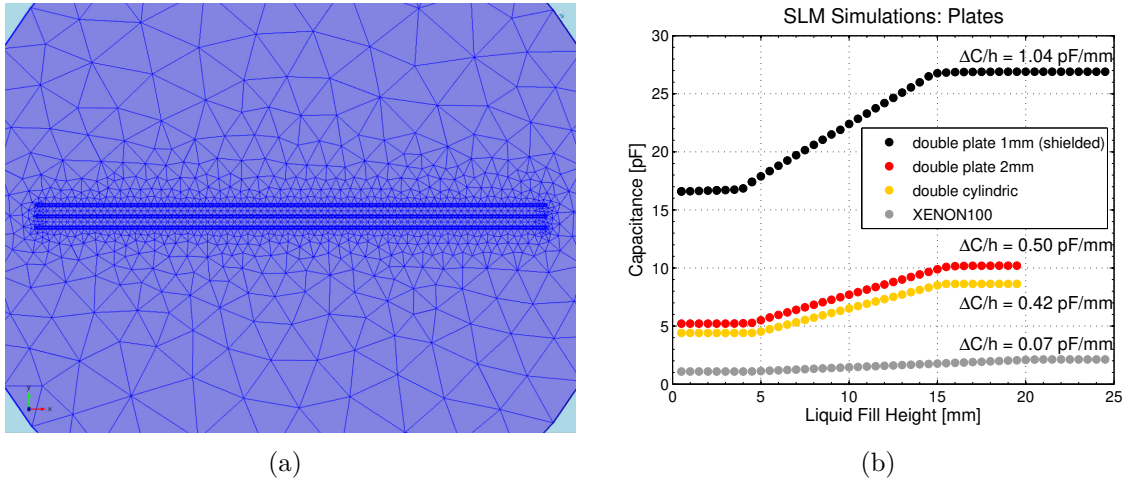


Figure 4.9: (a) Example of a tetrahedral mesh applied to the FEM simulation of the double plate capacitor; (b) Simulated capacitance values versus liquid level height for different plate level meters for XENON1T: the double plate capacitor with $d = 1$ mm separation between the plates (black dots) can reach twice the $\Delta C/h$ value as for $d = 2$ mm (red) and reaches therefore also higher resolution as the double cylindric level meter (yellow dots). Again the XENON100 short level meter is shown for comparison (gray dots).

level meter compound. The three plates of the capacitor are made of copper of the CW009A standard with $> 99.99\%$ pureness which has been machined in an oxygen free environment to avoid outgasing in vacuum [72], and held by two PEEK² pieces with a fixed distance between the plates of $d = 1$ mm. A cage as well as two side pieces of CW009A copper fully enclose the SLMs from every side except the bottom. Small $\varnothing 2$ mm holes allow gaseous xenon to escape the shield during filling.

The three plates have a small fin with an eyelet at the bottom side to allow the soldering of the signal cable. They are arranged such that the fin of the middle electrode (GND) and the fins of the two outer electrodes ($U_0 = +5$ V) point in opposite directions. As illustrated in figure 4.10(c) the PEEK parts cover 4 mm of the copper plates on each side, which act as a fixed capacitance offset of $C_{\text{PEEK}} = 2 \cdot \epsilon_0 \epsilon_r A' / d$, with A' representing the PEEK covered area of $4 \text{ mm} \times 10 \text{ mm}$ and $\epsilon_r = 3.3$ [54]. The expected capacitance is then $C = C_{\text{PEEK}} + C_{\text{Cu}}$ with C_{Cu} accounting for the capacitance of the 53 mm wide copper only part. The resulting values of $C_g = 14.06$ pF and $C_l = 23.07$ pF are now closer to the simulation results shown in figure 4.9(b), missing only the capacitance added by the fins.

²Polyether ether ketone, a thermoplastic polymer with excellent mechanical and chemical resistance properties and excellent outgasing properties.

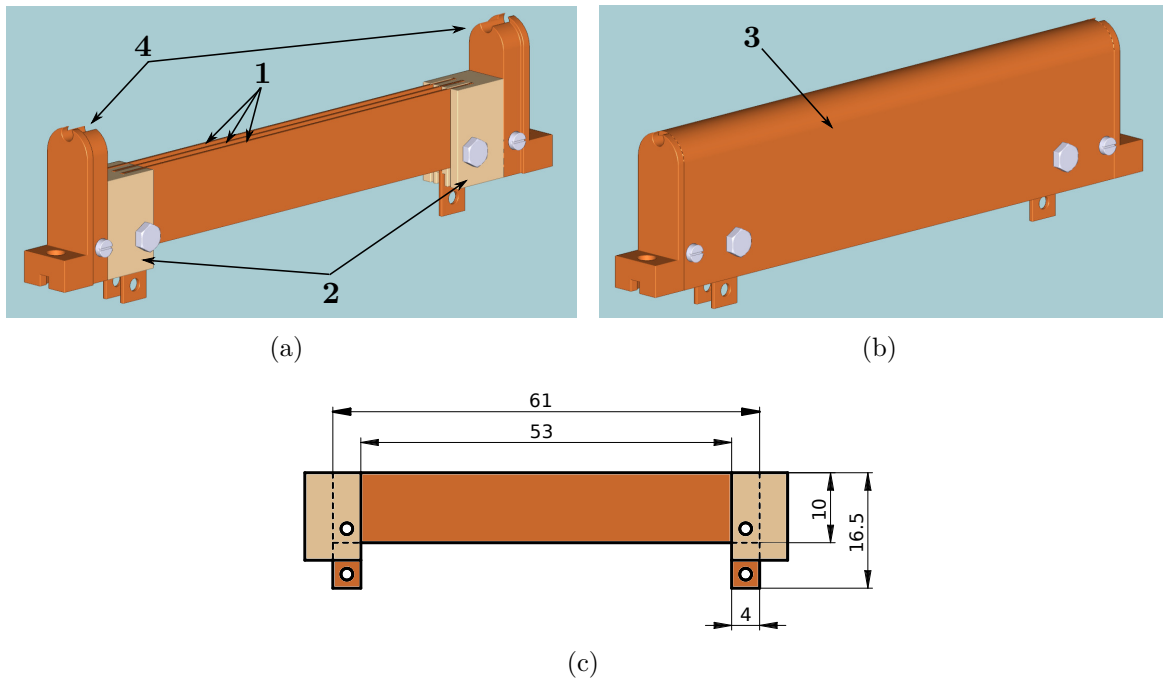


Figure 4.10: Technical drawings of the mechanical short level meter design (a) without shield and with shield (b). The three electrode plates (1) are made of copper and are fixed at equal separation by a PEEK holder on each side (b). They have eyelets at an extension on the bottom side for electric contact for the signal cables. Two copper side parts (4) connect all parts to a surrounding copper cage, connected to GND for electrical shielding (3); (c) The PEEK holders cover 4 mm of the plates at each side and increase the capacitance with a fixed offset.

As stated in the design specifications above, the SLMs must be located at the TPC top ring to cover the full range between gate and anode. Figure 4.11(a) shows the location of an SLM as a CAD drawing. It shows a cut view of the anode (gray), the gate (brown) and the top ring (blue). Cut surfaces are colored purple. The three plates of the SLM cover the full distance between gate and anode. Since the anode will be applied to up to $U_A = +5$ kV a electric field of up to $E_g = 10$ kV/cm can surround the level meter. This is much higher than the field within the level meter plates and would disable the measurement, necessitating a surrounding grounded cage. Figure 4.11(b) shows an implementation of the CAD drawing in COMSOL together with the bell, which is visible on the very right. It shows the electric potential on all visible surfaces. +5 kV are applied to the anode. Gate, top ring and bell are on GND. The SLM shield is on a separate GND and is insulated from the other parts, as there is a space of one mm to the top ring.

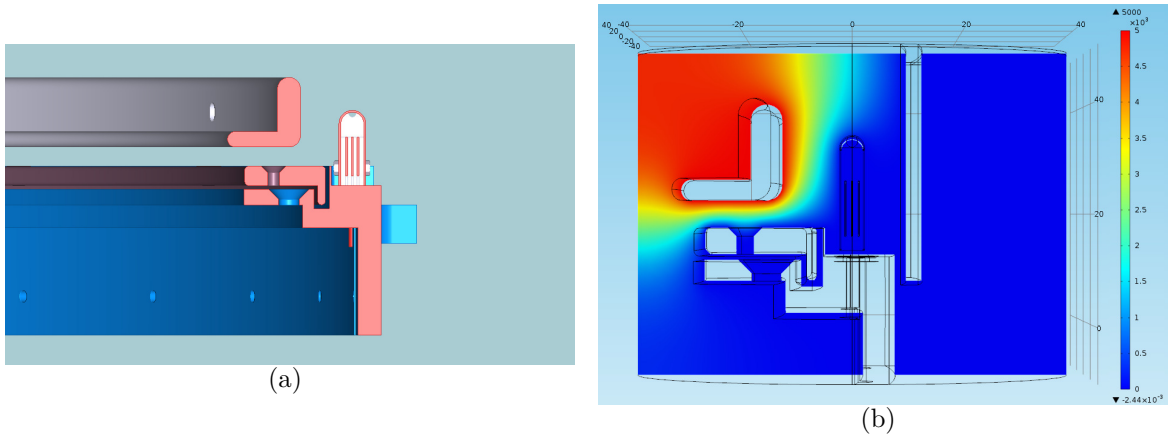


Figure 4.11: Implementation of the SLM position in CAD and FEM simulations. (a) Cut view of the TPC top section in the horizontal plane. Purple sections are cuts. The anode is shown in gray, gate in brown, top ring in blue. The short level meter is located in a machined gap in the top ring to be between anode and gate; (b) Implementation of the realistic electric environment of the SLMs in COMSOL. A voltage of $U_A = +5$ kV is applied to the anode. Gate, top ring and SLM shield are grounded. The bell is visible on the right side. The color scale ranges from 0 V (blue) to U_A (red).

Figure 4.12 shows the corresponding electric field simulation. Huge electric fields with highest values at corners up to 20 kV/cm surround the short level meter. The simulation shows that the designed shield is working well. The very much smaller field between the plates of ≈ 0.04 kV/cm is not affected by the larger fields outside. The radial view on figure 4.12(b) shows that the field leakage from outside into the shield through the two gas outlets as well as through the small gap to the top ring is not high enough to affect the electric field of the short level meter. In this view there are also two drilled holes in the top ring visible, acting as feedthroughs for the signal cable from below.

Capillarity in the SLMs

Capillarity forces the LXe to flow upwards the narrow distance between the SLM electrode plates. In general, the capillarity force is

$$F_C = L \cdot \sigma \cdot \cos \Theta, \quad (4.9)$$

where σ is the surface tension ($\sigma_{\text{LXe}} = 18.46$ dyn/cm = $18.46 \cdot 10^{-3}$ J/m² at $T = 165$ K [135]), L is the length of the contact line between liquid and solid surfaces and Θ is the contact angle between LXe and copper. Since this value was not found

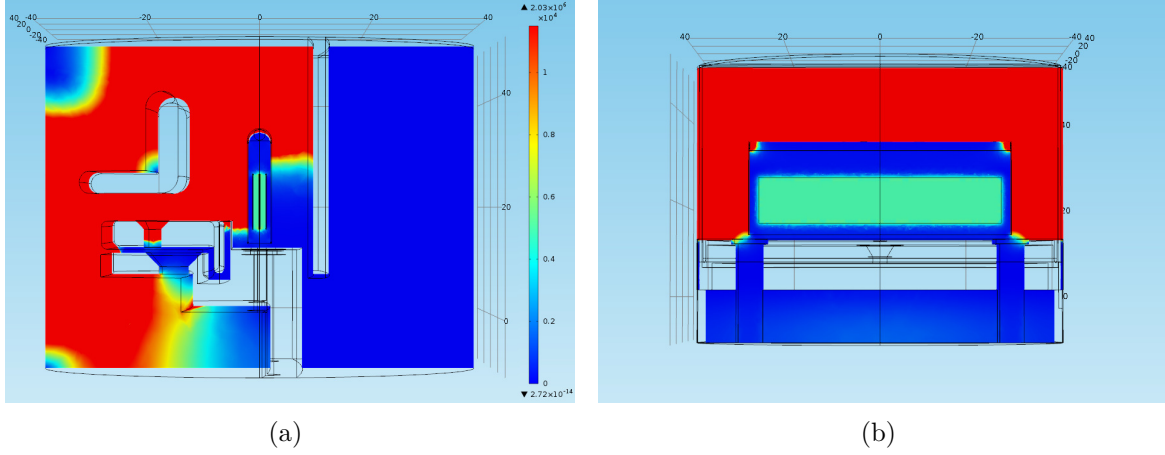


Figure 4.12: In situ electric simulation of an SLM on the TPC top ring in axial view (a) and radial view (b). At edges the electric field reaches values up to 20 kV/cm, while the field inside the capacitor is only 0.04 kV/cm. However, the SLM cage shields the inner electric field. There is field leakage from the outer field into the cage through the two gas outlets, but the level meter field is not affected. The color scale ranges from 0 kV/cm (blue) to 0.12 kV/cm.

in literature, a conservative assumption of $\cos \Theta = 1$ was chosen. The contact length between two plates of the SLM is two times the length of the plates, thus $L = 2l$. This capillarity force pulling a LXe column of the volume $V = ldh$ within the space between the SLM plate (separated by d) is in equilibrium with gravity.

$$F_C = F_g \quad \Leftrightarrow \quad 2l \cdot \sigma_{\text{LXe}} = \rho_{\text{LXe}} \cdot ldh \cdot g. \quad (4.10)$$

With $\rho_{\text{LXe}} = 2.8 \cdot 10^3 \text{ kg/m}^3$ is the density of liquid xenon at a typical operating temperature of $T \approx 180 \text{ K}$ [104]. Thus, the height h_C is

$$h_C = \frac{2\sigma_{\text{LXe}}}{\rho_{\text{LXe}} \cdot d \cdot g} \quad (4.11)$$

and thus independent of the SLM length l . One can therefore expect the height of the capillarity column in the SLMs to be $h_C = 1.34 \text{ mm}$, which will be visible in the level meters as a fixed offset. Given the $\Delta C/h$ simulation results for the SLM, this should result in a capacitance offset of $C_C = 1.04 \text{ pF/mm} \cdot 1.34 \text{ mm} = 1.39 \text{ pF}$.

Final choice of the SLM design

In summary table 4.1 lists all parameters of the SLMs final design as it has been machined

Short level meter design overview	
Number:	4
Type:	Three-plate-capacitor with cage
Material:	CW009A (copper)
Plate length l:	61 mm
Plate width w:	0.5 mm
Plate height h:	10 mm
Plate separation d:	1 mm
Min. Capacitance C_{\min}:	16.47 pF
Max. Capacitance C_{\max}:	26.90 pF
Dynamic range $\Delta C = C_{\max} - C_{\min}$:	10.43 pF
Dynamic range per unit height $\Delta C/h$:	1.04 pF/mm

Table 4.1: Overview of the final SLM design. The simulated numbers achieved for the dynamic range are factor 10 larger than those for XENON100, for dynamic range per unit height a factor of 15 could be reached as improvement compared to XENON100.

An overview technical drawing of the full SLM assembly with the overall dimension can be found in appendix C.1. Figure 4.13 shows pictures of five completely constructed short level meters, of which four later have been installed in the TPC (the fifth acting as a spare).

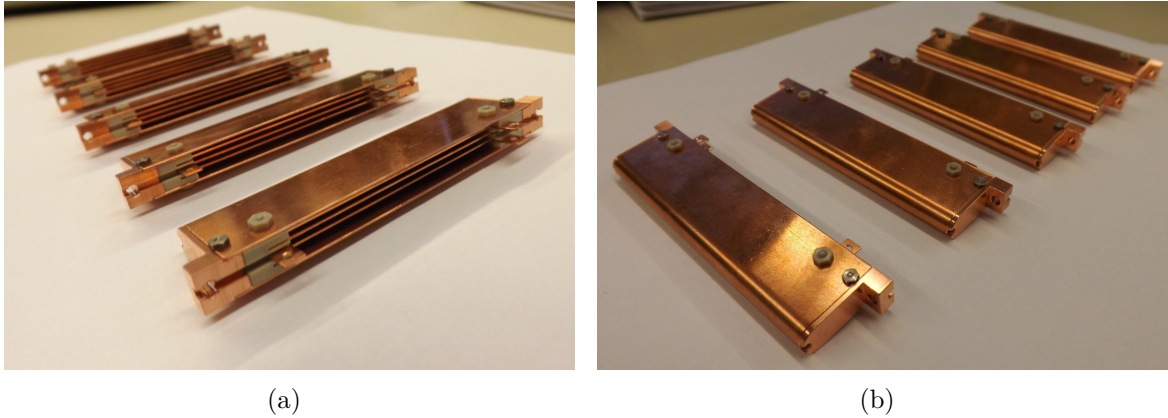


Figure 4.13: The fabricated five SLMs. Four of them have been ultimately installed in the XENON1T TPC, the fifth one acting as space.

A first test was performed immersing the SLMs in liquid nitrogen ($\epsilon_{\text{LN}_2} = 1.43$), which was slowly vaporizing afterwards emptying the level meters from top to bottom. This verified the linear capacitance change over liquid height. The readout was performed via a 15 m coax cable of the same type as used in XENON1T (RG196 coaxial cable with PTFE insulation and 1.83 mm diameter) with a Smartec UTI

evaluation board. This is a commercial product, based on the UTI chip used also for the self-designed readout board for the readout in XENON1T, presented in section 4.3. Since the evaluation board has a limitation in the number of chips and communication of data it has only been used for this quick test and is therefore not further explained here. Figure 4.14 shows the test result as capacitance over time.

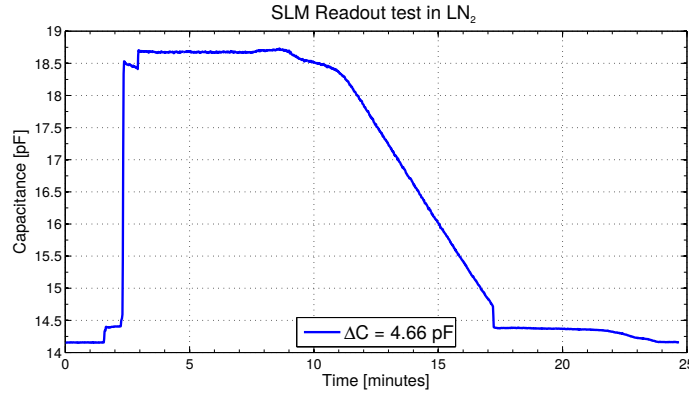


Figure 4.14: Short level meter laboratory tests with vaporizing liquid nitrogen. The capacitance is shown versus the measurement time. Within the first three minutes the step-wise filling of LN_2 causes steps in the curve. The following plateau is the maximum value of the SLM, when being completely immersed. Before reaching the top of the plates, surface tension effects cause a bump like structure at minutes 8 – 9, followed by the desired linear decrease of the capacitance until 17 minutes. Immediately following, capillarity is visible as a sudden jump down, before the capacitance reaches its original value again, after the liquid level went lower than the plate fins.

From 0 – 3 minutes the measurement vessel, containing the SLM was filled in three steps with LN_2 , resulting in two steps in the curve. Within minutes 3 – 8 the SLM was fully immersed. The bump in the curve towards higher values at 9 minutes is due to surface tension, when the liquid surface reaches the top of the level meter plates. From 11 – 17 minutes the linear decrease in capacitance is visible, followed by a sudden drop caused by capillarity, when the liquid reaches the bottom of the plates. From minute 18 until the end of the test, only the plate fins are still immersed, leading to another small linear decrease at the very end. The measured capacitance difference between completely full and empty level meter is $\Delta C = C_{\text{LN}_2} - C_0 = 4.66 \text{ pF}$. Given equation (4.8) the expected factor between capacitances of SLMs immersed in LXe and LN_2 is

$$\frac{\Delta C_{\text{LXe}}}{\Delta C_{\text{LN}_2}} = \frac{C_{\text{LXe}} - C_0}{C_{\text{LN}_2} - C_0} = \frac{\varepsilon_{\text{LXe}} - 1}{\varepsilon_{\text{LN}_2} - 1} = 2.233. \quad (4.12)$$

The measured $\Delta C \cdot 2.233 = 10.41 \text{ pF}$, which agrees with the simulated value (compare table 4.1). The absolute values of $C_0 = 14.31 \text{ pF}$ is roughly 2 pF lower than

the simulated value, but agrees with the calculated value in section 4.2.1 indicating that the absolute values of the simulation might be shifted by the offset of a non-simulated effect.

4.2.2 Long level meters (LLM)

Two long level meters at opposing positions in the TPC have to provide the liquid height information especially during a filling or emptying of the TPC, such that they have to cover its full height and further reach above the bell. Analogous to the description in section 4.2.1, simulations of long level meter designs have been performed. Again, two basic designs have been simulated: cylindric level meters and printed circuit (PC) type level meters, as they are described below.

Simulation of printed circuit designs

Two comb-shaped electrodes which consist of a shaft and teeth that are placed at a perpendicular angle to the shaft and which are interlocking each other can act as a capacitor and thus as a level meter. If realized as printed circuits on a flexible substrate, it would be advantageous in terms of a easy production and a low amount of raw material, minimizing the radioactive background budget. Two possibilities are conceivable: First, the teeth are vertical and perpendicular to the liquid level; second, the teeth are horizontal and parallel to the liquid level. both designs have been simulated in COMSOL. Exemplary, design and simulation results of the vertical teeth design are shown in figure 4.15.

The size of routes and PCB have been chosen according to the flexible circuit Pyralux AP 9222R by DuPont [74], where the substrate is made of Kapton³ with a thickness of 2 mil = 0.0508 mm. The thickness of the copper layer on top from which the circuit could be etched is 70 μm . The high aspect ratio of a level meter with more than 1 m length and single wire dimensions $\mathcal{O}(1 \mu\text{m})$ is difficult to simulate in FEM, so only a 50 mm high part was simulated. 4.15(b) and 4.15(c) show the simulation results for electric potential and field respectively. Between the two electrodes a voltage of $U_0 = +5 \text{ V}$ was applied and an electric field parallel to the liquid level establishes, as visible on the red streamlines in the plot. However, some streamlines show inhomogeneities. A screening over the liquid level h yields a capacitance change per unit height of very high $\Delta C/h_{\parallel} = 0.24 \text{ pF/mm}$ for the vertical teeth and $\Delta C/h_{\perp} = 0.23 \text{ pF/mm}$ for the horizontal teeth design. However, the electric field would easily be disturbed by outer

³Polyimide film developed by DuPont, able to resist wide temperature ranges.

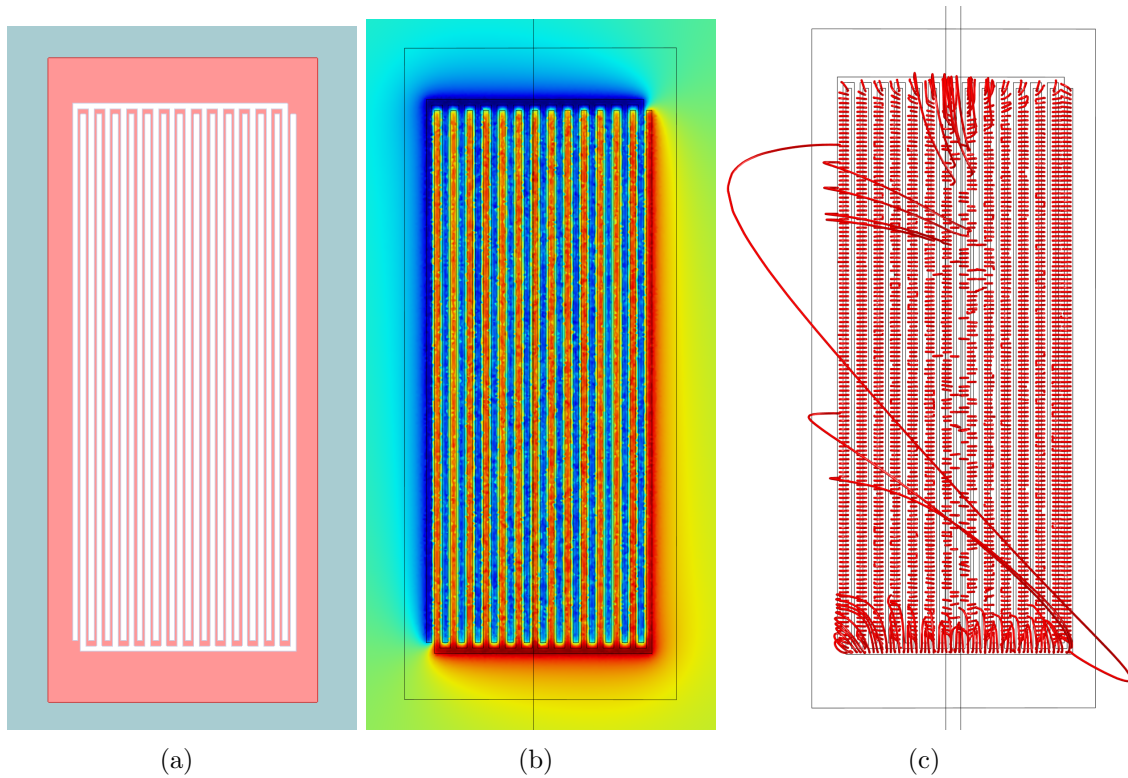


Figure 4.15: Design and simulation of a printed circuit comb-shaped long level meter with vertical teeth. (a) CAD model for illustration of the comb-shaped electrodes interlocking each other; (b) Application of U_0 and GND on the two electrodes leads to a ladder like structure with alternating electric potential (color scale reaches from 0 V (blue) to $U_0 = +5$ V (red)); (c) Streamlines (red) of the electric field between the two electrodes. Electric field lines reach from one tooth to the other over the full length and is parallel to the liquid level. Some field lines show inhomogeneities.

electric fields. A possible shielding was considered to be too complicated, such that the choice for the long level meters in XENON1T were cylindric capacitors as described in the next section.

Simulation of cylindric design

Considering standard tube diameters two single cylindric long level meters consisting of two tubes of d_1 as outer diameter of the inner electrode, d_2 as inner diameter of the outer electrode and D as outer Diameter of the outer electrode have been simulated. First, a combination of $d_1 = 6$ mm and $D = 11$ mm; second, a combination of $d_1 = 3$ mm and $D = 6$ mm. Each pipe has wall thickness of 0.3 mm. The outer electrode is on GND, the inner on U_0 to have a shielding effect. Figure 4.16 shows

the corresponding simulation results for a length $l_1 = 1392$ mm of the inner pipe and $l_2 = 1357$ mm of the outer pipe after a parameter sweep of the liquid level. The reason for the different length are for the sake of easier electrical connections and mechanical support structures. The simulated values for both level meters are in agreement with an evaluation of their capacitances using equation (4.7). The larger diameter level meter (blue circles) reaches larger absolute capacitance values than the smaller one (red circles) with the value $\Delta C/h = 0.10$ pF/mm being 10% higher. However, given the position of the long level meter along the field cage in the TPC, for the sake of electrical break through safety, the smaller diameter level meter design was chosen. For comparison, the long level meters in XENON100 were also cylindrical capacitors with $d_1 = 2.1$ mm, $d_2 = 5.54$ and $l = 500$ mm, reaching a $\Delta C/h = 0.057$ pF/mm.

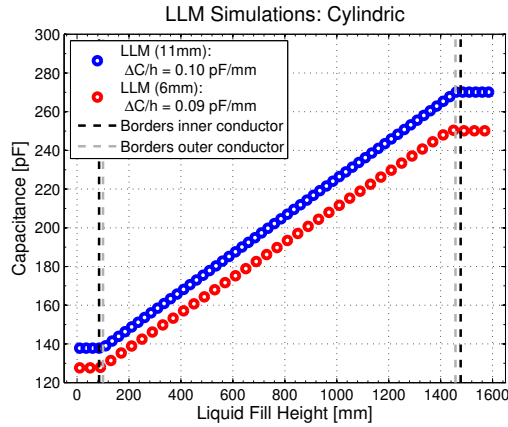


Figure 4.16: Simulated capacitance versus liquid level height for cylindric long level meters of two different sizes: Outer diameter of inner electrode $d_1 = 6$ mm and the outer diameter of the outer electrode $D = 11$ mm (blue circles) as well as $d_1 = 3$ mm and $D = 6$ mm (red circles). Despite of the higher capacitance per unit height values of the larger capacitor, the smaller one was chosen for the sake of electric break through hazards.

Mechanical design

The material chosen for the long level meters is stainless steel (SS) of type 1.4301. Two enlarged PTFE pillars in the TPC host the LLMs. in a groove of 6 mm diameter, fitting the LLM outside diameter. The LLMs are by PTFE holders. Figure 4.17 shows an overview of the mechanical holding structures. The LLMs covers the full TPC and bell. A bottom cap and a top cap fix the LLMs at both ends. Screws prevent the tubes from sliding out the caps. Both caps have foreseen holes to allow liquid to enter at the bottom and gas to escape the LLM at the top. Despite of this inlet and outlet, there is no opening in the cylinders to prevent electric field leakage into the level meter.

Electrical connection is done with two screws touching the individual pipes. Additional PTFE holders at fixed distances of 230 mm prevent the LLM to tilt out of the PTFE pillar.

A screw at the bottom is the only real fixation to the PTFE pillar, to prevent bending forces on the LLM due to contraction of the TPC while being cooled down. From a cold test of the field cage (performed by the XENON Zurich group), the pillar with a length of 1086 mm at room temperature contracted at a liquid xenon temperature of $-91\text{ }^\circ\text{C}$ by 14.7 mm, or 1.35%. Linear thermal expansion of a solid material of the initial length L_0 for a temperature difference ΔT is described by:

$$\Delta L = \alpha \cdot L_0 \cdot \Delta T, \quad (4.13)$$

with the linear expansion coefficient α . The long level meter tubes ($\alpha \approx 16 \cdot 10^{-6} \text{ K}^{-1}$ for 1.4301 stainless steel [71]) contract only by 2.6 mm and need to be allowed to slide upwards. Beginning from the bottom of the LLM, five PTFE spacer rings with an inner diameter of 3 mm, a outer diameter of 4 mm and a height of 3 mm have been slipped over the inner electrode at fixed positions of 23 cm, 46 cm, 69 cm, 92 cm and 115 from the lower end of the level meter. They act as a fixed capacitance, providing a visible effect on the overall capacitance during filling, which is used to calibrate the LLMs, as described in section 4.4.

Capillarity in the LLMs

As for the short level meters, we estimate the capillarity force to determine the height of the liquid xenon column in the long level meter. Equation (4.9) describes again the capillarity force. For a cylindric capacitor, the contact length of fluid and solid L is the sum of the circumference of the inner electrode πd_1 and the circumference of the inside of the outer electrode πd_2 , so $L = \pi(d_1 + d_2)$. The gravitational force on the liquid column of the height h inside the level meter is $F_g = mg = \rho_{\text{LXe}} \cdot \pi (d_2^2 - d_1^2) \cdot h \cdot g$. Similar to equation (4.11) one derives for the height of that column

$$h_C = \frac{\sigma_{\text{LXe}}}{\rho_{\text{LXe}} \cdot g (d_2 - d_1)}. \quad (4.14)$$

Inserting the values yields a height of $h = 0.3 \text{ mm}$. Given the $\Delta C/h$ simulation results for the LLM, this should result in a capacitance offset of $C_C = 0.09 \text{ pF/mm} \cdot 0.3 \text{ mm} = 0.027 \text{ pF}$.

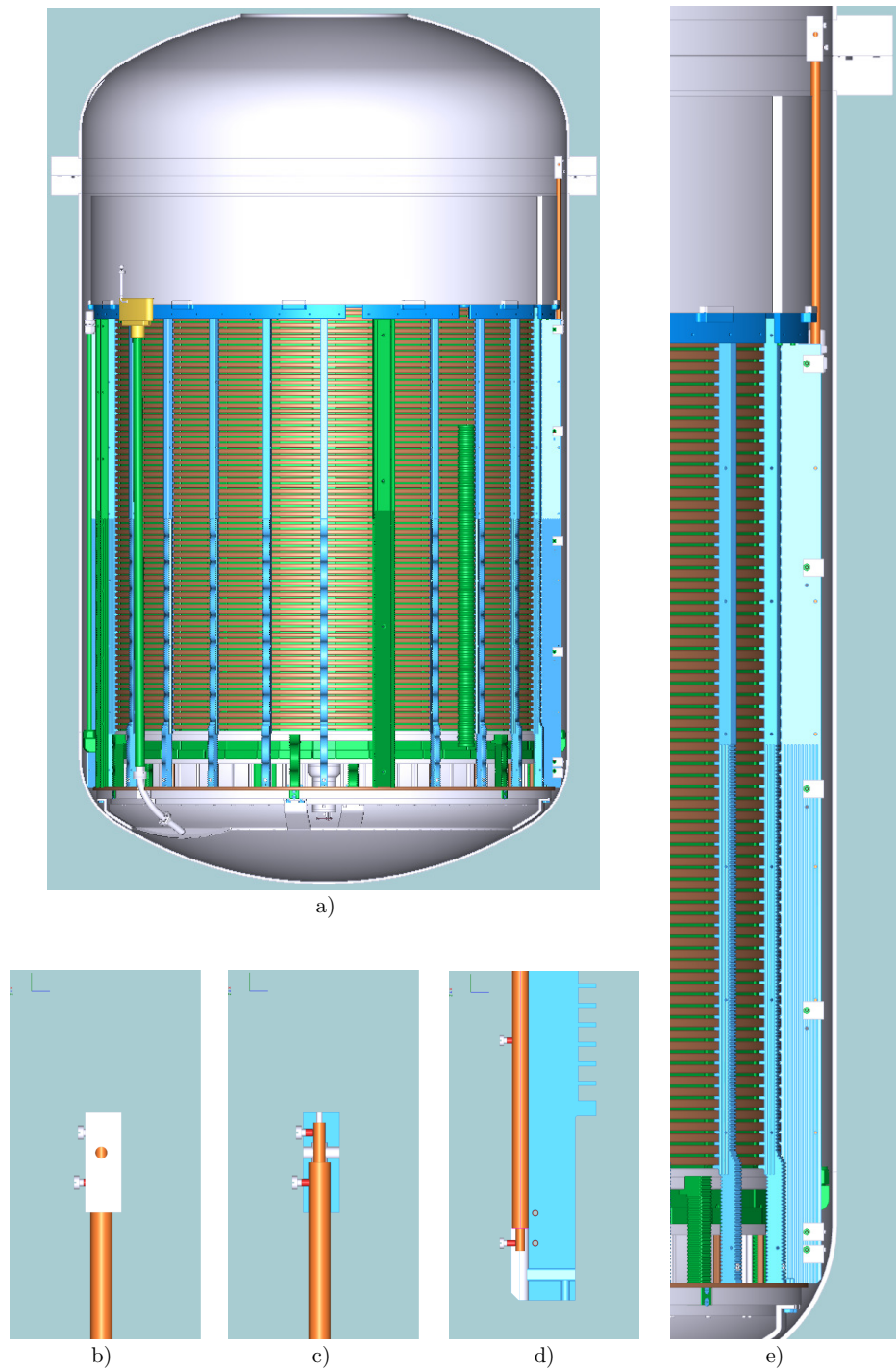


Figure 4.17: CAD model for mechanical incorporation of the LLMs in the TPC. (a) TPC with cut cryostat. The LLM is attached to a PTFE pillar on the very right; (b) PTFE top cap of the LLM; (c) cut view of the top cap with visible mechanism to hold and separate both electrode pipes. Electric connection via two screws; (d) cut view of bottom cap; (e) Zoom on the long level meter as it is located in the TPC design.

Final choice of the LLM design

Table 4.2 lists all parameters of the LLMs, as they have been machined.

Long level meter design overview	
Number:	2
Type:	Cylindric capacitor
Material:	1.4301 stainless steel
Electrode length l:	1357 mm
Outer diameter of inner electrode d_1:	3 mm
Inner diameter of outer electrode d_2:	5.4 mm
Outer diameter of outer electrode D:	6 mm
Min. Capacitance C_{\min}:	127.6 pF
Max. Capacitance C_{\max}:	250.4 pF
Dynamic range $\Delta C = C_{\max} - C_{\min}$:	122.8 pF
Dynamic range per unit height $\Delta C/h$:	0.09 pF/mm

Table 4.2: Overview of the final LLM design. The simulation shows that the dynamic range of the XENON1T LLMs is a factor 4.5 larger than their XENON100 counterparts, while the dynamic range per unit height improves by a factor 1.6.

An overview technical drawing of the full LLM assembly with the overall dimension can be found in appendix C.2.

4.2.3 Radioactivity measurements of the level meters

As part of the TPC, all level meters have been screened for radioactivity. The mass of a constructed short level meter is 35 g, the mass of a long level meter 169 g. Compared to the full TPC these masses are very small, so no big contribution to the radioactive background budget is expected. However, given their position directly next to the liquid/gas interface a screening was necessary. The screening was performed with the GeMPI2 Germanium detector located at LNGS (see [94] for further details). Table 4.3 shows the measured activities for SLM and LLM samples. The SLM sample consisted of the five assembled short level meters. Given the length of the LLMs, its sample consisted of pieces of stainless steel pipes from the same production batch as the real LLM pipes, together with every PTFE and PEEK part of the two LLMs which was installed later. The table shows detected activities with numbers as $\pm 1\sigma$ and upper limits with 90% confidence level if no clear line could be found within the measurement live time. It shows the activities per mass unit of different long-lived isotopes from the actinium-series (^{235}U), the uranium-series (^{238}U , ^{226}Ra and ^{228}Th)

and the thorium series (^{228}Ra and ^{228}Th). Given the very long half-lives of those isotopes and the comparably short live time of the measurement, the activity was inferred by measuring the activities of short lived daughters. Activities from ^{40}K , ^{60}Co and ^{137}Cs are not originated from decay chains but from contamination of the raw materials with natural radioactive isotopes. The results differ from each other given the use of materials procurable in different purity levels. The SLMs are mainly from very pure copper resulting almost in overall lower values than for the LLMs, which show, e.g., higher activities of ^{60}Co due to contaminations of the stainless steel tubes, probably induced during the steel alloy process. Overall, as stated in [36] the results show acceptable activities, with negligible impact on the radioactivity budget simulated for [32]. A change of the level meter material was therefore not necessary.

Level meter screening results		
Sample	Short level meters (SLM)	Long level meters (LLM)
Materials	Cu, PEEK	SS, PEEK, PTFE
Mass	166.8 g	237.7 g
Live time	14 d	14.6 d
^{235}U	< 0.67 mBq/kg	< 0.62 mBq/kg
^{238}U	< 14.55 mBq/kg	< 13.46 mBq/kg
^{226}Ra	< 1.1 mBq/kg	(1.4 ± 0.7) mBq/kg
^{228}Ra	< 1.2 mBq/kg	< 4.7 mBq/kg
^{228}Th	< 1.3 mBq/kg	(4 ± 1) mBq/kg
^{40}K	(22 ± 8) mBq/kg	(26 ± 9) mBq/kg
^{60}Co	< 0.56 mBq/kg	(17 ± 3) mBq/kg
^{137}Cs	< 0.61 mBq/kg	< 0.59 mBq/kg

Table 4.3: Results of the activity measurements of short and long level meters as part of the XENON1T screening campaign (as stated in [36]). Activities of isotopes of the actinium-, uranium- and thorium-series as well as impurities of natural radioactive isotopes have been found and evaluated. The activities are acceptable and no change of material for the level meters was necessary.

4.3 Level meter readout electronics

Reading out the XENON1T liquid level meters requires the development of a dedicated readout system. It is based on the use of capacitance sensitive Smartec UTI chips [134] and consists of a custom made electronic printed circuit board (PCB) and a

corresponding microcontroller based firmware, which allows to control the UTI chips, process their measurement information and communicate the results to the XENON1T slow control system. In the following subsections, the UTI chip is introduced in detail and the development and production of PCB and firmware is described.

4.3.1 The Smartec UTI chip

The UTI chip is a complete front end for the measurement of several types of passive sensors such as resistive or capacitive sensors in 16 different measurement modes. Despite of being developed already more than 10 years ago, it is still a state of the art chip and still the chip to choose for the measurement of very small capacitances over large cable lengths. Given the level meter capacitances of ≈ 10 pF and ≈ 300 pF (as described in section 4.2) and typical cable length in XENON1T of 33 m with a shunt capacitance per unit length $C/l = \mathcal{O}(100 \text{ pF/m})$ typical for coaxial cables, we seek to measure capacitances which are a factor of 10 – 100 smaller than the parasitic cable capacitance. The UTI chip can measure capacitance in three selectable modes with measurement ranges of 0 – 2 pF (mode C23/25), 0 – 12 pF (mode C12) and 0 – 300 pF (mode C300). Given the capacitance ranges mentioned in section 4.2, mode C300 was chosen for all XENON1T level meters, which will be explained in the following. For other measurement modes, as well as a multiplexer mode, the reader is referred to the datasheet of the UTI.

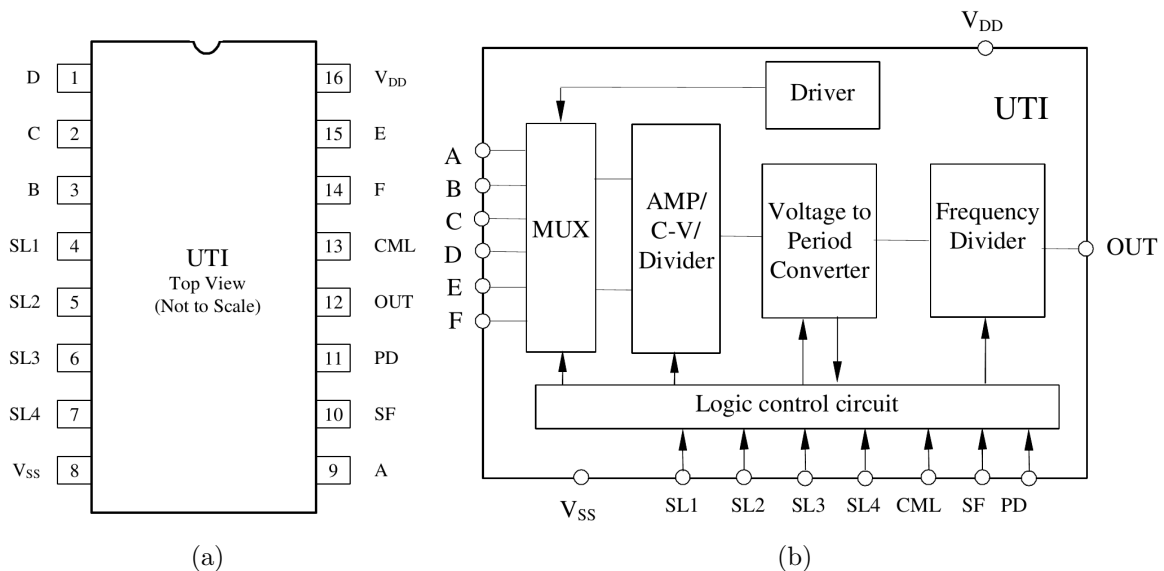


Figure 4.18: The Smartec UTI chip. (a) Pin layout of a 16-dual-in-line (DIL) housing; (b) Internal block diagram. Pictures from [134].

Figure 4.18 shows a pin layout and the functional block diagram of the UTI. The chip was purchased in a 16 DIL housing. It runs with a voltage of $V_{DD} = +5\text{ V}$ supplied at pin V_{DD} . Pin V_{SS} is GND (ground). The most important pins are the nodes for the capacitance measurement A-F as well as the signal output OUT. Pins SL1 – SL4 are the control bits of a 4-bit multiplexer in the logic control circuit to select the desired measurement mode. Pins SF and PD control the slow/fast mode and power down mode. Pin CML is unused, since it is needed only for the multiplexer mode. The block diagram indicates already how the UTI chip measures capacitance via a charge amplifier (AMP), which acts as a charge-to-voltage converter (C-V) and the voltage-to-period converter, which produces the output signal. After this coarse overview, a more detailed discussion of the functionalities is presented in the following.

Function principle of the UTI

The measurement principle of the UTI is based on two techniques: The *four wire measurement technique*, to overcome problems of parasitic cable and input capacitances, and the *three signal technique* in order to overcome offset and gain uncertainties. The following explanations summarize information given in the UTI chip datasheet ([134]), as well in application notes available on the Smartec homepage. The circuit shown in figure 4.19 represents how the measurement of a capacitor of the capacitance C_x would work with a simple multimeter. While for very short cable length this measurement could still work, for longer cable length the parasitic capacitance C_p between the two cables increases and, since $C_p \parallel C_x$, the display would show a capacitance $C_p + C_x$ on the display.

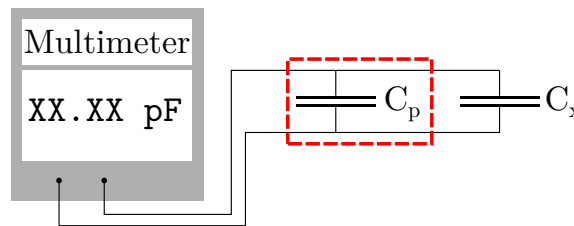


Figure 4.19: Schematic of a failing one port measurement of a capacitance C_x which is smaller than the parasitic cable capacitance C_p as e.g. done with a multimeter. The measurement would fail already for a few cm of cable length.

For capacitances $C_x = \mathcal{O}(1\text{ pF})$ already a few cm of coaxial cable length is enough to double the measurement result, since the parasitic capacitance C_p between signal and shield approaches the value of the measurement capacitor. The UTI avoids this problem as illustrated in the circuit shown in figure 4.20.

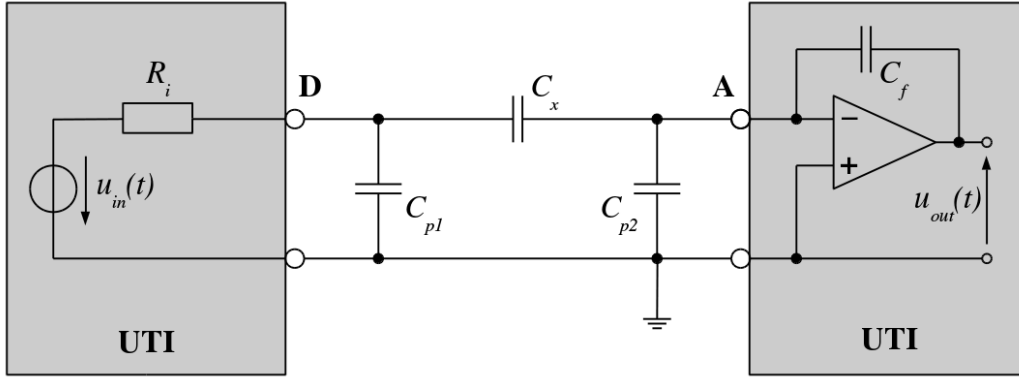


Figure 4.20: The UTI four wire measurement technique with the UTI chip displayed in two parts. An excitation signal $u_{in}(t)$ is applied to C_x . The collection of the transition charge at node A is independent of the parasitic cable capacitances C_{p1} and C_{p2} , which both are “virtually” short circuited by the use of a low output impedance voltage source at D and a charge amplifier at A.

Here, the UTI chip is displayed in two parts for the sake of clarity. Pin D provides an excitation signal $u_{in}(t)$ via a coaxial cable, the shield of which is connected to board ground GND, to charge one plate of the capacitor C_x by a nearly ideal voltage source. The very small output impedance R_i is negligible and thus, the parasitic capacitance C_{p1} , which is parallel to the source, is short-circuited and will not be charged. The excitation signal is a square wave signal with amplitude $U_{in} = V_{DD}$ and its period is modulated by the charge in capacitor C_x : the induced charge Q_x on the right plate of C_x is fed in the inverting input of a charge amplifier circuit behind pin A of the UTI with a second coaxial cable with grounded shield. It gets distributed to the cable capacitance C_{p2} , the differential input capacitance C_d of the amplifier (not shown) and the feedback capacitor C_f .

$$Q_x = Q_{p1} + Q_d + Q_f = U_d \cdot (C_{p1} + C_d) + U_{out} \cdot C_f, \quad (4.15)$$

where U_d is the voltage between the inputs of the amplifier and U_{out} is the amplitude of the output voltage signal $u_{out}(t)$. For a charge amplifier, the non-inverting (+) input is connected to ground, resulting in a “virtual ground” also at the inverting input (-), since the underlying operational amplifier maintains no potential difference between its inputs: $U_d = 0$. Hence,

$$Q_x = U_{out} \cdot C_f. \quad (4.16)$$

Thus, the capacitance C_{p2} will not be charged and hence, does not affect the measurement, neither does the input capacitance C_d . Nearly all the charge from C_x is integrated in the capacitor C_f of the charge amplifier's feedback loop. Let U_x be the voltage between the plates of C_x , the charge $Q_x = C_x U_x$, which transforms equation (4.16) to

$$U_{out} = -U_x \frac{C_x}{C_f}. \quad (4.17)$$

The negative sign is due to the fact, that C_x is connected to the inverting input of the amplifier. The output voltage U_{out} is proportional to the capacitance C_x , once U_x is constant. The subsequent use of a voltage to period converter transforms this voltage to a proportional period T_x of a square wave signal, which is also proportional to C_x :

$$T_x = a_0 + a_1 \cdot C_x. \quad (4.18)$$

a_0 and a_1 express the offset and the gain of the UTI chip. The square wave signal gets frequency divided by 32 for the “fast mode” or 256 for the “slow mode”, controllable by applying V_{DD} or GND to the pin SF of the UTI chip (compare figure 4.18(a)). The resulting period T_x is a quantity, which can be measured by a microcontroller (see 4.3.3) and enables the capacitance measurement. The parameters a_0 and a_1 are unknown and can vary for different UTI chips. The *three signal technique* allows to compensate this uncertainty. Figure 4.21 shows its principle schematically. Three capacitors are connected to nodes B, C and D and have a common node A.

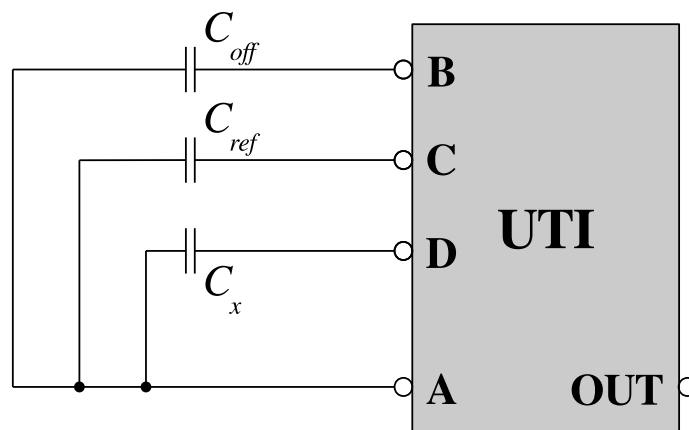


Figure 4.21: Schematic connection overview of the UTI three signal technique. Instead of measuring only C_x at node D, an additional reference capacitance C_{ref} and the internal offset is measured at nodes C and B, resulting in a three signal composed output at OUT.

C_x is the capacitance to be measured, C_{off} is an external offset capacitance and C_{ref} is a reference capacitor with a known capacitance, which must be very stable. The UTI chip applies the four wire technique to each of those nodes by applying the excitation signal sequentially to nodes B, C and D. Equation (4.18) holds for all capacitances:

$$T_{off} = a_0 + a_1 \cdot C_{off} \quad (4.19)$$

$$T_{ref} = a_0 + a_1 \cdot C_{ref} \quad (4.20)$$

$$T_x = a_0 + a_1 \cdot C_x \quad (4.21)$$

Connecting an external offset capacitor C_{off} makes sense if an increase in addition to the internal pin-to-pin offset capacitance C_{int} of the UTI chip is desired. This is not necessary here and therefore no external capacitor was connected between nodes B and A, so $C_{off} \approx 0$. The internal offset of each UTI chip is hence:

$$T_{off} = a_0. \quad (4.22)$$

Defining M as

$$M = \frac{T_x - T_{off}}{T_{ref} - T_{off}} = \frac{a_0 + a_1 \cdot C_x - a_0}{a_0 + a_1 \cdot C_{ref} - a_0} = \frac{C_x}{C_{ref}} \quad (4.23)$$

allows to derive C_x from the value of M and the known reference capacitance C_{ref} :

$$C_x = M \cdot C_{ref} = \frac{T_x - T_{off}}{T_{ref} - T_{off}} \cdot C_{ref}, \quad (4.24)$$

which is independent of the internal offset a_0 and gain a_1 of the UTI chip, and is accessible by measuring T_{off} , T_{ref} and T_x . Figure 4.22 shows an overview of how the three phases are concatenated to a rectangular output signal at pin **OUT**. The first line shows how the excitation square wave is applied to node B of the UTI chip to measure the internal offset of the chip. The frequency of this phase is internally doubled. This feature is used later to identify the sequence of phases as described in subsection 4.3.3. Depending on the logical state of pin **SF** the frequency of the signal gets either divided by 32 for the “fast” mode or 256 for the “slow” mode, before it gets output at the **OUT** pin of the chip. Once the offset phase is done, the excitation signal switches to node C to be applied to the reference capacitance and afterwards to pin D to the capacitor to be measured (compare second and third line in the figure. The composition of

these three phases is one cycle, which is continuously repeated. Depending on the capacitances used, measurements have a complete cycle length of ≈ 100 ms in the slow mode and ≈ 10 ms in the fast mode.

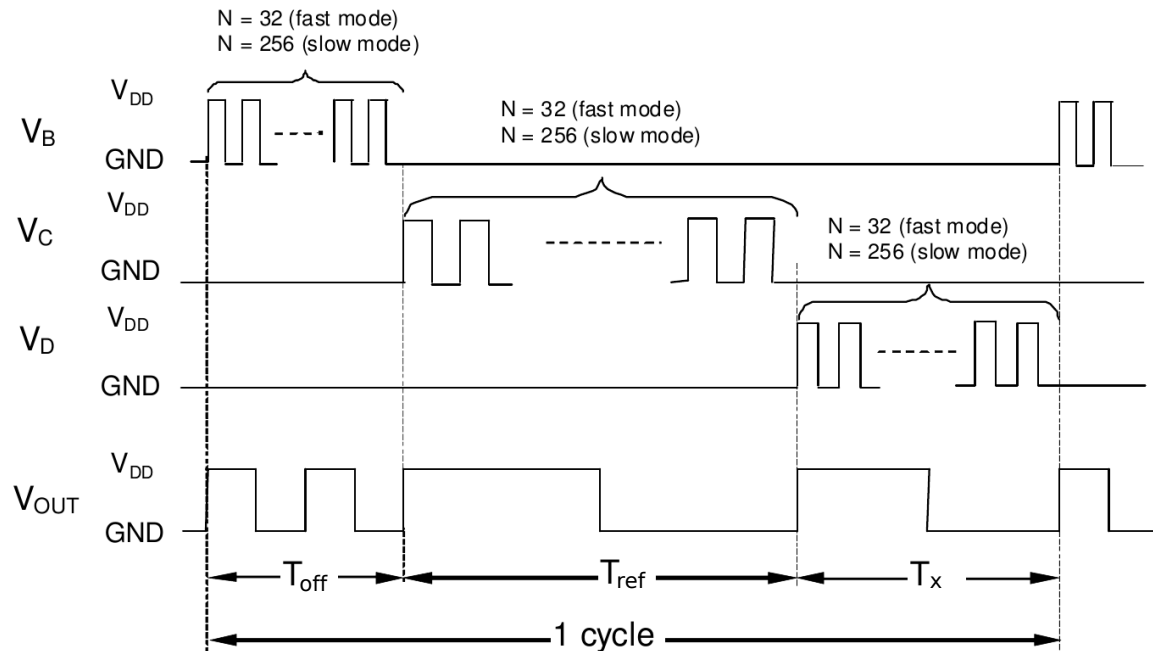


Figure 4.22: Output signal composition of the UTI. The three phases for T_{off} , T_{ref} and T_x concatenated build the output signal. Depending on the usage of “fast” or “slow” mode one obtains a cycle length in the order of ≈ 10 ms and ≈ 100 ms. Drawing taken from application note by Xiujun Li [134].

Exemplary figure 4.23 shows a screen capture of an oscilloscope measurement of the OUT pin of the UTI chip.

Here, a 22 pF capacitor was measured, while using a 10 pF capacitor as reference at a operating voltage of $V_{DD} = 4$ V. Both capacitors have a 10% tolerance. The horizontal scale is 10 ms, the vertical scale 1 V. One finds: $T_{off} = 2 \cdot 10.44$ ms = 20.88 ms, $T_{ref} = 27.11$ ms and $T_x = 35.11$ ms (measured with the oscilloscope markers placed by eye). The full cycle has a length of 83.11 ms, so it was obtained in the slow mode. Inserting these values in equation (4.24) yields a value of $C_x = 22.84$ pF, which agrees with the nominal value given its tolerances. The more precise measurement of these cycle and period lengths with the **Capture** feature of a microcontroller is described in 4.3.3.

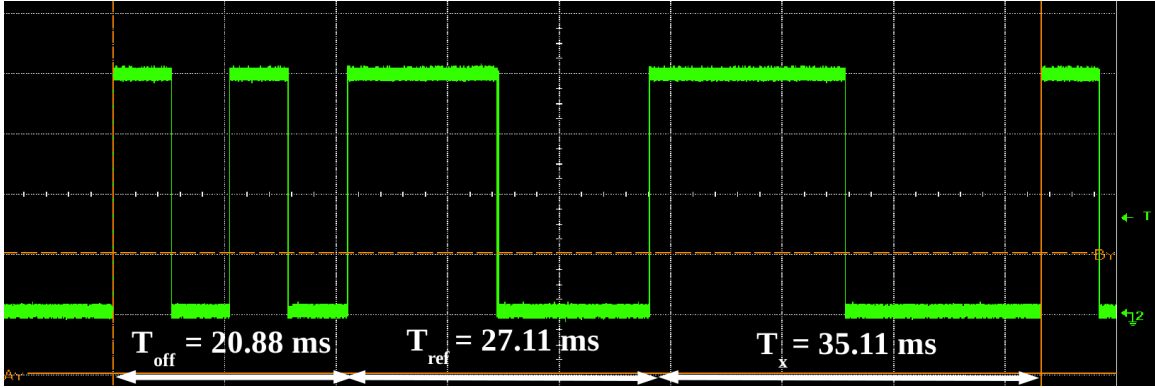


Figure 4.23: Example measurement with an oscilloscope connected to the OUT pin of the UTI chip. Given the displayed periods, the capacitance C_x was calculated with (4.24) as 22.84 pF and is in agreement with the nominal value of 22 pF.

4.3.2 Printed circuit board design

According to the requirement and design specifications defined at the beginning of section 4.2 six level meters have to be measured at the same time or in short sequence. Since all level meters have capacitances > 12 pF, the C300 mode of the UTI had to be used, resulting in the requirement of a single UTI chip for each level meter. A dedicated printed circuit board has been developed to enable the read out and the communication of the measurement data with the slow control system. Besides of numerous passive elements like resistors, capacitors, etc., its major elements are:

- Six UTI chips to read out four SLMs and two LLMs.
- One 74LS151N Multiplexer to switch between the UTI chips [140].
- One Maxim MAX481 RS-485 Transceiver for the RS485 communication with the slow control system [112].
- One Microchip PIC16F877A microcontroller [113].
- Reference capacitors for SLMs (10 pF) and LLMs (150 pF).

Figure 4.24 shows schematically how these elements work together in the read out system. The four SLM (dark red) and two LLM (green) are each read out by a single UTI chip. The board was designed to also allow readout of an initially planned reservoir level meter (RLM, red). The output of the UTIs OUT pin is routed each to the input of the 8-to-1 multiplexer (MUX), which is controlled by three control lines connected to the outputs of three multi-purpose In/Out (I/O) pins of the PIC16F877A

microcontroller. The output, which is selected by the logic state of the control lines is forwarded to the input of the microchips capture module, where the periods of the three UTI phases is measured. That module is able to recognize (“capture”) the rising edges of the UTI signals and trigger a software interrupt, which can be used to activate one of the microcontroller timers, counting the number of processor cycles between each rising edge. Given a known and precise oscillation frequency of the microcontroller, this is ultimately a measure of the phase length of the UTI cycle. The RS-485 Transceiver enables communication between the microcontroller and the slow control system by transmitting the measurement values to and receiving commands from the slow control.

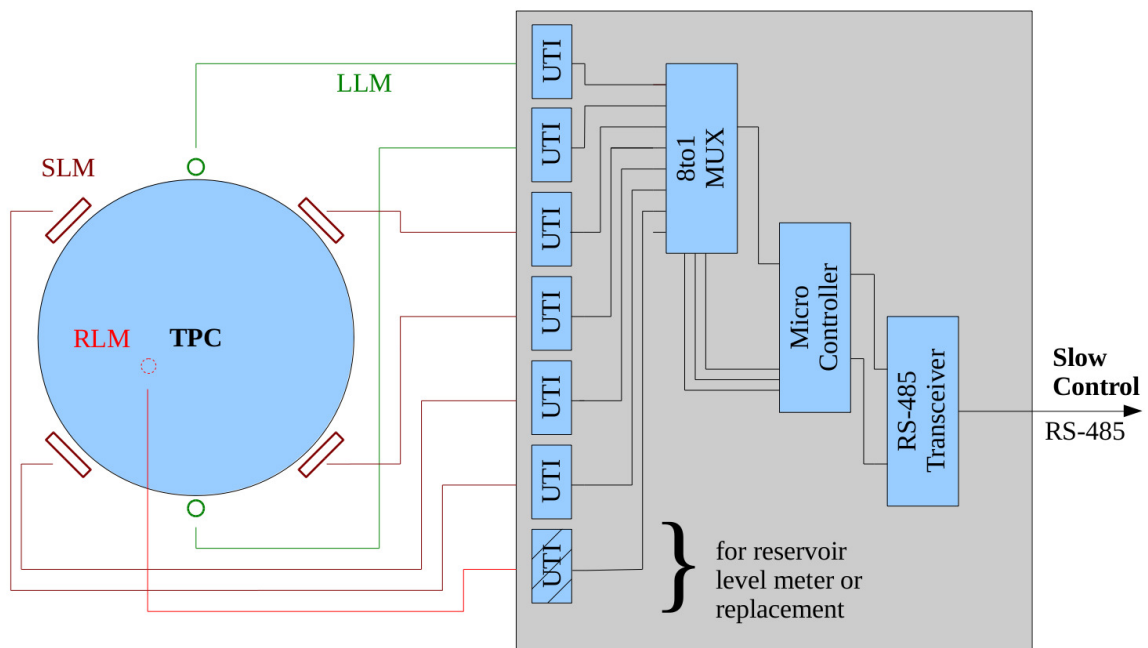


Figure 4.24: Schematic of the printed circuit board of the XENON1T level meter readout. The four short level meters and two long level meters are each read out with an individual UTI chip. The UTI outputs pass through a multiplexer to the input of the microchips capture module for the measurement of the three UTI phases. An RS-485 transceiver communicates the measurement data to the slow control server.

The full schematic of the electric circuit and the PCB layout was designed with EAGLE [42] and can be found in figures D.1 and D.2 in the appendix. Since they are very detailed, in the following the circuit and its components are introduced in a modular way, describing it piecewise rather than completely.

Power supply port

A original requirement by the slow control group of XENON1T was that the readout board should run on a +24 V power supply of the slow control system. To be able to also run on lower voltages down to +5 V, as well as for electrical safety a dedicated power supply port was designed for the PCB, shown in figure 4.25. In direct proximity of the supply voltage connector (X-15-1 and X-15-2) is a noise suppression filter BNX-022-01. It is followed by fuse F2 for over current protection and a transient-voltage-suppression diode D1 for protection against over voltage and voltage spikes. Finally, the routes are fed into a DC/DC converter DC1, which accepts voltages in the range of $U \in [+5 \text{ V}; +24 \text{ V}]$ at its input and provides $V_{DD} = +5 \text{ V}$ and **GND** at its output, providing power for the full PCB.

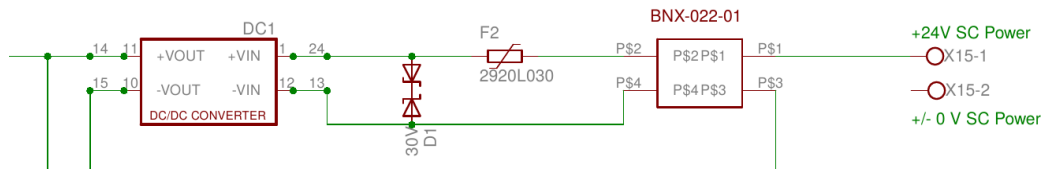


Figure 4.25: Power supply port of the level meter readout PCB. See text for further details.

UTI/level meter port

A very important part of the PCB is the UTI/level meter port, where the cables connected to the short and long level meters arrive at the circuit. Six times two coaxial cables (one for each pin A and B of each UTI chip) arrive from the level meters, with crimped male MMCX⁴ connectors. Hence, on the board there are female MMCX connectors X1, X2, . . . to connect the level meter cables. The ports of SLM 1 and SLM 2 are shown in figure 4.26. The highest horizontal line is the +5 V line coming from the DC/DC converter, the second vertical line from left is **GND**. For clarity all other ports are not displayed but are arranged congruently. The inner electrode of the level meter is connected to X1 and therefore connected to pin 1 of the chip SLM1 (which corresponds to pin D of the UTI⁵, compare figure 4.18(a) for the pin layout). X2 is correspondingly connected to pin 9. The shield of all coax cables are connected to **GND** (the second vertical line from left in the figure). C_REF1 is the reference capacitor of SLM 1 and thus connected to pin 2 (C). It is a special ceramic surface mount

⁴MMCX (**m**icro-**m**iniature **c**oaxial) connectors are commercial radio frequency connectors.

⁵EAGLE does not allow to change the pin numbers to letters. Since there is no EAGLE part library of the UTI chip, it had to be simulated by a standard 16 DIL housing in EAGLE with numbered pins.

(SMD) capacitor with 1% accuracy on its nominal value $C_{ref} = 10\text{ pF}$ and a very small temperature coefficient, reducing systematic errors in equation (4.24). The two reference capacitors for the long level meters (not shown) are of the same type, but with a nominal value of $C_{ref} = 150\text{ pF}$. The PCB provides pads for a capacitor C_OFF1, but the label DNP (“Do not place”) indicates that they were not placed at production. Pin 8 is the ground connection of the chip and connected to GND, the pins 4567 are hardwired to the logical state 0100 to select the mode of the UTI chip for a capacitance measurement in the range 0 – 300 pF. This holds also for all other UTI chips on the board.

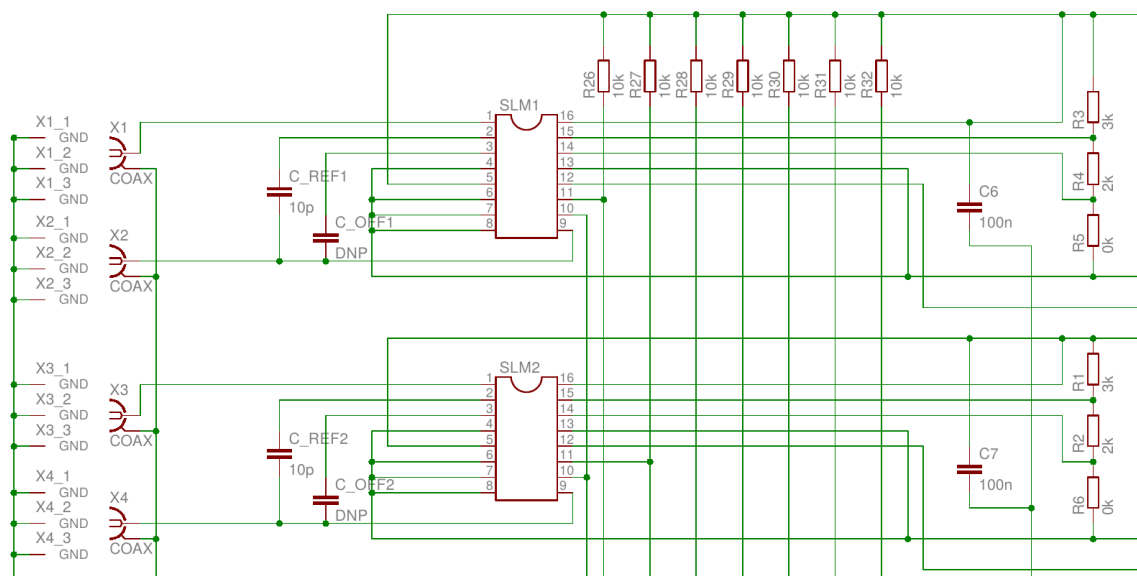


Figure 4.26: The UTI/level meter port of the PCB. Only ports for SLM 1 and SLM 2 are displayed, while all other ports are set up congruently. See text for further details.

Pins 10 are controlling the “slow”/“fast” mode of all UTIs and are connected to an I/O port (RC4) of the microcontroller (not shown). By default it is in logical state 0 (slow) mode, but, if desired, the microcontroller firmware can be changed to apply high logic level to this pin, switching to “fast” mode of the chip. Pin 11 controls the power down mode of the UTI. Given experiences with the UTI chip in the XENON100 experiment, where it introduced a lot of electronic noise, a possibility to enable the power down mode of all chips with a command from the slow control was foreseen (see more details in 4.3.3). Pins 11 of all UTI chips are connected to pins RD1–RD7 of the microcontroller. The input of the power down mode control pin is active high, which means that 10 kΩ pull-up resistors R26–R32 are connected also to pins 11 to maintain always a high logic level on that pin, as long as there is not actively low level provided

by the microcontroller. Pins 12 are the output pins and are each separately fed into an input of the multiplexer (as shown below in figure 4.27). As mentioned above pin 13 (CML) is not used in the scope of this thesis and therefore for reasons of safety connected to GND. Pin 16 connects the UTI to V_{DD} including a blocking capacitor C6 with $C_6 = 100$ nF. For the usage of the 0 – 300 pF measurement mode, according to the UTI data sheet, it is necessary to reduce the amplitude of the excitation signal for large capacitances, given that the charge amplifier behind node A of the UTI loses its linearity for a total charge higher than $Q_V = 60$ pC. The voltage V_{EF} between pins E and F of the UTI can set the excitation amplitudes for the connected capacitors and has to be lower than the minimum voltage across the level meter plates caused by Q_V at their maximum capacitance C_{max} , i.e. when completely filled with liquid.

$$V_{EF} \stackrel{!}{<} \frac{Q_V}{C_{max}}. \quad (4.25)$$

The values of C_{max} for SLM and LLM are known from the simulations presented in 4.2 and have been rounded up conservatively to be 30 pF for SLMs and 300 pF for LLMs, which results in values $V_{EF} < 2$ V for SLMs and $V_{EF} < 0.2$ V for LLMs. This can be achieved by connecting a resistor chain between V_{DD} , pins 14 (F), 15 (E) and GND. In the schematic for SLM 1 these are resistors R5 (between GND and F), R4 (between E and F) and R3 (between V_{DD} and E). The value of R5 is allowed to be zero, so a simple voltage divider

$$\frac{V_{EF}}{V_{DD}} = \frac{R_4}{R_4 + R_3}. \quad (4.26)$$

enables to identify the resistance values to be $R_3 = 3$ k Ω and $R_4 = 2$ k Ω . Those resistors are used for all SLM ports. For the LLM ports equation (4.26) yields $R_3 = 24$ k Ω and $R_4 = 1$ k Ω .

Processing unit and RS-485 communication port

Figure 4.27 shows the core system of the PCB, the Microchip PIC16F877A microcontroller [113] and its peripheral modules. It is a 40-pin 8-bit CMOS FLASH microcontroller with selectable oscillator options, 368×8 bytes of data memory, interrupt capability, 16-bit counter, two capture modules, an universal synchronous asynchronous receiver transmitter (USART) and four I/O ports. All the mentioned functions have been used to develop the readout system of the level meters and will be explained in detail in the following. The microchip can be found in the center of figure 4.27, labeled IC3.

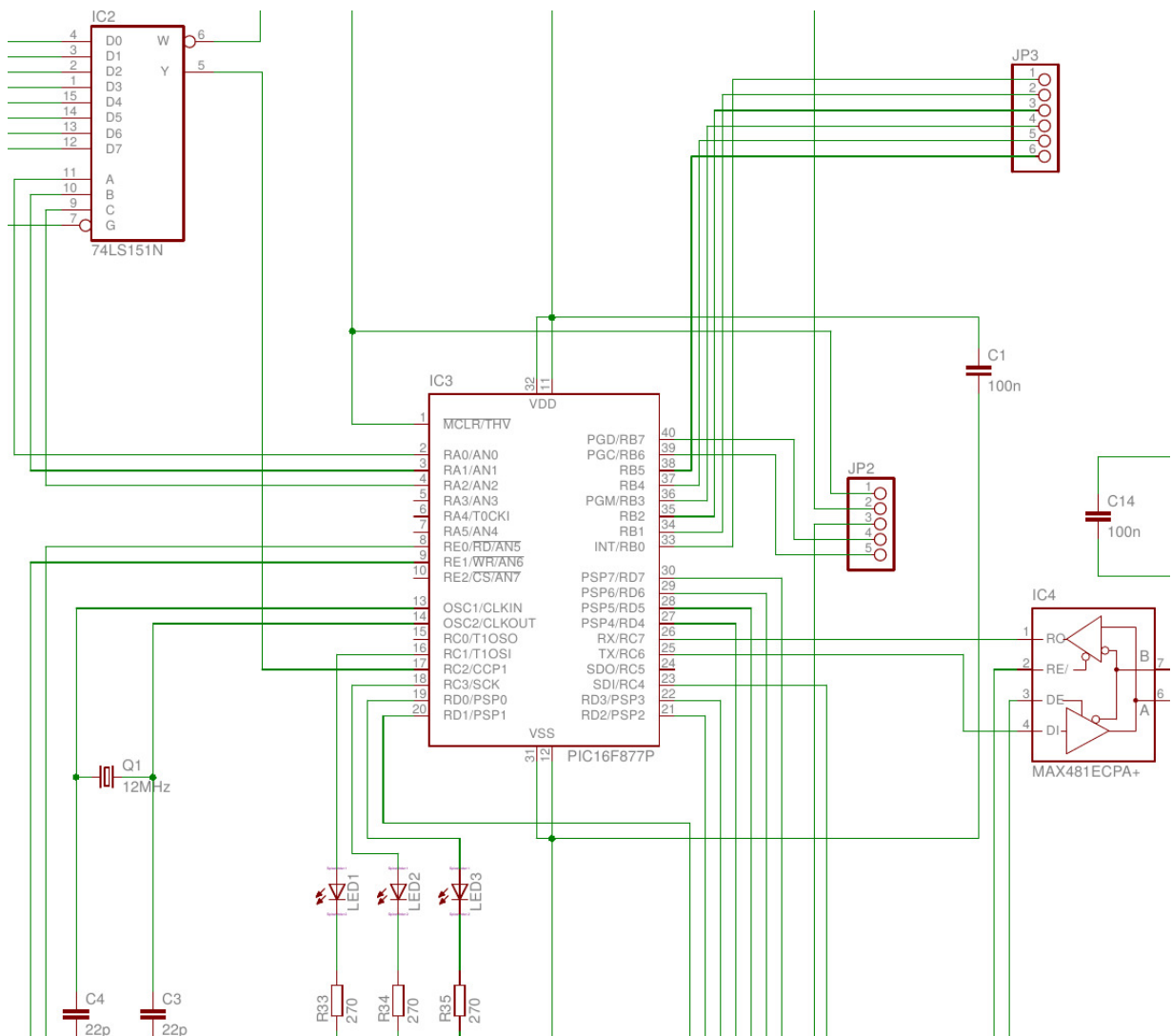


Figure 4.27: Processing unit and RS-485 communication port of the PCB. PIC16F877A microcontroller IC3 is processing the measurement data routed via multiplexer IC2 and provides functionality to communicate over a RS-485 transceiver IC4. See text for further details.

On the top left, the output signal lines from each UTI arrive at the inputs D0–D6 of multiplexer IC2. Pin (D7) and the unused strobe control pin G are connected to GND. The multiplexer control lines A, B and C are addressed by the microcontroller outputs RA0, RA1, RA2. Depending on the logic state at these pins, the corresponding UTI signal is forwarded via pin Y and enters the capture module of the microcontroller at pin RC4/CCP1, where the duration of each of the UTI phases is measured. The software implementation including further details are described in section 4.3.3. The inverted multiplexer output W is connected to a test pin to check the signal with an

oscilloscope (not shown). The VDD and VSS pins of the microcontroller are connected to VDD and GND with another 100 nF blocking capacitor in between (C1) to stabilize the operating voltage. An external quartz oscillator Q1 was connected to pins OSC1 and OSC2 and provides an oscillation frequency of $f_{osc} = 12$ MHz to the full microcontroller system. The frequency is stabilized by two 22 pF capacitors C3 and C4. Jumper JP2 is a five pin wide jumper bar. It is connected to several microcontroller pins, fitting the requirements for connection of the *PICkit 3*⁶ in-circuit debugger/programmer by microchip, which was used to program the microcontroller. Jumper JP3 was foreseen for debugging and an analog-digital converter, but is not used. The MAX481 RS-485 transceiver is labeled IC4. It contains a driver and receiver for RS-485 transmission and reception, respectively. Pin A is the non-inverting receiver input and non-inverting driver output, while pin B is the inverting receiver input and inverting driver output. The RS-485 standard is based on the concept that it transmits a non-inverted and inverted voltage level of the single bits of a signal. The receiver reconstructs the signal from the difference of both voltage levels. RS-485 therefore belongs to the *differential signal* techniques and provides high suppression of common-mode interferences. A 120 Ω termination resistor is located between inverting and non-inverting line to prevent signal reflections (not shown). Whether the MAX481 transceiver acts as receiver or transmitter is controlled by pins \overline{RE} and DE, which can be addressed by microcontroller pins RE0 and RE1. \overline{RE} is an active low pin, indicated by the overline. Applying low logic level to \overline{RE} and DE makes the MAX481 act as a receiver, high logic level on both pins as transmitter. Data being received at the transceiver is forwarded via receiver output pin R0 to pin RX/RC7 into the microcontrollers USART module, where it is stored in corresponding registers and can be processed. Analogously, data to be transmitted is forwarded via pin TX/RC6 of the USART module to driver input pin DI of the transceiver for transmission on the RS-485 line. Specific details about this are explained in the firm ware section 4.3.3. Three status LEDs are foreseen to indicate the board status. LED1 is controlled via I/O pin RC1 of the microcontroller and indicates transmission of the data. During operation, it will therefore blink in the frequency of data transmission. Status LEDs LED2 and LED3 indicate if the board is in normal operation mode (LED2 off, LED3 illuminated permanently) or in power down mode (LED2 illuminated permanently, LED3 off). All LEDs are in series with a current limiting 270 Ω resistor (R33, R34, R35). For a manual reset of the full circuit the active low master clear reset input \overline{MCLR}/VPP is connected via a push-button to

⁶The PICkit™ 3 In-Circuit Debugger is a device able to program every PIC microcontroller via USB connection to a computer. See <http://www.microchip.com/pickit3>.

GND. Activating the push-button resets the microcontroller for a clean restart of the program.

Figure 4.28 shows the assembled PCB as it was used for installation in the XENON1T experiment.

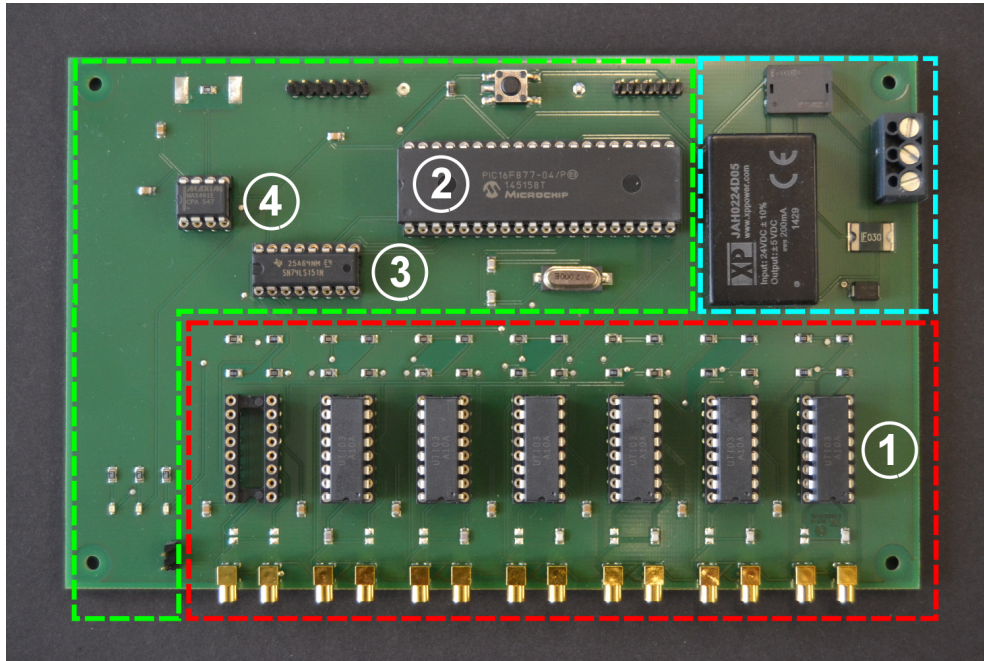


Figure 4.28: Picture of the level meter readout printed circuit board. The dash framed section correspond to the previously described modules of the PCB. Cyan: power supply port with wire terminal, over voltage/current protection and DC/DC converter; red: UTI/level meter port: seven UTI ports (with six of them mounted with a UTI, labeled (1)), golden MMCX connectors and resistor chains and reference capacitors as SMD elements; green: processing unit and RS-485 communication port with PIC16F877A microcontroller (2), multiplexer (3), RS-485 transceiver (4), jumpers, push-button, quartz (in between), connection pads for RS-485 cable with SMD termination resistor (top left) and three status SMD LEDs (bottom left).

It is indicated, which section on the board corresponds to which of the previously explained modular systems. Jumper J3 for programming of the microcontroller is above the upper right end of the microcontroller (2). The following section will provide details about the firmware and its programming to the program memory of the microcontroller.

4.3.3 Readout firmware

In the previous sections the microcontroller PIC16F877A was introduced as processing unit of the XENON1T level meter readout PCB. In the following, we discuss the

firmware controlling, monitoring and processing the level meter data as well as the corresponding registers of the microcontroller. Registers are here 8 bit wide sections of the microcontroller memory, which may be internally connected to a special function of the microcontroller (*Special function registers*) or may be used for, e.g., data storage or variable definition (*General purpose registers*). For a detailed register file map, the reader is referred to pages 12–14 of the datasheet [113]. The firmware was programmed in *Assembler* language of the PIC16F877A, which consists of an instruction set of 35 commands (see datasheet [113], section 13 “Instruction Set Summary”). Microchip provides its own integrated development environment MPLAB IDE which provides an editor, debugger functionalities and a programming tool in combination with the PIC kit 3 programmer.

Figure 4.29 provides an overview of the functionality of the firmware in form of a simplified flow chart⁷, illustrating the main program flow. The single elements can be distinguished in Start/Stops of functions, calls and definitions of subroutines, decisional and conditional statements. The explanations of the program are following the flow illustrated in the chart.

⁷Complying requirements defined in DIN 66001 “Sinnbilder für Datenfluss- und Programmablaufpläne.

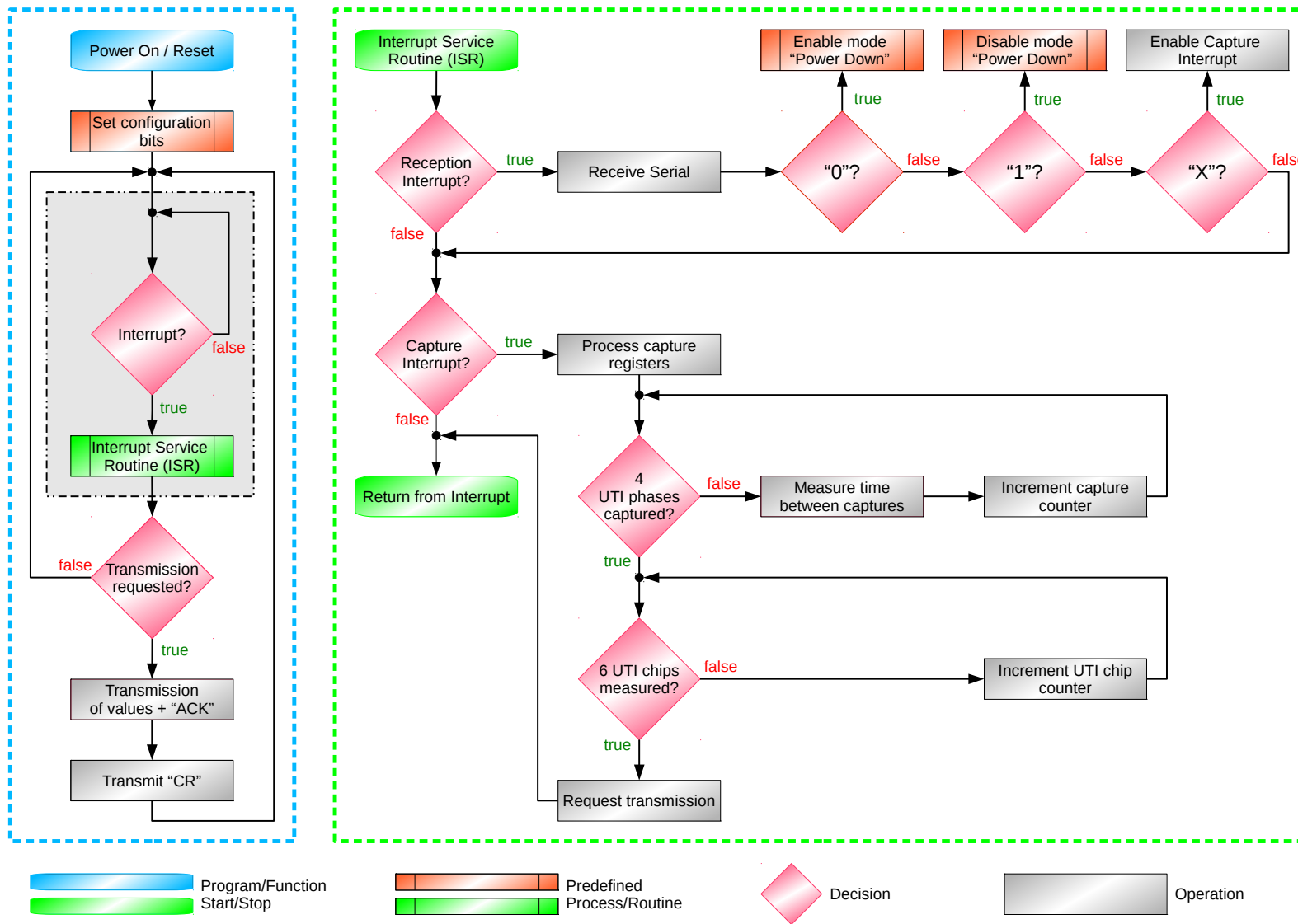


Figure 4.29: Firmware flow chart for the PIC16F877A microcontroller. See text for details.

The main program consists of an endless loop, which waits for a reception of a slow control command via RS-485. After connecting the PCB to operating voltage or pressing the push-button to trigger a master clear reset, the program starts with a POR ("Power on / Reset"). At first, several special function registers have to be set according to the desired functionality. In particular, the data direction of all used I/O pins has to be defined as input or output, using special data direction registers (e.g. register TRISA for PORTA). For instance, setting bit TRISA<2> to '1' will make the corresponding pin PORTA<2> an input. The following bullet list gives an overview of the configuration bits setup:

- Define data direction of ports PORTA, PORTB, PORTC, PORTD and PORTE according to their role as input or output. This is given by their connections shown in figure 4.27 and done by setting corresponding bits in the TRISA, TRISB, ... registers.
- Set bits FOSC1 and FOSC0 to '10' to enable the use of the external oscillator providing $f_{osc} = 12\text{ MHz}$.
- Move a decimal value of $x = 77$ to the SPBRG *Baud generator register* to set the Baud⁸ rate of the USART RS-485 communication to the closest value compared to $R_b = 9600\text{ Baud}$, given the equation

$$R_b = \frac{f_{osc}}{16(x + 1)}. \quad (4.27)$$

- Configure T1CON *timer1 control register* to count with a prescaling of 1 : 8 and to use internal clock, to count with a frequency of $f_{osc}/4$ (necessary for capture operation).
- Set several bits of the TXSTA *transmit status and control register* to enable or disable several options regarding the data transmission. Most important is bit TXEN (TXSTA<5>), which enables transmission if set to '1'.
- Set several bits of the RCSTA *receive status and control register* to enable the USART communication module and enables continuous reception with bit CREN (RCSTA<4>), which is the default mode of the program.
- Enable the capture mode for the measurement of the UTI phase lengths in the CCP1CON *capture control register*. This is done by setting the value of capture

⁸1 Baud = 1 Symbol/s. In digital systems such as this 1 Baud = 1 bit/s.

mode selection bits CCP1M3 to CCP1M0 to '0101' to configure the capture to happen at every rising edge of the signal at input RC2/CCP1.

- Enable all reception interrupts by setting the corresponding bit in the PIE1 *peripheral interrupt enable register*.

An interrupt is a signal indicating an event which needs immediate action. Once it appears, the central processing unit suspends the current program flow and jumps to a predefined memory location, where the so-called *interrupt service routine (ISR)* is saved, dealing with the interrupt in the desired way. Interrupts can be caused by several peripheral modules of the microcontroller and can be activated for each module in the PIE1 register. Flags in the PIR1 register indicate, which module caused the interrupt. Once the ISR finishes, the interrupt flags are cleared and the program continues at its previous memory position with the normal program flow. Table 4.4 lists all interrupts and their flag bits activated in the presented program.

Interrupts and corresponding flag bits	
Interrupt flag bit	Reason of interrupt
CCP1IF	A rising edge was recognized (captured) at pin RC2/CCP1
TMR1IF	The 16-bit timer counting the processor cycles between two rising edges has an overflow
RCIF	There was a RS-485 reception at pin RX/RC7

Table 4.4: Activated interrupts in the readout firmware. The interrupt flag bits indicate which of the listed peripheral functions caused the interrupt, and the interrupt service routine (ISR) takes action, accordingly.

As soon as an interrupt appears, the program jumps to the ISR. Since this is out of the usual program flow, that element is in the gray shaded box in figure 4.29. In the ISR, each interrupt flag bit is tested to identify the type of interrupt. In case of an RS-485 reception, the RCIF flag is set and the received byte is stored in RCREG register. The program then compares the received byte with the ASCII encoding of three allowed command characters:

1. Command '0': Enable power down mode. '0000 0000' is written to the output pins of PORTD enabling power down mode for all UTI chips, making them stop reading the level meters until next reception of command '1'. LED2 is switched on, LED3 is switched off.

2. Command '1': Disable power down mode. '1111 1111' is written to the output pins of PORTD disabling power down mode for all UTI chips, making them reading the level meters continuously. This is the default value at program start. LED3 is switched on, LED2 is switched off.
3. Command 'X': Request for level meter data. This request makes the microcontroller measure the cycle length of all level meters, process the data and transmit it via the RS-485 line. The frequency of this request by the slow control defines the sampling rate of the liquid level data points. It was chosen to be 1 s.

Upon reception of 'X', the initially disabled capture interrupt is activated, which will appear as soon as the first rising edge of the UTI output signal appears at pin RC2/CCP1. The value of the 16 bit internal program counter is automatically moved to the capture store registers CCP1L and CCP1H, from where it can be saved to a general purpose register. The counter TMR1 is reset and starts counting until the next capture interrupt due to the next rising edge in the signal, resulting again in new values in CCP1H and CCP1L. The difference of the two numbers is the duration of the period in units of $1/f_{osc}$. After each capture a defined counter is incremented. As introduced in figures 4.22 and 4.23, a measurement of all four periods requires capture of five rising edges. As soon as five captures have been made, the control pins of the multiplexer are incremented to forward the output of the next UTI chip to the capture module, where again all four periods are measured and saved in different general purpose registers. Once all phases of all UTI chips have been measured, the firmware sets a "requesting transmission" flag and jumps back to the main routine. The set flag is recognized in the main program as indicated in figure 4.29. The measurement data is then transmitted to the slow control sequentially from the general purpose registers.

For each UTI, the board transmits 4 measurement values consisting each of a 2 byte (16 bit) long number transmitted in hexadecimal format, e.g. for a SLM:

```
1 F9 2B 9B 0F 95 0F 33 28
```

Each pair of bytes represents the number of processor cycles to one of the four phases of a UTI measurement cycle. It is little-endian format, so in each pair the lower byte of the 16 bit number is least significant. Since 8 bit prescaling was selected, the counted values have to be multiplied by 8. As an example, the calculation of the measured number N of processor cycles from the data in the previous example is:

$$\begin{aligned}
2B F9_h &= 11257_d \cdot 8 = 90056 &= N_x \\
0F 9B_h &= 3995_d \cdot 8 = 31960 &= N_{off1} \\
0F 95_h &= 3989_d \cdot 8 = 31912 &= N_{off2} \\
28 33_h &= 10291_d \cdot 8 = 82328 &= N_{ref}
\end{aligned}$$

Note, that the sequence naturally does not have to start with an offset phase but can start with any phase of the cycle. Since the sequence is always kept, though, the duplicated offset phase enables the identification of each phase by the slow control system. With the time duration of N processor cycles

$$T = N \cdot \frac{4}{f_{osc}}, \quad (4.28)$$

$N_{off} = N_{off1} + N_{off2}$ and $C_{ref} = 10 \text{ pF}$, equation (4.18) yields $C_x = 14.18 \text{ pF}$ for this example. There is an uncertainty up to the second significant number in the counting of the phases, so one can assume conservatively $\Delta N = \mathcal{O}(100 \text{ counts})$, visible in the discrepancy of N_{off1} to N_{off2} . According to (4.28) this accounts for an uncertainty in the phase length of $\mathcal{O}(10 \mu\text{s})$, which amounts for a typical cycle length of tens of milliseconds to about 0.1%. In the transmission to the slow control each UTI data package is separated by an ASCII acknowledgment character 'ACK' (0x06). At the end of the sequence of all six UTIs, a carriage return ASCII character 'CR' (0x0D) is sent. The response of the readout board to a measurement request of the slow control is thus always 55 byte long:

1 `SLM1 06 SLM2 06 SLM3 06 SLM4 06 LLM1 06 LLM2 06 0D`

SLM1 to SLM4 and LLM1 to LLM2 represent the 8 byte measurement data of four phases of each UTI. The '06' character allows distinction between data of each UTI, the '0D' character at the end tells the slow control that the end of the transmission is reached.

4.4 Level meter system installation, calibration and data

4.4.1 Installation

During the integration of the XENON1T TPC in an above ground clean room at the LNGS, the four SLMs were installed on 2015/10/28. They are located on the TPC top ring as shown in figure 4.30(a). The stainless steel top ring is shown, as well as the white coax cables, which were fed through holes in the top ring and fixed with a PTFE strain relief. Afterwards there were guided towards and connected to the cable bunches and feedthroughs. The meshes had not yet been installed. The long level meters were installed later, on 2015/11/04, when the TPC was already moved underground and mounted in the cryostat inside the water tank. Figure 4.30(b) shows the upper part of an installed LLM. The PTFE top cap is visible with connection screws and the attached cables. Figure 4.30(c) shows the PTFE pillar hosting the LLM. Next to it is the cathode high voltage feedthrough as well as signal and HV cables leading to the bottom PMT array. Here, the TPC is already mounted to the cryostat and the LLM is reaching into it. Shortly after, the cryostats were closed and the XENON1T TPC installation was finished.

In the global TPC coordinate system, the level meter centers are at the following calculated positions:

Level meter positions		
	x	y
SLM 1	−193 mm	−478 mm
SLM 2	478 mm	−193 mm
SLM 3	193 mm	478 mm
SLM 4	−478 mm	193 mm
LLM 1	−70 mm	−529 mm
LLM 2	70 mm	529 mm

Table 4.5: Level meter positions in the XENON1T coordinate system.

After installation and closing of the cryostat all level meters were tested with the readout board for 30 minutes with a 1 s sampling under vacuum. The results are shown in figure 4.31.

The capacitance values of the SLMs agree with the results of the previous tests in liquid nitrogen. Only SLM1 showed a reduction of capacitance by a factor of

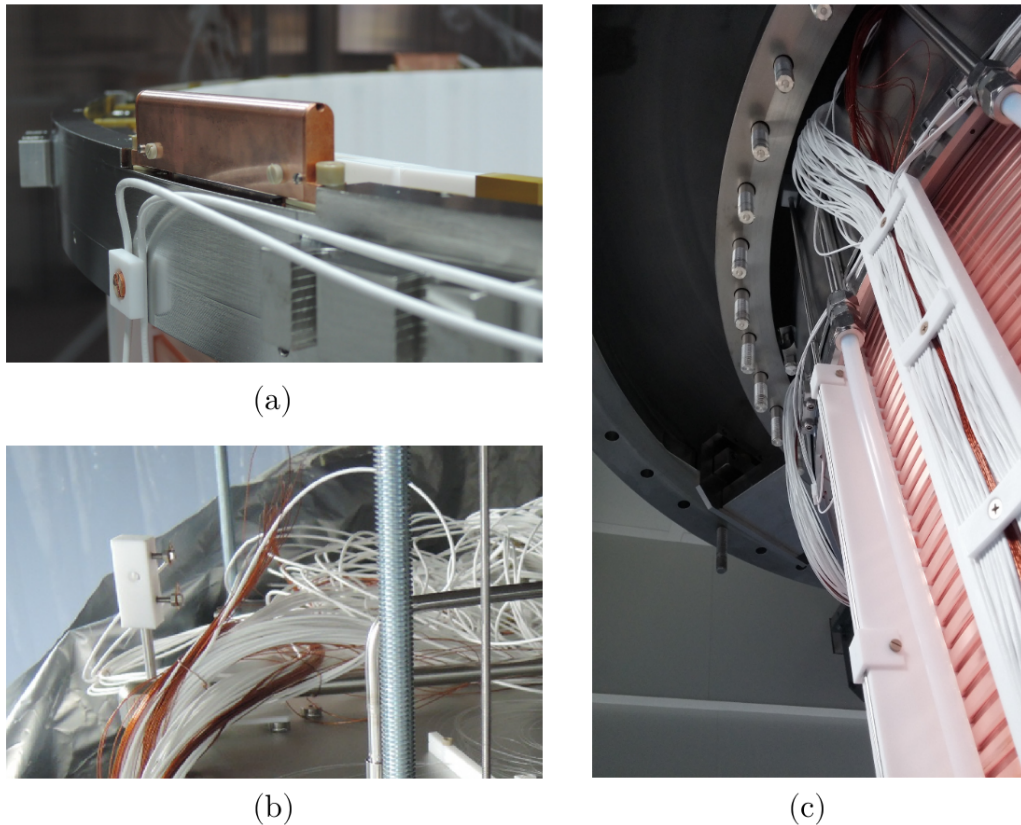


Figure 4.30: (a) Installed SLM on the TPC top ring. The signal cables are fed through holes in the top ring and are fixed with a PTFE strain relief (lower left on the picture); (b) Top cap of long level meter with attached connection screws and cables; (c) The PTFE pillar hosting the LLM. The LLM reaches into the top part of the cryostat once the TPC is lifted all the way up.

2. A possible explanation is that the electric contact of one of the outer plates got disconnected, reducing the effective area by two and thus the total capacitance. However, SLM 1 can still be used as a level meter with reduced dynamic capacitive range. The error on the mean value was measured to be ≈ 0.02 pF for SLM2-4 and 0.01 pF for SLM1. Both LLMs were working with ≈ 10 pF higher absolute capacitances than simulated. Their resolution is a factor of 10 less than for the short level meters, about 0.2 pF.

4.4.2 Detector filling and level meter calibration

Monitoring the LXe level during filling

After closing of the cryostats, a period of vacuum pumping and a cool down phase with cold xenon gas followed. Unfortunately, LLM1 stopped working at some time during

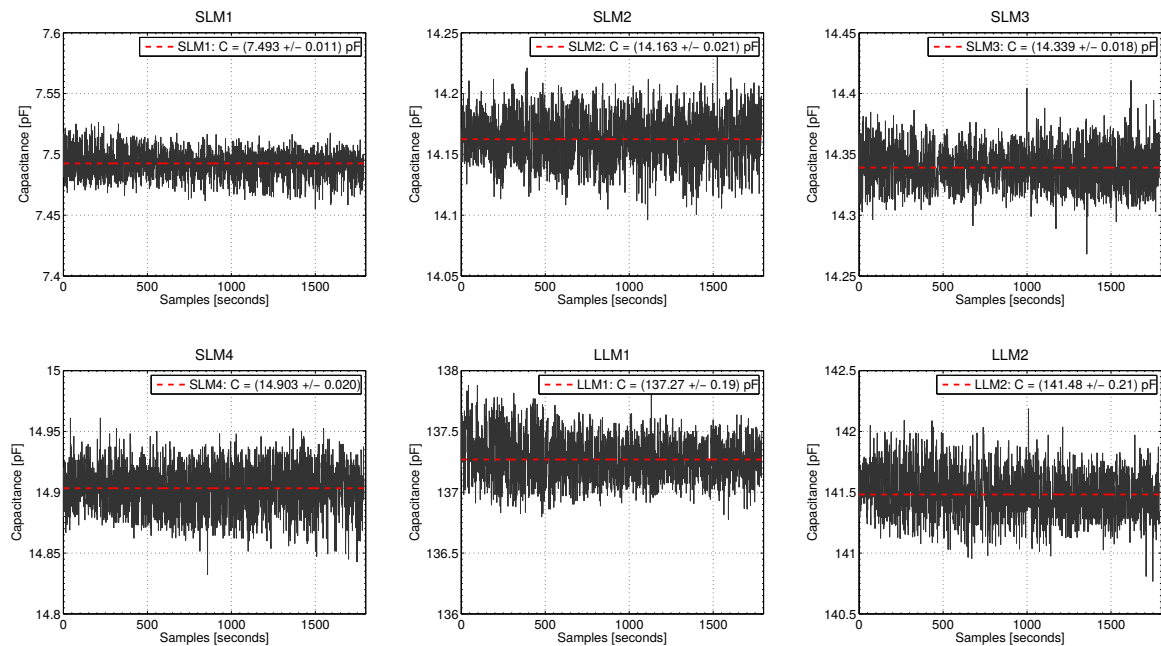


Figure 4.31: Post-installation tests of all level meters verify their full functionality.

the cool down period of the TPC and never recovered. Tests discovered, that both pipes were electrically connected, which could indicate, that the contraction of the TPC during cool down possibly squeezed the pipes at a position between two PTFE spacers until they touch each other. LLM2 remained operational. In April 2016 it was decided to start filling the TPC with xenon. Figure 4.32 shows the first filling of XENON1T over 6 days in April using the measured capacitance values of LLM2.

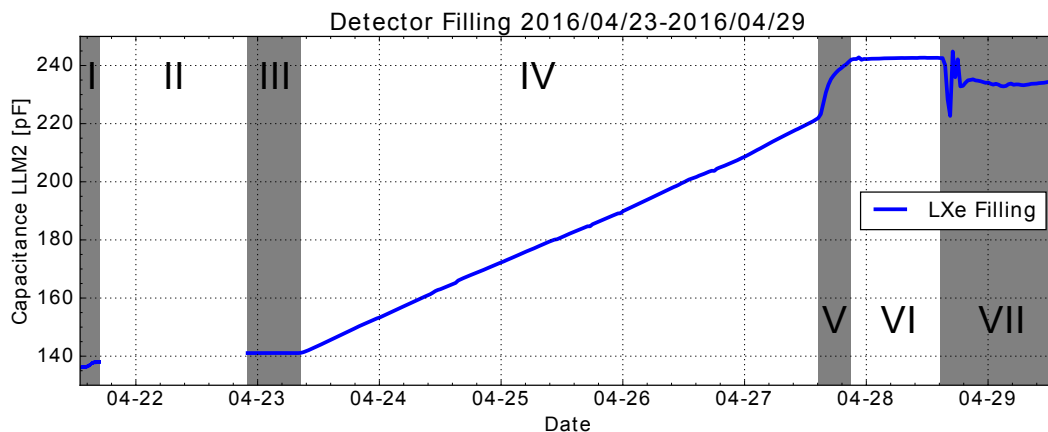


Figure 4.32: Observation of the LXe filling process of the XENON1T TPC using LLM2. I: Entry of LXe level in long level meter; II: GXe filling without recording the level meter readings; III stable phase before LXe filling; IV LXe filling of entire TPC; V bell reached - heat load causes non-linearity; VI observation of stability; VII recuperation tests.

The filling process was divided in several phases, labeled in Roman letters in the figure. Phase I was the first phase, where GXe was filled from ReStoX in the TPC with a flow of 20 slpm (≈ 86 kg/d) and condensed by controlling the temperature in the detector. This is a slow process, intended to minimize the thermal shock to the bottom PMTs and to not miss the entry of the liquid xenon in the long level meter (visible as slow jump in the figure). At this time the readout board was not yet implemented in the slow control system, such that in phase II GXe was continued to fill but the level meter measurements were not recorded by the slow control system. It followed a stable phase III during which preparations were made to start filling liquid xenon directly from ReStoX to the TPC with 100 slpm (≈ 430 kg/d). This phase IV lasted for about four days, monitored by LLM2. At the beginning of phase V the liquid level reached the bell, introducing a large heat load, which caused the rapid rise of the liquid outside of the bell. During this phase, also the SLMs were completely filled to calibrate them as explained below. After a phase VI without any actions to observe the stability of the detector several recuperation tests followed (VII), which had influence on the liquid level, also shown in the figure.

Calibration of SLMs and LLMs

The short level meters were calibrated during the filling of the TPC. The liquid level inside the bell was risen until all short level meters were overfilled. Exemplary, this is shown in figure 4.33(a) for SLM 3. It shows the capacitance trend over time. Several features known from the LN₂ test (figure 4.14) can also here be identified, such as the sudden capacitance jump caused by capillarity at 14:37 or the bump caused by surface tension of liquid xenon when reaching the top of the SLM. Dividing the difference of capacitance C_l of the overfilled level meter and the capacitance C_g of the completely gas filled level meter by the plate height 10 mm yields the calibration factor R . The formula to convert capacitance values C_{LM} in pF obtained with the level meters to height values h_{LM} in mm is then:

$$h_{LM} = \frac{C_{LM} - C_g - C_C}{R} - H_G. \quad (4.29)$$

This equation holds also for the long level meters. C_C is the capacitance increase due to capillarity in the level meter and has to be subtracted from the reading to ensure calculating the same liquid height values inside the level meter as outside. H_G is the height offset of the lower end of the level meter plates to the z coordinate of the gate mesh. It is convenient to express the liquid level height in mm above the

gate mesh. H_G for all small level meters is 1.5 mm, for LLMs it is 1057 mm. Table 4.6 shows the results of the SLM calibration. All calibration factors are $\approx 20\%$ smaller than the simulated values, due to the lower absolute capacitance values measured. The measured capacitances due to capillarity are even $> 50\%$ smaller than the expected ones. In addition to the lower real calibration factor, it seems that the estimation of the contact angle $\cos \Theta = 1$ in section 4.2.1 was too conservative.

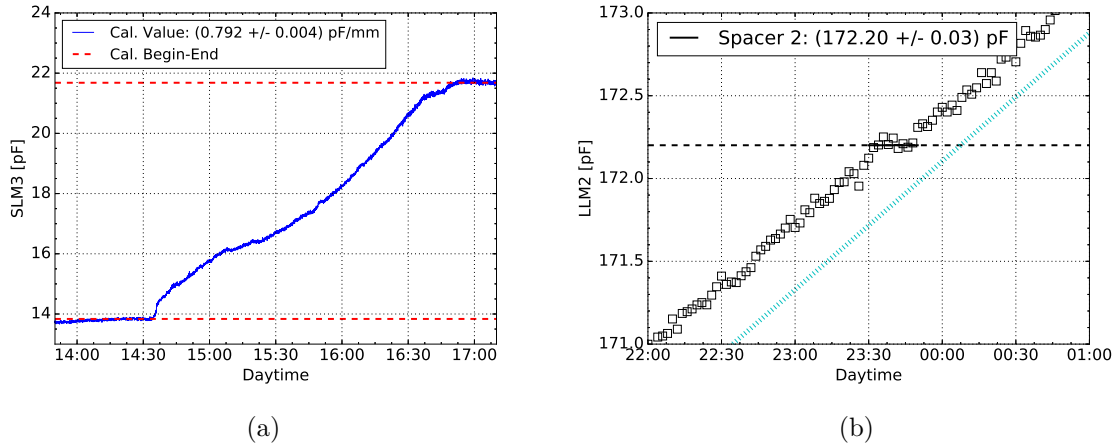


Figure 4.33: Examples for calibrations of the SLMs and LLM2. (a) Overfilling of SLM 3 enables a calibration by dividing the difference of capacitances of fully immersed and fully emptied level meter (red dashed lines) by the height of the SLM plates; (b) Preinstalled PTFE spacers at fixed distances on the inner pipe of the LLMs allow calibration by subtracting the capacitance values at each spacer and division by the distance in between (here, spacer 2 at 46 cm height). The spacers appear in the LLM2 reading (black boxes) as plateau (black dashed line). The blue dashed line is a line fit to the filling curve in figure 4.32 as comparison.

The long level meters reach too high above the bell to be overfilled. Instead we used the four PTFE spacers at known positions (compare section 4.2.2), which are covered by the liquid. Given the simulated $\Delta C/h$ value of the LLM, an expectation for the capacitance values could be calculated where the spacers should appear. The ring shape of the spacers surrounding the inner tube of an LLM acts as an additional dielectric between outer and inner tube, resulting in a constant capacitance value, visible as plateau in the filling curve. Figure 4.33(b) shows this exemplary for spacer 2 at 46 cm height from the lower end of LLM2. Each black square corresponds to the mean of two minutes (120 samples by the readout system). A plateau is visible at $C_2 = 172.2$ pF and 23:30 of 2017/04/25. As verification that the feature is really induced by a PTFE spacer holds the fact that the duration of the plateau (≈ 20 minutes) fits to the constant fill rate of the detector at that time of ≈ 1 cm/h. This means that the object causing

the kink is $\approx 1/3$ of a cm, which fits to the 3 mm height of the PTFE spacers. Given C_g of the LLM, calibration factors R_{ij} can be calculated between spacers i and j . For comparison, the blue dashed line indicates a line fit to the complete filling curve of figure 4.32 with a slope $m = (0.78 \pm 0.03)$ pF/mm. Table 4.7 shows the results of the calibration of LLM2 including all relevant parameters

Level meter calibration				
Parameter	SLM 1	SLM 2	SLM 3	SLM 4
C_g [pF]	7.53 ± 0.02	13.73 ± 0.02	13.93 ± 0.02	14.33 ± 0.03
C_l [pF]	11.62 ± 0.02	21.53 ± 0.05	21.85 ± 0.04	22.65 ± 0.04
C_C [pF]	0.24 ± 0.02	0.50 ± 0.03	0.46 ± 0.03	0.40 ± 0.02
R [pF/mm]	0.408 ± 0.002	0.779 ± 0.005	0.792 ± 0.005	0.832 ± 0.005

Table 4.6: Calibration values for the SLMs. Measurements of the capacitances of the fully immersed level meter C_l and the empty one C_g , and the capacitance increase from capillarity C_C allow to calculate a calibration factor R .

The capillarity effect in the LLM2 is not resolvable given its resolution of ± 0.2 pF. Also for the LLM, the calibration factor is lower than the simulated one ($\approx 10\%$): It appears that the COMSOL simulations yielded too high capacitances in general. The values of both tables have been implemented in the slow control and the level meter readings are recorded in pF and mm values.

4.4.3 Long term measurement of the LXe level

After presenting design, installation and calibration of data, now a few examples of data and correlations to other detector parameters are discussed. First, figure 4.34 shows level meter data of SLMs and LLM2 from June 2016 up to May 2017. This covers one full year, with exception of a few periods during filling and some basic tests afterwards resulting in high fluctuations of the level meter readings, which have been omitted for clarity. The gray shaded fields indicate the time of science data taking, science run 0 (SR0) and 1 (SR1). Each data point on the picture is the mean of 600 data points which were sampled in one minute intervals from the database, i.e. a time resolution of 10 h. Several long term features are visible, which correspond to different tests with a liquid level change needed, especially before SR0.

During SR0 an oscillation of SLMs with a continuous decrease of the LLM can be observed. This was due to krypton distillation, which was performed in parallel with data taking. This slowly reduced the amount of LXe in the TPC as krypton-enriched

Level meter calibration		
Parameter	LLM1 ^{†)}	LLM2
C_g [pF]	—	136.1 ± 0.2
C_1 [pF]	—	— ^{*)}
C_1 [pF]	—	153.16 ± 0.01
C_2 [pF]	—	172.20 ± 0.02
C_3 [pF]	—	189.32 ± 0.03
C_4 [pF]	—	208.46 ± 0.04
C_5 [pF]	—	— ^{‡)}
C_C [pF]	—	0.2 ± 0.2
R_{01} [pF/mm]	—	0.079 ± 0.002
R_{12} [pF/mm]	—	0.083 ± 0.002
R_{23} [pF/mm]	—	0.074 ± 0.002
R_{34} [pF/mm]	—	0.083 ± 0.002
R_{04} [pF/mm]	—	0.084 ± 0.003
\bar{R} [pF/mm]	—	0.080 ± 0.004

Table 4.7: Calibration values for the LLMs. Measurements of the capacitances at PTFE spacers $C_{1...5}$, of the empty level meters C_g , and the capacitance increase from capillarity C_C allow to calculate a mean calibration factor \bar{R} . ^{†)} LLM1 unfortunately stopped working during cool-down of the detector and never recovered. ^{*)} The LLMs are too long to be fully immersed in LXe. ^{‡)} Spacer 5 had to be skipped, since it was never reached by the liquid.

xenon off gas was recuperated. While inside the bell the loss of xenon was adjusted by a lowered gas flow lifting the liquid level, outside of the bell LLM2 measures a continuous decrease during that period. The increased fluctuation of the level inside the bell beginning from 2016/12/19 is induced by an increased gas flow. With begin of science run 1 the liquid level remained more or less untouched. Only after an earthquake on 2017/01/18 detector stability tests have been performed including changes of the liquid level.

4.5 TPC Leveling

The XENON1T cryostat is suspended from three vertical stainless steel rods. The length of each of the rods is adjustable by a mechanism on top of the XENON1T water tank. The goal of these adjustments is to align the grids in the TPC with the LXe level. translate the measured orientation of the grid plane in an adjustment of

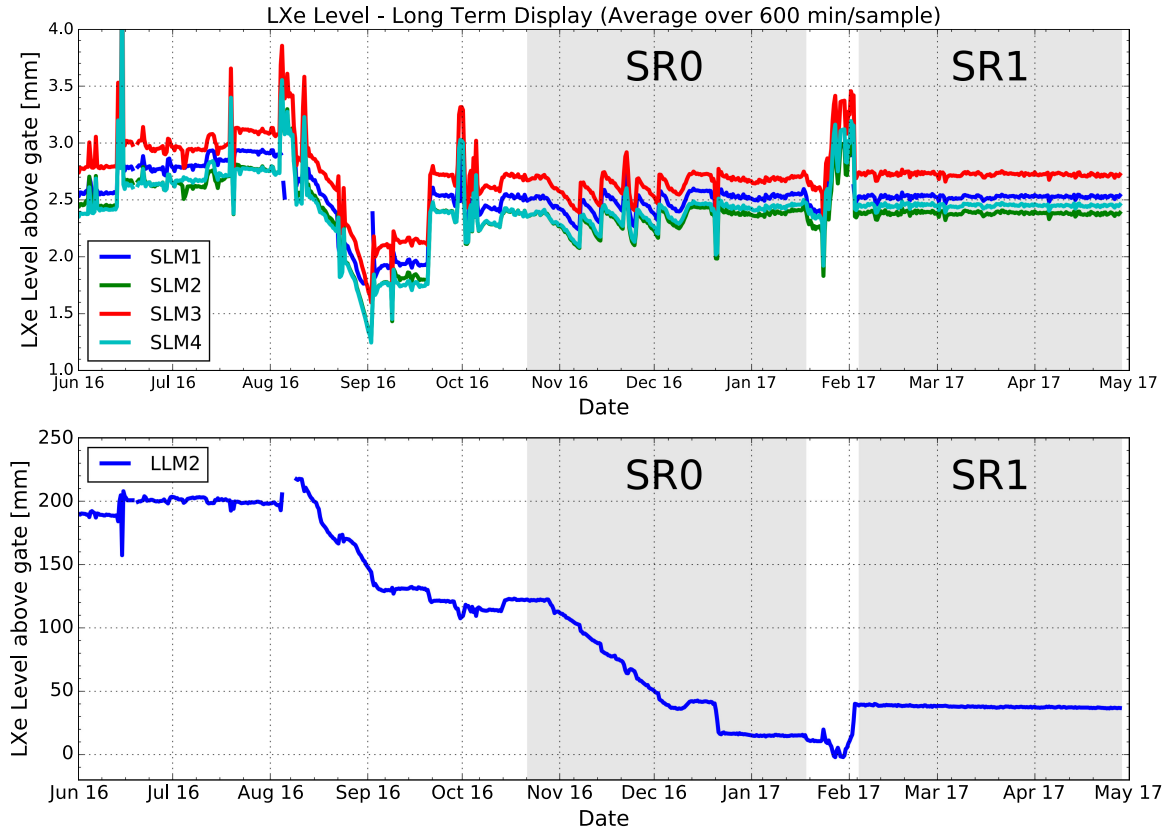


Figure 4.34: Long term display of short and long level meters from June 2016 until May 2017. Every data point represents the mean value of 600 single data points. After several tests the liquid level was kept stable for science runs SR0 and SR1. Oscillations in the SLM and a decrease in the LLM during SR0 is related to xenon losses in the off gas of the parallel running krypton distillation column.

the suspension rods. The coordinate system is right handed, defined with the z -axis pointing upwards as shown in figure 4.35.

The arms of the leveling mechanism all have length L , and the three suspension points of the rods are indicated with $S_{1/2/3}$. One can change the length of the rods by turning adjustment nuts of a coarse adjustment system, where one complete turn results in 2 mm length difference, and a fine adjustment system, where twelve complete turns result in 2 mm length difference. To tilt meters are installed on this leveling system. They are fixed on the support structure and measure relative tilt according to the y axis (TILTA) and the x axis (TILTB). In the following two sections, the leveling of the XENON1T TPC is presented, performed with data analysis of the short level meters as well as the S2 width signal.

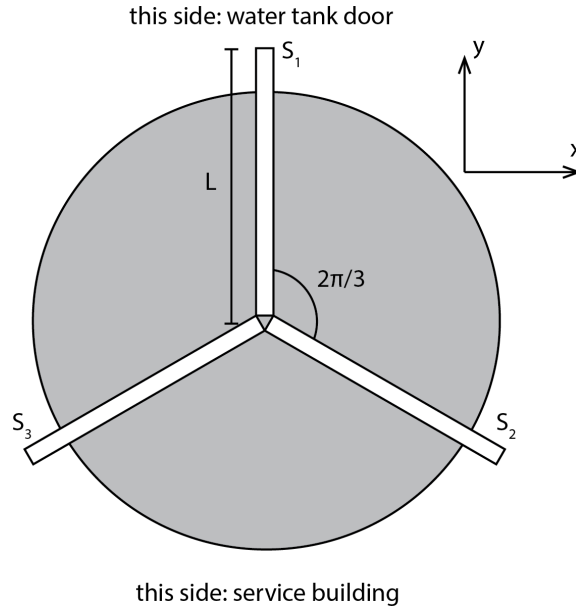


Figure 4.35: The XENON1T leveling system. The length of three rods S_1 , S_2 and S_3 can be adjusted to manipulate the tilt of the TPC. Figure created by Auke-Pieter Colijn.

4.5.1 Compensation of residual tilt based on level meter readings

The readings of all four short level meters provide a redundant measurement of the tilt of the TPC described by the corresponding normal vector, which is converted to an adjustment prescription on the leveling system. The goal is to have all short level meter readings as close as possible, within errors, at the same value. Like this, a finer leveling than the bubble-level measurement at installation stage of the TPC is possible. It works by using the `scipy.linalg.lstsq` function, which computes a least-squares solution to an equation $\mathbf{A} \cdot \vec{p} = \vec{h}$, where \vec{h} is a vector containing the readings of all short level meters, \mathbf{A} is a 4×3 -matrix constructed from the (x, y) coordinates of the level meter positions, such that \vec{p} is a vector of three parameters, which minimizes

$$\mathbf{A} \cdot \vec{p} = \vec{h} \quad \Leftrightarrow \quad \begin{pmatrix} x_{\text{SLM1}} & y_{\text{SLM1}} & 1 \\ x_{\text{SLM2}} & y_{\text{SLM2}} & 1 \\ x_{\text{SLM3}} & y_{\text{SLM3}} & 1 \\ x_{\text{SLM4}} & y_{\text{SLM4}} & 1 \end{pmatrix} \cdot \begin{pmatrix} p_0 \\ p_1 \\ p_2 \end{pmatrix} = \begin{pmatrix} h_{\text{SLM1}} \\ h_{\text{SLM2}} \\ h_{\text{SLM3}} \\ h_{\text{SLM4}} \end{pmatrix}. \quad (4.30)$$

The elements of \vec{p} describe a plane

$$p_0x + p_1y + p_2 = h \quad (4.31)$$

which is the best-fitting plane with respect to the level meter readings. The normal unit vector $\vec{n}_{0,\text{SLM}}$ of that plane is:

$$\vec{n}_{0,\text{SLM}} = \frac{\vec{n}_{\text{SLM}}}{|\vec{n}_{\text{SLM}}|} = \left(-\frac{p_0}{|\vec{n}_{\text{SLM}}|}, -\frac{p_1}{|\vec{n}_{\text{SLM}}|}, \frac{1}{|\vec{n}_{\text{SLM}}|} \right). \quad (4.32)$$

The tilt of the TPC obtained by the level meter readings is equal to the angle ξ_{SLM} between $\vec{n}_{0,\text{SLM}}$ and the unit normal vector of plane of the liquid surface $\vec{n}_0 = (0, 0, 1)$ and can thus be calculated as

$$\xi_{\text{SLM}} = \arccos(\vec{n}_{0,\text{SLM}} \cdot \vec{n}_0). \quad (4.33)$$

The gradient of the tilt points towards

$$\phi_{\text{SLM}} = \arctan(p_1/p_0) + 180^\circ. \quad (4.34)$$

Calculating those parameters allows to adjust the tilt with the coarse and fine tilt adjustment system of the cryostat. The following actions have been performed from 2016/05/16 to 2016/05/18 at a time, when the water tank was not yet filled and no water was surrounding the cryostat. Figure 4.36 shows the readings of the short level meters and the two tilt meters before the first tilt operation (Phase I). The four average level meter readings are far from each other (standard deviation of 0.6 mm). Application of equations (4.32) to (4.34) leads to the calculated values in table 4.8. The $\xi_{\text{SLM}} = 0.0968^\circ$ indicates a tilt large enough to require the coarse tilt mechanism, which resulted in the instructions of rotating nut “coarse S2” 0.5 turns clockwise and rotate nut “coarse S3” 0.5 turns counter-clockwise.

The evolution of the data values in the figure illustrates the tilting action on 2017/05/15 between 15:13 and 15:38. Tilt meter A observed a change of ≈ 2 mrad along the y axis. The SLM readings show a lower standard deviation of 0.25 mm afterwards (Phase II in table 4.8). The residual tilt angle was $\xi_{\text{SLM}} = 0.0389^\circ$. This value was small enough to require actions only on the fine tilt adjustment nuts, namely rotation of “fine S1” for 2.2 turns counter-clockwise and rotation of “fine S3” for 2.2 turns clockwise. These adjustments are visible in the level and tilt meter readings on 2017/05/18 between 14:40 and 14:55 in figure 4.37.

The residual tilt after the fine adjustments (Phase III) ended up to be very small ($\xi_{\text{SLM}} = 0.0011^\circ$). Error propagation for ξ_{SLM} is, according to equations (4.32) and (4.33), not very meaningful, since the statistical uncertainties of p_0 and p_1 have almost no effect on the calculation, resulting in the tiny statistical errors reported in table 4.11. Instead we estimate the systematic error, from the maximum and minimum tilt

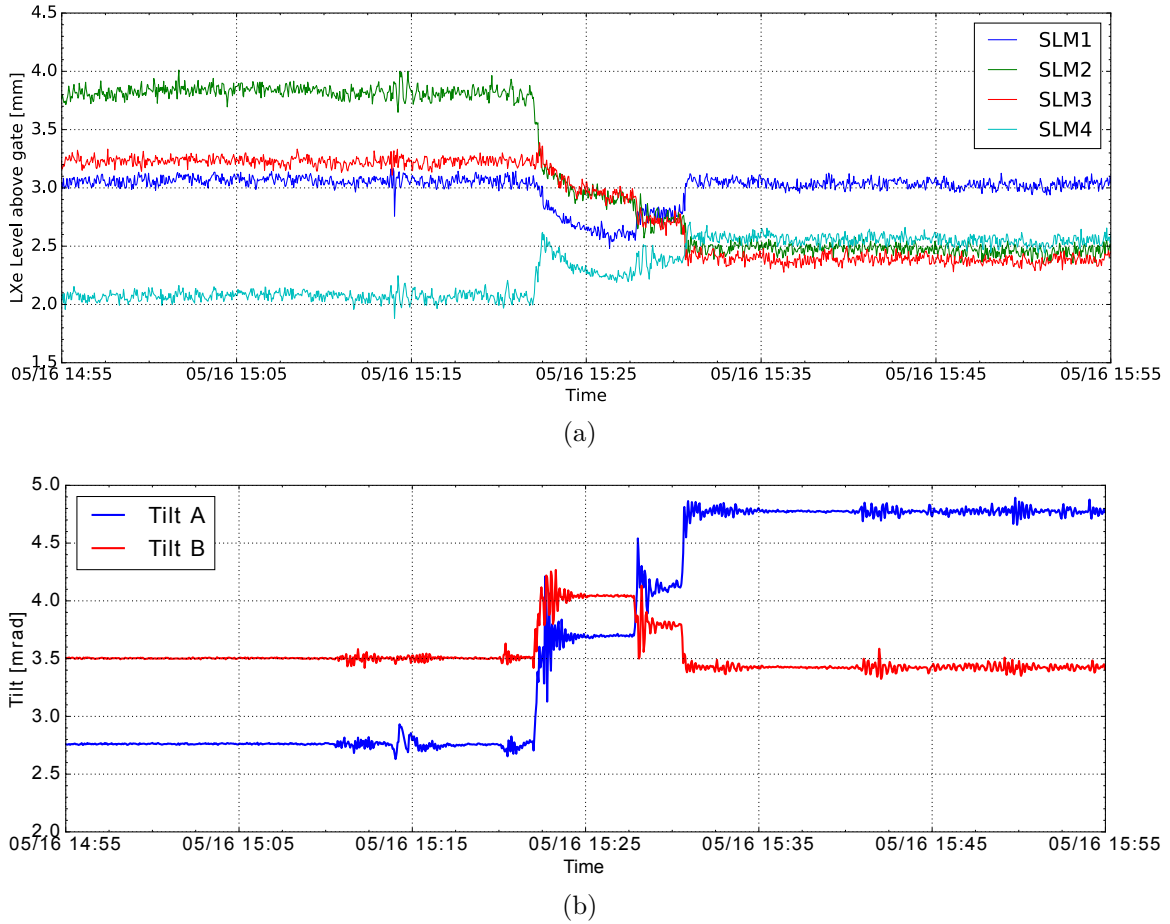


Figure 4.36: (a) The short level meter readings during the adjustment of the TPC tilt with the coarse leveling system. The leveling reduced the standard deviation between the single level meter readings from 0.62 mm to 0.25 mm; (b) Readings of tilt meters A (blue) and B (red) during the same period of time. While the reading of tilt meter B remains almost the same before and after the leveling operation, tilt meter A shows changes of ≈ 2 mrad. This indicates a tilt correction almost exactly along the y axis.

angle obtained by inserting the extreme values of the fit parameters in equation (4.31), yielding an uncertainty of $\approx 0.015^\circ$ for all ξ_{SLM} . The better the TPC is leveled, the less determined is the angle ϕ_{SLM} , nicely observable by the rise of its uncertainty for decreasing tilt. Due to the leveling corrections, the computed tilt angle ξ_{SLM} becomes essentially zero. However, it is evident that SLM 1 and 3, as well as SLM 2 and 4 each show equal values after phase III, separated by $200 \mu\text{m}$. This means that the residual tilt is not further improvable. Since only opposing SLMs show equal results, we consider two possible effects, which could explain this. First, a saddle-like deformation of the TPC top ring in the order of the discrepancies of the level meter readings possibly due to tensions after cool down. Second, one short level meter could be out-of-plane with

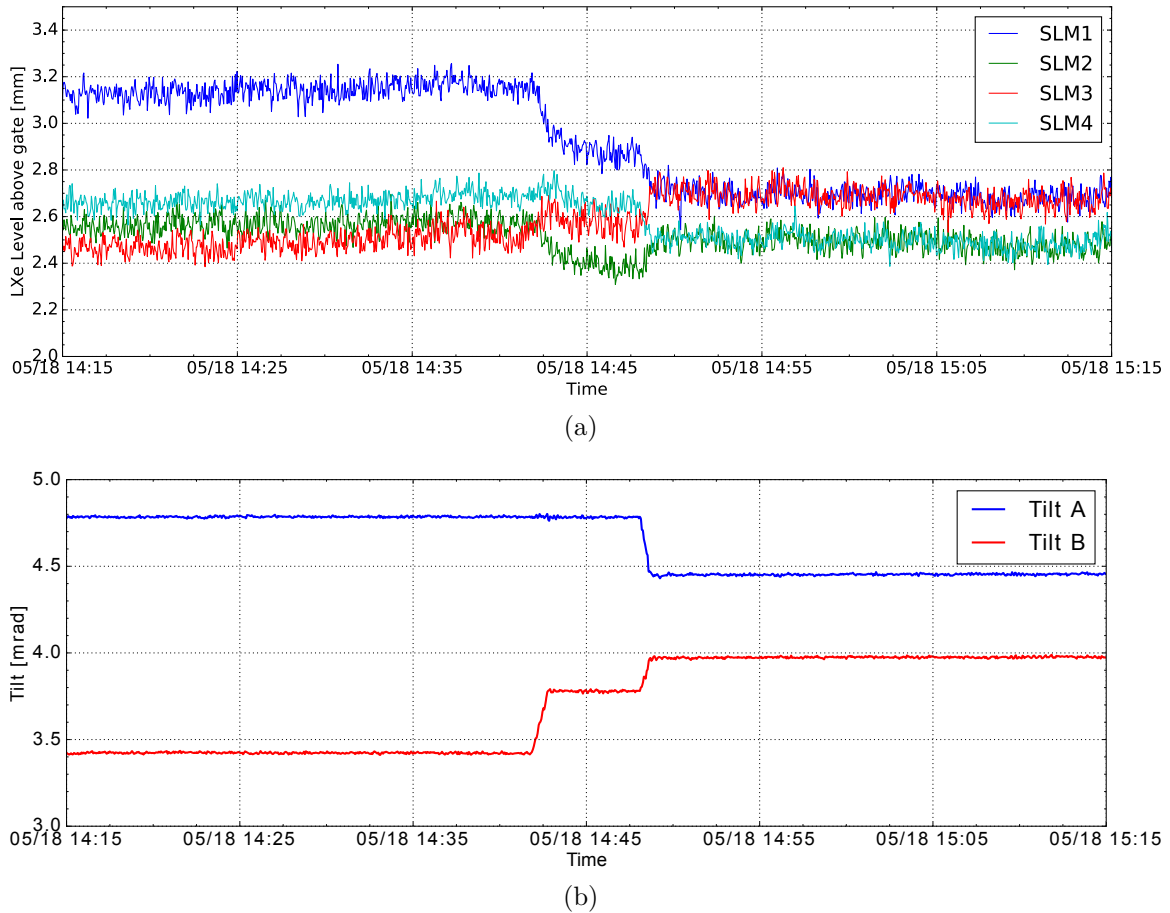


Figure 4.37: (a) The short level meter readings during the adjustment of the TPC tilt with the fine leveling system. The leveling reduced the standard deviation between the single level meter readings from 0.25 mm to 0.10 mm. Further tilt compensation is not possible. The residual tilt and the superposition of two opposing level meters indicate the possibility of one SLM being out-of-plane compared to the others; (b) The simultaneous readings of the TPC tilt meters show an decrease of ≈ 0.25 mrad for tilt meter A (blue) and an increase of ≈ 1 mrad for tilt meter B.

respect to the others as a result of not perfect installation. A best fitting plane to the four positions would result in the observed effect (see section 4.5.3 for a detailed study on this). While the first hypothesis is not very likely and hard to check, the second one can be tested with a cross-measurement of the TPC tilt using the S2 signal width, discussed in the following section.

4.5.2 S2 signal width based leveling and mesh warping

Due to the high electric field between gate mesh and anode, electrons get extracted at the liquid gas interface and drift towards the anode. Strictly speaking, it is the field in

Leveling operations from 2016/05/016 to 2016/05/18			
Tilt parameters	Phase I	Phase II	Phase III
h_{SLM1}	(3.07 ± 0.03) mm	(3.13 ± 0.03) mm	(2.61 ± 0.04) mm
h_{SLM2}	(3.82 ± 0.03) mm	(2.56 ± 0.03) mm	(2.41 ± 0.03) mm
h_{SLM3}	(3.26 ± 0.04) mm	(2.47 ± 0.03) mm	(2.62 ± 0.04) mm
h_{SLM4}	(2.09 ± 0.03) mm	(2.65 ± 0.03) mm	(2.42 ± 0.03) mm
\bar{h}_{SLM}	(3.06 ± 0.62) mm	(2.70 ± 0.25) mm	(2.51 ± 0.10) mm
ξ_{SLM}	$(0.09681 \pm 0.00002)^\circ$	$(0.03890 \pm 0.00001)^\circ$	$(0.00111 \pm 0.00001)^\circ$
ϕ_{SLM}	$(164.2 \pm 9.9)^\circ$	$(62.5 \pm 22.8)^\circ$	$(265.5 \pm 751.7)^\circ$

Table 4.8: SLM values and corresponding tilt parameters for the three TPC leveling phases: before the tilting operations (Phase I); after the coarse leveling and before the fine leveling (Phase II); after the fine leveling (Phase III). The statistical errors of ξ_{SLM} are very small, their systematic error is in the range of $\pm 0.015^\circ$. As more the tilt decreases as more ϕ_{SLM} is undetermined and reaches therefore arbitrary high uncertainties.

the liquid phase that is responsible for extraction. Its exact value is depending on the position of the liquid gas interface because of the different dielectric constants of LXe and GXe. The scintillation light produced during the passage of electrons through the gas is proportional to the number of electrons produced. The meshes which apply the electric fields in the detector are at fixed positions. Hence, a lower or higher level of the liquid-gas interface has direct influence on the drift length of the extracted electrons in the gas and thus on the width of the S2 signal. While an earlier study within the collaboration verified this behavior for single electron S2s, the study presented here was performed to verify it for large, possibly saturated, S2 signals. In the following, we use width and area information of those large S2 signals to infer the tilt of the TPC and effects due to anode or gate mesh warping.

For anode and gate mesh approximated as parallel plates, separated by a layer of x_g of GXe on top of an LXe layer of x_l , their separation is $x_g + x_l = 5$ mm everywhere, ignoring possible mesh warping. The electric field in the gas E_g is then

$$E_g = \frac{U}{x_g + x_l/\varepsilon_l}, \quad (4.35)$$

with U being the high voltage applied between anode and gate and ε_l being the relative permittivity of LXe, ignoring the tiny non-unity of the relative permittivity of GXe. The drift velocity v_d of electrons in the gas is proportional to E_g [60]. Since we assume the field in the gas to be constant, the drift velocity is also constant, so the width w_{S2} of an S2 signal resulting from the drift time t_d of the electrons is

$$w_{S2} \propto t_d = \frac{x_g}{v_d} \propto \frac{x_g}{E_g} = \frac{x_g(x_g + x_l/\varepsilon_l)}{U}. \quad (4.36)$$

For invariant electric field E_g the width w_{S2} of the S2 signal is therefore directly proportional to the gas gap length x_g .

S2 width data and event selection

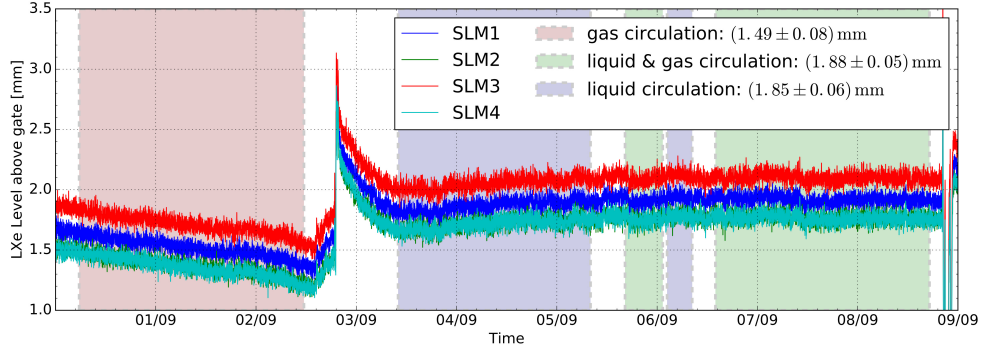
For this study, background datasets were used which have been taken during a test run in the period of 2016/08/31 - 2016/09/09. The high voltage on the anode mesh during the full data taking period was constantly at $U_A = +4$ kV. Background datasets have been preferred to external calibration datasets due to the more uniform distribution of events across the TPCs cross-section, while internal calibration datasets were not yet available. The data is divided in three sub-periods corresponding to three tested circulation methods (compare table 4.9)

Live time of S2 width study data	
Circulation Mode	Live Time
gas only	2.14 live-days
liquid & gas	1.89 live-days
liquid only	2.09 live-days

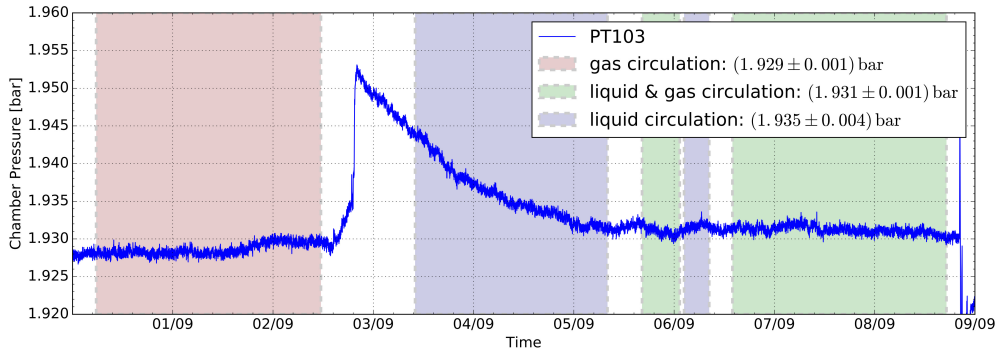
Table 4.9: Live time and data selection for the S2 width study.

Changing the circulation methods leads to an equilibrium change in the TPC, which results in different liquid levels for each circulation phase. During each phase, stable detector conditions are important for an inspection of the S2 width parameter. Figure 4.38(a) shows the reading of the short level meters in the above mentioned period in mm liquid level above gate mesh, figure 4.38(b) the pressure reading of PT103 in bar (xenon gas pressure in the detector) during the same period. The differently shaded backgrounds represent the different periods of data used for the analysis. There was a long term drift towards decreasing levels for the gas circulation due to losses of xenon in the off-gas of the distillation column which was running in parallel during that period. The visible peak with a tail was due to changes in the voltage settings of the QDrive helium compressors necessary for the circulation method change. Within the periods of gas & liquid and only liquid circulation, the liquid level was more stable than during the gas circulation period. Since the pressure was still decreasing during the liquid circulation phase and also the level was most stable in the liquid & gas circulation

phase all following plots show data from that period (the study has been performed on all circulation phases).



(a)



(b)

Figure 4.38: Liquid level and detector pressure stability during the data taking period of the S2 width analysis. For the study data was taken with three recirculation methods: gas only circulation for 2.14 live-days (transparent red), liquid only circulation for 2.09 live-days (transparent blue) and gas & liquid circulation for 1.89 live-days (transparent green). (a) the four short level meters (SLM 1–4); (b) the detector pressure. The spike between 2nd and 3rd of September was due to stopping the previously running xenon distillation and the change from gas to liquid circulation.

Given the measured values of all four short level meters, the gas gap can be calculated as $x_g = 5 \text{ mm} - 1.88 \text{ mm} = 3.12 \text{ mm}$, the pressure has been measured to be $P = 1.931 \text{ bar}$.

A first stage of data selection is necessary to select only S2 events for the analysis. A `hax.minitrees.TreeMaker` class was written to extract only S2 properties of processed data files and has been used to extract the data discussed in the following (compare section 2.2.5). Figure 4.39 shows the event rate of the TPC in 2D histograms for all

peaks (figure 4.39(a)) and an S2 peaks selection (figure 4.39(b)). Both histograms show the detection rate of S2 peaks for peak area A_{S2} (in PE) versus the S2 width w_{S2} in ns at 50% pulse area for the liquid circulation phase. This rate includes all peaks detected with the TPC which PAX considers as S2 signals. In fact, only a fraction of them are the S2 signals interesting for this study.

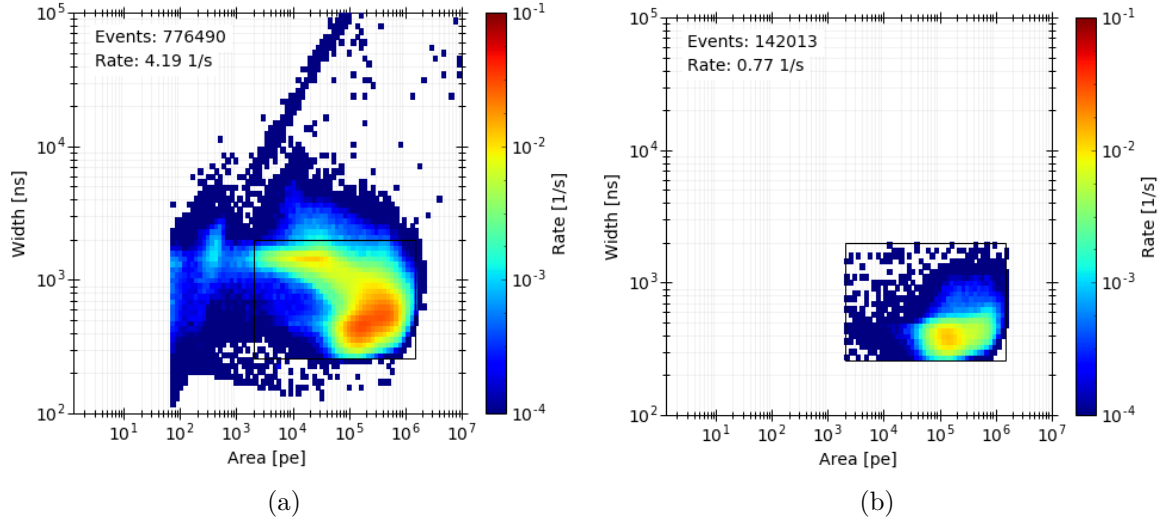


Figure 4.39: Peak rate and S2 event selection for the S2 width study. (a) Event rate for all peaks considered as S2 by PAX, including also single electrons, multi electron signals and uncorrected S2 peaks at all reconstructed z positions; (b) Surviving signals after application of selection cuts.

The population of large S2 signals ranges roughly from 10^3 – 10^6 PE and 200–2000 ns width. Populations of multi electron pileups following large S2 signals are visible as a line feature above 10^4 ns width. Single electrons would be visible at 100–1000 PE and 1000–3000 ns but have been cut before. Figure 4.39(b) shows a further selection of S2s being reconstructed only in a small z slice $z \in [-1, 0]$ cm, where 0 is the position of the gate mesh. This selection has been done to be independent of the electron lifetime correction, which has not yet been applied in the version of PAX used in this study. The study was also performed on $z \in [-5, -4]$ cm and $z \in [-2, -1]$ cm, but has highest statistics in the highest z slice $z \in [-1, 0]$ and all following results are from analyses in that region. The final selection cuts for S2 signals used in the following are:

- S2 area: $A_{S2} \in [2 \cdot 10^3, 1.5 \cdot 10^6]$ PE
- S2 width: $w_{S2} \in [260, 2000]$ ns
- Reconstructed interaction depth: $z \in [-1, 0]$ cm

To illustrate the effect of the event selection further, figure 4.40 shows the event rate distribution in 2D histograms across the TPC diameter, where x and y has been binned in 200×200 bins, each containing the mean rate of every event reconstructed in a certain bin. A comparison of both plots shows the clearly visible reduction of events. Since background datasets have been used to perform this analysis, the events are homogeneously distributed across the full TPC diameter. There are less events as their reconstructed vertex positions are closer to the center, since the self-shielding of the xenon in the TPC reduces their amount for short radii. A cold spot is visible roughly at $(x, y) = (-20, 5)$. This is actually not a real reduction of rate, but originates from PMT 88 (located at the top array), which has been excluded from analysis (usually done by setting its gain to zero) and does not contribute any signals to the analyzed datasets. In the version of PAX used here this PMT hasn't been excluded from position reconstruction yet, which ultimately results in the cold spot in rate.

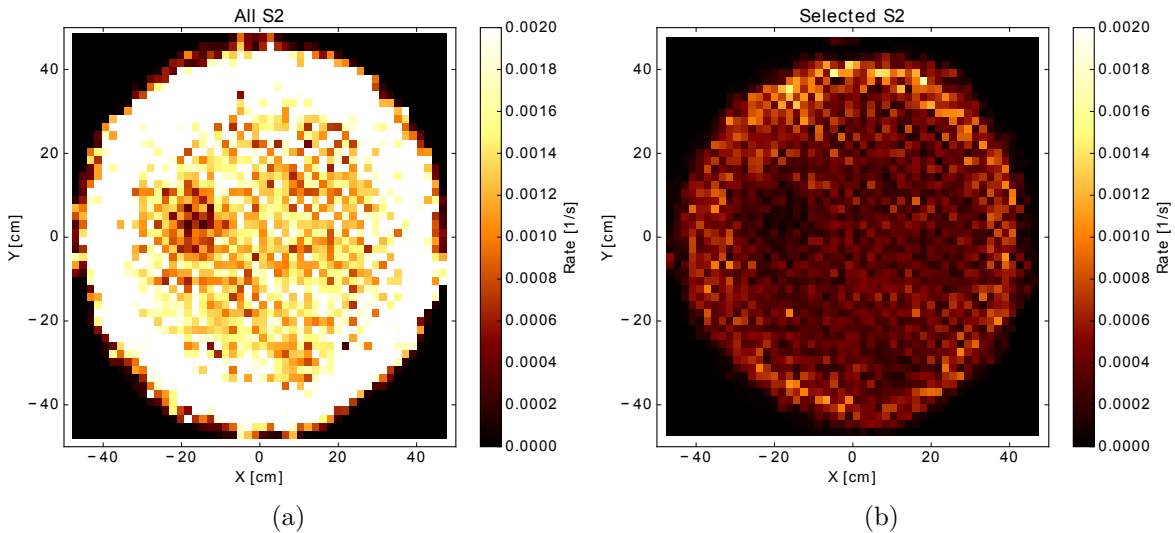


Figure 4.40: xy distribution of S2 peak rates across the TPC indicating the reduction of events given the selection cuts. The rate close to the center is lower than at large radii due to self-shielding of the xenon in these background datasets. A cold spot at about $(x, y) = (-20, 5)$ is due to PMT 88, which gain has been set to zero but hasn't been excluded from position reconstruction yet.

S2 width distribution fitting

To yield information about the tilt of the TPC one has to average the S2 widths inside each bin of the same binning applied in figure 4.40 and check for uniformity of the bin contents. Figure 4.41(a) shows such a plot. The color scale indicates the mean

width of the S2 signals within each bin. One can observe a non uniform distribution, where the S2 widths are larger at higher radii and getting smaller close to the center. This is an indication of mesh warping as anode and gate meshes attract each other electrostatically, being closest at the center. This leads to reduced S2 width values in the center, since the electrons drift a shorter way from the liquid/gas interface to the anode and produce less scintillation light. There is also a tilt visible by eye, where the S2 width decreases roughly from south-west to north-east in the plot, indicating that there is a residual tilt of the TPC in the opposite direction. Figure 4.41(b) shows the corresponding standard deviation of the S2 widths values within each bin, to indicate where on the TPCs cross-section the S2 width values are least uniform. There are high S2 width standard deviations at the very edge, due to single events with larger S2 widths, which are wrongly reconstructed into the $z \in [-1, 0]$ cm interval. Higher deviations towards the center of the TPC originate from lower statistics in that area, due to self-shielding.

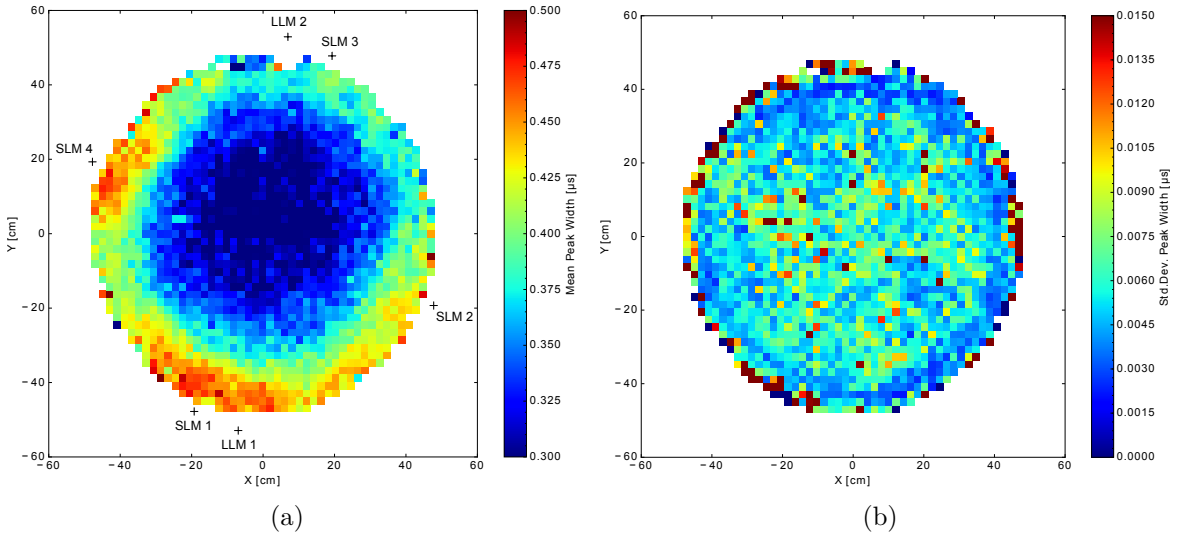


Figure 4.41: (a) Distribution of S2 width mean for each bin across the TPC including the positions of four short level meters (SLM 1–4) and two long level meters (LLM1–2). The non-uniform distribution with lower S2 width values at the center of the TPC indicate mesh warping. Overall, there is an observable tilt from south-west to north-east; (b) the corresponding standard deviation shows higher values at small radii due to lower statistics. Wrongly reconstructed z positions at very high radii leading to higher standard deviations at the outer bins.

The observed distribution is a superposition of the tilt of the TPC relative to the liquid level and mesh warping of anode and gate. A corresponding two dimensional fit function of the measured S2 widths must, thus, depend on the spatial coordinates

x and y and an array of fit parameters $p = [p_0, p_1, p_2, \dots]$, to be found to model the data best. The length of p , i.e. the number of fit parameters, depends on the function chosen to model mesh warping. As described in section 4.1 gate and anode consist of etched meshes with hexagonal pattern, stretched in eight directions. In addition to the electrostatic attraction, the meshes underly several other forces: gravitation forces both meshes downward and also the liquid itself as dielectric material between two electrodes is attracted by the anode due to electrostatic induction. In total seven different models have been used to fit the distribution of figure 4.40:

1. **Simple plane:** the general equation of a plane (compare equation (4.31)), modeling a liquid level tilt with respect to the meshes, ignoring mesh warping. It is not expected to match good given the distribution of figure 4.41(a).

$$f(p, x, y) = p_0x + p_1y + p_2 \quad (4.37)$$

2. **Simple plane + simple paraboloid:** assumes the mesh warping to have the shape of a symmetric two dimensional paraboloid and ignores stretching of the wires.

$$f(p, x, y) = p_0x + p_1y + p_2 + \frac{(x^2 + y^2) - r_{\max}^2}{2p_3} \quad (4.38)$$

3. **Simple plane + elliptic paraboloid:** assumes the mesh warping to have the shape of a two dimensional paraboloid and allows it to be stretched to an elliptic shape.

$$f(p, x, y) = p_0x + p_1y + p_2 + \frac{(p_3x^2 + y^2) - r_{\max}^2}{2p_4} \quad (4.39)$$

4. **Simple plane + simple catenary:** assumes the mesh warping to follow a two dimensional catenary (sagging) and ignores stretching of the wires.

$$f(p, x, y) = p_0x + p_1y + p_2 + \left(p_3 \cdot \cosh\left(\frac{\sqrt{x^2 + y^2}}{p_3}\right) - \cosh\left(\frac{r_{\max}}{p_3}\right) \right) \quad (4.40)$$

5. **Simple plane + elliptic catenary:** assumes the mesh warping to follow a two dimensional catenary (sagging) and allows it to be stretched to an elliptic shape.

$$f(p, x, y) = p_0x + p_1y + p_2 + \left(p_3 \cdot \cosh\left(\frac{\sqrt{p_3x^2 + y^2}}{p_3}\right) - \cosh\left(\frac{r_{\max}}{p_3}\right) \right) \quad (4.41)$$

6. **Simple plane + 4th power law:** assumes the mesh warping to follow the deflection of a circular plate with simply supported edge and uniform load, and thus to underly bending theory, following [142]. The corresponding function for the deflection w of a plate is

$$w = \frac{q_0 (r_{\max}^2 - r^2)}{64D} \cdot \left(\frac{5 + \nu}{1 + \nu} \cdot r_{\max}^2 - r^2 \right), \quad (4.42)$$

with q_0 is a uniform load with $[q_0] = \text{Pa}$, the flexural rigidity $D = \frac{EH^3}{12(1-\nu^2)}$, which depends on Young's modulus E , the thickness H of the plate and Poisson's ratio ν ($[D] = \text{Pa} \cdot \text{m}^3$). To construct a fit function from this, all coefficients are merged to two additional parameters p_3 and p_4 . Including the simple plane function one finds:

$$f(p, x, y) = p_0x + p_1y + p_2 + p_3 \cdot (r_{\max}^2 - (x^2 + y^2)) \cdot (p_4 \cdot r_{\max}^2 - (x^2 + y^2)). \quad (4.43)$$

7. **Zernike polynomials:** describes tilt and mesh warping as a sequence of Zernike polynomials⁹ that are orthogonal on the unit disk [147]. They are defined as:

$$Z_j(\rho, \varphi) = \sum_{k=0}^{\frac{n-m}{2}} \frac{(-1)^k (n-k)!}{k! \left(\frac{n+m}{2} - k\right)! \left(\frac{n-m}{2} - k\right)!} \rho^{n-2k} \cdot \begin{cases} \cos(m\varphi) & m \neq 0 \\ \sin(m\varphi) & m \neq 0 \\ 1 & m = 0 \end{cases}, \quad (4.44)$$

where m and n are non-negative integers, with $n \geq m$, φ is the azimuth angle and ρ is the radial distance $0 \leq \rho \leq 1$. The polynomials have been applied up to the 5th order ($n = 5$) and are ordered by the Noll index notation, which is a conventional mapping of the two indices m and n to a single index j [119]. Using Zernike polynomials allow to model for possible higher order mesh warping and their identification. To obtain a appropriate fit function, one can calculate the single Zernike polynomials for each j until the 5th order, convert them to Cartesian coordinates and add them up. The succeeding fit function (E.1) is stated in appendix E and depends on 20 fit parameters, each expressing the impact of the corresponding polynomial to the overall mesh warping. For illustration some Zernike polynomials up to the 4th order ($j = 14$) are drawn in figure 4.42.

Z_1 , Z_2 and Z_3 (first and second line) contribute together analogous to the function of a simple plane, Z_4 e.g. would contribute similar to a paraboloid. The other

⁹Frits Zernike, dutch physicist and Nobel prize winner, 1888 – 1966

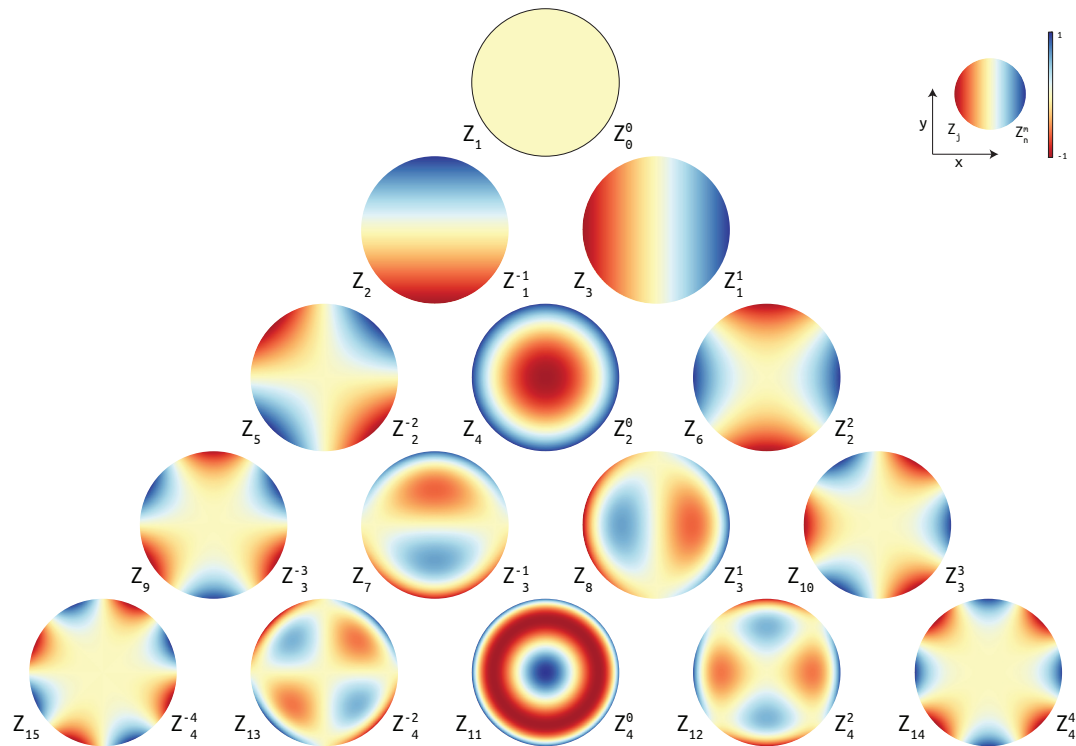


Figure 4.42: Zernike Polynomials up to the 4th order. The polynomials can be used to describe and identify possible higher order mesh warping [145]. Their value reaches from zero (red) to one (blue).

visible polynomials can account for higher order mesh warping with increasing order for increasing j .

Table 4.10 summarizes the fit results by comparing the χ_{red}^2 value for all obtained fits, while figure 4.43 shows the fits of three out of seven selected fit functions to the distribution drawn in figure 4.41(a), with the fit function values drawn on the left and the residuals of the fit on the right side.

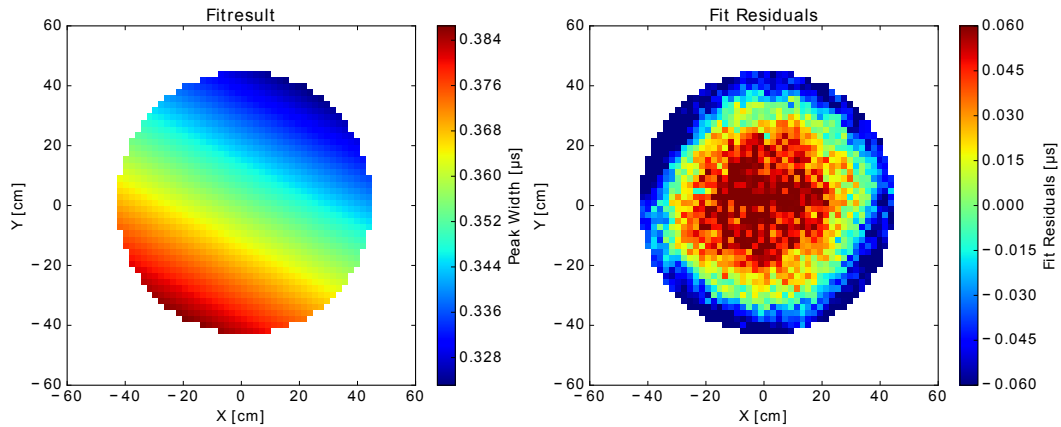
As expected only a simple plane fit is not able to match the distributions well, the χ_{red}^2 values are indicating poor fits to all distributions. Also, the fit residuals in figure 4.43(a) show clearly the inverted structure of the mesh sagging. The fits for additional paraboloids or catenary show basically all the same goodness for the fit. For all fits, were elliptic stretching was allowed, the corresponding stretching parameters p_3 were very close to one ($\langle p_3 \rangle = 0.98 \pm 0.01$), pointing out, that there is only a tiny elliptic deformation in the sagging. A difference between catenary and parabolic sagging is not observable in terms of goodness of fit. The fourth power model, motivated from bending theory, fits the data slightly better as the parabolic/catenary fits, with a small but over all fits consistent χ_{red}^2 improvement in the order of one percent. If the sagging

Choosing the model for fitting the S2 width xy distribution				
Circulation mode	gas only	liquid & gas	liquid only	—
Fit model	χ_{red}^2	χ_{red}^2	χ_{red}^2	$\langle \chi_{\text{red}}^2 \rangle$
Simple plane	67.96	53.16	58.30	59.81 ± 6.14
Plane + simple paraboloid	6.84	5.47	6.81	6.37 ± 0.64
Plane + elliptic paraboloid	6.87	5.46	6.86	6.39 ± 0.66
Plane + simple catenary	6.84	5.47	6.81	6.37 ± 0.64
Plane + elliptic catenary	6.87	5.46	6.87	6.40 ± 0.66
Plane + 4th power law	6.83	5.40	6.78	6.34 ± 0.66
Zernike polynomials	4.15	3.59	4.22	3.97 ± 0.28

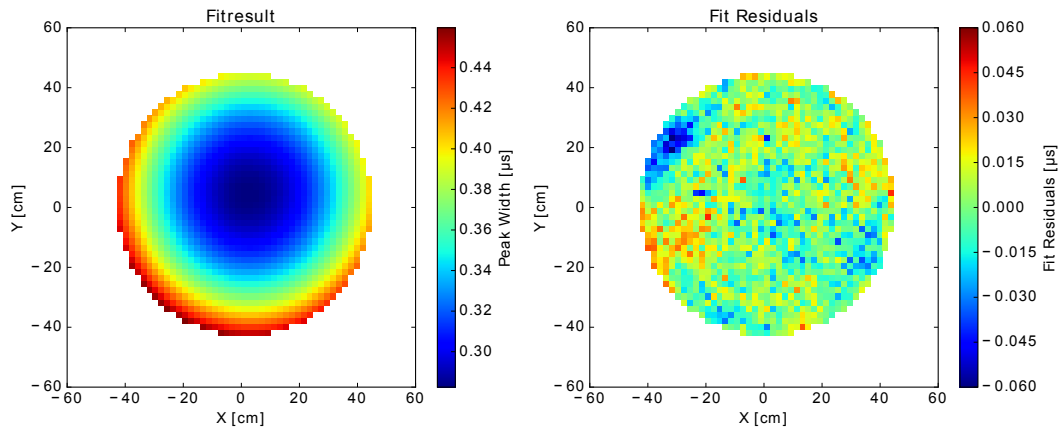
Table 4.10: Goodness of Fit for all tested models for fitting the S2 width xy distribution for data obtained with three circulation methods: gas circulation (g), liquid and gas circulation (lg) and liquid circulation (l) as well as the mean $\langle \chi_{\text{red}}^2 \rangle$ of all three circulation methods. The χ_{red}^2 values disfavor clearly the model for a simple plane, as expected. Parabolic and catenary fits show almost the same match to the data a bit less good than the 4th power model motivated by mechanics. As expected the Zernike polynomials fit the data best, accounting for all higher order warping. Overall is the agreement of model and data best for lg circulation.

of the anode is following more the sagging of a solid disk or e.g. a two-dimensional catenary is therefore hard to claim. The fit function values of all the “simple plane +” models are looking pretty similar. The residuals are in the order of 30 ns with a hot spot visible at negative x and negative y values and a cold spot at negative x but positive y values, both at high radii. This suggests that a higher order warping was not taken into account for by the fits. Exemplary, figure 4.43(b) shows the values of the fourth power function. Since it has the lowest χ_{red}^2 value, this is also the function chosen to be the one used for tilt calculation in the following. As expected the Zernike polynomials can match the data best, with a significant lower $\langle \chi_{\text{red}}^2 \rangle = 3.97$ for all circulation methods. The fit accounts for the before mentioned cold and hot spot and leaves residuals in the order of 15 ns (see right side of figure 4.43(c)). As an example, the absolute value of fit parameters $p_5 = (-6.8 \pm 1.3) \cdot 10^{-6}$ as well as $p_{13} = (-2.1 \pm 0.2)$ and $p_{14} = (-4.7 \pm 0.2)$ for liquid+gas circulation, show one order of magnitude higher values than the other polynomials of the n th order. Thus Z_5 , Z_{13} and Z_{14} account more for the whole polynomial sum. In fact, comparing with figure 4.42 confirms that a combination of those polynomials can match the cold and hot spot in the data. The stretching of the anode and gate mesh was done across the following angles:

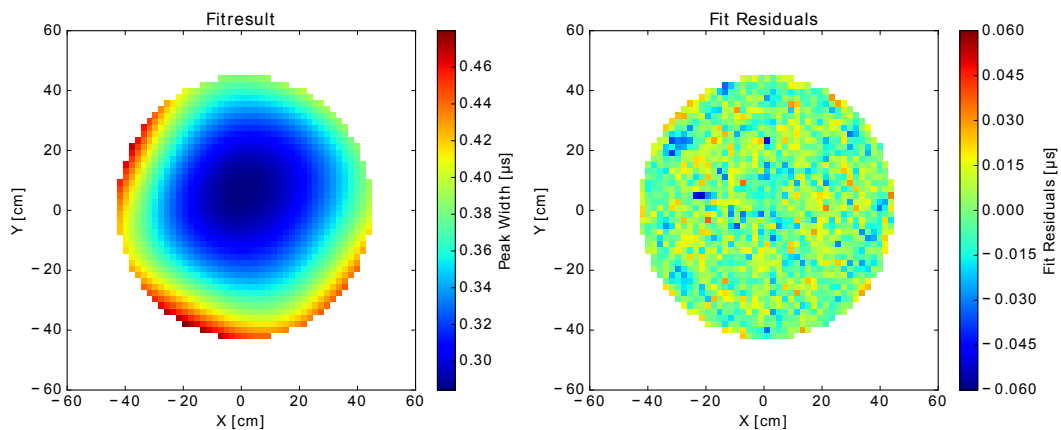
1. $10^\circ \longleftrightarrow 190^\circ$



(a) Simple plane fit



(b) Simple plane fit + 4th power law fit function



(c) Zernike polynomials fit

Figure 4.43: Fit function values (left) and fit residuals (right) for the S2 width xy distribution fits illustrating the match of model and data. The simple plane fit matches the data poorly, the 4th power law and Zernike polynomials show good agreement, with only the Zernike coefficients can account for a cold and a hotspot at large negative x values.

2. $55^\circ \longleftrightarrow 235^\circ$
3. $100^\circ \longleftrightarrow 280^\circ$
4. $145^\circ \longleftrightarrow 325^\circ$

from which stretching 1 and 3 might be roughly visible in their Zernike polynomials fit.

TPC tilt calculation

It is possible to derive the residual tilt of the TPC from the plane component of the fit function describing the S2 width distribution (see equation (4.43)). The tilt information can be converted into instructions of how to level the TPC via the fine and coarse leveling system as described at the beginning of section 4.5. The normal unit vector $\vec{n}_{0,S2}$ of the plane obtained by fitting the S2 width distributions and the tilt angle ξ_{S2} can be calculated with equations (4.32) and (4.33). The only difference to the tilt calculation with the level meter readings is that the angle ϕ_{S2} points in the opposite direction as ϕ_{SLM} and has to be added by 180° , since S2 width and liquid level height are indirect proportional to each other. The tilt can also be expressed as the gradient

$$|\text{grad } w| = \frac{w_{\max} - w_{\min}}{2R}, \quad (4.45)$$

where w_{\min} and w_{\max} are the minimum and maximum value of the plane function and R is the radius of the TPC. Calculations of ξ_{S2} , ϕ_{S2} and $|\text{grad } w|$ as well as the mean S2 width \bar{w}_{S2} for each circulation method is shown in table 4.11.

TPC Tilt from S2 width analysis				
Tilt parameters	gas only	liquid & gas	liquid only	Average
\bar{w}_{S2}	(410 ± 6) ns	(365 ± 7) ns	(369 ± 7) ns	—
ξ_{S2}	0.0416°	0.0415°	0.0388°	$(0.041 \pm 0.001)^\circ$
ϕ_{S2}	238.7°	243.2°	236.7°	$(240 \pm 3)^\circ$
$ \text{grad } w $	0.7238 ns/cm	0.7221 ns/cm	0.6729 ns/cm	(0.71 ± 0.02) ns/cm

Table 4.11: Tilt parameters obtained from the S2 width analysis for the TPC at different circulation methods.

The tilt of the TPC has a mean angle of $(0.041 \pm 0.001)^\circ$. Given the TPC diameter of $2R = 87.8$ cm the maximum tilt related height difference across the TPC diameter is

(0.63 ± 0.01) mm. The difference to the initial tilt measurements of the level meters is presumably due to tilting of the cryostat after filling of the water tank, caused by its buoyancy. After presenting these results to the XENON Detector Operations group, the residual tilt was considered to be negligible, so no further tilt corrections have been scheduled.

4.5.3 Liquid level height versus S2 signal width

As mentioned above, the width of the S2 signal is proportional to the gas gap length: $w_{S2} \propto x_g$. Given the results of \bar{w}_{S2} from table 4.11 and the mean level obtained from all short level meters, one can plot a data point for each of the three circulation periods to verify the proportionality between S2 width and gas gap length. Figure 4.44 shows the three data points and a corresponding line fit. The proportionality constant C can be found to be (1172 ± 3) ns/cm.

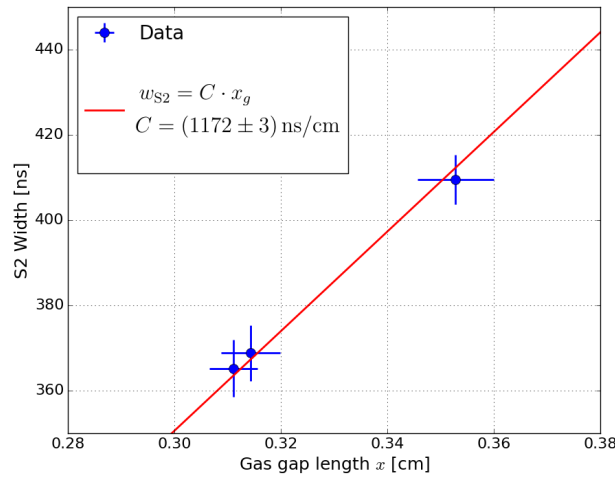


Figure 4.44: S2 width versus short level meter readings for each of the three circulation periods (blue dots). The proportionality according to equation (4.36) was fitted with a linear fit function (red line).

In section 4.5.1 there were indications, that possibly one of the level meters is out-of-plane by construction. Indeed, the tilt calculated from the values obtained by the short level meters of figure 4.38(a) is $\xi_{SLM} = 0.0101^\circ$ with the slope pointing towards $\phi_{SLM} = 246.4^\circ$, does not match ξ_{S2} calculated in the previous section. To probe the assumption of the out-of-plane short level meter four fits have been performed, each only with three of the four SLMs. Table 4.12 shows the obtained TPC tilts for each case.

Test for one SLM to be off-the-plane			
SLMs fitted	SLM excluded	ξ_{SLM}	ϕ_{SLM}
SLM 1,2,3,4	—	0.0101°	246.4°
SLM 1,2,3	SLM 4	0.0289°	317.5°
SLM 1,2,4	SLM 3	0.0172°	68.9°
SLM 1,3,4	SLM 2	0.0294°	178.1°
SLM 2,3,4	SLM 1	0.0374°	247.6°

Table 4.12: To probe the assumption of one SLM being out of plane fits have been performed with only three of four SLMs. Comparing the results to the ones obtained from the S2 width analysis, the best match is the fit with SLM 1 excluded.

It seems that the best match of ξ and ϕ is from the fit, where SLM 1 is excluded. If one plots the information of the S2 width study and the level meters in one graph, one could verify this and find out which level meter could have a height offset. To do that, one has to calculate the S2 width values of signals at the (x, y) position of the level meters (which would represent the true tilt) and compare it with the measurements of the single level meters. Figure 4.45 shows the percentual deviations of the S2 width values at the level meter position (squares) and the level meter readings (circles) relative to each position of the level meters. The colors indicate the different circulation modes.

In figure 4.45(a) the values are plotted as they are shown in table 4.12. Each plot is showing the level meter readings and of the S2 width calculations relative to one of the level meter positions. It is obvious that, while for SLM 2, 3 and 4 the values for S2 width and LM readings agree within their errorbars, the relative deviation relative to the position of SLM 1 does not match. In fact, in this case there is no match for all other SLM positions. This is the verification of the suggestion, that SLM 1 might be out-of-plane. It is possible to extract a offset from that plot, which could be applied to the reading of SLM 1 to correct for this error. This offset can be found to be $\Delta = (0.37 \pm 0.05)$ mm. The positive Δ indicates, that SLM 1 seems to be mounted too low (by 0.37 mm), meaning that the liquid level is measured too high and the gas gap is measured too low. Subtracting this value from the readings of SLM 1 yields a match of S2 width and level meter data also for SLM 1 (as shown in 4.45(b)), while the values relative to the other SLM positions are still in agreement. However, the liquid level fluctuations between the three circulation phases have been pretty small and it is thus not sure, but unlikely that Δ will be constant over all liquid levels, such that the correction was not included into the calibration of the short level meter readings.

4.5.4 Earthquakes striking L'Aquila region

The level meters are precise enough to measure different non dark matter search related events, e.g. somebody walking on the beams of the support structure as well as seismic effects. At 2016/08/24 at 03:36:32 an earthquake [141], measuring 6.2 on the moment magnitude scale struck the L'Aquila region causing severe destructions in the area and resulting in 299 people killed and an estimated economic loss in the order of billions of Euro. It was followed by two major aftershocks at 03:56:02 and 04:33:29 with moment magnitudes of 4.6 and 5.5 respectively. Three types of sensors in the XENON1T experiment are sensitive to earthquakes: The short level meters, two tilt meters TILTA and TILTB and the meter for the water level in the water tank LIT1. Figure 4.46 shows the readings of those three sensor type between 03:30 and 04:50 of 2016/08/24.

The two earthquakes with magnitude > 5 were visible in all sensors, while the smaller one at 03:56 could only be detected with the tilt meters. Comparing the readings of SLMs before and after the three earthquakes and calculating the tilt change as presented in section 4.5.1 leads to a difference of 0.005 mrad, which is comparable to the differences in the tilt meter readings of 0.002 mrad in TILTA and -0.005 mrad in TILTB. The august 2016 earthquake was the begin of a seismic active period in the L'Aquila region with several heavy earthquakes with momentum magnitudes of ≈ 5.5 following e.g. at 2016/10/26 and 2017/01/18 with the latter one causing high voltage trips in the TPC and forced to stop science run 0 (compare figure 4.34).

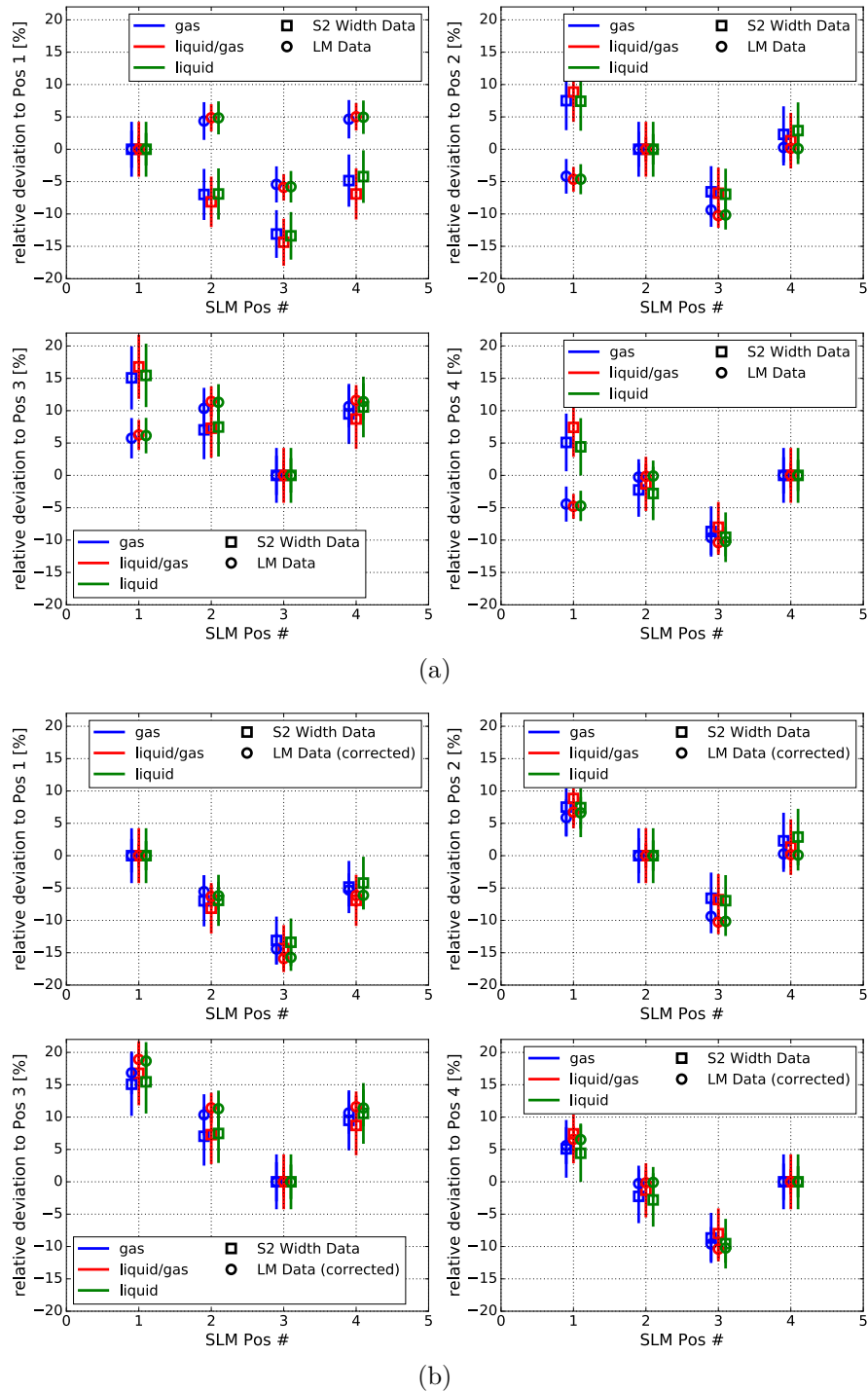


Figure 4.45: Comparing the calculated S2 width at the level meter positions with the level meter readings in the sequence: Relative to (x, y) position SLM 1 (upper-left) to relative to position of SLM 4 (lower-right) without correction (a), where the values relative to the position of SLM 1 do not agree with each other; (b) applying a correction factor for SLM 1 of $\Delta = 0.37$ mm, yields a match of S2 width and level meter data. This indicates that SLM 1 seems to be mounted too low.

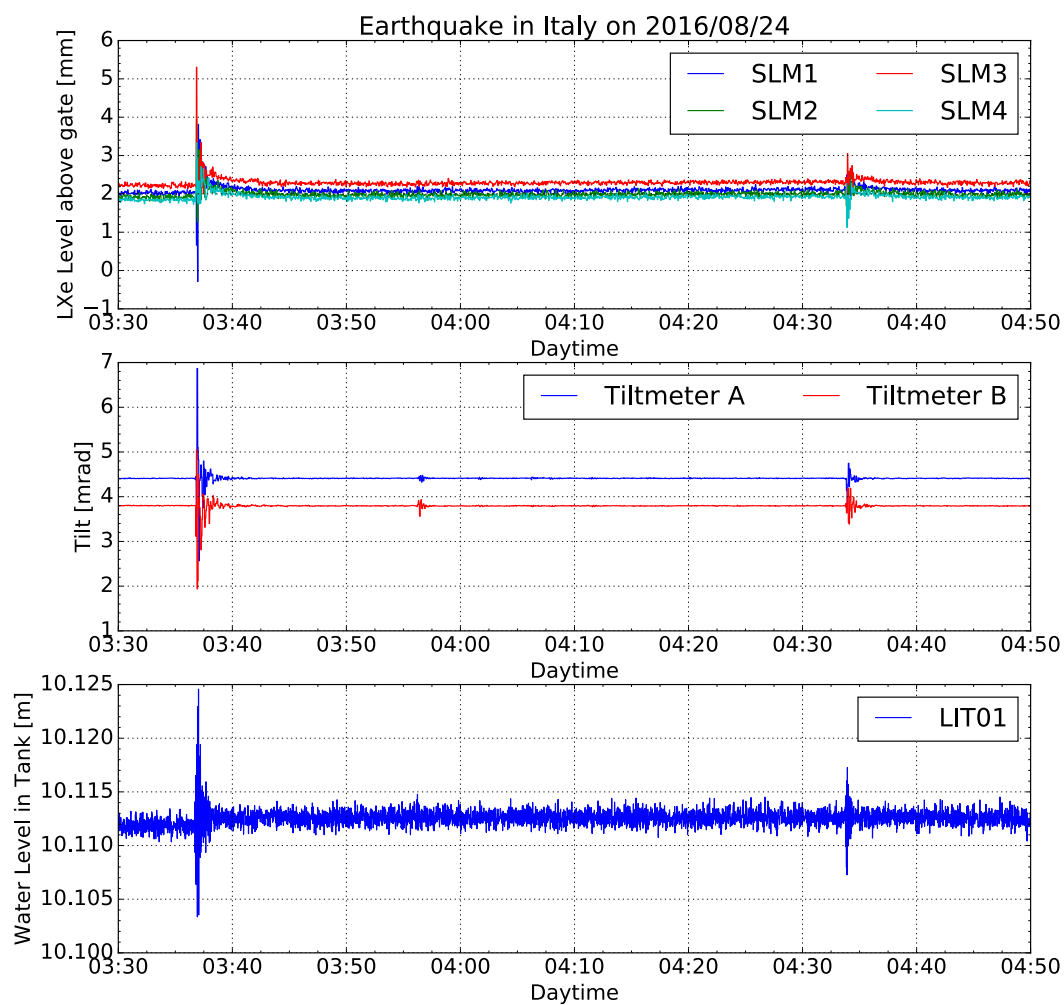


Figure 4.46: Sensor readings of an earthquake at 2016/08/24. The short level meters on top show clear fluctuations in the liquid level of ≈ 6 mm. This is confirmed by fluctuations in other tilt related sensors as tilt meters TILTA and TILTB with fluctuations of ≈ 4 mrad, as well as the water level in the water tank LIT1 with fluctuations of ≈ 20 mm.

Chapter 5

Conclusion and outlook

“Things turn out best for people who make the best out of the way things turn out.”

John Wooden, *American basketball player and coach*, * 1910; † 2010

XENON1T is the most sensitive direct experiment for the direct search of WIMP dark matter. Its recently published upper limit from a 34.2 live-days run in the (m_χ, σ) parameter space is leading the field with $\sigma = 7.7 \cdot 10^{-47} \text{cm}^2$ for a 35 GeV/c² WIMP [35]. Its second science run acquired already more than 150 live-days of dark matter data, still acquiring more as these lines are written (2017/10/01).

It is surrounded by a muon veto system consisting of 84 PMTs detecting the Cherenkov light of muons transiting the water tank. Simulations yielded detection efficiencies of 99.78% for muon events and 70.5% for shower events [29]. This enables the suppression of background in the TPC originating from cosmogenic neutrons. Series tests of dark rate, gain and afterpulses have been performed before installation to verify functionality and performance. They resulted in an expected normal distribution of gain and dark rate and acceptable afterpulsing rates. The PMTs have been installed in five ring-shaped patterns (top, bottom and three lateral rings) along the walls of the water tank. Work presented in this thesis, had been contributed to the design of holding mechanisms and calibration systems of the PMT. For the latter, two systems have been developed. An individual PMT calibration via optical fibers and a global muon veto calibration with diffuser balls, for which design, simulation and commissioning were presented. The reflective foil DF2000MA, which is clad on the tanks inner surfaces,

has been investigated in detail within the scope of this thesis. The results have been published in [84]. Adjusting the foils reflectance and wavelength shifting properties in the muon veto simulation code, however showed only minor improvements of the detection efficiencies. The XENON1T muon veto data analysis has been kicked off by programming of a `MuonVetoTreeMaker` providing the possibility off analyzing data being processed by the same data processor as used for TPC data (PAX). A first method has been developed to reconstruct muon tracks in the XENON1T muon veto, verified by comparing the data with simulations and muon flux measurements at LNGS.

In the course of this thesis, capacitive liquid level meters have been designed, manufactured and installed in XENON1T. They reach a precision of $\approx 30 \mu\text{m}$ for the position measurement of the liquid gas interface and $\approx 3 \text{mm}$ for the liquid level outside of the TPC, measured at a distance of 15 m. A microcontroller based electronics was developed to interface UTI readout chip with the slow control system, developing custom firmware. Their long term stability and usability have been verified over more than a year of permanent readout in a 1 Hz frequency. Several detector related (desired liquid level changes) and non-detector related (earthquakes) events have been detected and followed by the level meters. Analyzing their readings led to a leveling of the TPC smaller than a tilt angle of 0.001° . An analysis of the width of the TPC S2 signals at different liquid levels verified the level meter readings and enabled an investigation of mesh warping in the TPC.

The successor of XENON1T will be XENONnT, which is currently at the design phase and for which construction will start in 2018. It will have a target volume of $\approx 6.5 \text{t}$ of liquid xenon and will increase sensitivity down to cross-sections $\sigma \approx 10^{-48} \text{cm}^2$ for a 20 t·y exposure. Figure 5.1 shows the projected limit of XENONnT compared to XENON1T. Based on the concept that all the XENON1T infrastructure is designed to host also XENONnT, both items of this thesis, muon veto and level meters are conceptually designed to work also in XENONnT. To achieve this further increase of sensitivity, background has to be lowered by another order of magnitude. Regarding the muon veto, a liquid scintillator neutron veto is designed to fit into the water tank and being located around the cryostat to reduce neutron induced background even further (as simulated in [125]) to less than one event per ton-year exposure. Regarding the level meters, there is also the possibility to increase precision by a factor ≈ 10 of all level meters by using the “fast” mode of the UTI chip. The readout PCB provides the possibility to toggle the pin-output which can control this for all UTI chips on

the board. However, this requires more complicated firmware, which was not feasible in the time scale of the installation of XENON1T, but would be worth doing for XENONnT in terms of detections of tiny liquid level changes.

The ultimate dark matter detector project, named DARWIN (**D**ark matter **w**imp search with liquid xenon), is planned to be the future stage of liquid noble gas TPCs aiming to push the sensitivity to levels eventually covering the entire WIMP-parameter space before neutrino backgrounds dominate. Such a detector would basically be background free and consist of target masses of ≈ 40 t of liquid xenon and is projected to be realized around 2024. In any case, this might be the final stage of liquid noble gas based WIMP search and end in a discovery or rejection of the WIMP as dark matter candidate.

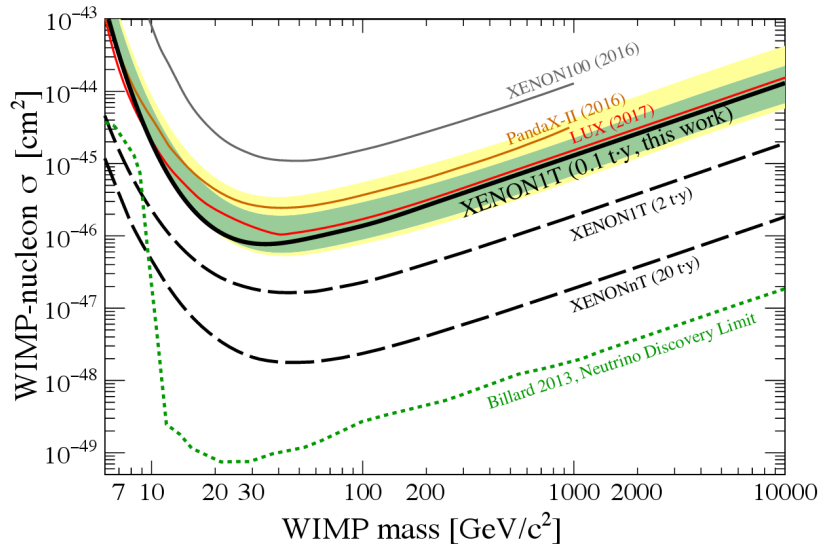


Figure 5.1: Projected sensitivity of XENONnT down to $\approx 10^{-48} \text{ cm}^2$, compared to XENON1T and other liquid xenon TPC experiments. Infrastructure of XENON1T is designed such, that it can host the larger XENONnT with no major upgrades necessary. Plot created by the XENON collaboration.

Appendices

A The MuonVetoTreeMaker

```

1 class MuonVetoTreemaker(hax.minitrees.TreeMaker):
2     """Computing properties of the Muon Veto Events
3
4     This TreeMaker will ignore all TPC related events which are stored
5     as objects of PAX classes like 'peaks' or 'interactions'. It gets
6     the information of the MV events from the array stored in
7     events.all_hits as numpy dtype array similar to objects from the
8     PAX 'Hit' class.
9
10    Versioning:
11    V0.0.1 - 2016/10/07 - ChG: Kick-Off
12    V1.0.0 - 2016/10/13 - ChG: First working version. Possible to get
13    all events of the file and successful comparison what one can see
14    in a ROOT TBrowser
15    V1.0.1 - 2016/10/19 - ChG: Added 'Hit_width' in computations
16    V1.1.0 - 2016/10/20 - ChG: Accepts now datasets with empty first
17    event entry (error before)
18    V1.1.1 - 2017/02/15 - ChG: Added 'Hit_noise_sigma' for calculation
19    of threshold for each hit
20    V2.0.0 - 2017/03/10 - ChG: imported hax and numpy to enable
21    compatibility with hax GitHub repository
22    """
23
24    extra_branches = ['*'] # Activate all of ROOT file
25    __version__ = '2.0.0'
26    uses_arrays = True
27
28    def extract_data(self, event): # This runs on each event
29
30        # Create default dictionary
31        values = {}
32
33        values['PMTs'] = [] # PMT Channel which got hit in the
34                           # event
35        values['Hit_area'] = [] # Area of signal in each PMT
36                               # Channel [PE]
37        values['Hit_height'] = [] # Height of signal in each PMT
38                                  # Channel [PE/samples]
39        values['Hit_left'] = [] # left boundary of signal in each
40                                # PMT Channel [samples after
41                                # event start]
42        values['Hit_center'] = [] # Center of signal in each PMT

```

```

43         # Channel [ns] 1 ns = 0.1 samples
44     values['Hit_right'] = []      # right boundary of signal in each
45                                 # PMT Channel [samples after
46                                 # event start]
47     values['Hit_width'] = []     # peak width of each PMT Channel
48                                 # [samples]
49     values['Hit_noise_sigma'] = [] # Noise sigma of the pulse in
50                                 # which the hit was found
51                                 # [PE/samples]
52     #values['NumPMTsHit'] = 0     # Number of PMT Channels which got
53                                 # hit in the event
54
55     # Store start/stop time of event (Unixtime)
56     values['tStart'] = event.start_time # Start time of the event
57     values['tStop'] = event.stop_time   # Stop time of the event
58
59     # Some events do not have a single hit, whatever that means...
60     # if so, do nothing and jump to next event
61     if not len(event.all_hits):
62         values['PMTs'].append(np.nan)    # necessary to not fail if
63                                           # first event is empty
64         values['Hit_area'].append(np.nan) # ^
65         values['Hit_height'].append(np.nan) # |
66         values['Hit_left'].append(np.nan)  # |
67         values['Hit_center'].append(np.nan) # |
68         values['Hit_right'].append(np.nan) # |
69         values['Hit_width'].append(np.nan) # |
70         values['Hit_noise_sigma'].append(np.nan) # |
71         return values
72
73     #values['NumPMTsHit'] = len(event.all_hits)
74
75     for i in range(len(event.all_hits)):
76         values['PMTs'].append(event.all_hits[i].channel)
77         values['Hit_area'].append(event.all_hits[i].area)
78         values['Hit_height'].append(event.all_hits[i].height)
79         values['Hit_left'].append(event.all_hits[i].left)
80         values['Hit_center'].append(event.all_hits[i].center)
81         values['Hit_right'].append(event.all_hits[i].right)
82         values['Hit_width'].append(event.all_hits[i].right
83                                     - event.all_hits[i].left)
84         values['Hit_noise_sigma'].append(event.all_hits[i].noise_sigma)
85
86     return values

```

B Examples of muon track reconstructions

Examples for a working reconstruction

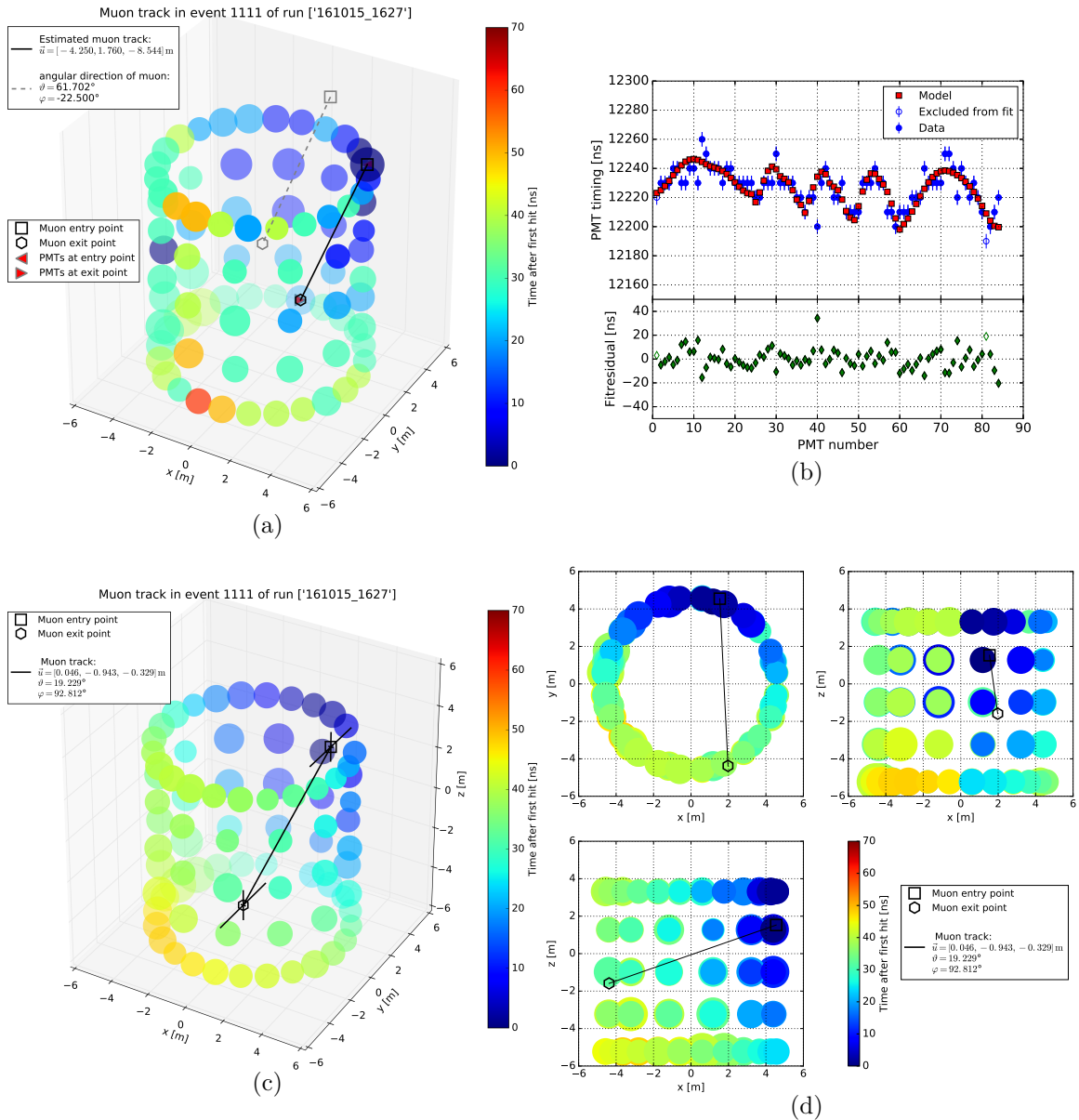


Figure B.2: Muon track reconstruction example with a muon intersecting only the lateral surface. The reconstruction is working well ($\chi_{\text{red}}^2 = 2.91$). (a) Event display and estimation of start values; (b) Fit and residuals; (c) Event display of fit function values; (d) Event display projection of fit function values.

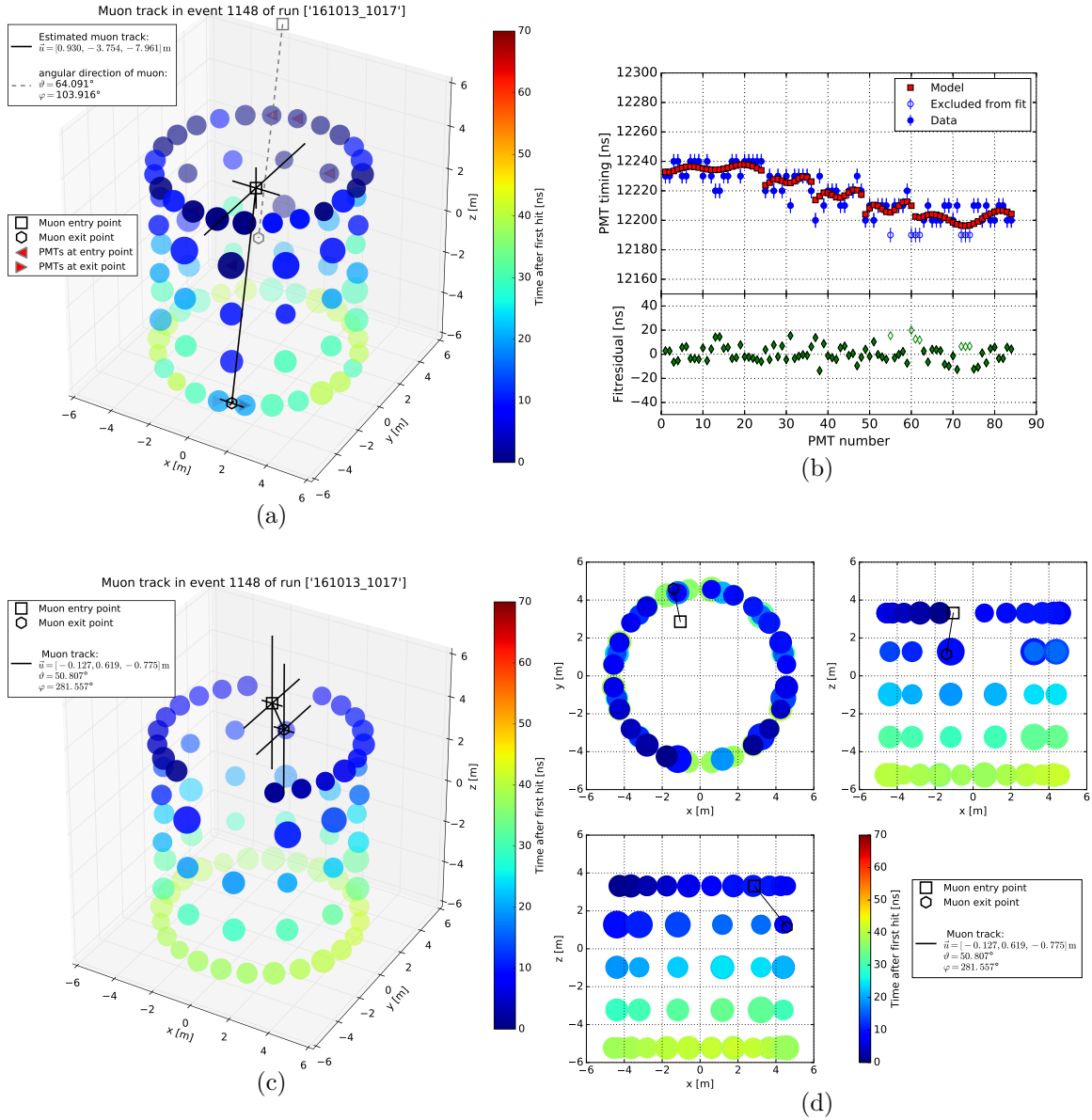


Figure B.3: Muon track reconstruction example with a muon only barely intersecting the tank volume. There is an intersection through the tanks top surface. The reconstruction is working well ($\chi_{\text{red}}^2 = 1.74$). (a) Event display and estimation of start values; (b) Fit and residuals; (c) Event display of fit function values; (d) Event display projection of fit function values.

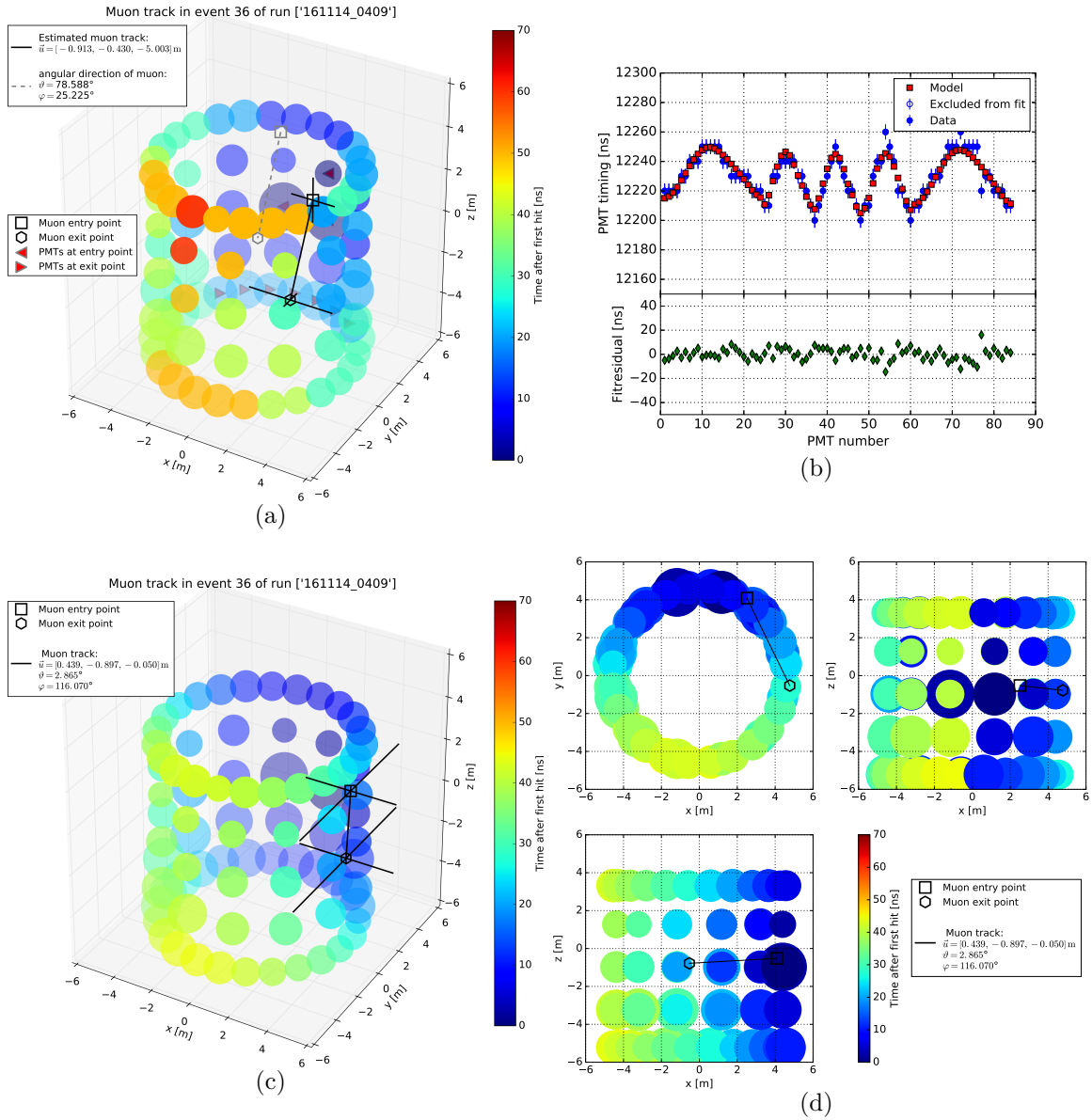


Figure B.4: Muon track reconstruction example with a muon transiting the tank only at very high radii. The reconstruction is working very well ($\chi_{\text{red}}^2 = 1.07$). (a) Event display and estimation of start values; (b) Fit and residuals; (c) Event display of fit function values; (d) Event display projection of fit function values.

Examples for a failing reconstruction

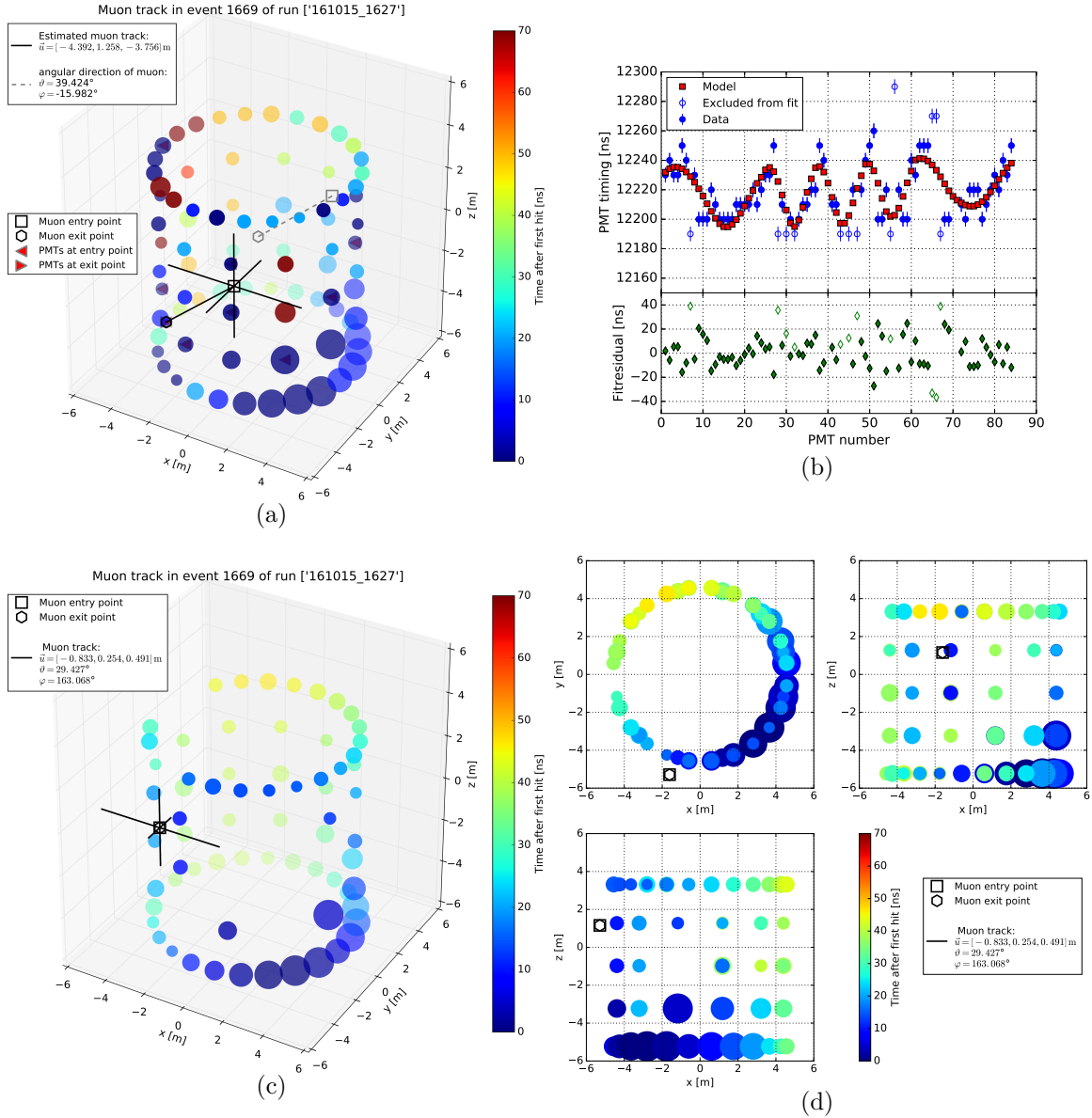


Figure B.5: Muon track reconstruction example with the track reconstructed such that no intersection with the tanks volume can be found, resulting in congruent entry and exit points. The event was sorted out. The fit is still working though ($\chi_{\text{red}}^2 = 5.50$), which indicates that the underlying event has still a physical origin. Thus, this event might be a candidate for a shower event. (a) Event display and estimation of start values; (b) Fit and residuals; (c) Event display of fit function values; (d) Event display projection of fit function values.

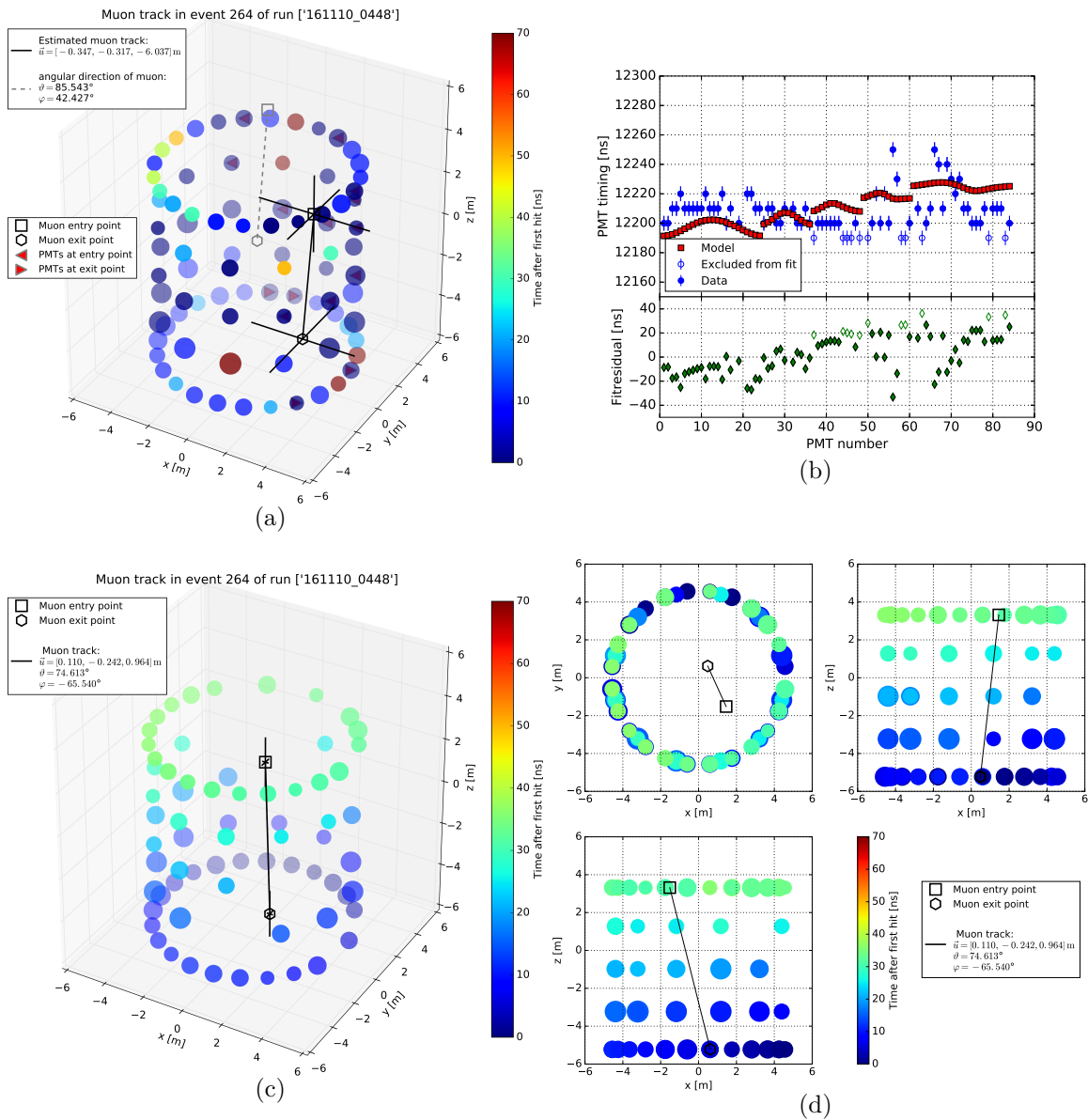


Figure B.6: Muon track reconstruction example with the reconstruction algorithm fitting the data poorly ($\chi_{\text{red}}^2 = 39.51$). There is no clear track-line pattern recognizable. The fit turns the pattern even upside down. The event was sorted out. (a) Event display and estimation of start values; (b) Fit and residuals; (c) Event display of fit function values; (d) Event display projection of fit function values.

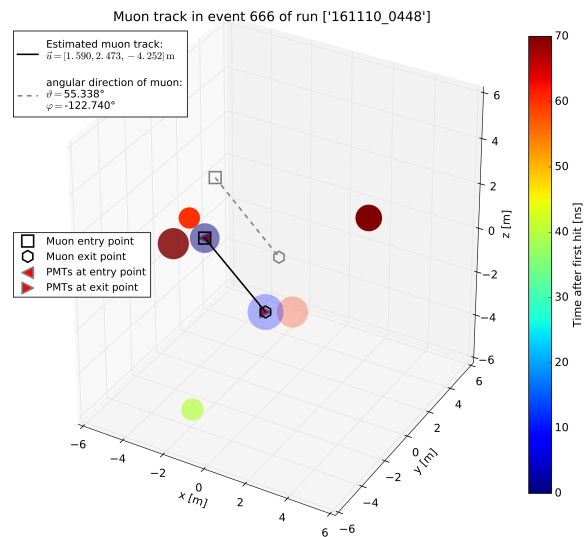
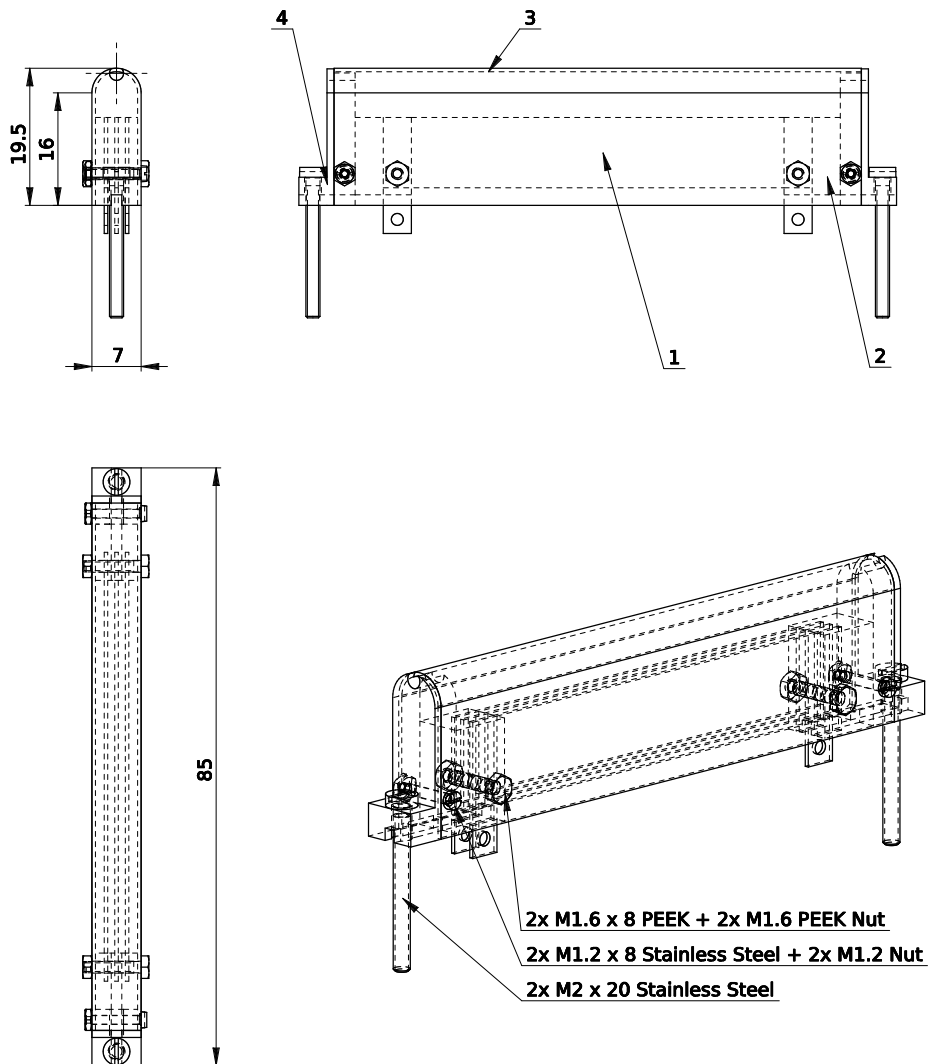


Figure B.7: Event display of a random noise coincidence of enough PMTs to enable a muon veto trigger. After application of all cuts, not enough PMTs survive to be considered as a real event. There reconstruction algorithm was thus not applied on this event and it was sorted out.

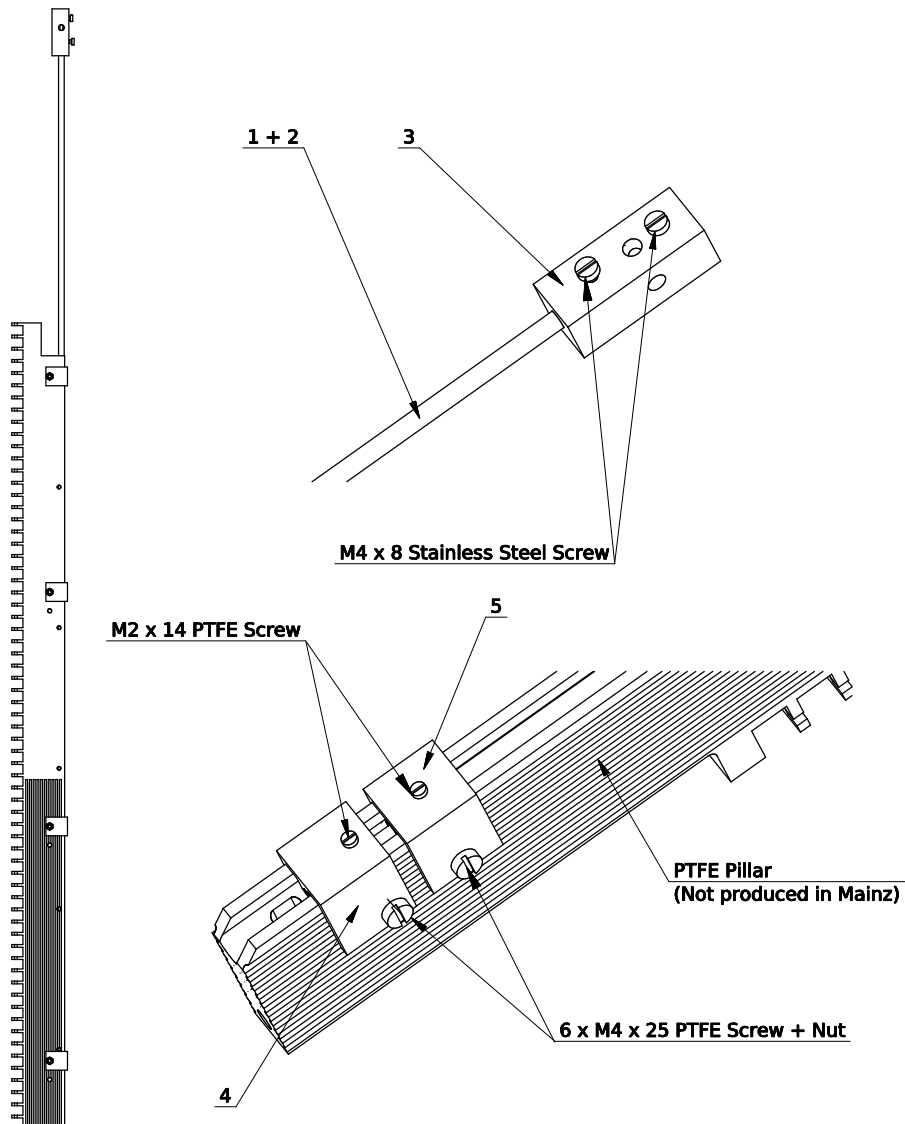
C Level meter technical drawings

C.1 Short level meters



Drawing #		Description	
Christopher Geis (25168)		See drawings for parts 1-4	
Material	Copper (CW009A) + PEEK	Serial No.	
Weight		Assembly No.	0
Surface		Date	2015-01-29
Scale 1.5		Name	
Quantity: 5x		Level Meter Assembly V5	

C.2 Long level meters



Drawing #	Christopher Geis	Description	
Material		Serial No.	
Weight		Assembly No.	0
Surface		Date	2015-03-26
Scale	Quantity: 2x	Note	Long Levelmeter Assembly

D Level meter readout

The following listing shows the header of the XENON1T level meter readout code as overview over its versions. The code is copyleft licensed available at https://github.com/geisch/XENON1T_LM.

```

1 ;*****
2 ;
3 ; Files Required: P16F877A.INC
4 ;
5 ; Assembler Code for the readout of the XENON1T capacitive level
6 ; meter system.
7 ; Basic principle:
8 ; - Readout of 6+1 UTI chips in a row using a multiplexer
9 ; - Using capture module to measure UTI phases (propto capacitance)
10 ; - Using USART module to communicate with Slow Control via RS485
11 ;*****
12 ;
13 ; Author: CHRISTOPHER WERNER GEIS (ChG)
14 ; University: Institut fuer Physik,
15 ;           Johannes Gutenberg-Universitaet Mainz
16 ; Email: geisch@uni-mainz.de, christopher.geis@gmx.de
17 ;
18 ;*****
19 ; History:
20 ; - V0.0: 2015/07/01 Kickoff
21 ; - V0.1: 2015/07/15 Multiplexing implemented
22 ; - V0.2: 2015/09/01 USART module setup (buggy) communication
23 ;           over RS485 bus possible
24 ; - V0.3: 2015/11/15 CCP1 module setup (buggy) measurement of
25 ;           UTI phases possible
26 ; - V0.4: 2015/12/01 USART communication works bugfree
27 ; - V0.5: 2015/12/15 CCP1 capture works bugfree
28 ; - V1.0: 2015/12/16 First released code with full functio-
29 ;           nality
30 ; - V1.1: 2016/01/23 Added also OD CR character response after
31 ;           Enable/Disable Power down mode
32 ; - V2.0: 2016/04/23 Adjustments according to usage of an up-
33 ;           dated readout board version
34 ; - V2.1: 2016/06/01 Allows nor to select (in code) for UTI
35 ;           fast mode
36 ;*****

```

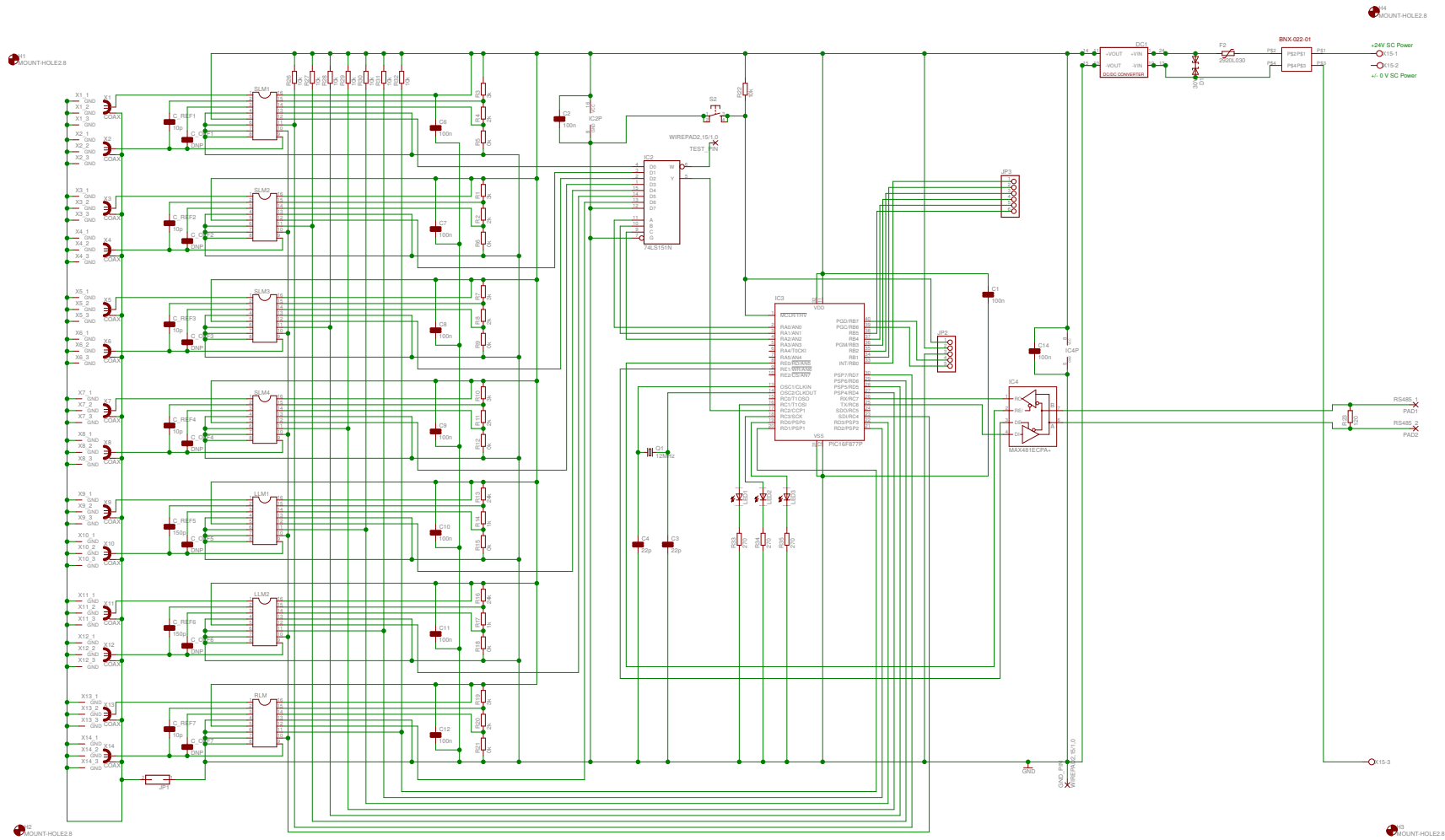


Figure D.1: Level meter Readout PCB - Schematic diagram of the electric circuit.

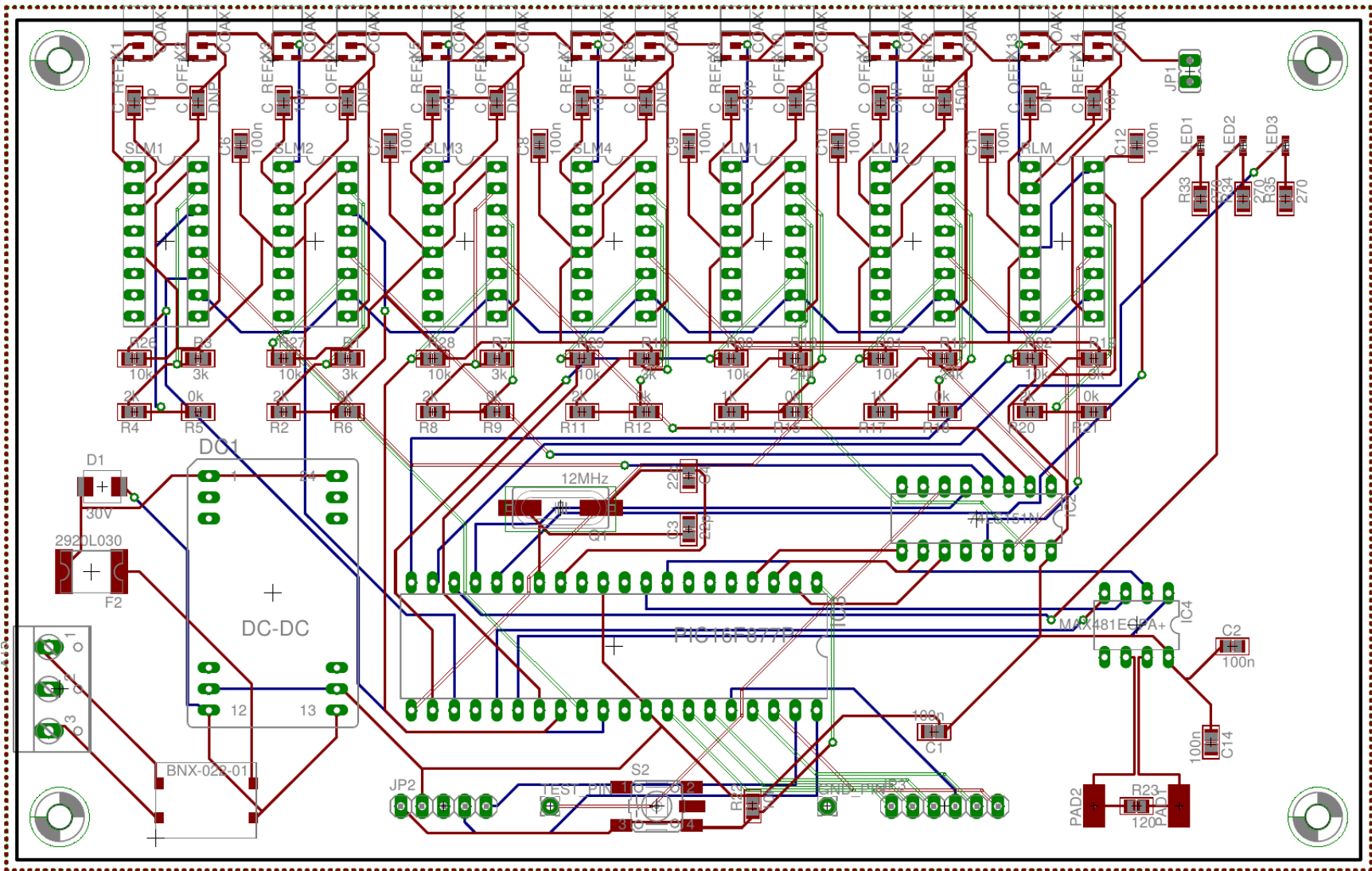


Figure D.2: Level meter readout PCB - Board layout.

E Zernike polynomials

Fit function of the S2 width distribution

The fit function used in section 4.5.2 is the sum of all Zernike polynomials $Z_j(x, y)$ until the 5th order in Cartesian coordinates, ordered by the Noll index j .

$$\begin{aligned}
f(p, x, y) = & p_0 \\
& + p_1 \cdot 2y \\
& + p_2 \cdot 2x \\
& + p_3 \cdot \sqrt{6}(2xy) \\
& + p_4 \cdot \sqrt{3}(2x^2 + 2y^2 - 1) \\
& + p_5 \cdot \sqrt{6}(x^2 - y^2) \\
& + p_6 \cdot \sqrt{8}(3x^2y - y^3) \\
& + p_7 \cdot \sqrt{8}(3x^2y + 3y^3 - 2y) \\
& + p_8 \cdot \sqrt{8}(3x^3 + 3xy^2 - 2x) \\
& + p_9 \cdot \sqrt{8}(x^3 - 3xy^2) \\
& + p_{10} \cdot \sqrt{10}(4x^3y - 4xy^3) \\
& + p_{11} \cdot \sqrt{10}(8x^3y + 8xy^3 - 6xy) \\
& + p_{12} \cdot \sqrt{5}(6x^4 + 12x^2y^2 + 6y^4 - 6x^2 - 6y^2 + 1) \\
& + p_{13} \cdot \sqrt{10}(4x^4 - 4y^4 - 3x^2 + 3y^2) \\
& + p_{14} \cdot \sqrt{10}(x^4 - 6x^2y^2 + y^4) \\
& + p_{15} \cdot \sqrt{12}(5x^4y - 10x^2y^3 + y^5) \\
& + p_{16} \cdot \sqrt{12}(15x^4y + 10x^2y^3 - 5y^5 - 12x^2y + 4y^3) \\
& + p_{17} \cdot \sqrt{12}(10x^4y + 20x^2y^3 + 10y^5 - 12x^2y - 12y^3 + 3y) \\
& + p_{18} \cdot \sqrt{12}(10x^5 + 20x^3y^2 + 10xy^4 - 12x^3 - 12xy^2 + 3x) \\
& + p_{19} \cdot \sqrt{12}(5x^5 - 10x^3y^2 - 15xy^4 - 4x^3 + 12xy^2) \\
& + p_{20} \cdot \sqrt{12}(x^5 - 10x^3y^2 + 5xy^4).
\end{aligned} \tag{E.1}$$

Bibliography

- [1] G. Aad *et al.*, (**ATLAS** Collaboration), “Search for pair production of gluinos decaying via stop and sbottom in events with b -jets and large missing transverse momentum in pp collisions at 13 TeV with the ATLAS detector”, *Phys. Rev. D* **94** no. 3, (Aug., 2016) 032003, [arXiv:1605.09318](#) [**hep-ex**].
- [2] J. Aalbers and C. Tunnell, “HAX - Handy Analysis tools for XENON”.
<https://github.com/XENON1T/hax>.
- [3] J. Aalbers and C. Tunnell, “PAX - Processor for Analysing XENON”.
<https://github.com/XENON1T/pax>.
- [4] M. G. Aartsen *et al.*, (**IceCube** Collaboration), “Improved limits on dark matter annihilation in the Sun with the 79-string IceCube detector and implications for supersymmetry”, *JCAP* **4** (Apr., 2016) 022, [arXiv:1601.00653](#) [**hep-ph**].
- [5] M. G. Aartsen *et al.*, (**IceCube** Collaboration), “Searches for Sterile Neutrinos with the IceCube Detector”, *Physical Review Letters* **117** no. 7, (Aug., 2016) 071801, [arXiv:1605.01990](#) [**hep-ex**].
- [6] S. Abrahamyan *et al.*, (**APEX** Collaboration), “Search for a New Gauge Boson in Electron-Nucleus Fixed-Target Scattering by the APEX Experiment”, *Physical Review Letters* **107** no. 19, (Nov., 2011) 191804, [arXiv:1108.2750](#) [**hep-ex**].
- [7] L. Ackerman, M. R. Buckley, S. M. Carroll, and M. Kamionkowski, “Dark matter and dark radiation”, *Physical Review D* **79** no. 2, (Jan., 2009) 023519, [arXiv:0810.5126](#) [**hep-ph**].
- [8] P. A. R. Ade *et al.*, (**Planck** Collaboration), “Planck 2013 results. I. Overview of products and scientific results”, *Astron. and Astroph.* **571** (Nov., 2014) A1, [arXiv:1303.5062](#).
- [9] M. Aglietta *et al.*, (**LVD** Collaboration), “Single muon angular distributions observed in the LVD particle astrophysics experiment”, *Astroparticle Physics* **2** (Oct., 1994) 103–116.
- [10] S. Agostinelli *et al.*, (**GEANT4** Collaboration), “GEANT4: A Simulation toolkit”, *Nucl. Instrum. Meth.* **A506** (2003) 250–303. <http://geant4.cern.ch/>. [Accessed: 2017/05/15].

- [11] J. A. Aguilar *et al.*, (**ANTARES** Collaboration), “A fast algorithm for muon track reconstruction and its application to the ANTARES neutrino telescope”, *Astroparticle Physics* **34** (Apr., 2011) 652–662, [arXiv:1105.4116](#) [[astro-ph.IM](#)].
- [12] J. Ahrens *et al.*, (**AMANDA** Collaboration), “Muon track reconstruction and data selection techniques in AMANDA”, *Nuclear Instruments and Methods in Physics Research A* **524** (May, 2004) 169–194, [astro-ph/0407044](#).
- [13] D. S. Akerib *et al.*, (**LUX** Collaboration), “The Large Underground Xenon (LUX) experiment”, *Nuclear Instruments and Methods in Physics Research A* **704** (Mar., 2013) 111–126, [arXiv:1211.3788](#).
- [14] D. S. Akerib *et al.*, (**LUX** Collaboration), “First Results from the LUX Dark Matter Experiment at the Sanford Underground Research Facility”, *Physical Review Letters* **112** no. 9, (Mar., 2014) 091303, [arXiv:1310.8214](#) [[astro-ph.CO](#)].
- [15] D. S. Akerib *et al.*, (**LUX** Collaboration), “Results from a Search for Dark Matter in the Complete LUX Exposure”, *Phys. Rev. Lett.* **118** (Jan, 2017) 021303, [arXiv:1608.07648](#).
- [16] R. A. Alpher, H. Bethe, and G. Gamow, “The Origin of Chemical Elements”, *Phys. Rev.* **73** (Apr, 1948) 803–804.
<http://link.aps.org/doi/10.1103/PhysRev.73.803>.
- [17] M. Ambrosio *et al.*, (**MACRO** Collaboration), “Measurement of the residual energy of muons in the Gran Sasso underground laboratories”, *Astroparticle Physics* **19** (June, 2003) 313–328, [hep-ex/0207043](#).
- [18] S. Andreas, C. Niebuhr, and A. Ringwald, “New limits on hidden photons from past electron beam dumps”, *Physical Review D* **86** no. 9, (Nov., 2012) 095019, [arXiv:1209.6083](#) [[hep-ph](#)].
- [19] G. Angloher *et al.*, (**CRESST** Collaboration), “Limits on WIMP dark matter using scintillating CaWO_4 cryogenic detectors with active background suppression”, *Astroparticle Physics* **23** (Apr., 2005) 325–339, [astro-ph/0408006](#).
- [20] R. E. Angulo, V. Springel, S. D. M. White, A. Jenkins, C. M. Baugh, and C. S. Frenk, “Scaling relations for galaxy clusters in the Millennium-XXL simulation”, *MNRAS* **426** (Nov., 2012) 2046–2062, [arXiv:1203.3216](#).
- [21] P. Antonioli, C. Ghetti, E. V. Korolkova, V. A. Kudryavtsev, and G. Sartorelli, “A three-dimensional code for muon propagation through the rock: MUSIC”, *Astroparticle Physics* **7** (Oct., 1997) 357–368, [hep-ph/9705408](#).
- [22] APOD, “Astronomy Picture of the Day”, December, 2011.
<http://apod.nasa.gov/apod/ap111221.html>. [Accessed: 2017/06/22].

- [23] E. Aprile and T. Doke, “Liquid xenon detectors for particle physics and astrophysics”, *Reviews of Modern Physics* **82** (July, 2010) 2053–2097, arXiv:0910.4956 [physics.ins-det].
- [24] E. Aprile *et al.*, (XENON Collaboration), “New measurement of the relative scintillation efficiency of xenon nuclear recoils below 10 keV”, *Phys. Rev. C* **79** (Apr, 2009) 045807.
- [25] E. Aprile *et al.*, (XENON Collaboration), “Design and performance of the XENON10 dark matter experiment”, *Astroparticle Physics* **34** (Apr., 2011) 679–698, arXiv:1001.2834 [astro-ph.IM].
- [26] E. Aprile *et al.*, (XENON Collaboration), “Dark Matter Results from 225 Live Days of XENON100 Data”, *Physical Review Letters* **109** no. 18, (Nov., 2012) 181301, arXiv:1207.5988 [astro-ph.CO].
- [27] E. Aprile *et al.*, (XENON Collaboration), “The XENON100 dark matter experiment”, *Astroparticle Physics* **35** (Apr., 2012) 573–590, arXiv:1107.2155 [astro-ph.IM].
- [28] E. Aprile *et al.*, (XENON Collaboration), “Response of the XENON100 dark matter detector to nuclear recoils”, *Phys. Rev. D* **88** no. 1, (July, 2013) 012006, arXiv:1304.1427 [astro-ph.IM].
- [29] E. Aprile *et al.*, (XENON Collaboration), “Conceptual design and simulation of a water Cherenkov muon veto for the XENON1T experiment”, *Journal of Instrumentation* **9** (Nov., 2014) P11006, arXiv:1406.2374 [astro-ph.IM].
- [30] E. Aprile *et al.*, (XENON Collaboration), “Lowering the radioactivity of the photomultiplier tubes for the XENON1T dark matter experiment”, *European Physical Journal C* **75** (Nov., 2015) 546, arXiv:1503.07698 [astro-ph.IM].
- [31] E. Aprile *et al.*, (XENON Collaboration), “Search for Event Rate Modulation in XENON100 Electronic Recoil Data”, arXiv:1507.07748.
- [32] E. Aprile *et al.*, (XENON Collaboration), “Physics reach of the XENON1T dark matter experiment.”, *JCAP* **4** (Apr., 2016) 027, arXiv:1512.07501 [physics.ins-det].
- [33] E. Aprile *et al.*, (XENON Collaboration), “Removing krypton from xenon by cryogenic distillation to the ppq level”, arXiv:1612.04284 [physics.ins-det].
- [34] E. Aprile *et al.*, (XENON Collaboration), “XENON100 dark matter results from a combination of 477 live days”, *Phys. Rev. D* **94** no. 12, (Dec., 2016) 122001, arXiv:1609.06154.
- [35] E. Aprile *et al.*, (XENON Collaboration), “First Dark Matter Search Results from the XENON1T Experiment”, *Phys. Rev. Lett.* **119** (Oct, 2017) 181301, arXiv:1705.06655.

- [36] E. Aprile *et al.*, (**XENON** Collaboration), “Material radioassay and selection for the XENON1T dark matter experiment”, *The European Physics Journal C* **77** no. 12, (2017) 890, [arXiv:1705.01828](#).
- [37] E. Aprile *et al.*, (**XENON** Collaboration), “Online ^{222}Rn removal by cryogenic distillation in the XENON100 experiment”, *The European Physical Journal C* **77** no. 6, (2017) 358, [arXiv:1702.06942](#).
- [38] E. Aprile *et al.*, (**XENON** Collaboration), “Search for Electronic Recoil Event Rate Modulation with 4 Years of XENON100 Data”, [arXiv:1701.00769](#).
- [39] E. Aprile *et al.*, (**XENON** Collaboration), “The XENON1T Dark Matter Experiment”, *ArXiv e-prints* (Aug., 2017), [arXiv:1708.07051](#) [[astro-ph.IM](#)].
- [40] V. N. Aseev, A. I. Belev, A. I. Berlev, E. V. Geraskin, A. A. Golubev, N. A. Likhovid, V. M. Lobashev, A. A. Nozik, V. S. Pantuev, V. I. Parfenov, A. K. Skasyrskaya, F. V. Tkachov, and S. V. Zadorozhny, “Upper limit on the electron antineutrino mass from the Troitsk experiment”, *Phys. Rev. D* **84** no. 11, (Dec., 2011) 112003, [arXiv:1108.5034](#) [[hep-ex](#)].
- [41] P. Atkins and J. de Paula, *Atkins’ Physical Chemistry*. OUP Oxford, 2010.
- [42] Autodesk, Inc., “EAGLE Software”.
<http://www.autodesk.com/products/eagle/overview>.
- [43] D. Babusci *et al.*, (**KLOE-2** Collaboration), “Limit on the production of a light vector gauge boson in phi meson decays with the KLOE detector”, *Physics Letters B* **720** (Mar., 2013) 111–115, [arXiv:1210.3927](#) [[hep-ex](#)].
- [44] E. A. Bagnaschi, O. Buchmueller, R. Cavanaugh, M. Citron, A. De Roeck, M. J. Dolan, J. R. Ellis, H. Flächer, S. Heinemeyer, G. Isidori, S. Malik, D. Martínez Santos, K. A. Olive, K. Sakurai, K. J. de Vries, and G. Weiglein, “Supersymmetric dark matter after LHC run 1”, *European Physical Journal C* **75** (Oct., 2015) 500, [arXiv:1508.01173](#) [[hep-ph](#)].
- [45] L. Baudis, A. Behrens, A. Ferella, A. Kish, T. Marrodán Undagoitia, D. Mayani, and M. Schumann, “Performance of the Hamamatsu R11410 photomultiplier tube in cryogenic xenon environments”, *Journal of Instrumentation* **8** (Apr., 2013) P04026, [arXiv:1303.0226](#) [[astro-ph.IM](#)].
- [46] L. Baudis, H. Dujmovic, C. Geis, A. James, A. Kish, A. Manalaysay, T. Marrodán Undagoitia, and M. Schumann, “Response of liquid xenon to Compton electrons down to 1.5 keV”, *Phys. Rev. D* **87** no. 11, (June, 2013) 115015, [arXiv:1303.6891](#) [[astro-ph.IM](#)].
- [47] D. Bay *et al.*, (**MINOS** Collaboration), “Limits on Active to Sterile Neutrino Oscillations from Disappearance Searches in the MINOS, Daya Bay, and Bugey-3 Experiments”, *ArXiv e-prints* (July, 2016), [arXiv:1607.01177](#) [[hep-ex](#)].

- [48] K. G. Begeman, A. H. Broeils, and R. H. Sanders, “Extended rotation curves of spiral galaxies - Dark halos and modified dynamics”, *MNRAS* **249** (Apr., 1991) 523–537.
- [49] J. D. Bekenstein, “Relativistic gravitation theory for the modified Newtonian dynamics paradigm”, *Phys. Rev. D* **70** no. 8, (Oct., 2004) 083509, [astro-ph/0403694](#).
- [50] G. Bellini *et al.*, (**BOREXINO** Collaboration), “Muon and cosmogenic neutron detection in Borexino”, *Journal of Instrumentation* **6** (May, 2011) 5005, [arXiv:1101.3101](#) [[physics.ins-det](#)].
- [51] R. Bernabei *et al.*, (**DAMA/LIBRA** Collaboration), “Final model independent result of DAMA/LIBRA-phase1”, *European Physical Journal C* **73** (Dec., 2013) 2648, [arXiv:1308.5109](#).
- [52] J. Billard, E. Figueroa-Feliciano, and L. Strigari, “Implication of neutrino backgrounds on the reach of next generation dark matter direct detection experiments”, *Phys. Rev. D* **89** no. 2, (Jan., 2014) 023524, [arXiv:1307.5458](#) [[hep-ph](#)].
- [53] S. Bird, I. Cholis, J. B. Muñoz, Y. Ali-Haïmoud, M. Kamionkowski, E. D. Kovetz, A. Raccanelli, and A. G. Riess, “Did LIGO Detect Dark Matter?”, *Physical Review Letters* **116** no. 20, (May, 2016) 201301, [arXiv:1603.00464](#).
- [54] Boedeker Plastics, Inc., “PEEK (PolyEtherEtherKetone) Specifications”. http://www.boedeker.com/peek_p.htm. [Accessed: 2017/03/28].
- [55] A. Boyarsky, D. Iakubovskiy, and O. Ruchayskiy, “Next decade of sterile neutrino studies”, *Physics of the Dark Universe* **1** (Nov., 2012) 136–154, [arXiv:1306.4954](#) [[astro-ph.CO](#)].
- [56] M. Boylan-Kolchin, V. Springel, S. D. M. White, and A. Jenkins, “There’s no place like home? Statistics of Milky Way-mass dark matter haloes”, *MNRAS* **406** (Aug., 2010) 896–912, [arXiv:0911.4484](#) [[astro-ph.CO](#)].
- [57] M. Bradač, S. W. Allen, T. Treu, H. Ebeling, R. Massey, R. Glenn Morris, A. v.d. Linden, and D. Applegate, “Revealing the Properties of Dark Matter in the Merging Cluster MACS J0025.4-1222”, *The Astrophysical Journal* **687** no. 2, (2008) 959. <http://stacks.iop.org/0004-637X/687/i=2/a=959>.
- [58] R. Bradley, J. Clarke, D. Kinion, L. J. Rosenberg, K. van Bibber, S. Matsuki, M. Mück, and P. Sikivie, “Microwave cavity searches for dark-matter axions”, *Rev. Mod. Phys.* **75** (Jun, 2003) 777–817.
- [59] V. Brdar, J. Kopp, J. Liu, and X.-P. Wang, “Return of the X-rays: A New Hope for Fermionic Dark Matter at the keV Scale”, *ArXiv e-prints* (Oct., 2017) , [arXiv:1710.02146](#) [[hep-ph](#)].
- [60] H. L. Brooks, M. C. Cornell, J. Fletcher, I. M. Littlewood, and K. J. Nygaard, “Electron drift velocities in xenon”, *Journal of Physics D: Applied Physics* **15** no. 6, (1982) L51. <http://stacks.iop.org/0022-3727/15/i=6/a=002>.

- [61] R. Brunetti *et al.*, (**WARP** Collaboration), “WARP liquid argon detector for dark matter survey”, *New Astronomy Reviews* **49** (May, 2005) 265–269, [astro-ph/0405342](#).
- [62] D. Budker *et al.*, “Proposal for a Cosmic Axion Spin Precession Experiment (CASPER)”, *Physical Review X* **4** no. 2, (Apr., 2014) 021030, [arXiv:1306.6089 \[hep-ph\]](#).
- [63] E. M. Burbidge, G. R. Burbidge, W. A. Fowler, and F. Hoyle, “Synthesis of the Elements in Stars”, *Rev. Mod. Phys.* **29** (Oct, 1957) 547–650.
- [64] X. Cao *et al.*, (**PandaX** Collaboration), “PandaX: a liquid xenon dark matter experiment at CJPL”, *Science China Physics, Mechanics, and Astronomy* **57** (Aug., 2014) 1476–1494, [arXiv:1405.2882 \[physics.ins-det\]](#).
- [65] S. Chatrchyan *et al.*, (**CMS** Collaboration), “Search for dark matter and unparticles in events with a Z boson and missing transverse momentum in proton-proton collisions at $\sqrt{s} = 13$ TeV”, [arXiv:1701.02042 \[hep-ex\]](#).
- [66] K. Choi *et al.*, (**Super-Kamiokande** Collaboration), “Search for neutrinos from annihilation of captured low-mass dark matter particles in the Sun by Super-Kamiokande”, *ArXiv e-prints* (Mar., 2015) , [arXiv:1503.04858 \[hep-ex\]](#).
- [67] D. Clowe, M. Bradač, A. H. Gonzalez, M. Markevitch, S. W. Randall, C. Jones, and D. Zaritsky, “A Direct Empirical Proof of the Existence of Dark Matter”, *The Astrophysical Journal Letters* **648** (Sept., 2006) L109–L113, [astro-ph/0608407](#).
- [68] COMSOL, Inc., “COMSOL Multiphysics”. <http://www.comsol.com>.
- [69] J. M. Conrad and M. H. Shaevitz, “Sterile Neutrinos: An Introduction to Experiments”, *ArXiv e-prints* (Sept., 2016) , [arXiv:1609.07803 \[hep-ex\]](#).
- [70] G. Cowan, K. Cranmer, E. Gross, and O. Vitells, “Asymptotic formulae for likelihood-based tests of new physics”, *European Physical Journal C* **71** (Feb., 2011) 1554, [arXiv:1007.1727 \[physics.data-an\]](#).
- [71] J. R. Davis and A. Committee, *Stainless Steels*. ASM specialty handbook. ASM International, 1994.
- [72] J. R. Davis and A. Committee, *Copper and Copper Alloys*. ASM specialty handbook. ASM International, 2001.
- [73] J. M. De Freitas and K. van Caekenberghe, *SPHERE3D: A Matlab Function to Plot 3-Dimensional Data on a Spherical Surface.*, 2009. <https://de.mathworks.com/matlabcentral/fileexchange/23385-nf2ff?focused=3805866&tab=function>. [Accessed: 2017/05/24].
- [74] DuPont, *Datasheet Pyralux AP 9222R*, 2016. <http://www.dupont.com/products-and-services/electronic-electrical-materials/flexible-rigidflex-circuit-materials/brands/pyralux-flexible-circuit/products/pyralux-ap.html>. [Accessed: 2017/03/30].

- [75] S. Dye, N. W. Evans, V. Belokurov, S. J. Warren, and P. Hewett, “Models of the Cosmic Horseshoe gravitational lens J1004+4112”, *MNRAS* **388** (July, 2008) 384–392, [arXiv:0804.4002](#).
- [76] DYMAX corporation, *Datasheet DYMAX OP-29*, 2013. <https://www.dymax.com/images/pdf/pds/op-29.pdf>. [Accessed: 2017/05/23].
- [77] A. Einstein, “Lens-Like Action of a Star by the Deviation of Light in the Gravitational Field”, *Science* **84** (Dec., 1936) 506–507.
- [78] W. Erni *et al.*, (**PANDA** Collaboration), “Technical Design Report for PANDA Electromagnetic Calorimeter (EMC)”, [arXiv:0810.1216](#) [physics.ins-det].
- [79] R. Essig *et al.*, “Dark Sectors and New, Light, Weakly-Coupled Particles”, *ArXiv e-prints* (Oct., 2013) , [arXiv:1311.0029](#) [hep-ph].
- [80] J. L. Feng, “Dark Matter Candidates from Particle Physics and Methods of Detection”, *Ann. Rev. Astron. Astroph.* **48** (Sept., 2010) 495–545, [arXiv:1003.0904](#) [astro-ph.CO].
- [81] D. J. Fixsen, “The Temperature of the Cosmic Microwave Background”, *The Astrophysical Journal* **707** (Dec., 2009) 916–920, [arXiv:0911.1955](#).
- [82] K. Freund *et al.*, (**GERDA** Collaboration), “The performance of the Muon Veto of the GERDA experiment”, *European Physical Journal C* **76** (May, 2016) 298, [arXiv:1601.05935](#) [physics.ins-det].
- [83] J. M. Gaskins, “A review of indirect searches for particle dark matter”, *Contemporary Physics* **57** (Oct., 2016) 496–525, [arXiv:1604.00014](#) [astro-ph.HE].
- [84] C. Geis, U. Oberlack, C. Grignon, D. Ramírez García, and Q. Weitzel, “Optical response of highly reflective film used in the water Cherenkov muon veto of the XENON1T dark matter experiment”, *Journal of Instrumentation* **12** (June, 2017) P06017, [arXiv:1706.03687](#) [physics.ins-det].
- [85] G. Gelmini and P. Gondolo, *DM production mechanisms*, p. 121. Cambridge University Press, 2010. [arXiv:1009.3690](#).
- [86] General Electric, *Historian*. <https://www.ge.com/digital/products/historian>. [Accessed: 2017/11/18].
- [87] M. W. Goodman and E. Witten, “Detectability of certain dark-matter candidates”, *Phys. Rev. D* **31** (Jun, 1985) 3059–3063.
- [88] C. Grupen, *Astroteilchenphysik: Das Universum im Licht der kosmischen Strahlung*. Vieweg+Teubner Verlag, 2000.
- [89] L. J. Hall, K. Jedamzik, J. March-Russell, and S. M. West, “Freeze-in production of FIMP dark matter”, *Journal of High Energy Physics* **3** (Mar., 2010) 80, [arXiv:0911.1120](#) [hep-ph].

- [90] Hamamatsu Photonics K. K., *Datasheet R5912 ASSY PMT*, 2012.
- [91] Hamamatsu Photonics K.K. Editorial Committee, *Photomultiplier Tubes - Basics and Applications*, vol. 3a. Hamamatsu Photonics K.K. Electron Tube Division, 2007. http://www.hamamatsu.com/jp/en/community/optical_sensors/articles/photomultiplier_tube_handbook/index.html. [Accessed: 2017/05/18].
- [92] D. Harvey, R. Massey, T. Kitching, A. Taylor, and E. Tittley, “The nongravitational interactions of dark matter in colliding galaxy clusters”, *Science* **347** (Mar., 2015) 1462–1465, [arXiv:1503.07675](https://arxiv.org/abs/1503.07675).
- [93] R. Heine, K. Aulenbacher, and R. Eichhorn, “MESA - Sketch of an energy recovery LINAC for nuclear physics experiments at Mainz”, *Proceedings of IPAC2012* (2012) .
- [94] G. Heusser, M. Laubenstein, and H. Neder, “Low-level germanium gamma-ray spectrometry at the $\mu\text{Bq}/\text{kg}$ level and future developments towards higher sensitivity”, *Radioactivity in the Environment* **8** (2006) 495–510.
- [95] G. Hinshaw *et al.*, (**WMAP** Collaboration), “Nine-year Wilkinson Microwave Anisotropy Probe (WMAP) Observations: Cosmological Parameter Results”, *The Astrophysical Journal, Supplement* **208** (Oct., 2013) 19, [arXiv:1212.5226](https://arxiv.org/abs/1212.5226).
- [96] M. Holz, S. R. Heil, and A. Sacco, “Temperature-dependent self-diffusion coefficients of water and six selected molecular liquids for calibration in accurate 1H NMR PFG measurements”, *Phys. Chem. Chem. Phys.* **2** (2000) 4740–4742.
- [97] G. Jungman, M. Kamionkowski, and K. Griest, “Supersymmetric dark matter”, *Physics Reports* **267** (Mar., 1996) 195–373, [hep-ph/9506380](https://arxiv.org/abs/hep-ph/9506380).
- [98] M. A. Knapp, *Design, Simulation und Aufbau des GERDA-Myonvetos*. PhD thesis, Eberhard-Karls-Universität Tübingen, 2009.
- [99] S. Kubota, A. Nakamoto, T. Takahashi, T. Hamada, E. Shibamura, M. Miyajima, K. Masuda, and T. Doke, “Recombination luminescence in liquid argon and in liquid xenon”, *Phys. Rev. B* **17** (Mar., 1978) 2762–2765.
- [100] A. Kurylov and M. Kamionkowski, “Generalized analysis of the direct weakly interacting massive particle searches”, *Phys. Rev. D* **69** no. 6, (Mar., 2004) 063503, [hep-ph/0307185](https://arxiv.org/abs/hep-ph/0307185).
- [101] J. Lee and E. Komatsu, “Bullet Cluster: A Challenge to ΛCDM Cosmology”, *The Astrophysical Journal* **718** (July, 2010) 60–65, [arXiv:1003.0939](https://arxiv.org/abs/1003.0939).
- [102] W. R. Leo, *Techniques for Nuclear and Particle Physics Experiments: A How-To Approach*. U.S. Government Printing Office, 1994.
- [103] J. D. Lewin and P. F. Smith, “Review of mathematics, numerical factors, and corrections for dark matter experiments based on elastic nuclear recoil”, *Astroparticle Physics* **6** no. 1, (1996) 87–112.

- [104] D. R. Lide, *CRC Handbook of Chemistry and Physics, 85th Edition*. No. Bd. 85 in CRC Handbook of Chemistry and Physics, 85th Ed. Taylor & Francis, 2004.
- [105] LOT-QuantumDesign GmbH, *Manual LOT LSH-150 Monochromator*, 2015.
- [106] D. Lyapustin, “The Axion Dark Matter eXperiment”, *ArXiv e-prints* (Dec., 2011), [arXiv:1112.1167](https://arxiv.org/abs/1112.1167) [astro-ph.CO].
- [107] A. Lyashenko, T. Nguyen, A. Snyder, H. Wang, and K. Arisaka, “Measurement of the absolute Quantum Efficiency of Hamamatsu model R11410-10 photomultiplier tubes at low temperatures down to liquid xenon boiling point”, *Journal of Instrumentation* **9** (Nov., 2014) P11021, [arXiv:1410.3890](https://arxiv.org/abs/1410.3890) [astro-ph.IM].
- [108] C. J. Ma, H. Ebeling, and E. Barrett, “An X-Ray/Optical Study of the Complex Dynamics of the Core of the Massive Intermediate-Redshift Cluster MACSJ0717.5+3745”, *The Astrophysical Journal Letters* **693** (Mar., 2009) L56–L60, [arXiv:0901.4783](https://arxiv.org/abs/0901.4783) [astro-ph.CO].
- [109] A. Mahdavi, H. Hoekstra, A. Babul, D. D. Balam, and P. L. Capak, “A Dark Core in Abell 520”, *The Astrophysical Journal* **668** (Oct., 2007) 806–814, [arXiv:0706.3048](https://arxiv.org/abs/0706.3048).
- [110] D. C. Malling *et al.*, (LZ Collaboration), “After LUX: The LZ Program”, *ArXiv e-prints* (Oct., 2011), [arXiv:1110.0103](https://arxiv.org/abs/1110.0103) [astro-ph.IM].
- [111] G. Mangano, G. Miele, S. Pastor, T. Pinto, O. Pisanti, and P. D. Serpico, “Relic neutrino decoupling including flavour oscillations”, *Nuclear Physics B* **729** (Nov., 2005) 221–234, [hep-ph/0506164](https://arxiv.org/abs/hep-ph/0506164).
- [112] Maxim Integrated Products Incorporated, *Datasheet MAX481E RS-485 Transceiver*, 2014. <https://datasheets.maximintegrated.com/en/ds/MAX1487-MAX491.pdf>. [Accessed: 2017/04/24].
- [113] Microchip Incorporated, *Datasheet PIC16F87XA Microcontroller*, 2003. <http://ww1.microchip.com/downloads/en/DeviceDoc/39582b.pdf>. [Accessed: 2017/04/24].
- [114] M. Milgrom, “Dynamics with a Nonstandard Inertia-Acceleration Relation: An Alternative to Dark Matter in Galactic Systems”, *Annals of Physics* **229** (Feb., 1994) 384–415, [astro-ph/9303012](https://arxiv.org/abs/astro-ph/9303012).
- [115] Minnesota Mining and Manufacturing (3M), *Datasheet DF2000MA Specular Film (Old)*, 2007. <http://multimedia.3m.com/mws/media/746469O/3m-daylighting-film-df2000ma.pdf>. [Accessed: 2017/05/29].
- [116] Minnesota Mining and Manufacturing (3M), *Datasheet Glass Bubbles S32*, 2009. <http://multimedia.3m.com/mws/media/619093O/3m-glass-bubbles-types-k-and-s-uk-data-sheet.pdf>. [Accessed: 2017/05/23].

- [117] Minnesota Mining and Manufacturing (3M), *Datasheet DF2000MA Specular Film*, 2017. <http://multimedia.3m.com/mws/media/9824490/3mtm-specular-film-df2000ma-technical-data-sheet.pdf>. [Accessed: 2017/05/10].
- [118] L. Miramonti, “European underground laboratories: An overview”, *Proceedings of the Topical Workshop on Low Radioactivity Techniques: LRT 2004*. **785** (Sept., 2005) 3–11, [hep-ex/0503054](https://arxiv.org/abs/hep-ex/0503054).
- [119] R. J. Noll, “Zernike polynomials and atmospheric turbulence”, *Journal of the Optical Society of America (1917-1983)* **66** (Mar., 1976) 207–211.
- [120] C. Patrignani *et al.*, (**Particle Data Group** Collaboration), “Review of particle physics”, *Chin. Phys.* **C40** (2016) 100001.
- [121] R. D. Peccei and H. R. Quinn, “*CP* Conservation in the Presence of Pseudoparticles”, *Phys. Rev. Lett.* **38** (Jun, 1977) 1440–1443.
- [122] F. Pedrotti, L. Pedrotti, W. Bausch, and H. Schmidt, *Optik für Ingenieure: Grundlagen*. Springer Berlin Heidelberg, 2005.
- [123] PFLITSCH GmbH & Co. KG, *Catalogue PFLITSCH cable feedthroughs, Uni Dicht series*, 2017. https://www.pflitsch.de/fileadmin/user_upload/Downloads/Kataloge/Katalog_kv_5_UNI_Dicht.pdf. [Accessed: 2017/11/29].
- [124] M. Pospelov, “Secluded U(1) below the weak scale”, *Physical Review D* **80** no. 9, (Nov., 2009) 095002, [arXiv:0811.1030](https://arxiv.org/abs/0811.1030) [hep-ph].
- [125] D. Ramírez García, “Monte Carlo simulations of a neutron veto for the XENONnT dark matter experiment”. Master thesis, 2017.
- [126] S. Rosendahl, K. Bokeloh, E. Brown, I. Cristescu, A. Fieguth, C. Huhmann, O. Lebeda, C. Levy, M. Murra, S. Schneider, D. Venos, and C. Weinheimer, “A novel 83m Kr tracer method for characterizing xenon gas and cryogenic distillation systems”, *Journal of Instrumentation* **9** no. 10, (2014) P10010. <http://stacks.iop.org/1748-0221/9/i=10/a=P10010>.
- [127] S. Rosendahl, E. Brown, I. Cristescu, A. Fieguth, C. Huhmann, O. Lebeda, M. Murra, and C. Weinheimer, “Determination of the separation efficiencies of a single-stage cryogenic distillation setup to remove krypton out of xenon by using a ^{83m}Kr tracer method”, *Review of Scientific Instruments* **86** no. 11, (2015) 115104.
- [128] S. Rosendahl, E. Brown, I. Cristescu, A. Fieguth, C. Huhmann, M. Murra, and C. Weinheimer, “A cryogenic distillation column for the XENON1T experiment”, *Journal of Physics: Conference Series* **564** no. 1, (2014) 012006. <http://stacks.iop.org/1742-6596/564/i=1/a=012006>.
- [129] L. Roszkowski, E. M. Sessolo, and A. J. Williams, “Prospects for dark matter searches in the pMSSM”, *Journal of High Energy Physics* **2** (Feb., 2015) 14, [arXiv:1411.5214](https://arxiv.org/abs/1411.5214) [hep-ph].

- [130] R. H. Sanders and S. S. McGaugh, “Modified Newtonian Dynamics as an Alternative to Dark Matter”, *Annual Review of Astronomy and Astrophysics* **40** (2002) 263–317, [astro-ph/0204521](#).
- [131] M. Schumann, L. Baudis, L. Büttikofer, A. Kish, and M. Selvi, “Dark matter sensitivity of multi-ton liquid xenon detectors”, *JCAP* **10** (Oct., 2015) 016, [arXiv:1506.08309 \[physics.ins-det\]](#).
- [132] M. Selvi *et al.*, (**LVD** Collaboration), “Analysis of the seasonal modulation of the cosmic muon flux in the LVD detector during 2001-2008”, *Proceedings of the 31st ICRC* (2009) .
- [133] P. Shirley and R. K. Morley, *Realistic Ray Tracing, Second Edition*. Ak Peters Series. Taylor & Francis, 2003.
- [134] Smartec BV, *Datasheet Universal Transducer Interface*, 2016. http://www.smartec-sensors.com/cms/media/Datasheets/UTI_interface/UTI_datasheet.pdf. [Accessed: 2017/03/22].
- [135] B. L. Smith, P. R. Gardner, and E. H. C. Parker, “Surface Tension and Energy of Liquid Xenon”, *The Journal of Chemical Physics* **47** no. 3, (1967) 1148–1152.
- [136] SphereOptics GmbH, *Datasheet Zenith Polymer Diffuse Reflectance Standards*, 2012. http://sphereoptics.de/wp-content/uploads/2014/03/Zenith_Product-Brochure.pdf. [Accessed: 2017/05/30].
- [137] V. Springel, S. D. M. White, A. Jenkins, C. S. Frenk, N. Yoshida, L. Gao, J. Navarro, R. Thacker, D. Croton, J. Helly, J. A. Peacock, S. Cole, P. Thomas, H. Couchman, A. Evrard, J. Colberg, and F. Pearce, “Simulations of the formation, evolution and clustering of galaxies and quasars”, *Nature* **435** (June, 2005) 629–636, [astro-ph/0504097](#).
- [138] G. Steigman, B. Dasgupta, and J. F. Beacom, “Precise relic WIMP abundance and its impact on searches for dark matter annihilation”, *Phys. Rev. D* **86** no. 2, (July, 2012) 023506, [arXiv:1204.3622 \[hep-ph\]](#).
- [139] A. Tan *et al.*, (**PandaX** Collaboration), “Dark Matter Results from First 98.7-day Data of PandaX-II Experiment”, *ArXiv e-prints* (July, 2016) , [arXiv:1607.07400 \[hep-ex\]](#).
- [140] Texas Instruments Incorporated, *Datasheet 74LS151N Multiplexer*, 2017. <http://www.ti.com/lit/ds/symlink/sn54150.pdf>. [Accessed: 2017/04/24].
- [141] U.S. Geological Survey (USGS), *M 6.2 Earthquake in Central Italy*, 2016. <https://earthquake.usgs.gov/earthquakes/eventpage/us10006g7d>. [Accessed: 2017/05/11].
- [142] E. Ventsel and T. Krauthammer, *Thin Plates and Shells: Theory: Analysis, and Applications*. CRC Press, 2001.

- [143] M. Vogelsberger, A. Helmi, V. Springel, S. D. M. White, J. Wang, C. S. Frenk, A. Jenkins, A. Ludlow, and J. F. Navarro, “Phase-space structure in the local dark matter distribution and its signature in direct detection experiments”, *MNRAS* **395** (May, 2009) 797–811, [arXiv:0812.0362](https://arxiv.org/abs/0812.0362).
- [144] Wacker Chemie AG, *Datasheet DYMAX OP-29*, 2014. <https://www.wacker.com/cms/en/products/product/product.jsp?product=10549>. [Accessed: 2017/05/23].
- [145] Wikimedia Commons, “The first 15 Zernike polynomials”, 2012. <https://commons.wikimedia.org/wiki/File:ZernikePolynome6.pdf>. [Accessed: 2017/03/14].
- [146] L. Wyrzykowski, J. Skowron, S. Kozłowski, A. Udalski, M. K. Szymański, M. Kubiak, G. Pietrzyński, I. Soszyński, O. Szewczyk, K. Ulaczyk, R. Poleski, and P. Tisserand, “The OGLE view of microlensing towards the Magellanic Clouds - IV. OGLE-III SMC data and final conclusions on MACHOs”, *MNRAS* **416** (Oct., 2011) 2949–2961, [arXiv:1106.2925](https://arxiv.org/abs/1106.2925).
- [147] F. Zernike, “Beugungstheorie des Schneidensverfahrens und seiner verbesserten Form, der Phasenkontrastmethode”, *Physica* **1** (May, 1934) 689–704.
- [148] K. Zioutas *et al.*, (CAST Collaboration), “First Results from the CERN Axion Solar Telescope”, *Physical Review Letters* **94** no. 12, (Apr., 2005) 121301, [hep-ex/0411033](https://arxiv.org/abs/hep-ex/0411033).
- [149] F. Zwicky, “Die Rotverschiebung von extragalaktischen Nebeln”, *Helvetica Physica Acta* **6** (1933) 110–127.